Effect of microstructure on mechanical behaviour of arterial tissue

Aziz TOKGOZ

Department of Engineering

University of Cambridge

This dissertation is submitted for the degree of Doctor of Philosophy

St Edmund's College February 2019

Declaration

I hereby declare that except where specific reference is made to the work of others, the contents of this dissertation are original. This dissertation is not substantially the same as any that has been submitted, or, is being concurrently submitted for a degree or diploma or other qualification at the University of Cambridge or any other University or similar institution. This dissertation includes nothing which is the outcome of work done in collaboration, except where specifically indicated in the text and it does not exceed the 65000 words limit.

Aziz TOKGOZ

February 2019

Acknowledgements

First of all, I would like to express my deepest gratitude to my supervisors Prof Michael Sutcliffe and Dr Zhongzhao Teng for giving me the opportunity to be part of their research team. The guidance and motivation provided by them have been highly instrumental while tackling all the problems that I have encountered during my PhD.

I owe special thanks to my dear friend Dr Shuo Wang, with whom I have been working with since the beginning of my studies in Cambridge. We have collaborated on various projects and he has provided me with all kinds of support along the way. I also want to thank Dr Graeham Douglas who has introduced me to the preliminary studies of my PhD project and provided me with very valuable multiphoton microscopy and mechanical data. The knowledge and ideas that I obtained from him have been highly useful while designing the course of my PhD.

I owe many thanks to my friends Dr Yuan Huang and Dr Ammara Usman. Their vast knowledge and guidance on many aspects of my PhD project have been extremely useful. I also owe many thanks to my friend Chang Sun for his help in analysis of the mechanical data.

I want to thank Dr Priya Sastry for providing me with the diseased human aortic tissue pieces and for the continued support that she provided during the mechanical experiments. I also want to thank Nichola Figg for immunohistochemical processing of the aortic tissue samples and for her assistance in optimisation of the digital histological image processing platform. I also want to thank Prof Jonathan Gillard and Prof Martin Bennett for arranging the laboratory facilities at the Addenbrooke's Hospital. The guidance provided by Prof Jonathan Gillard and his comforting attitude have also been highly instrumental in completion of my PhD.

I owe my deepest gratitude to the Engineering and Physical Sciences Research Council (EPSRC) for the financial support that they have provided for my PhD.

Finally, I would like to thank my parents Emine Tokgoz and Hakan Tokgoz. Without their love and support, I would not be where I am today. I especially want to thank my partner Dr Hatice Kasap, who has been with me every step of the way and sacrificed whatever necessary to support me in the last decade and particularly during my studies in Cambridge. I am looking very much forward to the next chapter of our life, which I hope will be filled with lots of happiness and joy.

This dissertation is dedicated to my parents and my partner.

Publications

The work in the paper below is included in **Chapter 2** and **Chapter 3**:

Tokgoz, A. [†], *Wang, S.* [†], *Sastry, P., Sun, C., Figg, N., Huang, Y., Bennett M.R., Sinha S., Gillard, J.H., Sutcliffe, M.P.F., Teng, Z., 2019. Association of collagen, elastin, glycosaminoglycans and macrophages with tissue ultimate material strength and extreme extensibility in human thoracic aortic aneurysms: a tensile testing study.* - ***Submitted***.

[†] *First authors*

The work in the paper below is included in **Chapter 4**:

Wang, S. [†], ***Tokgoz, A.*** [†], *Huang, Y., Zhang, Y., Feng, J., Sastry, P., Sun, C., Figg, N., Lu, Q., Sutcliffe, M.P.F., Teng, Z., Gillard, J.H., 2019. Bayesian inference-based estimation of normal aortic, aneurysmal and atherosclerotic tissue mechanical properties: from material testing, modelling and histology. IEEE Transactions on Biomedical Engineering 1–1. https://doi.org/10.1109/TBME.2018.2886681* - ***Published***.

[†] *First authors*

Permission has been obtained to use the contents of the published paper above in this dissertation.

Abstract

The total number of annual deaths caused by cardiovascular diseases (CVDs), aortic aneurysms (AAs) and aortic dissections (ADs) is more than from any other cause. Most CVDs are a result of atherosclerosis, in which a fibrous cap covered lipid-rich plaque is formed in the arteries. The fibrous cap can rupture, blocking the artery and limiting the flow of blood to vital organs. AAs and ADs manifest as localised dilatations of the aorta, while simultaneously weakening the aortic wall. In atherosclerosis, AAs and ADs disruptions of the fibrous network and incorporation of microstructural defects make the artery vulnerable to rupture.

This dissertation is aimed at describing the relationship between microstructure and mechanical, including fracture behaviour of arterial tissue. Unnotched and notched mechanical tests were performed on tissue samples from aneurysm-affected aortas. Mechanical parameters of ultimate material strength and extreme extensibility were measured, showing arterial layer and direction dependent differences in both unnotched and notched test. Similar differences were observed in fracture parameters of J-integral and crack tip curvature at failure. Interestingly, aneurysmal tissues were found to be notch-insensitive as the notched samples did not fail at a low stretch level. Histopathological analysis was performed on the mechanically tested tissues to investigate the influence of collagen, elastin, macrophage and glycosaminoglycan (GAG) contents, as well as collagen fibre dispersion on the mechanical and fracture behaviours. Both collagen and GAGs were associated with tissue strength, while higher GAG deposition was found to result in larger local collagen fibre dispersion in media and adventitia layers, but not in the intima.

Stress-stretch behaviour of healthy, aneurysmal and atherosclerotic tissues were characterised with the modified Mooney-Rivlin constitutive material model. Curve fitting was used to compute the corresponding values of the model constants for each tissue type. Fitted material constants were found to differ amongst distinct types of tissue, while histological analyses showed that material constants were associated with waviness and dispersion of collagen fibres. To study the stretch driven microstructural reorganisations of the fibrous network, tensile tests with unnotched and notched tissue strips from porcine carotid arteries were performed while imaging with multiphoton microscopy. In general, fibres rotated towards the direction of stretch, where in notched samples, fibres rearranged themselves to redistribute loads away from the notch tip. Finally, a complete microstructural component based finite element model of the arterial tissue was developed, which consisted of the collagen fibres and the other structural entities such as elastin and GAGs. The collagen fibres were modelled as discrete entities within the model, where all the other structural entities were modelled in the form of ground matrix. The developed model was used to study the influence of distinct microstructural parameters on the mechanical behaviour of arterial tissues.

Contents

Abbreviations

AA	Aortic Aneurysm
AD	Aortic Dissection
AHA	American Heart Association
ATA	Ascending Thoracic Aneurysm
CCDF	Complementary Cumulative Distribution Function
CD68	Cluster of Differentiation 68
CFCL	Collagen Fibre Cross-link
CVD	Cardiovascular Disease
dGEMRIC	Delayed Gadolinium-enhanced MRI of Cartilage
DMSO	Dimethylsulfoxide
ECM	Extracellular Matrix
EDTA	Ethylenediaminetetraacetic Acid
EEL	External Elastic Lamina
EVG	Elastin Van Gieson
FC	Fibrous Cap
FEA	Finite Element Analysis
FGML	Fibre to Ground Matrix Links
GAG	Glycosaminoglycan
H&E	Hematoxylin and Eosin
HLA-DR	Human Leukocyte Antigen – DR Isotype

IEL	Internal Elastic Lamina
IPH/T	Intraplaque Haemorrhage/Thrombus
LDL	Low Density Lipoprotein
MCMC	Markov Chain Monte Carlo
MCA	Middle Cerebral Artery
MIP	Maximum Intensity Projection
MMP	Matrix Metalloproteinase
MRI	Magnetic Resonance Imaging
NBF	Neutral Buffered Formalin
OLS	Ordinary Least Square
PBS	Phosphate Buffered Saline
PDF	Probability Density Function
RGB	Red-Green-Blue
ROI	Region of Interest
SEDF	Strain Energy Density Function
SHG	Second Harmonic Generation
SMC	Smooth Muscle Cell
TAA	Thoracic Aortic Aneurysm
TCFA	Thin-cap Fibroatheroma
TPF	Two-photon Fluorescence
3D	Three Dimensional

Chapter 1

Introduction

1.1 Overview

Arterial diseases such as AAs, ADs and atherosclerosis are amongst the most costly and deadly diseases. AAs are most common in men, with approximately 8% of those aged 65 years or older experiencing the condition in the remainder of their lifetime, while the condition usually remains asymptomatic until it causes a clinical event[1]. On the other hand, ADs can occur in up to 30 people in a million per year, depending on the population considered[2].

AAs are localised and permanent dilatations of the aorta that cause its diameter to exceed its normal size by more than 50%, where a healthy aorta has a diameter of ~2.1 cm and AA are considered to be clinically relevant when their diameters exceed 4 cm[1]. ADs occur when a tear in the intimal layer allows blood flow between various arterial layers of the aorta, causing the arterial layers to separate. The separated arterial layers allow continuous flow of blood in between them, facilitating formation of a true and a false lumen either with or without communication[2]. Enlargement of the formed false lumen continuously dilates the aorta and increases the amount of blood that is directed away from the true lumen, therefore decreasing the flow of blood into arteries that branch off from the aorta. The decreased blood flow in the aortic branches results in ischemia, which may cause temporary or permanent damage to the organs that feed from the affected aortic branches[2,3]. Both AAs and ADs have mortality rates over 80%, which are caused by the rupture of the dilated aorta[1–3].

Along with AAs and ADs, it has been projected that atherosclerosis will continue to be the leading cause of death until 2020[4,5]. Coronary artery disease, which is caused by atherosclerosis, is the number one killer in developed countries[6,7]. Atherosclerosis causes fatal clinical conditions by either completely blocking or limiting the flow of blood to the heart or the brain[5,8].

In atherosclerosis, AAs and ADs the arterial wall becomes prone to rupture mainly as a result of disruptions of the fibrous network and incorporation of microstructural defects. Under physiological conditions, the diseased artery wall is subject to structural loading by the blood pressure and flow. From the mechanical point of view, when the applied loading leads to structural stress concentrations that exceed the ultimate material strength of the wall, cracks initiate and propagate, leading to rupture. Therefore, it is critically important to understand the structural features that manifest within diseased arteries, as well as the mechanisms by which they weaken the arterial wall structure.

This project is aimed to identify the key pathophysiological changes that occur within the arterial wall microstructure and their corresponding influences on the mechanical behaviour and structural integrity. Unnotched and notched tensile tests, immunohistochemical analysis, constitutive modelling, multiphoton microscopy, as well as microstructural component based finite element modelling were used to study the relationship between microstructure and mechanical, as well as fracture behaviours of the arterial tissue.

The following literature review provides a thorough understanding of the key microstructural components and their healthy organisation within the artery wall. The main contributors of mechanical properties and the various forms in which they are found within the wall structure are explained to provide a complete explanation of the physiological microstructure and mechanics relationship of arteries. Descriptions of the systems that are used to classify AAs and ADs are provided next, which is followed by explanations of the pathophysiological changes that occur with developments of AAs and ADs. The pathophysiology, progression and classification of atherosclerotic plaques are also explained. Literature reviews of the architecture and load driven reorganisations of the arterial fibrous network, as well as mechanical modelling of arterial tissues are also provided. The introduction is then finalised with project aims and an outline of the following dissertation chapters.

1.2 Physiological microstructure and mechanics relationship of arteries

Arteries are tubular channels that carry blood from the heart to the tissues and organs. The structure of a particular artery and, therefore, its biomechanical behaviour is highly dependent on its location within the arterial system. The arterial system consists of two main types of arteries, which are referred to as the pulmonary and the systemic arteries[9–12]. The pulmonary arteries are low pressure vessels that carry deoxygenated blood from the heart to the lungs for oxygenation, while the systemic arteries are high pressure arteries that carry oxygenated blood from the heart to the rest of the body[9–12]. Arterial diseases, such as AAs, ADs and atherosclerosis, cause malfunctioning of the systemic arteries much more frequently than the pulmonary arteries. Therefore, most of the research effort has been concentrated on understanding the microstructure and mechanics relationship of high-pressure systemic arteries. Examples of systemic arteries include aorta, coronary arteries that feed the heart muscles, carotid arteries in the neck and the cerebral arteries that supply oxygenated blood to the brain[13–16].

1.2.1 Organisation of microstructural components in the arterial wall

All systemic arteries consist of three concentric layers, which are the intima, media and the adventitia, as illustrated in Figure 1.1. The intima is the innermost arterial layer and consists of a single layer of endothelial cells that lie on an underlying ~80 nm thick basal lamina, which is an extracellular matrix (ECM) membrane that consists mainly of highly cross-linked collagen, laminin, perlecan and entactin proteins[11].

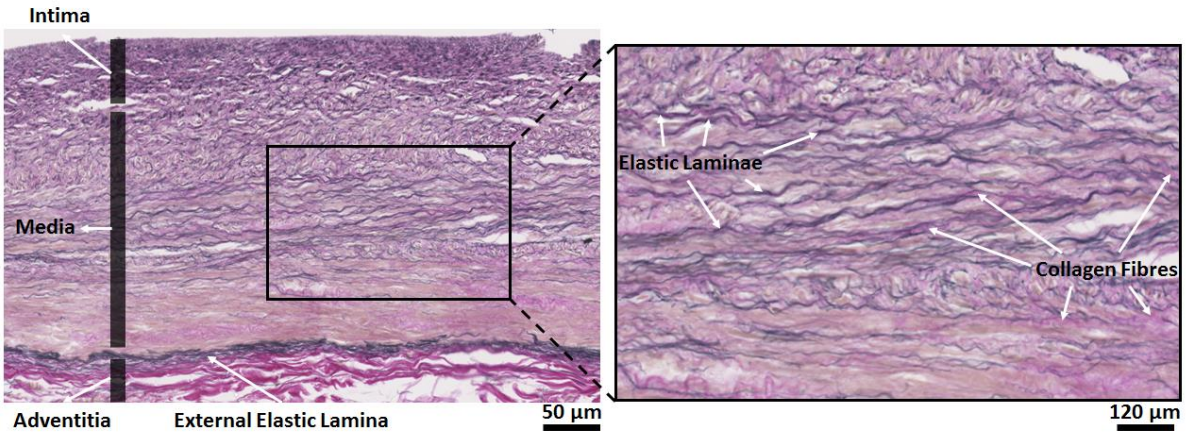

Figure 1.1. Cross-sectional view of a human arterial wall that is perpendicular to its longitudinal direction.

The intima is separated from the middle arterial layer media by the internal elastic lamina (IEL), which is a fenestrated sheet that is made up of tightly interwoven elastin fibres[9–11]. The arterial media is a fibrous network that consists primarily of collagen, elastin and GAGs. The medial fibrous network is embedded with spindle-shaped smooth muscle cells (SMCs), which are positioned in the form of two intermingling helices that surround the arterial lumen[9–12]. The basic microstructural unit of systemic artery medias differ depending on the location and function of the artery. As the systemic arteries recede away from the heart, the amount of blood and pressure that they have to accommodate continuously change. The systemic arteries are divided into three categories depending on their location and function, which are the elastic arteries, muscular arteries and the arterioles[9,10].

Elastic arteries are those that accommodate the blood coming directly from the heart, where the main example of an elastic artery is the aorta. Following its ejection from the heart, the surged blood is initially contained within the elastic arteries. The stretched arteries then recoil and push the blood into the muscular arteries. The coronary, carotid and cerebral arteries all fall under the muscular arteries category. The amount of blood that is delivered to each tissue and organ is controlled by the contractions and relaxations of the muscular artery walls, depending on the demand. The arterioles are relatively small blood vessels whose luminal diameter is ≤300 µm. They deliver the blood from the muscular arteries to the capillaries[9–11]. The elastic and muscular arteries are the main systemic arteries that develop AAs, ADs and atherosclerosis[13–16].

One of the main constituents of the elastic artery medial fibrous network are ~3 µm thick fenestrated sheets of densely interwoven elastin fibres, whose structures are similar to that of IEL. These fenestrated sheets of elastin are referred to as the elastic laminae. The number of elastic lamina and SMC layers within the elastic artery media increase with an increase in the luminal diameter[11,17–19]. Fenestrations of elastic laminae allow radial passage of the connective tissue across the arterial wall to make connections that tie the adjacent concentric entities of the wall together. The media is separated from the outermost adventitial layer of an elastic artery by the external elastic lamina (EEL), which also consists of tightly interwoven elastin fibres, but is thicker compared to the other medial elastic laminae[9–11]. The scanning electron microscopy image of an aortic wall section in Figure 1.2 shows the architecture of elastin features within its media. It is evident that, in addition to the elastic laminae, elastin fibres are organised into two other distinct forms, which are the interlaminar elastin fibres and elastic struts[18].

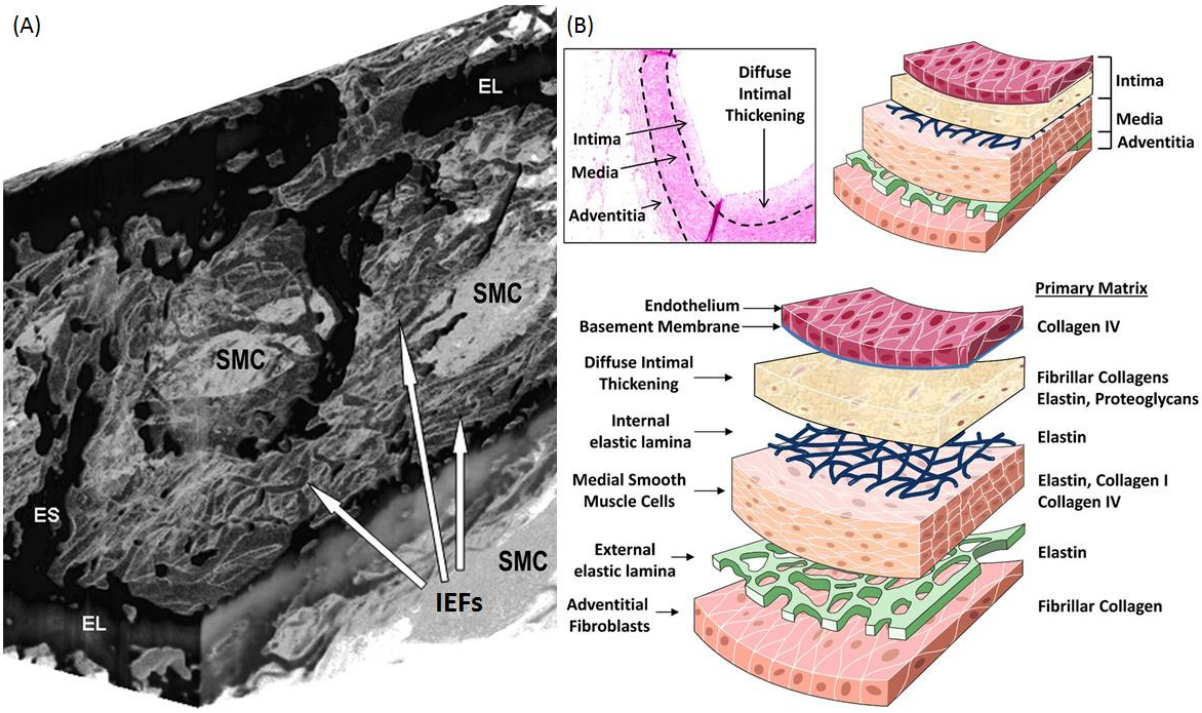

Figure 1.2. A: Scanning electron microscopy image of an aortic wall section, where EL, IEFs and ES stand for elastic lamina, interlaminar elastin fibres and elastic strut, respectively. B: Changes in the primary vascular matrix components in the different arterial layers. Dashed lines on the histology image represent the internal and external elastic lamina. (Adapted with permissions from[18,20]).

The interlaminar elastin fibres are groups of distinct numbers of elastin fibres that bundle together and protrude from the top and bottom concentric elastic laminae surfaces, randomly towards both the circumferential and the radial directions. The interlaminar elastin fibres terminate between the two elastic laminae, within which they start to protrude, where they assist formation of a fibrous frame[9–11,18]. On the other hand, the elastic struts establish direct radial links between adjacent elastic laminae[18].

Another key constituent of the elastic artery media and one of the main structural proteins that dictate the mechanical behaviour of an artery is the collagen. The medial collagen exists in the form of individual fibres, as well as thick and thin fibre bundles interspersed between the elastic laminae of an elastic artery. The individual and bundled collagen fibres are grouped into separate parallel layers, which are arranged concentrically across the thickness of the elastic artery media, adjacent to the elastic laminae surfaces. The preferred collagen fibre orientation of each layer differs from the collagen fibre orientation of the adjacent parallel layers[11,12,17,18,21–23].

The media of muscular arteries consist of a thick circular fibrous network of collagen and elastin, which is embedded densely with SMCs[9–11]. The medial fibrous network of a muscular artery is less dense compared to that of an elastic artery with fewer number of concentric elastic laminae and predominantly parallel arranged layers of cross-linked collagen fibres. The IEL and EEL are also present at the intima-media and the media-adventitia borders of muscular arteries, respectively[11].

The adventitia layer of both the elastic and the muscular arteries consists primarily of a dense collagen fibre network that is mixed with elastin fibres and embedded with fibroblasts. The collagen fibres of the adventitia are primarily orientated in the longitudinal direction of the artery, which assist the medial collagen fibres in preventing overstretching of the arterial wall to prevent structural failure during its extensions[9–11,21]. The adventitia accounts for ~10% and ~50% of the arterial wall thickness of elastic and muscular arteries, respectively. The thinner elastic artery adventitia surrounds the medial layer of the elastic arterial wall with a relatively thin layer of primarily collagenous matrix, allowing the elastic arteries to expand sufficiently to accommodate large volumes of surging blood. On the other hand, the relatively thick adventitias of muscular arteries reinforce their arterial walls, allowing them to maintain a relatively stable rate of blood flowing into the downstream tissues and organs[9–12].

1.2.2 Microstructure and mechanics relationship of arteries

In the media, the preferred collagen fibre orientation of the parallel collagen layers is always closer to the circumferential direction than the longitudinal direction of the artery, so as to assist the arterial wall in supporting the physiological loads[11,12,17,18]. Collagen fibres are considered to be the main load bearing microstructural component of arteries. The collagen fibres are also the smallest microstructural component, whose mechanical properties can be quantified directly with sufficient accuracy. A collection of collagen molecules organise into a staggered array and covalently cross-link to form a collagen fibril, where several collagen fibrils bundle together and cross-link to form a collagen fibre[12,23–27].

The terms *collagen fibril* and *collagen fibre* are commonly utilised interchangeably in literature, therefore, it is of critical importance to clarify that, collagen *fibrils* are filamentous assemblies, whose diameter range from ~20 nm to ~40 nm, where the collagen *fibres* are microstructural components, whose diameter range from ~0.2 μm to ~12 μm. The collagen fibres are formed by lateral packing and cross-linking of several collagen fibrils[12,24–27]. The identified collagen fibril and collagen fibre diameter ranges were utilised to differentiate between the two collagenous structures in the literature, so as to retrieve the correct information on the mechanical behaviour of collagen fibres.

The arterial wall is a composite material that behaves in a nonlinear manner upon loading. For large extensions, the integrity of the arterial wall is preserved by transmission of the tension within the wall through the network of cross-linked collagen fibres[11,12,21–23]. The typical nonlinear mechanical response of a tensile tested arterial tissue strip is illustrated in Figure 1.3. For relatively small values of stress, the arterial tissue maintains a linear mechanical response, after which the increasing value of stress is accompanied with a corresponding increase in the arterial stiffness, until the value of stress reaches the end of the elbow region of the curve in Figure 1.3.

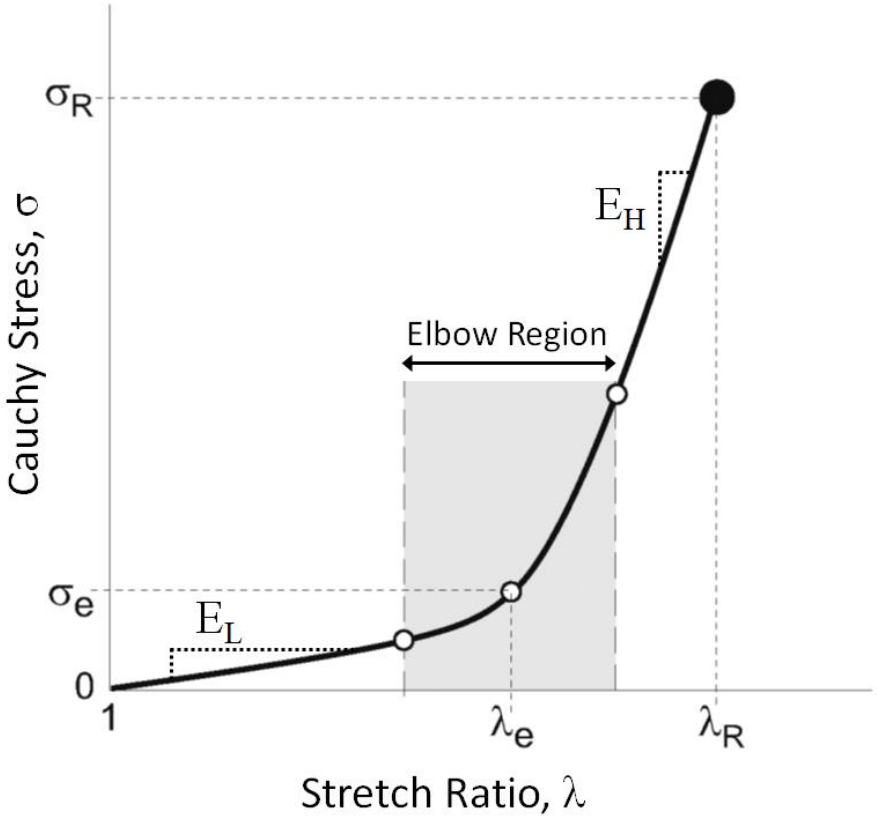

Figure 1.3. Typical nonlinear mechanical response of a tensile tested arterial tissue strip (Adapted with permission from[28]).

The elbow region of the curve is followed by the second and stiffer response of the arterial tissue until failure[11,12,21,22]. Analysis of the stress versus stretch ratio curve of an arterial tissue strip is commonly based on six parameters, which are the rupture stress, σ_R and stretch, λ_R, middle elbow region stress, σ_e and stretch, λ_e, low linear stiffness, E_L and the high linear stiffness, E_H, as illustrated in Figure 1.3[11,12,21,22,28].

In the initial low linear stiffness region, the load that is applied to the arterial tissue is carried by the network of elastin fibres. This is confirmed by the fact that, upon selective enzymatic digestion of collagen, the arterial tissue does not enter the high stiffness region, exhibiting a mechanical behaviour that is similar to that of the elastin fibres. Experiments using selective enzymatic digestion have also identified that, upon removal of elastin, the mechanical behaviour becomes relatively similar to that of the individual collagen fibres. Typical stress versus stretch ratio curve changes that are obtained by tensile testing after enzymatic removals of collagen and elastin are illustrated in Figure 1.4[23,29,30].

The elbow region of the control curve corresponds to the load transfer from the network of elastin fibres to that of the collagen. Therefore, both the elastin and the collagen fibres are loaded within the elbow region, where further increase in the stress enhances load transfer from elastin to collagen, resulting in continuous recruitment of collagen fibres within the fibrous network[11,12,21–23,29,30]. In the body, the mechanical stress within the arterial wall is never equal to zero. In its unloaded state, the arterial wall is always under continuous tension, which is referred to as being under residual stress[11,12,21–23].

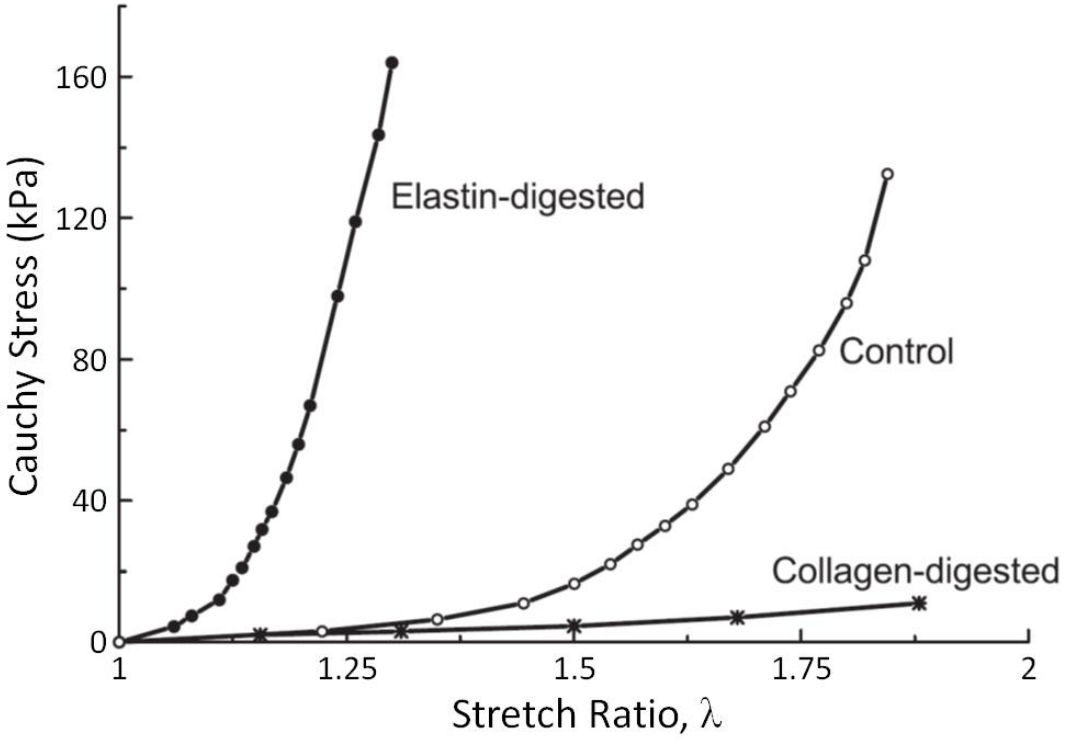

Figure 1.4. Typical stress versus stretch ratio curve changes that are obtained by tensile testing after enzymatic removals of collagen and elastin (Adapted with permission from[31]).

Although the overall stress versus stretch ratio curve shapes of the intima, media and adventitia layers are similar, their rupture stress and stretch, beginning and end points of the elbow region, as well as the low and high linear stiffness values are relatively different, as illustrated in Figure 1.5. Nevertheless, the cross-linked collagen fibre network is the common major load bearing component of intimal, medial and adventitial arterial tissue microstructures, when each tissue is loaded within and beyond the elbow region of its stress versus stretch ratio curve[11,12,21,22,28].

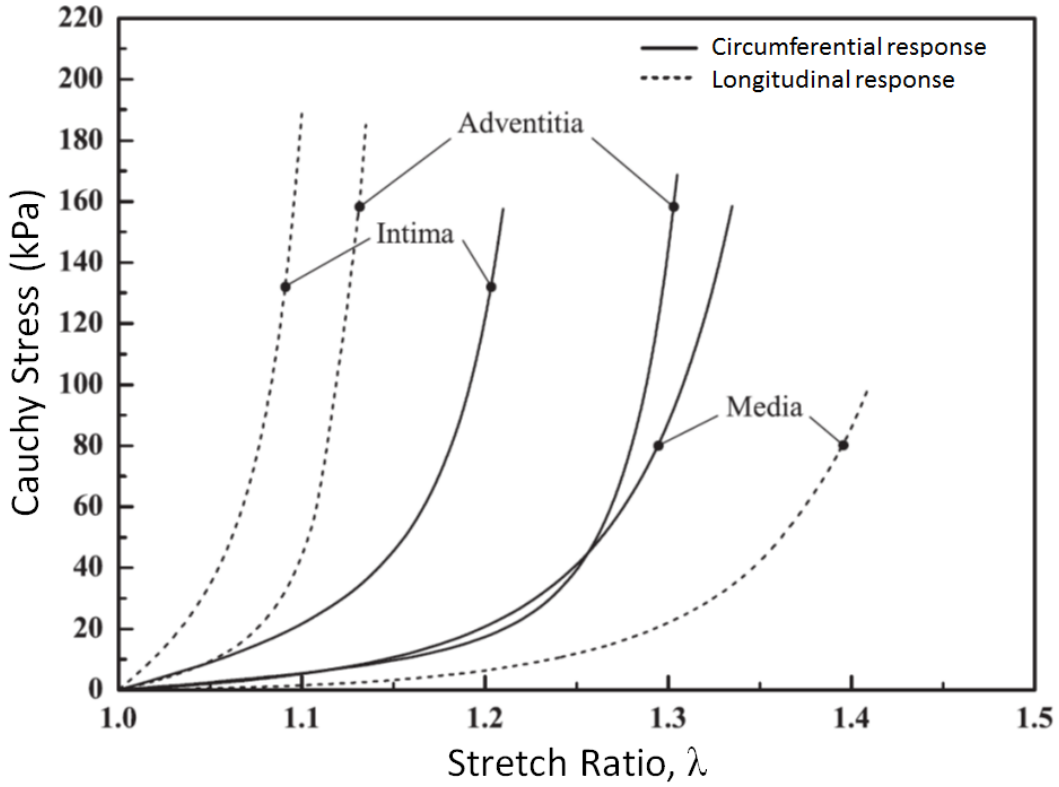

Figure 1.5. Typical stress versus stretch ratio curves of the intima, media and adventitia layers (Adapted with permission from[32]).

Consequently, the changes in mechanical behaviour of the arterial wall are mainly a result of variations in the density of collagen and its integrity within the fibrous network. The distribution of collagen fibre orientations in the arterial layers is also a critical determinant of mechanical behaviour. The density and integrity of the collagen fibres often undergo significant structurally detrimental changes, which are accompanied by local randomisation of their orientations, during developments of clinical conditions, such as AAs, ADs and atherosclerosis[11,12,17,18,21,22].

1.3 Classifications of aortic aneurysms and aortic dissections

This section describes the classification systems that are used to categorise AAs and ADs based on their location in the aorta, shape, extent, pathophysiological state and severity in the clinical setting.

1.3.1 Classification of aortic aneurysms

AAs are classified under 4 categories, which are the location of the aneurysm on the aorta, shape and size of the developed aneurysm, as well as involvement of the aortic wall layers in the aneurysmal dilatation of the aorta[3,14,33]. The aorta is divided into 6 segments that are illustrated in Figure 1.6. It initiates with the aortic root, which connects the aorta to the heart and ends with the abdominal aorta[3,10,14,33].

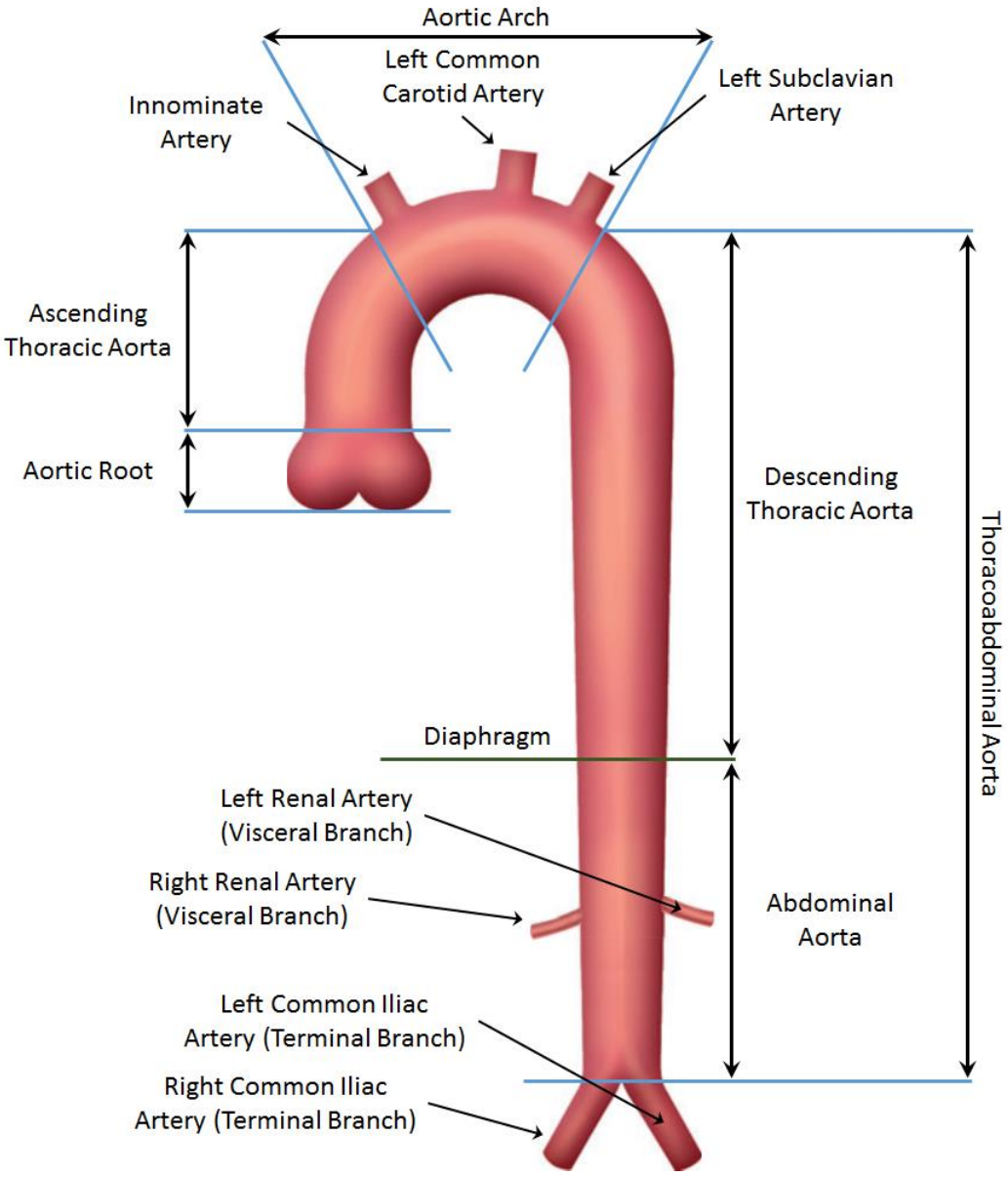

Figure 1.6. Segments and main branches of the aorta (Adapted with permission from[14]).

In location-based classification of AAs, each aneurysm is assigned to a distinct category depending on the aortic segment at which the aneurysm has developed. For instance, an AA that has developed at the ascending thoracic aorta is referred to as an ascending thoracic aneurysm (ATA)[3,14,33].

In shape-based classification, AAs are divided into two categories, which are fusiform and saccular. In the case of a fusiform AA, the whole circumference of the affected aortic segment expands outwards, resulting in the formation of a cylindrical dilatation, as illustrated in Figure 1.7. On the other hand, saccular AAs develop only on part of the affected aortic segment circumference, in the shape of an oval or spherical cyst[3,13,14,33].

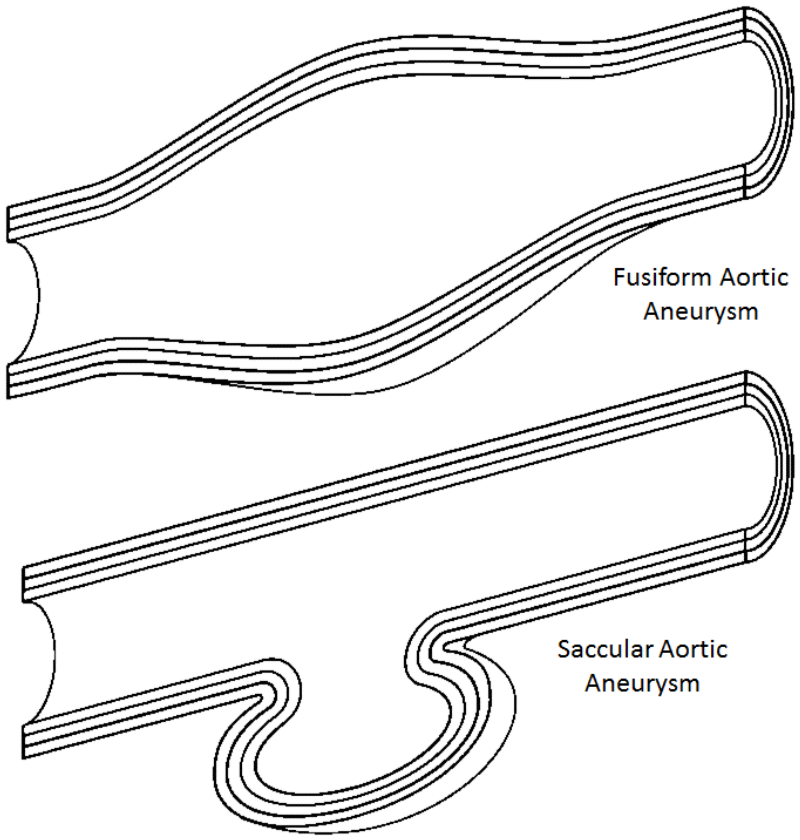

Figure 1.7. Schematics of fusiform and saccular AAs (Adapted with permission from[13]).

The AA classification that is dependent on the involvement of aortic wall layers in the aneurysmal dilatation of the aorta, divides the AAs into two categories, which are referred to as true and false AAs. True AAs are formed by simultaneous dilatations of all aortic wall layers into a circumferential fusiform or a sac, as illustrated in Figure 1.8. On the other hand, a false AA develops by disruptions of either all or the intimal and medial aortic wall layers, as a result of a trauma or an infection[13,14,33].

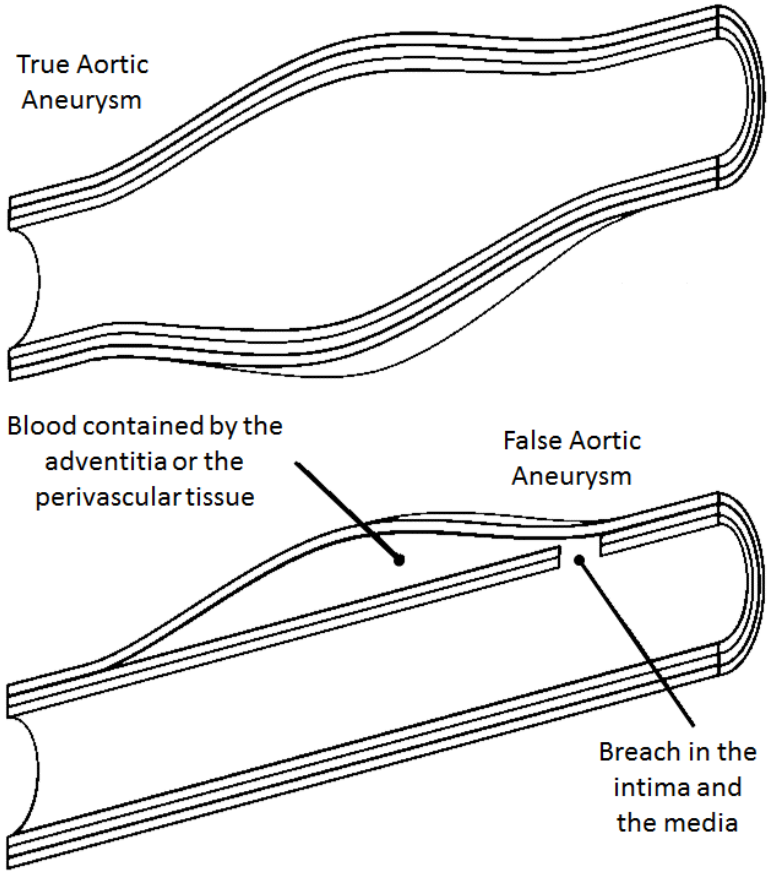

Figure 1.8. Schematics of true and false AAs (Adapted with permission from[13]).

Size dependent classification of AAs categorises the rupture risk, and therefore, the likelihood of fatal clinical event occurrence[13,14,33–35]. A very sharp increase in the probability of AA rupture to ~31% was identified for ATAs, whose aortic segment diameter exceeded 6 cm, where a similar increase to ~43% probability of rupture was identified for descending thoracic aneurysms, whose aortic segment diameter exceeded 7 cm. These probabilities were found to be significantly higher than the death risk of <10%, which is associated with the complications that can arise during surgical repair of AAs. Consequently, a surgical repair referral threshold of 5.5 cm aneurysmal diameter was set for patients with dilated aortic segments[13,14,33–35].

1.3.2 Classification of aortic dissections

ADs are mainly classified with two different classification systems. The first type of classification is based on the location of initiation, as well as the direction and extent of progression of an AD. The second type of classification is based on the pathological event that triggers development of an AD and the pathophysiological changes that are undergone by the aortic wall during its development[2,3,14,34,36,37]. The most comprehensive location of initiation, as well as direction and extent of progression-based classification system is the DeBakey classification, which divides ADs into three main types. The first, DeBakey Type I ADs are those that initiate with an intimal tear at the ascending thoracic aorta, develop into a dissection and propagate through the aortic arch into the descending thoracic aorta. The DeBakey Type II ADs also initiate with an intimal tear at the ascending thoracic aorta but remain confined and develop at the same location. The third, DeBakey Type III ADs initiate with an intimal teat at the region between the left subclavian artery inlet on the aortic arch and the beginning of the descending thoracic aorta. After the intimal tear, the first class of DeBakey Type III ADs, which is called Type IIIa, propagate from the location of the intimal tear into the descending thoracic aorta and stop propagating before they reach the diaphragm, whereas, Type IIIb continue through the diaphragm into the abdominal aorta[2,3,14,37].

ADs are also divided into 5 distinct classes, which are called Class 1, 2, 3, 4, and 5, based on the triggering pathological event and the pathophysiological changes that are undergone by the aortic wall during their development. The 5 pathophysiologically distinct classes of ADs are illustrated in Figure 1.9[3,14,34,37]. In Class 1 ADs, the aortic wall layers separate and result in formation of a false lumen within the wall, therefore separating the original aortic lumen into true and false sections. The true and false Class 1 AD lumens can form both with and without luminal communication, while the fresh blood flow from the heart into both lumens is always maintained. In Class 2 ADs, an intramural haematoma is formed as a result of bleeding into the aortic wall without an observable flap tear or other form of disruption within the aortic intima. The Class 3 ADs initiate with intimal tears and develop in the form of subtle and discrete outpouches on the aortic wall, while the Class 4 ADs develop from ulcerations of aortic atherosclerotic plaques, following their rupture. Unlike the other four classes, the Class 5 ADs are induced by trauma to the intimal layer, which is commonly caused by careless aortic catheterisation[3,14,37].

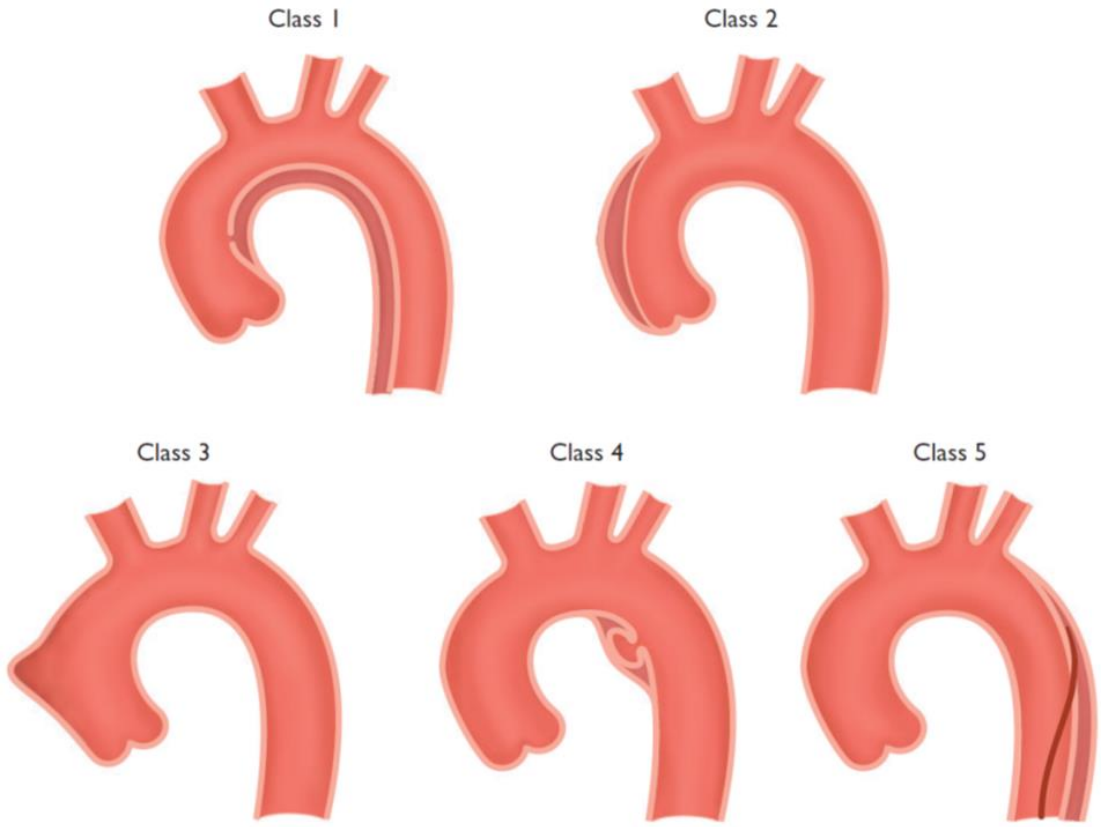

Figure 1.9. Schematics of the pathophysiologically distinct classes of ADs (Reprinted with permission from[14]).

1.4 Pathophysiologies of aortic aneurysms and aortic dissections

The main difference between the pathophysiologies of AAs and ADs is the initiation by spontaneous tearing of the intimal layer in ADs, which does not occur in the beginning of an AA[3,38]. The intimal tears that initiate ADs occur within the regions that experience greater levels of surface shear and structural stresses, as a result of undergoing larger fluctuations in blood pressure compared to the rest of the aorta[3,37]. While hypertension and generalised atherosclerosis are the main risk factors that are shared by AAs and ADs, the exact pathophysiological mechanisms that lead to development of AAs and ADs have not yet been established[1–3,37,38]. Aortic dilatation has been identified to be the key morphological manifestation that is shared by AAs and ADs. Consequently, significant research effort has been invested in understanding the changes undergone by the aortic tissue, as it dilates during developments of AAs and ADs[3,39–67].

1.4.1 Changes in microstructural components with disease

This section summarises the key findings in literature on the disease-driven changes in concentration, integrity and organisation of main aortic tissue microstructural components. The dilatation of the aortic wall during developments of AAs and ADs is generally accompanied by local imbalances in the homeostatic turnover, as well as local changes in organisation of collagen and elastin fibres within the aortic tissue, which causes the aorta to undergo local changes in mechanical properties[3,39,45–59,61,62]. GAGs are also key ECM constituents as they act as a water-based filler between the other ECM constituents, enabling the tissue to resists compressive forces[17,61,62].

1.4.1.1 Changes in collagen

Panek et al. performed a biochemical study to understand the changes in collagen turnover upon development of AAs[58]. In their study, AA tissues were collected from random aortic locations of 10 male patients who underwent open aortic repair surgeries. A control set of healthy aortic tissues were also collected from a separate set of 10 males. The diseased and healthy aortic tissues were biochemically assessed to determine the dry weight of collagen in their structures. The collagen content in each aortic tissue sample was also separated into two groups as intact tissue collagen and collagen degradation products. Results of their biochemical analysis showed that, while the total dry weight of collagen was similar in diseased and healthy aortic tissue samples, the percentage of total dry weight that corresponds to collagen degradation products was approximately three times larger in AAs (44.9% > 16.6%). Their data indicated that, although the total collagen content may remain unchanged in the aortic tissue upon development of an aneurysm, a big part of the remaining collagen is degraded and broken away from the intact fibrous network, therefore, degrading the mechanical properties of aortic tissue[58].

In another study, imbalances in collagen turnover with AD development was investigated by Whittle et al. on thoracic ADs[59]. AD tissue samples were obtained from a total of 12 locations from the thoracic aortas of 10 patients, where healthy control samples were obtained from a separate set of 10 patients. Two types of samples were obtained from each one of the 12 thoracic AD locations, where one sample was from the actually diseased tissue region and the other one from a nearby region that was not part of the dissection tissue.

All samples were biochemically assessed to determine the dry weights of collagen and other ECM proteins, as well as the concentration of collagen in each tissue. Comparison of the biochemical analysis outcomes of samples from actually diseased tissue regions and samples from healthy patient aortas showed that the dry weights of collagen and other ECM proteins were significantly increased ($p < 0.001$ for all), while concentration of collagen was significantly decreased ($p = 0.016$) in the diseased tissue samples. On the other hand, an insignificant difference was obtained between the biochemical parameters of samples that were obtained from nearby an AD and the samples from healthy patients. These results lead to the conclusion that thoracic ADs cause the aortic ECM to undergo increased local depositions of collagen and other proteins at the diseased regions, which results in reduction of the local concentration of structurally viable collagen[59].

The study by Borges et al. investigated the disease-driven changes in percentage area occupied by collagen fibres, across the thickness of thoracic aortic tissue media[53]. AA and AD tissues from thoracic aortas, as well as thoracic aorta samples from healthy aortas were immunohistochemically stained with Sirius Red to identify collagen fibres. Media of each tissue was divided into two halves at its centre into internal and external portions, which were near the intima and near the adventitia, respectively. Percentage area occupied by collagen was determined separately for each media portion. External portions of AD tissues were found to have significantly lower ($p < 0.01$) collagen percentages compared to their internal portions, where the same trend was also observed in healthy aortic medias with less significance ($p < 0.05$). The internal and external portions of AA medias were found to have similar amounts of collagen. Compared to the healthy aortic tissues, the collagen content was lower in both internal and external portions of AA and AD tissue medias. These outcomes indicated that thoracic aortic tissue experienced a decrease in collagen content with developments of both AAs and ADs, where this decrease is localised to the external portion of the media in ADs and distributed across the whole thickness of AA tissue medias[53].

In the case of abdominal AAs, Rizzo et al. found that the total tissue protein dry weight percentage of collagen was significantly increased ($p < 0.05$) from 24% to 37%[47]. On the other hand, Carmo et al. have used high-performance liquid chromatography to study both the content and the degree of cross-linking of collagen fibres in abdominal AAs.

Despite finding a significant increase ($p < 0.01$) in the cross-linking protein content, Carmo et al. have observed a significant decrease ($p < 0.01$) in the collagen content of abdominal aortic tissues with disease[45]. Their findings indicate that, although the collagen synthesis mechanisms in the abdominal aortic tissues are hampered with disease, it is able to develop compensating mechanisms that can strengthen the existing collagen fibre network by generation of more cross-links, in an attempt to maintain the physiological mechanical properties of the tissue. In contrast, the study by Wilson et al. have identified an increase in collagen fibre turnover with abdominal AA development and related this to the reduced distensibility of aneurysmal abdominal aortic tisssue[49]. Another study by Sobolewski et al. have reported similar amounts of collagen in abdominal AAs and healthy abdominal aortas[66].

It is evident in the available literature that collagen fibres in thoracic and abdominal aortas can undergo distinct changes depending on their aortic location with development of AAs and ADs[45,47,49,53,59,66]. In the case of thoracic AAs and ADs, the published studies indicate that the aortic tissue undergoes local reductions in the concentration of structurally viable collagen fibres, where the decrease in concentration is localised towards the adventitia in thoracic ADs and distributed across the whole thickness of the tissue in thoracic AAs[53,59]. On the other hand, studies on disease driven changes in abdominal aortic collagen concentration and integrity often yielded contradictory outcomes[45,47,49,66]. Some studies indicated an increase in collagen content[47,49], where one study showed a decrease in collagen content with disease[45], while another study found similar amounts of collagen in healthy and diseased abdominal aortic tissues[66]. Despite the differences in collagen content change between distinct aortic locations and regardless of the different results that are obtained for the same aortic location by different studies, collagen fibres in the diseased aortic tissue undergo structural changes and loose the physiological architecture of their fibrous network, therefore, hampering the native mechanical properties of aortic tissue[39,45,47,49,53,58,59,62,66].

1.4.1.2 Changes in elastin

Busuttil et al. have performed a study with aneurysmal tissue samples from random aortic locations of 14 patients on the activity of elastase enzyme, which is responsible for breakdown of elastin fibres in the aortic tissue. They identified correlations between the aneurysm size and elastase enzyme activity, which were localised to the intima and media layers of the aorta[56]. On the other hand, Cattell et al. have performed a study on the content and structural integrity of elastin in thoracic ADs[57].

The elastin concentration and degree of elastin fibre cross-linking in thoracic ADs of 10 patients were compared with those of healthy thoracic aortas from a separate set of 10 patients. Tissue samples were also obtained from a region that was remote from the dissection on each diseased aorta. It was found that, compared to samples from healthy patient aortas, concentration of elastin in dissected thoracic aorta tissues was significantly decreased ($p < 0.01$), where the decrease in elastin concentration was less significant ($p < 0.05$) in the regions that were remote to the dissected tissue on the diseased aortas. Moreover, Cattell et al. did not observe any change in elastin cross-linking with disease[57]. The studies by Busuttil et al. and Cattell et al. indicate that, integrity of elastin fibre network is disrupted in both AAs at random aortic locations and in thoracic ADs, where these disruptions are often localised to regions of tissue that are most affected by disease[56,57].

In another study, Paik et al. have investigated the disease-driven increase in the concentration of nitrite ion in abdominal AA tissue[54]. It is known that elevated levels of nitrite ion are destructive to elastin fibres in the aortic tissue[54,55]. After measuring the nitrite ion concentration in human abdominal AAs and in control samples from the abdominal aortas of healthy patients, Paik et al. found a sevenfold increase ($p < 0.01$) in nitrite ion concentration of abdominal AAs, indicating severe disruptions to the elastin fibre network of the diseased tissue[54]. Another study by Nakashima et al. have looked into the structural disruptions of elastin fibres in ADs with histopathological analysis on 111 autopsied cases, which involved ADs from multiple aortic locations. They found that dissected aortic tissue microstructures were characterised with a decrease in elastin concentration and a corresponding decrease in interlaminar elastin fibre content[46].

In their study on abdominal AAs, Rizzo et al. have found a significant decrease ($p < 0.001$) in elastin content from 12% of total tissue protein dry weight to 1% with disease. They have also observed the structure and organisation of elastin in arterial tissue microstructure with immunohistochemical Elastin Van Gieson staining and found that the elastin fibre network was highly fragmented and disrupted with disease.[47]. In a separate study, compared to healthy abdominal aortic tissues, Carmo et al. have found significant decreases in both the concentration and the degree of cross-linking of elastin fibres in abdominal AAs[45]. Sobolewski et al. and Gandhi et al. have also found similar results that showed a decrease in abdominal aortic tissue elastin content upon development of an aneurysm[48,66].

On the other hand, Minion et al. have found that, although the amount of aortic tissue elastin can increase with abdominal AA development, since the diseased tissue is also incorporated with increasing amounts of other structural proteins, the concentration of elastin is always decreased[51]. In another immunohistochemical study with the Elastin van Gieson stain, Campa et al. have found that, compared to the healthy abdominal aorta, elastin fibres were less densely positioned and more randomly oriented in abdominal AA tissue. The same study also showed that, compared to the healthy tissues, the total tissue protein dry weight percentage of elastin was significantly decreased ($p < 0.05$) from 35% to 8.1% with disease[52]. A histochemical study by Wilson et al. have also found elevated levels of elastin fibre breakdown in abdominal AAs[49].

To sum up, the concentration of elastin was found to decrease at all aortic locations upon development of both AAs and ADs[45–49,51,52,54–57,66]. Elastin fibres in the diseased aortic tissue microstructure were also fragmented and their network was disrupted with disease[46,47,52,56,57]. Since the intimal and medial aortic tissue layers often undergo greater levels of disease-driven pathophysiological changes compared to the adventitia, a localisation of elastin fibre disruptions in the intima and media layers were also observed[56,57]. Concentration of the interlaminar elastin fibres within the media were also decreased in ADs[46]. Along with these microstructural deteriorations that are experienced by elastin, the significant decrease in elastin fibre cross-linking with disease further indicates that the integrity of the elastin fibre network is largely lost[45]. The resulting diseased elastin fibre network cannot provide the necessary physiological contribution to the aortic tissue mechanical behaviour[39,62].

1.4.1.3 Changes in glycosaminoglycans

Gutierrez et al. have compared the GAG content of thoracic AD tissue samples from 10 patients with that of healthy aorta samples from 9 patients without any aortic disease[64]. They determined the dry weight amounts of three GAG types, which were chondroitin sulphate, heparan sulphate and dermatan sulphate in all aortic tissue samples. Although an insignificant difference was found between the chondroitin sulphate contents of dissected and healthy aortic tissues, the heparan sulphate and dermatan sulphate contents of thoracic AD tissues were significantly lower ($p < 0.05$ for heparan sulphate and $p < 0.001$ for dermatan sulphate). Consequently, the total GAG content of thoracic AD tissues was also found to be significantly lowered ($p < 0.001$) with disease[64].

In another study, Cattell et al. have found a highly significant ($p < 0.0001$) disease driven increase in the GAG content of thoracic ADs, where the increase in hyaluronan content was relatively larger compared to those of other GAG types.[67]. Despite the observed increase in GAG content, Cattell et al. showed that the amount of other ECM constituents, such as collagen and elastin were also increased at the dissected aortic locations, which caused concentrations of GAGs to remain largely unchanged, except for chondroitin sulphate. Concentration of chondroitin sulphate was found to decrease significantly ($p < 0.05$) with disease. They also found that increases in the contents of hyaluronan and dermatan sulphate GAG types were localised only at the dissected regions of diseased thoracic aortas. The collagen and elastin content increases were found to be localised at the same dissected aorta regions as hyaluronan and dermatan sulphate[67].

The first conclusion that can be deduced from the findings by Cattell et al. is that, although the GAG content of dissected thoracic aortas may increase with disease, the simultaneous increases in other ECM constituents often causes the resulting GAG concentration to be similar to that of the healthy aortic tissue. On the other hand, a decrease in concentration of only one GAG type and differences in relative increases of others indicate that the physiological balance between the turnover rates of different GAG types is lost with development of thoracic ADs. The second conclusion is that selective localisation of hyaluronan and dermatan sulphate GAG types, along with collagen and elastin at the same dissected thoracic aorta locations, indicates a functional relationship between these microstructural components.

In his review on changes in GAG content of diseased thoracic aortas, Humphrey has concluded that a unique histopathological characteristic of thoracic AAs and ADs is the large amounts of GAG accumulation in their aortic tissue microstructures, where the increase in GAG content is localised particularly to the medial aortic layer[40]. In a separate study, Humphrey et al. have studied the biomechanical consequences of disease-driven GAG pooling in the thoracic aorta microstructure. They showed that the increased GAG pooling can lead to severe stress concentrations within aortic media and, therefore, generate sites that can act as initiators of ADs[41].

Achilleas et al. have performed a biochemical study on GAG content of abdominal AAs, which yielded a 60% decrease in total GAG content with disease[65]. The corresponding decreases in heparan sulphate, chondroitin sulphate, hyaluronan and dermatan sulphate GAG types were 90%, 65%, 73% and 8%, respectively, where the decreases in all GAG types were statistically significant ($p < 0.001$). It is evident from these outcomes that the decrease in abdominal aortic tissue GAG content is also accompanied by variations in metabolic turnover of distinct GAG types, upon development of an AA[65]. Studies by Sobolewski et al. and Gandhi et al. have also observed an overall decrease in GAG content with abdominal AA development[48,66], where Sobolewski et al. have also observed corresponding differences in the amount of change between distinct GAG types[66]. A genetic study by Tamarina et al. has also identified a significant decrease ($p < 0.001$) in expression of a gene that regulates GAG biosynthesis with abdominal AA development[60]. It is also highlighted in the review by Humphrey that, abdominal AAs often undergo a decrease in GAG content with disease and they do not tend to dissect[40].

Overall, the majority of the literature showed that the GAG content of thoracic AAs and ADs increase with disease, which leads to accumulation of GAG pools within the thoracic aortic tissue microstructure[40,67], where the pooling GAGs were found to generate stress concentrations within aortic media[41]. On the other hand, all of the literature on disease driven changes in abdominal aortic tissue GAGs demonstrated an overall decrease in GAG content with disease development[40,48,60,65,66]. Moreover, the corresponding disease-driven increase and decrease magnitudes were different for each thoracic and abdominal aortic tissue GAG type[64–67]. It can be concluded that GAGs in aortic tissue microstructure undergo both location and type dependent changes with disease, while the physiological state of tissue is always lost and its mechanical properties are hampered regardless of nature of the experienced changes[40].

1.4.2 Inflammatory biomarkers

At the cellular and molecular levels, developments of AAs and ADs are a consequence of inflammation, which leads to pathological aortic tissue remodelling and ECM degradation[68–75]. During the inflammatory process, macrophages infiltrate the aortic tissue microstructure and start releasing biochemicals that cause unbalanced syntheses and destructions of the primary ECM components elastin and collagen. This causes the aorta to undergo local changes in mechanical properties and become susceptible to dilatations and dissections[68,69,71–73,75].

Kuehl et al. and Reeps et al. have used positron emission tomography and computed tomography to show that patients with severe AA and AD disease symptoms or with other highly progressed aortic conditions displayed more inflammatory cell activity in their aortic tissues, compared to the patients that were classified as clinically stable[70,74].

Amongst all inflammatory biochemicals that are released by macrophages in the diseased aortic tissue, the matrix metalloproteinases (MMPs) have attracted most of the research effort on understanding the origin of homeostatic imbalances, which occur during developments of AAs and ADs[3,39,42–44,61–63]. MMPs are enzymes that are capable of fragmenting the collagen and elastin fibres within the aortic tissue. Local release of MMPs causes the ECM to undergo local destructions, which leads to generation of AA and AD prone sites on the aortic wall. There are currently a total of 26 MMPs that were found to function in human tissues, where MMP-1, MMP-8, MMP-13 and MMP-18 were found to fragment collagen, while MMP-2 and MMP-9 are responsible for the fragmentation of elastin[3,39,61–63]. Several studies have identified significant levels of increase in the collagen and elastin denaturing MMPs within AA and AD tissues compared to control tissues from healthy aortas[3,39,42–44,61–63].

To sum up, the significance of macrophages and their MMPs at the cellular and molecular levels of the inflammatory process have shifted considerable research effort towards their use as biomarkers. The ultimate goal of inflammatory biomarker studies is to use the amounts and activities of macrophages and MMPs in diseased aortic tissue to target the local impairments in homeostatic maintenances of collagen and elastin, as well as to monitor the progression of AAs and ADs[3,39,61–63,68,70,71,73–75].

1.5 Pathophysiology of atherosclerosis

The exact cause of atherosclerosis initiation is unknown. Nevertheless, many scientists believe that it is triggered by damage to the inner artery wall. Once damaged, tissues underlying the inner wall are exposed to blood constituents. Substances transported by blood such as cholesterol accumulate within the damaged area, planting the seeds of a multicellular process, which will eventually lead to atherosclerotic plaque formation[15,76,77].

The schematic in Figure 1.10 illustrates the morphological changes that occur within a diseased artery and the mechanism of its eventual rupture[77,78].

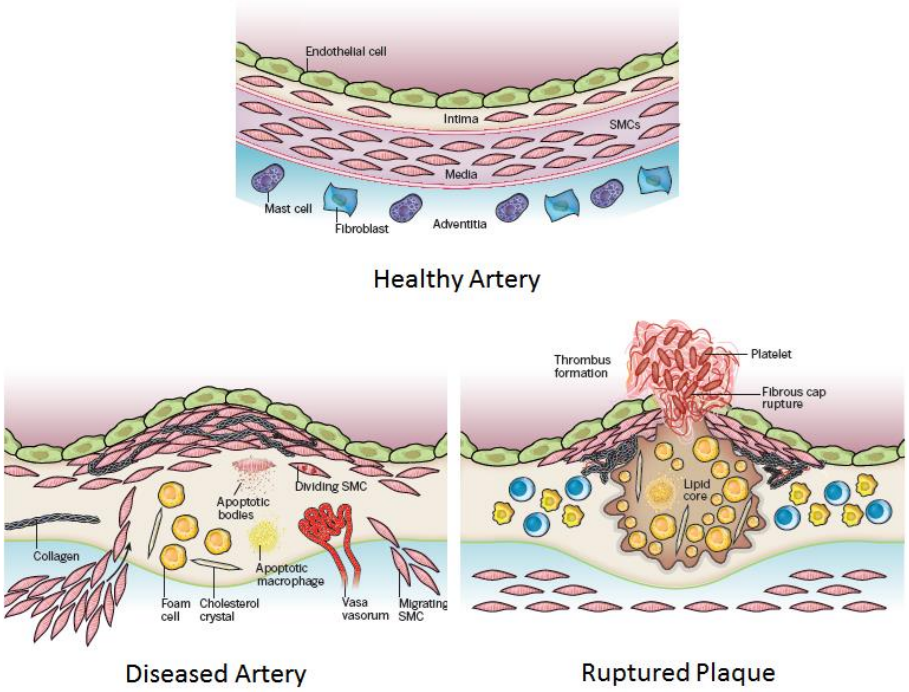

Figure 1.10. Schematic illustrating the morphological changes of an artery during atherosclerosis that leads to its rupture. Characteristic cells of each layer are also schematised (Adapted with permission from[78]).

As illustrated in Figure 1.10, atherosclerosis occurs within the intima[16,76,79]. Lipids in various forms are essential to maintain metabolic functions of many human tissues such as the cell membrane. Most of the lipid in the form of liver-produced cholesterol is transported to the target tissue by low-density lipoproteins (LDLs). Once the endothelial lining of intima is damaged, LDL macromolecules can enter the artery wall. The atherosclerotic process initiates with excessive accumulation of LDL in the wall. After entering the intima, the LDLs are oxidised, which makes them toxic. The inflammatory process begins once surrounding cells realise the toxic nature of oxidised LDLs[16,78,80]. Monocytes respond to the inflammation by migrating from the bloodstream into the artery wall followed by transformation into macrophages. Inside the artery wall, macrophages engulf and digest the cholesterol rich oxidised LDLs and transform into foam cells. Afterwards, the foam cells undergo apoptosis and release their contents, forming a lipid core. In response, the body initiates a secondary reaction which involves fibrous encapsulation of the growing lipid core[13,77,78,81,82].

Along with encapsulation, the formed entity is transformed into an actual atherosclerotic plaque. The fibrous cap forces expansion of plaque into the elastic artery wall, so that it is stretched circumferentially, as part of the body's attempt to preserve blood flow[13,77,78,81,82].

The bottom left diagram in Figure 1.10 illustrates a diseased artery undergoing plaque progression, during which SMCs migrate from media to the intima to assist fibrous cap generation. Once they arrive in the intima, both resident and media-migrated SMCs proliferate and start producing ECM molecules (collagen, elastin, GAGs, etc.)[78,81,83]. Advanced lesions occasionally contain cholesterol crystals, where the lesions with relatively large atheromas also undergo neovascularization, so that cells within the plaque are nourished sufficiently. Although the atherosclerotic process is initiated to maintain homeostasis by preserving flow of blood, at times, the morphology of advanced lesion does not develop into stable structures[13,81]. As schematised in the bottom right diagram of Figure 1.10, fibrous caps of such complicated plaques can rupture, enabling platelets to come in contact with biochemical factors inside the plaque, resulting in thrombus formation, which could obstruct the blood flow. Atherosclerotic plaques can progress through various routes and attain several distinct morphologies, where each characteristic lesion possesses a different level of vulnerability to rupture[77,78,81,83].

Another common morphological feature of atherosclerotic lesions is calcification. Atherosclerotic calcification is an organised process similar to bone formation, which occurs only when other aspects of atherosclerosis are also present. Proteins such as osteocalcin and osteopontin which are respectively involved in transport of calcium out of vessel walls and in mineralization of bone, have both been identified in calcified atherosclerotic lesions, and therefore, they are suspected to lead the pathogenesis of calcification in atherosclerotic plaques[84,85]. Moreover, calcified human atherosclerotic plaques have also been found to contain biochemical protein factors that drive osteoblast differentiation, which are cells that can synthesize bone. These cells are thought to be the ones from which the vascular calcifying cells are derived[77].

All of these findings indicate that calcification is an active process and not simply a passive precipitation of calcium phosphate crystals[84]. In a recent study, Roijers et al. have also demonstrated that precipitation of calcium rich material at the micrometre scale occurred before changes in the intimal content of calcification driving proteins, and that such small scale calcifications may be caused by local events, such as deposition of iron and zinc atoms[77,86].

Although atherosclerosis is a systemic chronic inflammatory disease, atherosclerotic plaques are distributed throughout the vascular tree in a non-uniform fashion. Studies have highlighted the importance of low wall shear stress in the development of endothelial cell dysfunction and atherosclerosis[87–91]. Wall shear stress is defined as the frictional force of blood exerted against the inner vessel wall. Low levels of wall shear stress increases permeability of the endothelial cell surface to LDLs, where areas of low wall shear stress also drive progressive atherosclerosis by stimulating the production of vasoconstrictors, reactive oxygen species and inflammatory mediators[87–89]. Clinical studies have indicated that vascular segments with alterations in wall shear stress can lead to atherosclerosis development in site-specific areas, resulting in non-uniform distribution of atherosclerotic plaques throughout the vascular tree[77,87–89].

Similar to the developments of AAs and ADs, the unbalanced syntheses and destructions of the primary ECM components collagen and elastin, also occur during the development of atherosclerotic plaques and drive the changes in local arterial tissue mechanical properties, elevating the risk of atherosclerotic plaque rupture. Consequently, significant effort has been invested in identification of the biomarkers that can be utilised to target the local impairments in homeostatic maintenances of collagen and elastin within atherosclerotic plaques as well[92–99]. Analogous to the findings on AA and AD developments, the MMPs were identified to play a key role in the origination of homeostatic imbalances during atherosclerosis, which lead to degradation of collagen and elastin within the formed atherosclerotic fibrous cap, therefore, rendering the developed atherosclerotic plaque vulnerable to rupture[77,92–95].

Moreover, quantification of GAG and fibrillin contents in healthy and atherosclerotic tissues has also attracted significant research focus[96–99]. The atherosclerotic fibrous caps were found to have lower GAG contents compared to the healthy arterial tissue, with their ulcerated fibrous cap centres possessing the minimum GAG density levels[96,97]. On the other hand, fibrillin-1 was found to localise within the plaque during atherosclerosis development, while impaired forms of fibrillin-1 was found to promote development of rupture prone atherosclerotic plaque structures[77,98,99].

1.6 Progression and classification of atherosclerotic plaques

Initial reports on progression of atherosclerosis suggested that plaque growth was always inwards, decreasing the artery's inner diameter and therefore, obstructing flow of blood. Elevation in complete blockage risk as a result of increased obstruction was thought to be the main driving factor behind fatal clinical events[100]. But with subsequent developments in techniques of non-invasive imaging and histological analysis, researchers identified that plaque progression was not limited to inward growth of the atherosclerotic plaque. By comparing diseased cross-sections with healthy cross-sections near the centre of the same vessels, Glagov et al. and McPherson et al. demonstrated that an atherosclerotic plaque can also remodel outwards[101,102]. Schematics and histological cross-sections in Figure 1.11 illustrate the difference between inward and outward remodelling[77,103,104].

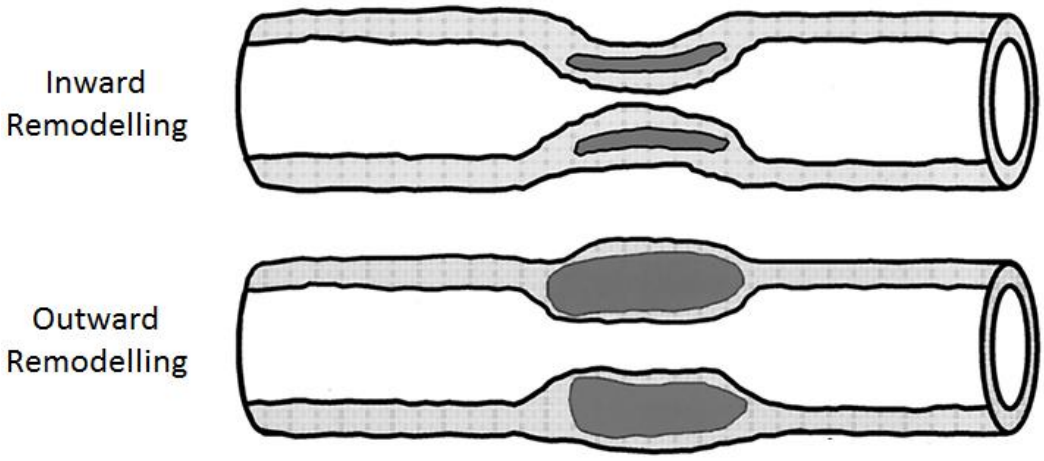

Figure 1.11. Schematics illustrating the difference between inward and outward atherosclerotic plaque remodelling (Adapted with permission from[103]).

As illustrated in Figure 1.11, although inward remodelling leads to a significantly narrowed artery, in the case of outward remodelling, the inner diameter of the artery is relatively well preserved. The initial conjecture on the theory of inward remodelling dominated plaque progression has directed clinicians and researchers to use luminal narrowing, as a predictor of atherosclerosis progression[77,100–104].

Along with realisation of outward remodelling, new research and diagnosis methodologies looking not only at luminal geometry but also at the morphology of atherosclerotic plaque were adopted[103,104]. Overall, studies published after this realisation that have investigated the pathology of vulnerable coronary atherosclerotic lesions have supported its validity, and highlighted the fact that outward remodelling plaques are morphologically complex and generally more prone to rupture[105–111]. Rupture of an atherosclerotic plaque could directly clog the artery on site by thrombus accumulation, or the blood can carry pieces of thrombus as emboli to a downstream location where the artery is narrowed, blocking the flow at a remote site[76,77].

There is extensive evidence that both the inflammatory process and multiple plaque ruptures consisting of healed silent and healed acute plaques may be the factors that drive plaque remodelling. Silent ruptures are atherosclerotic plaque ruptures that occur cyclically, without causing discomfort or giving any symptoms throughout the lifetime of a patient. Acute plaque ruptures are symptomatic ones that may result in unstable angina or myocardial infarction[112–115]. In a study involving 142 hearts that were obtained from male patients who died suddenly as a result of coronary artery disease, Burke et al. investigated the consequent morphological adaptations and prevalence of multiple plaque ruptures. They have stained cross-sectional slices of dissected coronary arteries to identify healing-related structural adaptations. A stained histology slice of a ruptured plaque that has healed twice is provided in Figure 1.12[77,113,114].

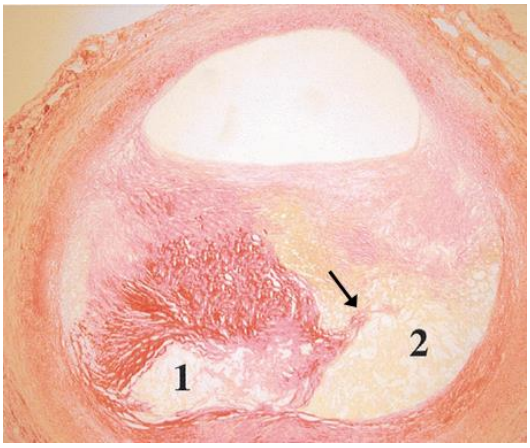

Figure 1.12. Histological cross-section of an atherosclerotic plaque that has undergone two cycles of rupture and subsequent healing. Two yellow stained lipid cores are separated with red stained collagen fibres. A strand of collagen indicating the more recent rupture site is identified by an arrow (Adapted with permission from[114]).

Atherosclerotic plaques are commonly classified according to the scheme introduced by American Heart Association (AHA)[116]. Although this scheme may not be complete in enabling accurate vulnerability assessment, it is widely accepted as a descriptor of natural disease progression[115,116]. A committee of scientists have classified the consecutive lesions into six main categories as schematised in Figure 1.13[77,116].

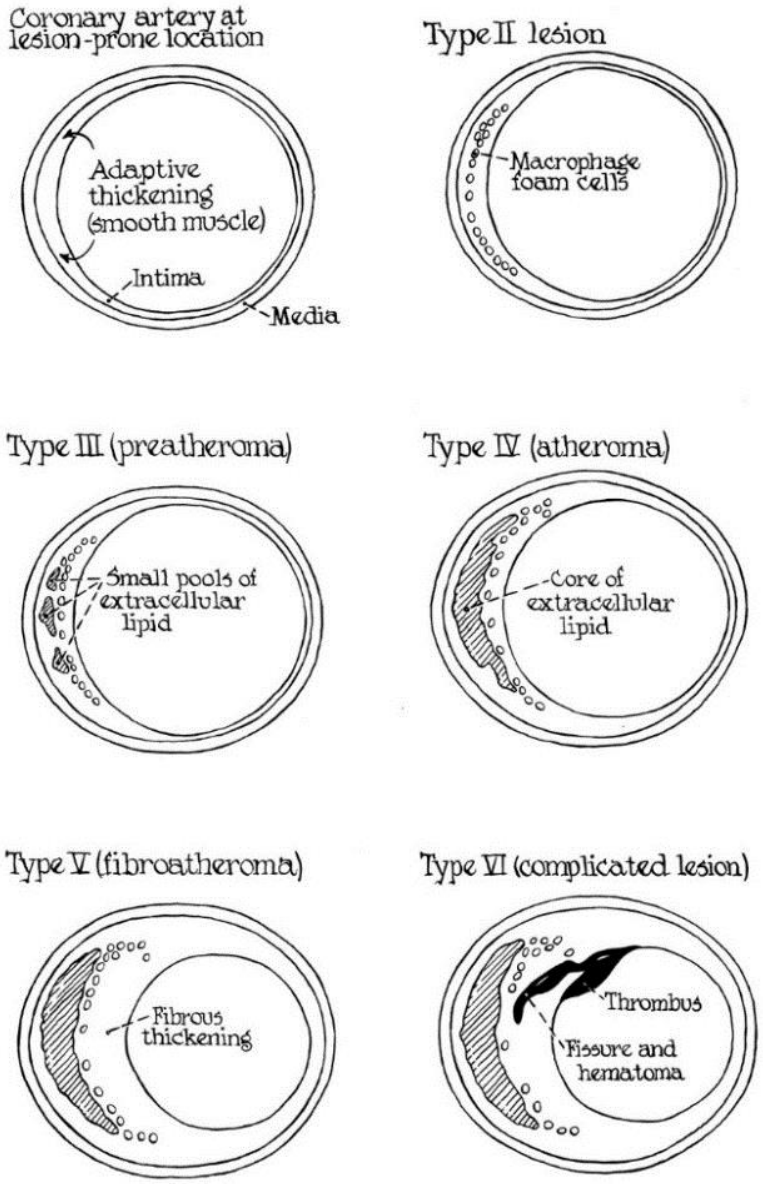

Figure 1.13. Schematic of lesion morphologies that develop during successive stages of atherosclerosis (Reprinted with permission from[116]).

The same scientific committee has also devised a flow diagram, outlining possible pathways followed by the disease across different lesion types, which is provided in Figure 1.14[77,116].

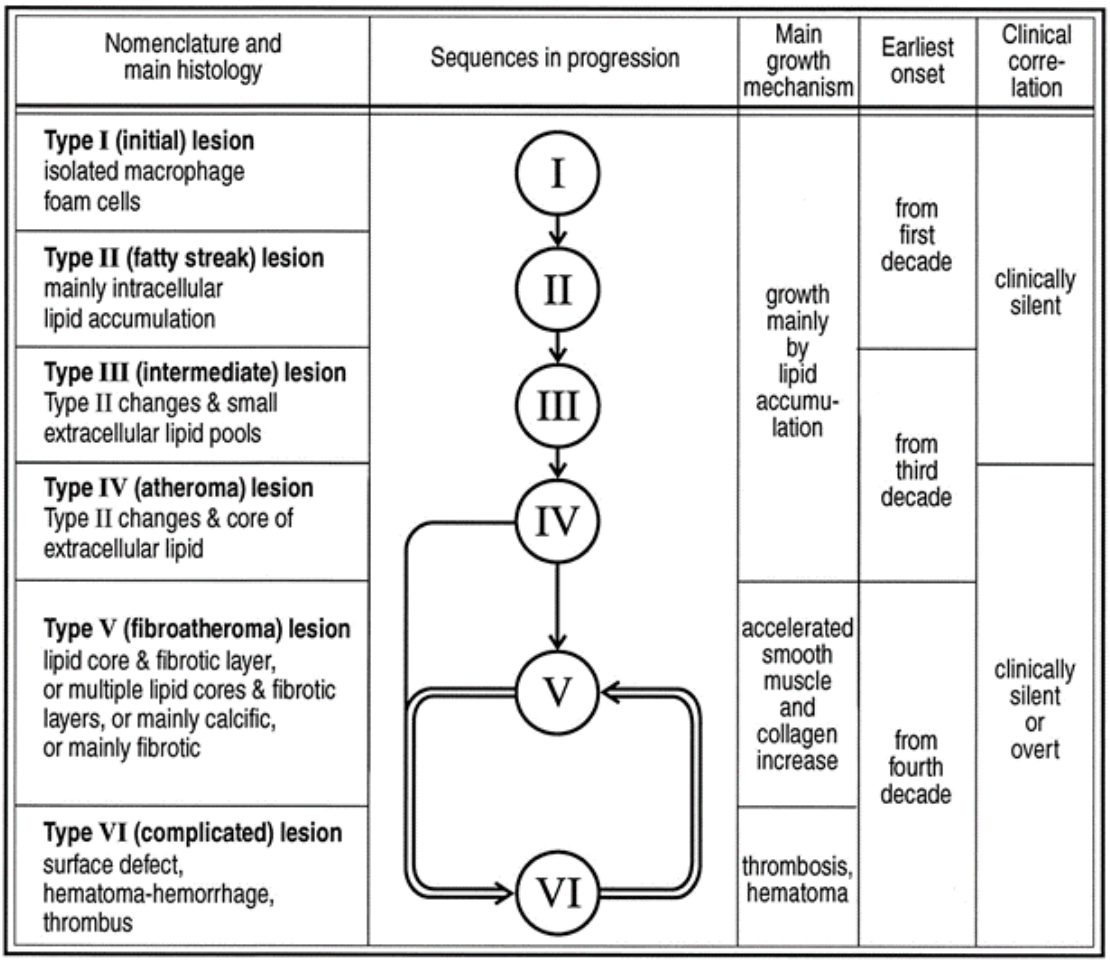

Figure 1.14. Flow chart outlining possible evolutional pathways of atherosclerotic plaques (Reprinted with permission from[116]).

Having a large lipid core and a thin fibrous cap signifies plaque vulnerability, where atheroma of Type VI lesions generally attains similar rupture prone morphologies. Fibrous caps of such lesions often undergo superficial erosion, which results in surface defects. Neovessels that penetrate into significantly enlarged lesions can occasionally result in intraplaque haemorrhage, by rupturing and bleeding within the plaque[84,116–118]. A combination of all or a number of these structural changes cause Type VI lesions to rupture, resulting in thrombus formation. If the rupture is not followed by fatal clinical events, a Type VI lesion can heal and revert back to Type V, restarting the cycle which is schematised by thick arrows in Figure 1.14[77,116,118].

Calcification can occur in both the advanced (Type V and Type VI) and in the earlier lesions (Type I to Type IV), where calcium particles are often found within the lipid cores of young adults[84,116,118]. Nevertheless, a clear relationship between arterial calcification and atherosclerotic plaque vulnerability has not yet been established[84,119]. Moreover, a relationship between the change in quantity of calcification and the corresponding change in atherosclerotic plaque progression has also not been found[77,84].

The AHA classification scheme assumes that Type IV atheromas are relatively stable, as the lipid core is contained within a fibrous cap that is rich in smooth muscle cells and collagen, where clinical events are generally associated with fatal Type VI lesions that rupture and lead to thrombosis[116,118]. After realising that thrombosis can occur without rupture, and at both Type IV and Type VI lesion sites, Virmani et al. performed comprehensive histological investigations to reassess the AHA proposed culprit lesion model. Their findings were used to categorise clinical event responsible lesions based on both the plaque morphology and mechanistic events. More than 65% of the clinical events were associated with thin-cap fibroatheromas (TCFAs), which are plaques that consist of large lipid cores encapsulated in macrophage infiltrated thin fibrous caps, where an example can be seen in Figure 1.15. The majority of the remaining events were found to occur as a result of superficial erosion, while a fewer number of events were associated with intra-plaque haemorrhage and superficial calcified nodules[77,107,111,115,120].

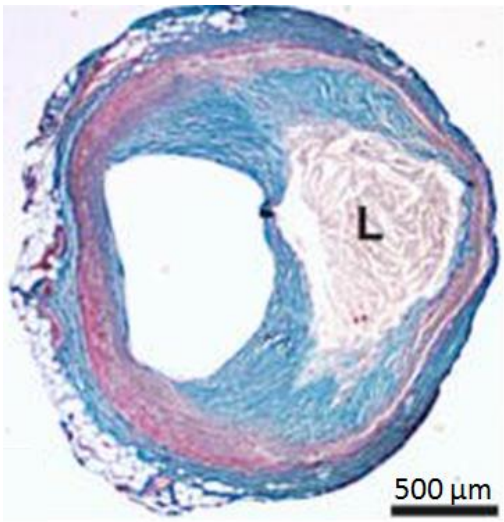

Figure 1.15. Image of a histological TCFA slice dyed with Masson's trichrome stain. Pink lipid core (L) is encapsulated within the blue coloured collagenous fibrous cap (Adapted with permission from[121]).

1.7 Architecture and load driven reorganisation of the arterial fibrous network

The arterial fibrous network is the main microstructural entity that dictates the mechanical behaviour of arterial tissue[11,12]. The main constituents of the fibrous network are the collagen and elastin fibres, while the collagen fibres are the primary contributor of mechanical properties in both healthy and diseased arteries[11,22]. Each of the intima, media and adventitia layers of an artery have distinct fibrous network architectures, where the organisation of distinct fibrous entities within each arterial layer has been described in section 1.2.1.

The collagen fibres in each arterial layer are aligned in different orientations, giving them unique mechanical properties. Collagen fibres of the intima generally have wider orientation distributions compared to those of the media and the adventitia layers. On the other hand, the media consists of parallel sublayers whose collagen fibres are well aligned within each layer[22]. The main types of collagen that are found in ECMs of all arterial layers are the Type I and Type III collagen. The basement membranes of endothelial cells and SMCs in healthy artery intimas and medias also contain Type IV and Type V collagens, while the Type V collagen is also found scattered throughout the intima[122].

Schriefl et al. have used polarised light microscopy to study the organisation of collagen fibres in the intima, media and adventitia layers of healthy human thoracic and abdominal aortas, as well as those of common iliac arteries[123,124]. Their study identified distinct fibre families, orientations and dispersions for each layer and for all of the examined vessel types. Most of the arterial layers consisted of two fibre families that were wrapped helically around the longitudinal vessel axis, where the preferred orientations of collagen fibres in the two families were opposite to each other. Fibres within each family also had a distribution of orientations around their corresponding preferred orientation. The media layer of common iliac arteries showed an exception by having only a single fibre family, whose collagen fibre orientations were distributed in the circumferential plane[124].

Schriefl et al. also found that the opposite preferred orientations of the families in the two-family fibre system were oriented approximately 45° to the axial direction. Nevertheless, the preferred two-family fibre orientations were found to be more axial in the adventitia and more circumferential in the media layer. Orientations of the collagen fibres were also found to be least dispersed in the adventitia and most dispersed in the intima. On the other hand, the fibre orientations in all arterial layers were mostly tangential to the lumen, with almost no radial component of orientation[123,124].

The fibrous network is the main load bearing microstructural entity of the artery wall. Hence, it is particularly important to note that collagen and elastin fibres undergo spatial reorganisations to efficiently bear the applied loads. Krasny et al. have performed a study to explore the differences in reorganisation of collagen and elastin fibres across distinct layers of the carotid artery wall. They performed uniaxial tensile tests with tissue strips from seven rabbit carotid arteries, while imaging their microstructures with multiphoton microscopy. They found that realignment of collagen and elastin fibres in the media layer, as well as the realignment of elastin fibres in the adventitia layer were relatively small. In the adventitia, the collagen fibres were found to exist as thick bundles which showed a high sensitivity to applied loads, always realigning themselves in the direction of stretch[125].

In a separate study, Krasny et al. have measured the reorganisation of adventitial collagen fibres in rabbit carotid arteries with multiphoton microscopy, under two distinct types of loading configurations, which were axial tension under constant pressurisation (type 1) and pressurisation at a fixed axial length (type 2). In the case of type 1 loading, the fibres were realigned highly in the axial stretching direction, while in the case of type 2 loading, despite experiencing >1.5 stretches in the circumferential direction, the collagen fibre orientations remained largely unchanged[126].

In another study, Sugita et al. performed pressurisation tests on rabbit and mouse thoracic aortas while imaging the collagen and elastin fibre networks of their media layers with multiphoton microscopy. Both collagen and elastin fibres were found to be mainly oriented along the circumferential direction of the aorta, while the waviness of collagen fibres was found to remain higher than that of the elastin fibres during pressurisation. Nevertheless, waviness of the collagen fibres decreased with increasing intraluminal pressure[127].

Sugita et al. also showed that the medial collagen fibres which were located outside the elastic laminae and in adjacent SMC rich regions became straight at lower levels of intraluminal pressure compared to the collagen fibres within the elastic laminae. This indicated that the collagen fibres between elastic laminae were stretched more than those within them. The main conclusion from these findings is that, the heterogeneous layers of the aortic media and differences in mechanical properties of its distinct layers cause a peculiar microstructural reorganisation under applied loads[127].

Cavinato et al. have performed bulge inflation tests on healthy porcine, as well as on healthy and aneurysmal human aortic tissue samples while imaging the collagen fibre network of their adventitia layers with multiphoton microscopy. In the unloaded state, the adventitia was found to consist of densely arranged and wavy collagen fibre bundles. As the inflation pressure was increased, the collagen fibre bundles were continuously straightened and eventually separated into a network of thinner fibre bundles at relatively high pressures. Three main families of fibres were identified, which were oriented approximately 45°, 90° and 135° to the circumferential direction of the aorta and in the circumferential-axial plane. Preferred orientations of the fibre families were not found to change under pressurisation. Nevertheless, the fibres were progressively straightened and their orientations became less dispersed with increasing pressure[128].

As described above, the architecture and load driven reorganisation of the fibrous network in aorta[123,124,127,128] and carotid artery[125,126] microstructures has been studied by a number of scientists. These studies provide critical information on the organisation of collagen and elastin fibres within the intima, media and adventitia layers, while describing the distinct reorganisations which are mainly experienced by collagen fibres under uniaxial loading[125], pressurisation[127], pressurisation with axial tension[126] and bulge inflation[128]. Nevertheless, the role of the arterial fibrous network is not limited to reorganisation of collagen fibres to support the applied loads. Failure mechanisms and fracture toughness of arterial tissue are also determined by the integrity of its fibrous network. However, comprehensive investigations on the role of arterial fibrous network on fracture behaviour and on resistance of tissue to structural defects does not yet exist.

1.8 Mechanical modelling of arterial tissues

Microstructure of an artery particularly resembles that of a short fibre composite, whose ground matrix also plays a key role in maintaining adequate distribution of the induced structural stresses throughout the fibrous network to prevent local stress concentrations. In arterial tissue, the ground matrix binds the cross-linked collagen fibre network further together and acts as a stress transmitter between the collagen fibres, ensuring that the fibres are efficiently recruited as the arterial tissue is continuously loaded with a varying magnitude of load. Arterial tissue rupture is an event that is driven by environmental biomechanical and biochemical changes experienced by the artery[33,129]. Regardless of the underlying pathological mechanisms, homeostatic imbalances trigger and drive the disruption of the fibrous network and incorporation of microstructural defects within the arterial tissue, which lead to localized structural weakening and therefore, origination of sites that are prone to stress concentrations.

The constitutive material models have been successful in replicating the nonlinearity and the collagen fibre orientation dependent anisotropy of the arterial tissue. Constitutive models are mathematical formulations that describe the response of materials to the applied loads. Engineers often utilise constitutive material formulae for finding practical estimates to complex mechanical problems. Nevertheless, in the case of arterial tissue, using back-of-the-envelope calculations with a constitutive equation is not practical for obtaining enough information about the stress distribution across the whole length and thickness of the considered arterial section. Consequently, computers are employed to solve the constitutive equations for whole of the considered arterial geometry. The most commonly utilised computer-based technique is finite element analysis (FEA). The fundamental objective of FEA is to use many finite sized elements to construct the desired arterial tissue geometry, while assigning each element with the constitutive formulation that describes the mechanical behaviour of arterial tissue. FEA uses the applied loads and boundary conditions of the model to solve the constitutive formulation of each element, in order to propagate the loading from the boundaries to the remainder of the model, so as to compute the stress distribution of the whole geometry[130].

The constitutive models commonly group the non-collagenous components of the arterial tissue, which consists mainly of elastin and GAGs into a single entity called the ground matrix[130,131]. The ground matrix is often assigned with an isotropic mechanical behaviour, where the collagen fibres are assumed to be embedded within the ground matrix and modelled with statistically distributed orientations, which gives the constitutive models an overall anisotropic behaviour[21,22,130,131]. Although the constitutive models can efficiently replicate the stress dependent anisotropic mechanical response of arteries, they cannot provide actual microstructural information on stress dependent recruitment and reorganisation of the load bearing collagen fibres, nor the directions and magnitudes of stress transfers amongst distinct microstructural components[130,132]. In addition to the anisotropic constitutive models, simpler constitutive models with isotropic material formulations also exist[133]. Performance of the isotropic constitutive models that are most commonly used in modelling diseased arterial tissue have been compared by Teng et al., who concluded that Demiray[134–136] and modified Mooney-Rivlin[137–139] constitutive models are the most stable models for correct characterisation of the material behaviour[133].

Finite element models that are built bottom-up from the microstructural components provide an improved alternative to the constitutive material models, as they allow extraction of microstructural information based on the individual microscale constituents. These bottom-up built models are constructed directly from distinct microstructural components of the arterial tissue and their architecture resembles that of the actual tissue microstructure. For instance, the collagen fibres are modelled with beam type elements in FEA and are cross-linked with special connector elements to resemble their fibrous network in the tissue structure. The studies performed by Koh et al. were identified as examples of microstructural constituent based modelling of soft fibrous materials and tissues[140–144]. Their micromechanical finite element model was developed to study the mechanical response and failure of biomimetic fibrous and biological fibrous membranes in separate studies. The developed model was validated based on mechanical experiments and scanning electron microscopy images of the membrane microstructures[140–142]. Membranes were imaged with scanning electron microscopy both in the unloaded and the loaded states by mechanical fixing after stretching, while being tested both with and without notches to investigate the response of the fibres in the presence of structural defects. Moreover, influences of the degree of fibre cross-linking and fibre length on the membrane mechanical properties were also studied, which yielded stiffer and tougher mechanical responses with increases in both parameters[140–143].

The finite element model of Koh et al. was not incorporated with a ground matrix, consequently, it fell behind in providing valuable information on the directions and magnitudes of stress transfers amongst distinct microstructural components within the membranes and particularly around the structural defects. Moreover, the influence of local randomisations in the collagen fibre orientations on the structural distribution of stress and global mechanical behaviour were not studied. Influence of such structural characteristics on the mechanical response of arterial tissues can only be studied with a complete microstructural mechanics model that contains collagen fibres and the ground matrix as two separate structural entities. However, a comprehensive arterial micromechanics study involving such a model does not yet exist.

1.9 Project aims and dissertation outline

The fracture properties of diseased human aortic tissue have not yet been measured. In addition, although the contribution of collagen, elastin and GAGs to the mechanical behaviour of healthy aortic tissue has been studied, influence of the pathological changes in the contents and organisation of these microstructural components on the mechanics of diseased arterial tissue requires further investigation. The first aim of this project is to fill these gaps in the literature. Mechanical tests with unnotched and notched diseased aortic tissue samples as well as immunohistochemical analysis have been performed to fulfil this aim. This project also aims to establish a framework for constitutive material modelling of healthy aortic, aneurysmal and atherosclerotic tissues, and to identify relationships between constitutive model parameters and microstructural features. Moreover, images of the fibrous network in unnotched and notched healthy porcine carotid arteries have been recorded during stretching with a multiphoton microscope to study its load driven reorganisations, and to investigate its behaviour around structural defects. A microstructural component based finite element model has also been developed and optimised to study the influence of various microstructural parameters on the mechanical behaviour of arterial tissue.

Potential findings from this project could unravel the key players of arterial micromechanics that dictate the mechanical behaviour of healthy and diseased arterial tissues. These findings can inform clinical researchers in targeting the correct structural components during development of diagnostic tools, as well as for creation of new therapeutic drugs.

Researchers could also utilise the identified mechanical contributors and further study their potential use as biomarkers of structural integrity. On the other hand, findings on microstructural component dependent variations in distinct mechanical properties could guide tissue engineers in fine-tuning the mechanical properties of their biological vessel grafts. Finally, the unique methodology that has been developed to investigate the microstructure-mechanics and microstructure-fracture behaviours of arterial tissue could be utilised to study the same relationships in other tissue types. Brief descriptions of the chapters that constitute the remainder of this dissertation are as follows:

Chapter 2 describes the uniaxial unnotched and notched tensile tests that were performed on diseased human aortic aneurysmal and dissection tissue samples. The data obtained from the two distinct types of mechanical tests were used to characterise the mechanical and fracture behaviours of diseased human aortic tissue. The unnotched and notched tensile test results from different arterial layers were analysed and compared to understand the influence of an externally induced structural defect, on both the mechanical response, as well as the corresponding failure behaviour of each arterial layer.

Chapter 3 describes the histological processing that was performed on the mechanically tested diseased human aortic tissues, as well as the subsequent analysis that was aimed at identifying the influence of diseased tissue microstructural components on mechanical and fracture behaviours. The tissues were stained on separate microscope slides with distinct dyes to differentiate collagen, elastin, GAGs and macrophages from one another and from the remaining microstructural components of the diseased aortic tissue. This was followed by digitisation of the generated aortic tissue microscope slides into digital image data, where the obtained images were processed to compute structural and organisational parameters of distinct microstructural components. The computed microstructural component parameters were analysed with the corresponding uniaxial tensile test data to understand the influence of microstructure on mechanical and fracture behaviours.

Chapter 4 describes the constitutive material modelling of healthy aortic, aneurysmal and atherosclerotic tissues. The stress-stretch curves of all arterial tissue types were fitted with the modified Mooney-Rivlin material model to parameterise the mechanical behaviour of each tissue type with the model material constants. The correlation of the obtained constants with the corresponding microscopic structures were also investigated.

The capability of the determined material constants to differentiate tissues from normal aorta, carotid atherosclerotic plaque and aortic aneurysm were assessed and the association between determined material constants and collagen fibre architecture in the tissue was explored.

Chapter 5 describes investigation of microstructural reorganisations in the arterial tissue during stretching, both in the presence and absence of a structural defect. Unnotched and notched tissue strips of healthy porcine carotid arteries were stretched uniaxially, while 3D image stacks were acquired with a multiphoton microscope. The fibre microstructure was characterised by the orientation and fibre dispersion. The degree to which the fibre structure changed with increasing stretch and the details of fibre microstructural changes around structural defects were explored.

Chapter 6 describes the development and optimisation of a microstructural component-based unit cell model, which was used to investigate the micromechanical behaviour of arterial tissue during stretching. Influence of distinct microstructural parameters on the micromechanical behaviour were studied.

Chapter 7 consists of the conclusion of the whole dissertation and the future work that can be pursued.

1.10 References

1. Nordon, I. M., Hinchliffe, R. J., Loftus, I. M. & Thompson, M. M. Pathophysiology and epidemiology of abdominal aortic aneurysms. *Nat. Rev. Cardiol.* **8,** 92–102 (2011).
2. Khan, I. A. & Nair, C. K. Clinical, diagnostic, and management perspectives of aortic dissection. *Chest* **122,** 311–28 (2002).
3. Fitridge, R. & Thompson, M. *Mechanisms of Vascular Disease*. (University of Adelaide Press, 2012). doi:10.1017/UPO9781922064004
4. Yusuf, S., Reddy, S., Ounpuu, S. & Anand, S. Global burden of cardiovascular diseases: part I: general considerations, the epidemiologic transition, risk factors, and impact of urbanization. *Circulation* **104,** 2746–2753 (2001).
5. Fonarow, G. C. The global burden of atherosclerotic vascular disease. *Nat. Clin. Pract.*

Cardiovasc. Med. **4,** 530–531 (2007).

6. Jamison, D. T. *Disease control priorities in developing countries*. (Oxford University Press ; World Bank, 2006).

7. Mozaffarian, D. *et al.* Heart Disease and Stroke Statistics - 2015 Update: A Report From the American Heart Association. *Circulation* **131,** e29–e322 (2014).

8. Lahoz, C. & Mostaza, J. M. Atherosclerosis As a Systemic Disease. *Rev. Española Cardiol. (English Ed.* **60,** 184–195 (2007).

9. Levick, J. R. *An introduction to cardiovascular physiology*. (Butterworths, 1991).

10. Levy, M. N., Wier, W. G. & Pappano, A. J. *Cardiovascular physiology*. (Elsevier/Mosby, 2013).

11. Humphrey, J. D. *Cardiovascular Solid Mechanics: Cells, Tissues, and Organs*. (Springer New York, 2002). doi:10.1007/978-0-387-21576-1

12. Fung, Y.-C. *Biomechanics: Mechanical Properties of Living Tissues*. (Springer New York, 1993). doi:10.1007/978-1-4757-2257-4

13. Anand, A. & Xiu, P. *Pathology*. (Elsevier, 2012).

14. Erbel, R. *et al.* 2014 ESC Guidelines on the diagnosis and treatment of aortic diseases. *Kardiol. Pol.* **72,** 1169–252 (2014).

15. Libby, P. & Theroux, P. Pathophysiology of coronary artery disease. *Circulation* **111,** 3481–3488 (2005).

16. Weber, C. & Noels, H. Atherosclerosis: current pathogenesis and therapeutic options. *Nature Medicine* **17,** 1410–1422 (2011).

17. Dingemans, K. P., Teeling, P., Lagendijk, J. H. & Becker, A. E. Extracellular matrix of the human aortic media: an ultrastructural histochemical and immunohistochemical study of the adult aortic media. *Anat. Rec.* **258,** 1–14 (2000).

18. O'Connell, M. *et al.* The three-dimensional micro- and nanostructure of the aortic medial lamellar unit measured using 3D confocal and electron microscopy imaging. *Matrix Biol.* **27,** 171–181 (2008).

19. Clark, T. E., Lillie, M. A., Vogl, A. W., Gosline, J. M. & Shadwick, R. E. Mechanical contribution of lamellar and interlamellar elastin along the mouse aorta. *J. Biomech.*

48, 3599–605 (2015).

20. Yurdagul, A., Finney, A. C., Woolard, M. D. & Orr, A. W. The arterial microenvironment: the where and why of atherosclerosis. *Biochem. J.* **473,** 1281–1295 (2016).

21. Holzapfel, G. A., Gasser, T. C. & Ogden, R. W. A New Constitutive Framework for Arterial Wall Mechanics and a Comparative Study of Material Models. *J. Elast.* **61,** 1–48 (2000).

22. Gasser, T. C., Ogden, R. W. & Holzapfel, G. A. Hyperelastic modelling of arterial layers with distributed collagen fibre orientations. *J. R. Soc. Interface* **3,** 15–35 (2006).

23. Fratzl, P. *Collagen: Structure and Mechanics*. (Springer US, 2008). doi:10.1007/978-0-387-73906-9

24. O'Brien, M. Structure and metabolism of tendons. *Scand. J. Med. Sci. Sports* **7,** 55–61 (2007).

25. Gupta, R., Stallcup, R., Geisberger, A., Hughes, G. & Layton, B. Manipulation of Collagen Fibers for Mechanical Characterization. *Zyvex Corporation* 1–6 (2006).

26. Yang, W. *et al.* On the tear resistance of skin. *Nat. Commun.* **6,** 6649 (2015).

27. Christiansen, D. L., Huang, E. K. & Silver, F. H. Assembly of type I collagen: fusion of fibril subunits and the influence of fibril diameter on mechanical properties. *Matrix Biol.* **19,** 409–20 (2000).

28. García-Herrera, C. M. *et al.* Mechanical behaviour and rupture of normal and pathological human ascending aortic wall. *Med. Biol. Eng. Comput.* **50,** 559–66 (2012).

29. Schriefl, A. J., Schmidt, T., Balzani, D., Sommer, G. & Holzapfel, G. A. Selective enzymatic removal of elastin and collagen from human abdominal aortas: uniaxial mechanical response and constitutive modeling. *Acta Biomater.* **17,** 125–36 (2015).

30. Kobielarz, M., Chwiłkowska, A., Turek, A., Maksymowicz, K. & Marciniak, M. Influence of selective digestion of elastin and collagen on mechanical properties of human aortas. *Acta Bioeng. Biomech. / Wrocław Univ. Technol.* **17,** 55–62 (2015).

31. Holzapfel, G. A. in *Collagen* (ed. Fratzl, P.) 285–324 (Springer US, 2008). doi:10.1007/978-0-387-73906-9_11

32. Holzapfel, G. A., Sommer, G., Gasser, C. T. & Regitnig, P. Determination of layer-specific mechanical properties of human coronary arteries with nonatherosclerotic intimal thickening and related constitutive modeling. *Am. J. Physiol. Circ. Physiol.* **289,** H2048–H2058 (2005).

33. Isselbacher, E. M. Thoracic and abdominal aortic aneurysms. *Circulation* **111,** 816–28 (2005).

34. Goldfinger, J. Z. *et al.* Thoracic aortic aneurysm and dissection. *J. Am. Coll. Cardiol.* **64,** 1725–39 (2014).

35. Brewster, D. C. *et al.* Guidelines for the treatment of abdominal aortic aneurysms. Report of a subcommittee of the Joint Council of the American Association for Vascular Surgery and Society for Vascular Surgery. *J. Vasc. Surg.* **37,** 1106–17 (2003).

36. Erbel, R. & Eggebrecht, H. Aortic dimensions and the risk of dissection. *Heart* **92,** 137–42 (2006).

37. Erbel, R. *et al.* Diagnosis and management of aortic dissection. *Eur. Heart J.* **22,** 1642–81 (2001).

38. Baumann, F., Makaloski, V. & Diehm, N. Aortic aneurysms and aortic dissection: epidemiology, pathophysiology and diagnostics. *Internist (Berl).* **54,** 535–42 (2013).

39. Tsamis, A., Krawiec, J. T. & Vorp, D. A. Elastin and collagen fibre microstructure of the human aorta in ageing and disease: a review. *J. R. Soc. Interface* **10,** 20121004 (2013).

40. Humphrey, J. D. Possible mechanical roles of glycosaminoglycans in thoracic aortic dissection and associations with dysregulated transforming growth factor-β. *J. Vasc. Res.* **50,** 1–10 (2013).

41. Roccabianca, S., Ateshian, G. A. & Humphrey, J. D. Biomechanical roles of medial pooling of glycosaminoglycans in thoracic aortic dissection. *Biomech. Model. Mechanobiol.* **13,** 13–25 (2014).

42. Jacob, M. P. Extracellular matrix remodeling and matrix metalloproteinases in the vascular wall during aging and in pathological conditions. *Biomed. Pharmacother.* **57,** 195–202 (2003).

43. Manabe, T., Imoto, K., Uchida, K., Doi, C. & Takanashi, Y. Decreased tissue inhibitor of metalloproteinase-2/matrix metalloproteinase ratio in the acute phase of aortic dissection. *Surg. Today* **34,** 220–5 (2004).

44. Zhang, X., Shen, Y. H. & LeMaire, S. A. Thoracic aortic dissection: are matrix metalloproteinases involved? *Vascular* **17,** 147–57 (2009).

45. Carmo, M. *et al.* Alteration of elastin, collagen and their cross-links in abdominal aortic aneurysms. *Eur. J. Vasc. Endovasc. Surg.* **23,** 543–9 (2002).

46. Nakashima, Y., Kurozumi, T., Sueishi, K. & Tanaka, K. Dissecting aneurysm: a clinicopathologic and histopathologic study of 111 autopsied cases. *Hum. Pathol.* **21,** 291–6 (1990).

47. Rizzo, R. J. *et al.* Collagen types and matrix protein content in human abdominal aortic aneurysms. *J. Vasc. Surg.* **10,** 365–73 (1989).

48. Gandhi, R. H. *et al.* Analysis of elastin cross-linking and the connective tissue matrix of abdominal aortic aneurysms. *Surgery* **115,** 617–20 (1994).

49. Wilson, K. A. *et al.* The relationship between abdominal aortic aneurysm distensibility and serum markers of elastin and collagen metabolism. *Eur. J. Vasc. Endovasc. Surg.* **21,** 175–8 (2001).

50. Sariola, H., Viljanen, T. & Luosto, R. Histological pattern and changes in extracellular matrix in aortic dissections. *J. Clin. Pathol.* **39,** 1074–81 (1986).

51. Minion, D. J. *et al.* Elastin is increased in abdominal aortic aneurysms. *J. Surg. Res.* **57,** 443–6 (1994).

52. Campa, J. S., Greenhalgh, R. M. & Powell, J. T. Elastin degradation in abdominal aortic aneurysms. *Atherosclerosis* **65,** 13–21 (1987).

53. de Figueiredo Borges, L. *et al.* Collagen is reduced and disrupted in human aneurysms and dissections of ascending aorta. *Hum. Pathol.* **39,** 437–443 (2008).

54. Paik, D. & Tilson, M. D. Neovascularization in the abdominal aortic aneurysm. Endothelial nitric oxide synthase, nitric oxide, and elastolysis. *Ann. N. Y. Acad. Sci.* **800,** 277 (1996).

55. Paik, D. C., Ramey, W. G., Dillon, J. & Tilson, M. D. The nitrite/elastin reaction: implications for in vivo degenerative effects. *Connect. Tissue Res.* **36,** 241–51 (1997).

56. Busuttil, R. W., Rinderbriecht, H., Flesher, A. & Carmack, C. Elastase activity: The role of elastase in aortic aneurysm formation. *J. Surg. Res.* **32,** 214–217 (1982).

57. Cattell, M. A., Hasleton, P. S. & Anderson, J. C. Increased elastin content and decreased elastin concentration may be predisposing factors in dissecting aneurysms of human thoracic aorta. *Cardiovasc. Res.* **27,** 176–181 (1993).

58. Panek, B., Gacko, M. & Pałka, J. Metalloproteinases, insulin-like growth factor-I and its binding proteins in aortic aneurysm. *Int. J. Exp. Pathol.* **85,** 159–164 (2004).

59. Whittle, M. A., Hasleton, P. S., Anderson, J. C. & Gibbs, A. C. Collagen in dissecting aneurysms of the human thoracic aorta. Increased collagen content and decreased collagen concentration may be predisposing factors in dissecting aneurysms. *Am. J. Cardiovasc. Pathol.* **3,** 311–9 (1990).

60. Tamarina, N. A., Grassi, M. A., Johnson, D. A. & Pearce, W. H. Proteoglycan gene expression is decreased in abdominal aortic aneurysms. *J. Surg. Res.* **74,** 76–80 (1998).

61. Zhang, L. & Wang, H.-H. The genetics and pathogenesis of thoracic aortic aneurysm disorder and dissections. *Clin. Genet.* **89,** 639–46 (2016).

62. Zamaneh Kassiri, R. B. Extracellular Matrix Remodelling and Abdominal Aortic Aneurysm. *J. Clin. Exp. Cardiolog.* **04,** 259 (2013).

63. Hellenthal, F. A. M. V. I., Buurman, W. A., Wodzig, W. K. W. H. & Schurink, G. W. H. Biomarkers of AAA progression. Part 1: extracellular matrix degeneration. *Nat. Rev. Cardiol.* **6,** 464–74 (2009).

64. Gutierrez, P. S. *et al.* Decrease in sulphated glycosaminoglycans in aortic dissection--possible role in the pathogenesis. *Cardiovasc. Res.* **25,** 742–8 (1991).

65. Theocharis, A. D., Tsolakis, I., Tsegenidis, T. & Karamanos, N. K. Human abdominal aortic aneurysm is closely associated with compositional and specific structural modifications at the glycosaminoglycan level. *Atherosclerosis* **145,** 359–68 (1999).

66. Sobolewski, K., Wolańska, M., Bańkowski, E., Gacko, M. & Głowiński, S. Collagen, elastin and glycosaminoglycans in aortic aneurysms. *Acta biochimica Polonica* **42,** 301–307 (1995).

67. Cattell, M. A., Hasleton, P. S. & Anderson, J. C. Glycosaminoglycan content is increased in dissecting aneurysms of human thoracic aorta. *Clin. Chim. Acta.* **226,** 29–

46 (1994).

68. Raffort, J. *et al.* Monocytes and macrophages in abdominal aortic aneurysm. *Nat. Rev. Cardiol.* **14,** 457–471 (2017).

69. Nakashima, Y. Pathogenesis of aortic dissection: elastic fiber abnormalities and aortic medial weakness. *Ann. Vasc. Dis.* **3,** 28–36 (2010).

70. Kuehl, H. *et al.* Detection of inflammation in patients with acute aortic syndrome: comparison of FDG-PET/CT imaging and serological markers of inflammation. *Heart* **94,** 1472–7 (2008).

71. Ghigliotti, G. *et al.* CD16(+) monocyte subsets are increased in large abdominal aortic aneurysms and are differentially related with circulating and cell-associated biochemical and inflammatory biomarkers. *Dis. Markers* **34,** 131–42 (2013).

72. Gawinecka, J., Schönrath, F. & von Eckardstein, A. Acute aortic dissection: pathogenesis, risk factors and diagnosis. *Swiss Med. Wkly.* **147,** w14489 (2017).

73. Pan, J.-H. *et al.* Macrophage migration inhibitory factor is associated with aneurysmal expansion. *J. Vasc. Surg.* **37,** 628–35 (2003).

74. Reeps, C. *et al.* Increased 18F-fluorodeoxyglucose uptake in abdominal aortic aneurysms in positron emission/computed tomography is associated with inflammation, aortic wall instability, and acute symptoms. *J. Vasc. Surg.* **48,** 417–23; discussion 424 (2008).

75. Wu, D. *et al.* Inflammatory Cell Infiltrates in Acute and Chronic Thoracic Aortic Dissection. *Aorta (Stamford, Conn.)* **1,** 259–67 (2013).

76. Willerson, J. T. & Holmes, D. R. *Coronary artery disease*. (Springer Berlin Heidelberg, 2014).

77. Tokgoz, A. Characterizing Coronary Atherosclerotic Plaque Morphology and Critical Mechanical Conditions Using Dual Energy Computed Tomography. (MPhil Thesis, University of Cambridge, 2015).

78. Libby, P., Ridker, P. M. & Hansson, G. K. Progress and challenges in translating the biology of atherosclerosis. *Nature* **473,** 317–325 (2011).

79. Wilcken, D. E. & Wilcken, B. The pathogenesis of coronary artery disease. A possible role for methionine metabolism. *J. Clin. Invest.* **57,** 1079–1082 (1976).

80. Jensen, M. K. *et al.* Novel metabolic biomarkers of cardiovascular disease. *Nat. Rev. Endocrinol.* **10,** 659–672 (2014).

81. Robbins, S. L., Aster, J. C., Abbas, A. K. & Kumar, V. *Robbins basic pathology*. (Elsevier/Saunders, 2013).

82. Cotran, R. S., Robbins, S. L. & Klatt, E. C. *Robbins and Cotran atlas of pathology*. (Saunders/Elsevier, 2010).

83. Szanto, P. A. & Schneider, A. S. *Pathology*. (Wolters Kluwer Health/Lippincott Williams & Wilkins, 2014).

84. Wexler, L. *et al.* Coronary Artery Calcification: Pathophysiology, Epidemiology, Imaging Methods, and Clinical Implications: A Statement for Health Professionals From the American Heart Association. *Circulation* **94,** 1175–1192 (1996).

85. Burke, A. P., Weber, D. K., Kolodgie, F. D., Farb, A. & Taylor, A. J. Pathophysiology of Calcium Deposition in Coronary Arteries. *Herz* **26,** 239–244 (2001).

86. Roijers, R. B. *et al.* Microcalcifications in Early Intimal Lesions of Atherosclerotic Human Coronary Arteries. *Am. J. Pathol.* **178,** 2879–2887 (2011).

87. Chatzizisis, Y. S. *et al.* Role of Endothelial Shear Stress in the Natural History of Coronary Atherosclerosis and Vascular Remodeling. *J. Am. Coll. Cardiol.* **49,** 2379–2393 (2007).

88. Van der Heiden, K. *et al.* Endothelial primary cilia in areas of disturbed flow are at the base of atherosclerosis. *Atherosclerosis* **196,** 542–550 (2008).

89. Davies, P. F. Hemodynamic shear stress and the endothelium in cardiovascular pathophysiology. *Nat. Clin. Pract. Cardiovasc. Med.* **6,** 16–26 (2009).

90. Ku, D. N., Giddens, D. P., Zarins, C. K. & Glagov, S. Pulsatile flow and atherosclerosis in the human carotid bifurcation. Positive correlation between plaque location and low oscillating shear stress. *Arterioscler. Thromb. Vasc. Biol.* **5,** 293–302 (1985).

91. Stone, P. H. *et al.* Regions of low endothelial shear stress are the sites where coronary plaque progresses and vascular remodelling occurs in humans: an in vivo serial study. *Eur. Heart J.* **28,** 705–710 (2007).

92. Dollery, C. M. & Libby, P. Atherosclerosis and proteinase activation. *Cardiovasc. Res.*

69, 625–35 (2006).

93. Galis, Z. S. & Khatri, J. J. Matrix metalloproteinases in vascular remodeling and atherogenesis: the good, the bad, and the ugly. *Circ. Res.* **90,** 251–62 (2002).

94. Adiguzel, E., Ahmad, P. J., Franco, C. & Bendeck, M. P. Collagens in the progression and complications of atherosclerosis. *Vasc. Med.* **14,** 73–89 (2009).

95. Libby, P. Inflammation in atherosclerosis. *Nature* **420,** 868–74 (2002).

96. Stevens, R. L., Colombo, M., Gonzales, J. J., Hollander, W. & Schmid, K. The glycosaminoglycans of the human artery and their changes in atherosclerosis. *J. Clin. Invest.* **58,** 470–81 (1976).

97. Burleigh, M. C. *et al.* Collagen types I and III, collagen content, GAGs and mechanical strength of human atherosclerotic plaque caps: span-wise variations. *Atherosclerosis* **96,** 71–81 (1992).

98. Van Herck, J. L. *et al.* Impaired fibrillin-1 function promotes features of plaque instability in apolipoprotein E-deficient mice. *Circulation* **120,** 2478–87 (2009).

99. Panetta, C., Fallon, J. T., Zhang, H., Ramirez, F. & Taubman, M. B. Identification of Fibrillins as a Major Component of Coronary Atherosclerotic Plaques. *Cardiovasc. Pathol.* **7,** 69–74 (1998).

100. Velican, C. & Velican, D. Progression of coronary atherosclerosis from adolescents to mature adults. *Atherosclerosis* **47,** 131–144 (1983).

101. Glagov, S., Weisenberg, E., Zarins, C. K., Stankunavicius, R. & Kolettis, G. J. Compensatory enlargement of human atherosclerotic coronary arteries. *N. Engl. J. Med.* **316,** 1371–1375 (1987).

102. McPherson, D. D. *et al.* Coronary arterial remodeling studied by high-frequency epicardial echocardiography: an early compensatory mechanism in patients with obstructive coronary atherosclerosis. *J. Am. Coll. Cardiol.* **17,** 79–86 (1991).

103. Schoenhagen, P., Ziada, K. M., Vince, D. G., Nissen, S. E. & Tuzcu, E. M. Arterial remodeling and coronary artery disease: The concept of ‘Dilated’ versus ‘Obstructive’ coronary atherosclerosis. *Journal of the American College of Cardiology* **38,** 297–306 (2001).

104. Varnava, A. M., Mills, P. G. & Davies, M. J. Relationship between coronary artery

remodeling and plaque vulnerability. *Circulation* **105,** 939–943 (2002).

105. Narula, J. *et al.* Histopathologic characteristics of atherosclerotic coronary disease and implications of the findings for the invasive and noninvasive detection of vulnerable plaques. *J. Am. Coll. Cardiol.* **61,** 1041–1051 (2013).

106. Narula, J. & Strauss, H. W. The popcorn plaques. *Nature medicine* **13,** 532–534 (2007).

107. Burke, a P. *et al.* Coronary risk factors and plaque morphology in men with coronary disease who died suddenly. *N. Engl. J. Med.* **336,** 1276–1282 (1997).

108. Falk, E. Morphologic features of unstable atherothrombotic plaques underlying acute coronary syndromes. *Am. J. Cardiol.* **63,** 114E–120E (1989).

109. Kragel, A. H., Reddy, S. G., Wittes, J. T. & Roberts, W. C. Morphometric analysis of the composition of coronary arterial plaques in isolated unstable angina pectoris with pain at rest. *Am. J. Cardiol.* **66,** 562–567 (1990).

110. Kragel, A. H., Reddy, S. G., Wittes, J. T. & Roberts, W. C. Morphometric analysis of the composition of atherosclerotic plaques in the four major epicardial coronary arteries in acute myocardial infarction and in sudden coronary death. *Circulation* **80,** 1747–1756 (1989).

111. Otsuka, F., Joner, M., Prati, F., Virmani, R. & Narula, J. Clinical classification of plaque morphology in coronary disease. *Nat. Rev. Cardiol.* **11,** 379–389 (2014).

112. Libby, P. Inflammation and cardiovascular disease mechanisms. *Am. J. Clin. Nutr.* **83,** 456S–460S (2006).

113. Burke, A. P. *et al.* Plaque rupture and sudden death related to exertion in men with coronary artery disease. *JAMA* **281,** 921–926 (1999).

114. Burke, A. P. *et al.* Healed plaque ruptures and sudden coronary death: evidence that subclinical rupture has a role in plaque progression. *Circulation* **103,** 934–940 (2001).

115. Virmani, R., Kolodgie, F. D., Burke, A. P., Farb, A. & Schwartz, S. M. Lessons from sudden coronary death: a comprehensive morphological classification scheme for atherosclerotic lesions. *Arterioscler. Thromb. Vasc. Biol.* **20,** 1262–1275 (2000).

116. Stary, H. C. *et al.* A definition of advanced types of atherosclerotic lesions and a histological classification of atherosclerosis. A report from the Committee on Vascular

Lesions of the Council on Arteriosclerosis, American Heart Association. *Arterioscler. Thromb. Vasc. Biol.* **15,** 1512–1531 (1995).

117. Kolodgie, F. D. *et al.* Intraplaque hemorrhage and progression of coronary atheroma. *N. Engl. J. Med.* **349,** 2316–2325 (2003).

118. Stary, H. C. *et al.* A definition of initial, fatty streak, and intermediate lesions of atherosclerosis. A report from the Committee on Vascular Lesions of the Council on Arteriosclerosis, American Heart Association. *Circulation* **89,** 2462–2478 (1994).

119. Otsuka, F., Finn, A. V & Virmani, R. Do vulnerable and ruptured plaques hide in heavily calcified arteries? *Atherosclerosis* **229,** 34–37 (2013).

120. Naghavi, M. *et al.* From Vulnerable Plaque to Vulnerable Patient: A Call for New Definitions and Risk Assessment Strategies: Part II. *Circulation* **108,** 1772–1778 (2003).

121. Tearney, G. J., Jang, I.-K. & Bouma, B. E. Optical coherence tomography for imaging the vulnerable plaque. *Journal of Biomedical Optics* **11,** 021002 (2006).

122. Shekhonin, B. V, Domogatsky, S. P., Muzykantov, V. R., Idelson, G. L. & Rukosuev, V. S. Distribution of type I, III, IV and V collagen in normal and atherosclerotic human arterial wall: immunomorphological characteristics. *Coll. Relat. Res.* **5,** 355–68 (1985).

123. Schriefl, A. J., Reinisch, A. J., Sankaran, S., Pierce, D. M. & Holzapfel, G. A. Quantitative assessment of collagen fibre orientations from two-dimensional images of soft biological tissues. *J. R. Soc. Interface* **9,** 3081–93 (2012).

124. Schriefl, A. J., Zeindlinger, G., Pierce, D. M., Regitnig, P. & Holzapfel, G. A. Determination of the layer-specific distributed collagen fibre orientations in human thoracic and abdominal aortas and common iliac arteries. *J. R. Soc. Interface* **9,** 1275–86 (2012).

125. Krasny, W., Morin, C., Magoariec, H. & Avril, S. A comprehensive study of layer-specific morphological changes in the microstructure of carotid arteries under uniaxial load. *Acta Biomater.* **57,** 342–351 (2017).

126. Krasny, W., Magoariec, H., Morin, C. & Avril, S. Kinematics of collagen fibers in carotid arteries under tension-inflation loading. *J. Mech. Behav. Biomed. Mater.* **77,** 718–726 (2018).

127. Sugita, S. & Matsumoto, T. Multiphoton microscopy observations of 3D elastin and collagen fiber microstructure changes during pressurization in aortic media. *Biomech. Model. Mechanobiol.* **16,** 763–773 (2017).

128. Cavinato, C. *et al.* Biaxial loading of arterial tissues with 3D in situ observations of adventitia fibrous microstructure: A method coupling multi-photon confocal microscopy and bulge inflation test. *J. Mech. Behav. Biomed. Mater.* **74,** 488–498 (2017).

129. Virmani, R., Burke, A. P., Farb, A. & Kolodgie, F. D. Pathology of the Vulnerable Plaque. *J. Am. Coll. Cardiol.* **47,** C13–C18 (2006).

130. Holzapfel, G. A. & Ogden, R. W. Constitutive modelling of arteries. *Proc. R. Soc. A Math. Phys. Eng. Sci.* **466,** 1551–1597 (2010).

131. Cacho, F., Elbischger, P. J., Rodríguez, J. F., Doblaré, M. & Holzapfel, G. A. A constitutive model for fibrous tissues considering collagen fiber crimp. *Int. J. Non. Linear. Mech.* **42,** 391–402 (2007).

132. Taylor, C. A. & Humphrey, J. D. Open problems in computational vascular biomechanics: Hemodynamics and arterial wall mechanics. *Comput. Methods Appl. Mech. Eng.* **198,** 3514–3523 (2009).

133. Teng, Z. *et al.* The influence of constitutive law choice used to characterise atherosclerotic tissue material properties on computing stress values in human carotid plaques. *J. Biomech.* **48,** 3912–21 (2015).

134. Delfino, A., Stergiopulos, N., Moore, J. E. & Meister, J. J. Residual strain effects on the stress field in a thick wall finite element model of the human carotid bifurcation. *J. Biomech.* **30,** 777–86 (1997).

135. Chau, A. H. *et al.* Mechanical Analysis of Atherosclerotic Plaques Based on Optical Coherence Tomography. *Ann. Biomed. Eng.* **32,** 1494–1503 (2004).

136. Kaazempur-Mofrad, M. R. *et al.* Cyclic strain in human carotid bifurcation and its potential correlation to atherogenesis: Idealized and anatomically-realistic models. *J. Eng. Math.* **47,** 299–314 (2003).

137. Tang, D. *et al.* Correlations between carotid plaque progression and mechanical stresses change sign over time: a patient follow up study using MRI and 3D FSI models. *Biomed. Eng. Online* **12,** 105 (2013).

138. Tang, D. *et al.* Sites of rupture in human atherosclerotic carotid plaques are associated with high structural stresses: an in vivo MRI-based 3D fluid-structure interaction study. *Stroke* **40,** 3258–63 (2009).

139. Teng, Z. *et al.* How does juxtaluminal calcium affect critical mechanical conditions in carotid atherosclerotic plaque? An exploratory study. *IEEE Trans. Biomed. Eng.* **61,** 35–40 (2014).

140. Koh, C. T. & Oyen, M. L. Branching toughens fibrous networks. *J. Mech. Behav. Biomed. Mater.* **12,** 74–82 (2012).

141. Koh, C. T., Strange, D. G. T., Tonsomboon, K. & Oyen, M. L. Failure mechanisms in fibrous scaffolds. *Acta Biomater.* **9,** 7326–7334 (2013).

142. Koh, C. T. & Oyen, M. L. Toughening in electrospun fibrous scaffolds. *APL Mater.* **3,** 014908 (2015).

143. Koh, C. T. & Oyen, M. L. Fracture toughness of fibrous membranes. *Tech. Mech.* **32,** 333–341 (2012).

144. Koh, C. T., Low, C. Y. & Yusof, Y. Bin. Structure-property Relationship of Bio-Inspired Fibrous Materials. *Procedia Comput. Sci.* **76,** 411–416 (2015).

Chapter 2

Characterisation of diseased human aortic tissue mechanical and fracture behaviours

The author of this dissertation carried out all of the work and analysis in this chapter except as specified below. Collected diseased aortic tissue pieces were dissected into tissue strips of the three arterial layers and prepared for mechanical testing together with Shuo Wang from Department of Radiology, University of Cambridge. The crack tip curvature computation algorithm was also developed together with Shuo Wang. Diseased aortic tissue pieces were collected by Dr Priya Sastry from Department of Medicine, University of Cambridge. Part of the work described in this chapter has been submitted for publication as described in the **Publications** *section at the beginning of this dissertation.*

2.1 Abstract

Aortic aneurysms are amongst the leading vascular diseases claiming millions of lives every year. They cause dilatation of aorta, leading to pathological changes in its microstructure and resulting in ruptures and fatal clinical events. Although mechanical properties of the diseased human aorta, such as its nonlinear stress-strain behaviour and ultimate tensile strength have been measured, literature on its fracture properties does not yet exist. The objective of this study is to comprehensively investigate both mechanical and fracture behaviours of the diseased human aorta. Aneurysm-affected aorta regions were collected from eight patients and stored in liquid nitrogen. Tissue pieces were thawed prior to testing and tissue strips were cut from their intima, media and adventitia layers, along both the circumferential and the axial artery directions. Unnotched and notched uniaxial tensile tests were performed on all types of tissue strips. The obtained mechanical and fracture parameters were compared amongst distinct tissue types. In the case of unnotched tensile tests, the circumferential adventitia was found to have the highest material strength, while the intima and media layers were found to have similar ultimate material strengths in both axial and circumferential directions of the aorta. Media and adventitia layers were stronger in the circumferential than the axial direction (both with $p=0.02$). In the case of notched tissue strips, the material strength of the adventitia in both directions was higher than the strength of intima or media in any direction. Moreover, the failure point J-integral value of notched adventitia samples was found to be significantly larger than that of intima samples in both the axial ($p=0.047$) and circumferential ($p=0.038$) artery directions. Aneurysmal tissues were notch-insensitive as the strips with notches did not fail at a low stretch level.

2.2 Introduction

Thoracic aortic aneurysms (TAAs) represent an important cause of death due to vascular disease[1]. Most patients with TAA are asymptomatic at the time of diagnosis, because the aneurysms are usually discovered incidentally during echocardiography or CT, or on a routine chest X-ray. A mean rate of growth for all thoracic aneurysms was reported as 0.1 cm/year and varied with lesion location[2]. The annual rate of rupture or dissection in patients with aneurysms ≥6.0 cm is at least 7%, which is more than 25 times higher than those between 4.0 cm and 4.9 cm[2].

However, rupture or dissection also occur in lesions smaller than 6 cm^3. Careful radiological follow-up is therefore needed to identify those aneurysms that are under the threshold of surgical repair but with a rapid growth. In contrast, there is an urgent need to identify the factors and mechanisms that are associated with development and rupture of TAAs.

The pulsatile arterial blood pressure keeps the aortic aneurysms under continuous mechanical loading. The diseased artery will rupture if the applied loads can generate structural stresses that are larger than the mechanical strength of its wall[4,5]. Therefore, sufficiently accurate calculations of structural stress distribution within aortic aneurysms can provide valuable data that would be used to assess their critical mechanical conditions and vulnerability to rupture. In-vivo medical image-based mechanical modelling appeals as a very promising technique that could allow determination of patient-specific stress distributions within the aortic wall[4,6,7]. Nevertheless, calculation of reliable stress distributions requires accurate mechanical properties of the aneurysm-affected aortic wall. Moreover, adequately accurate computations of rupture behaviour also need information on fracture mechanics of diseased aortic tissue, so that reliable mathematical models can be developed for use in mechanical simulations.

Conventional material properties, such as the extreme extensibility and ultimate material strength of healthy[8–10] and aneurysmal[10–14] aortic tissues have been measured by a number of studies for distinct arterial layers, in both circumferential and axial directions of the aorta. However, a comprehensive investigation on both the mechanical and fracture behaviours of aneurysmal tissue does not yet exist. This study aims to explore the layer and direction-dependent mechanical, as well as fracture behaviours of TAAs by quantification and analysis of parameters from unnotched and notched uniaxial tensile tests.

2.3 Materials and methods

This section explains the steps of the uniaxial unnotched and notched tensile testing protocols that were used during the experiments. Descriptions of the mechanical data analysis tools and mathematical procedures are also provided.

2.3.1 Collection and preparation of tissues

Eight aortic aneurysmal and dissection tissue pieces (3 from ascending aorta, 4 from aortic arch and 1 from descending aorta; 3 were chronic dissections and 5 true aneurysms) were collected from 8 patients (one female; ages of 61.4±12.2 years), who underwent open aortic repair in Royal Papworth Hospital, NHS Foundation Trust, Cambridge, UK. The local ethics committee approved this study and informed consents were obtained from all patients. The patient data were anonymised, and each patient was assigned with a distinct code.

Upon collection from the patient, each arterial tissue piece was immediately stored in liquid nitrogen, where cryoprotectant (20% dimethylsulfoxide (DMSO) in 5% human albumin) solution added to a final concentration of 10% DMSO was utilised to minimise potential damage caused by freezing. Diseased aortic tissue pieces were transferred to Addenbrooke's Hospital, NHS Foundation Trust, Cambridge, UK for mechanical testing. The laboratory that hosted the mechanical tests is licenced under the Human Tissue Act for storage and use of human tissue for research.

The thickened intima, media and adventitia layers of each tissue piece were separated and cut into rectangular mechanical testing strips. Prior to separation into the three distinct arterial tissue layers, each tissue piece was immersed in phosphate buffered saline (PBS) and defrosted in a 37 °C tissue bath. The intact arterial rings were first cut open, flattened and then cut further into smaller sections with a scalpel, along with the other relatively large noncircular pieces, to allow easier separation of the three layers. The thickened intima, media and adventitia of each tissue section were then separated with tweezers and cut into rectangular tissue strips of ~1.5 mm width and ~15 mm length, along both the axial and the circumferential directions to the blood flow, as shown in Figure 2.1.

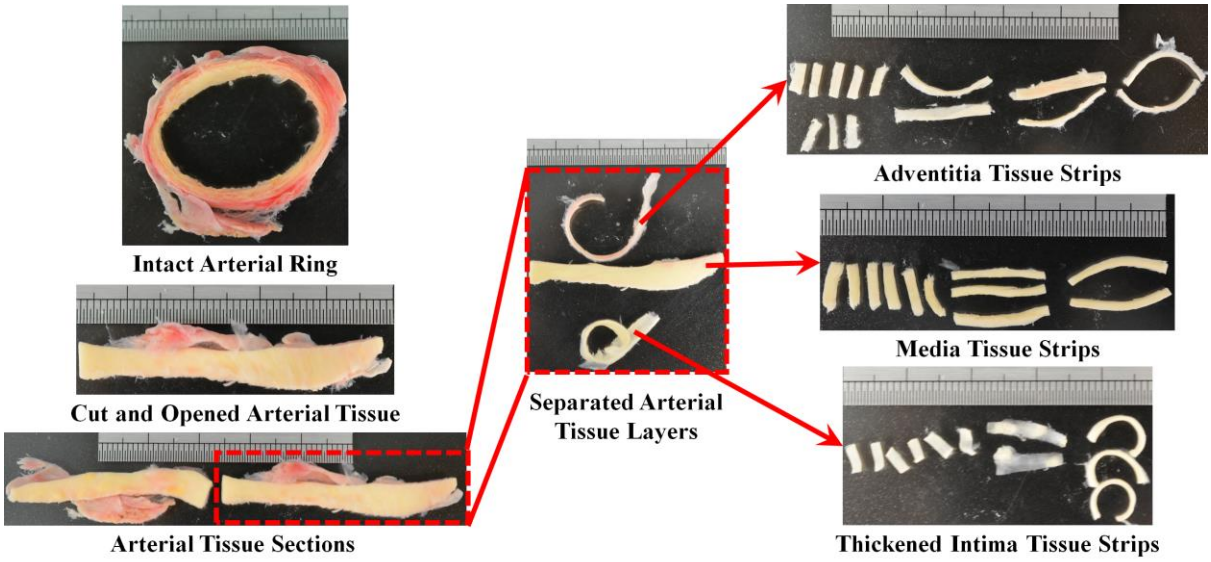

Figure 2.1. Dissection of an arterial tissue piece into separate sections and tissue strips of the three arterial layers.

2.3.2 Uniaxial unnotched and notched tensile testing

A uniaxial tensile testing system comprising a uniaxial stepper motor (Miniature Steel Motorised Linear Stage, Newport Corporation, Irvine, California, USA), a custom made linear load cell, a camera (PixeLink PL-B776U 3.1 MP USB2 Colour Camera, PixeLink, Ottawa, Canada) and a custom control interface that was developed in LabVIEW (National Instruments, Austin, Texas, USA) was built and programmed to perform the tensile tests. Parts of the mechanical tester are labelled on the image in Figure 2.2.

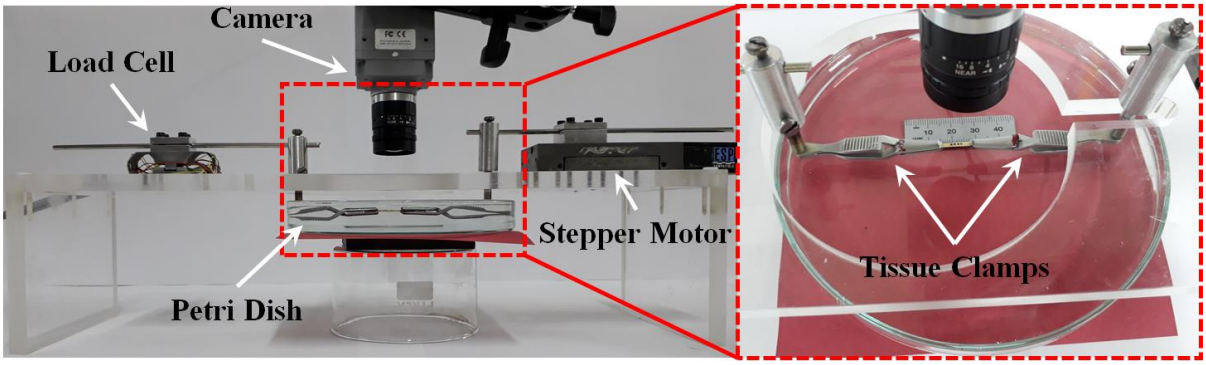

Figure 2.2. Parts of the uniaxial mechanical tester.

The position resolution of the stepper motor was 0.1 µm and the precision of the load cell was 0.0005 N. The developed custom LabVIEW control interface showing the camera view and force against motor displacement data is provided in Figure 2.3. The load cell was calibrated by hanging known weights on the load cell clamp. The load cell was regularly recalibrated to ensure that the voltage to force conversions were always accurate.

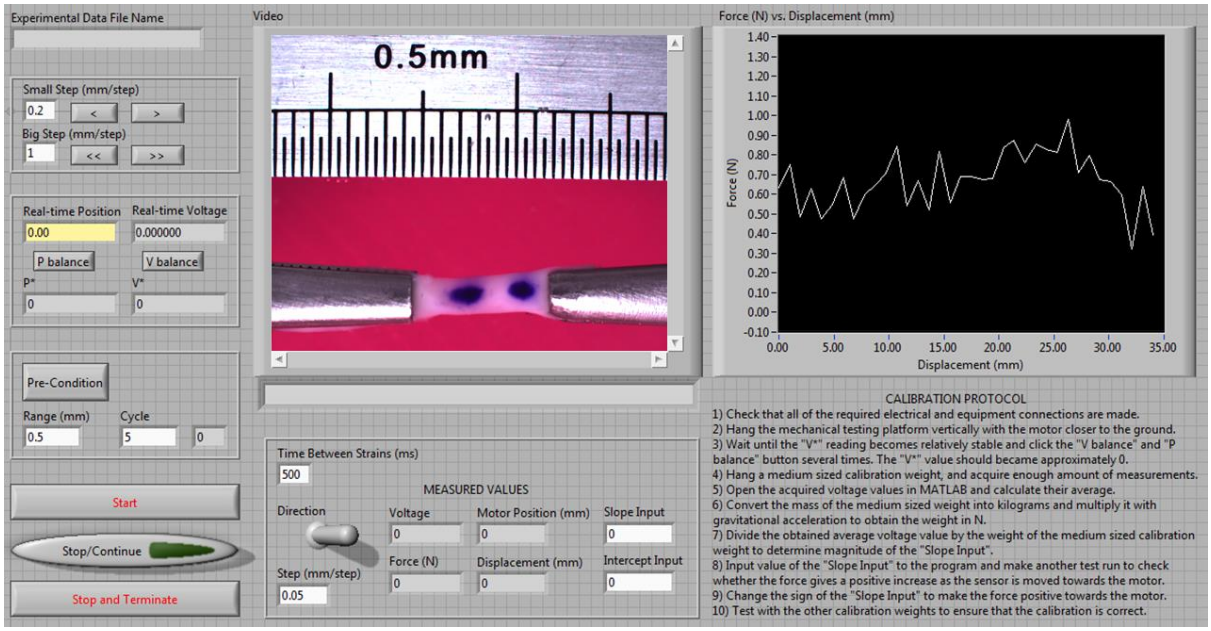

Figure 2.3. LabVIEW control interface showing the camera view and variation of force with motor displacement.

It can be seen in Figure 2.4 that the surface of each arterial tissue strip was marked at adjacent locations along its length with a water-proof dark blue surgical tissue marker, to be able to record the local deformation of the arteria tissue. Once clamped in a 37 °C PBS filled petri dish, each arterial tissue strip was preconditioned with 5 continuous cycles of ~5% stretch at a speed of 0.05 $mm.s^{-1}$ and then strained uniaxially until failure at a speed of 0.01 $mm.s^{-1}$. Therefore, the loading can be considered quasi-static. The camera was stabilised with a clamped arm, focused onto the tissue markers and set to acquire an image frame of the strained tissue at the end of each displacement increment of the stepper motor. The size of each image frame was 2048 x 1536 pixels, with an 80 x 60 mm^2 field of view.

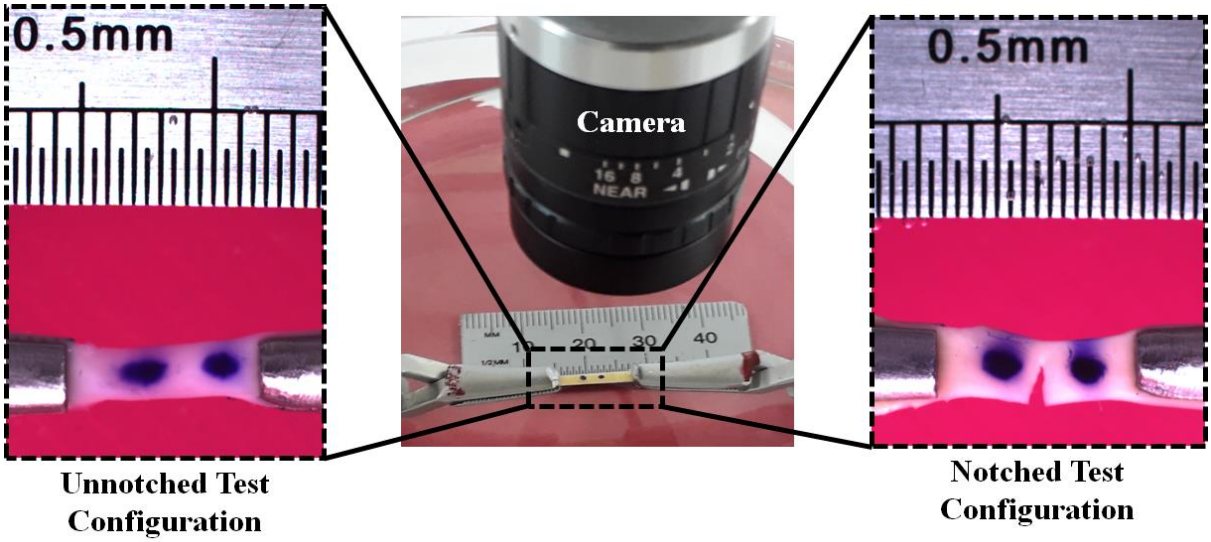

Figure 2.4. Surface marks of arterial tissue strips in uniaxial unnotched and notched test configurations.

The obtained axial and circumferential thickened intima, media and adventitia tissue strips were uniaxially tested with both unnotched and notched configurations. The notched tissue strips were generated by making an incision that was approximately one third of the tissue strip width, at the edge and in the middle of the gauge section with small surgical scissors. An example notched tissue strip can be seen in Figure 2.4.

2.3.3 Data processing

2.3.3.1 Calculation of unnotched tissue strip Cauchy stress

To compute the local displacements of each arterial tissue from the image frames acquired at the end of each stepper motor displacement, a semi-automatic MATLAB (MathWorks, Inc., Natick, Massachusetts, USA) platform was developed. The platform can segment the adjacent dark blue marker spots, determine their centroid coordinates and compute the separation distances between their centroids. A screenshot of the MATLAB platform in operation is given in Figure 2.5. A dark blue colour threshold and standard morphological image operations available in MATLAB (*imclearborder*, *imerode*, *imfill* and *imclose* functions of MATLAB) were utilised to generate marker spot binary masks from the acquired Red-Green-Blue (RGB) colour space images.

The marker spot centroid separations were converted into instantaneous stretch ratio, λ_i values at each displacement increment for use in the subsequent stages of data processing with the following equation[15]:

$$\lambda_i = \frac{s_i}{s_0} \tag{2.1}$$

where,

s_i = Separation of the marker spot centroids in each image frame

s_0 = Separation of the marker spot centroids in the first image frame, prior to extension

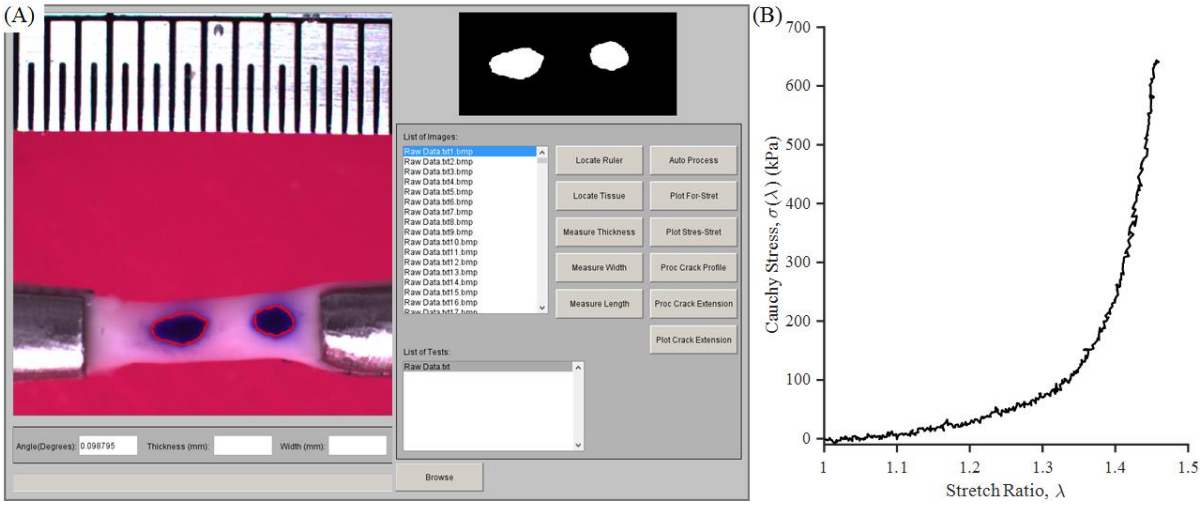

Figure 2.5. A: The semi-automatic MATLAB platform that was used to process the tensile testing image data. B: Cauchy stress versus stretch ratio curve of a tested tissues strip.

All uniaxially tested unnotched and notched arterial tissue strips were assumed to be incompressible. For the tissue strips that were tested in the unnotched configuration, the Cauchy stress, σ_i was determined as F_i/A_i, where F_i and A_i are the instantaneous force and instantaneous cross-sectional area values at each displacement increment, respectively. The value of A_i was evaluated through the incompressibility condition, which leads to $A_i = A_0/\lambda_i$, where A_0 and λ_i are the initial cross-sectional area and instantaneous stretch ratio (Equation 2.1), respectively[15]. The final form of the equation that was used to calculate the Cauchy stress, σ_i of unnotched tissue strips was obtained by substituting $A_i = A_0/\lambda_i$ into $\sigma_i = F_i/A_i$, which yielded:

$$\sigma_i = \frac{F_i \lambda_i}{A_0} \tag{2.2}$$

The initial cross-sectional area, A_0 was calculated by multiplying the width and thickness values of the tissue strip gauge sections at rest. The width and thickness values were measured from images that were acquired at rest with ruler calibration. Edge detections were performed in MATLAB to identify the tissue strip edges. The thickness and width of each tissue strip was determined as the average value of the distances between 100 pairs of closest points that were distributed evenly along each edge.

2.3.3.2 Calculation of notched tissue strip parameters

2.3.3.2.1 Average stress across the ligament

The presence of an externally induced edge crack required development of an image processing tool to be able to approximate the average stress within the ligament region of notched tissue strips. The MATLAB platform in Figure 2.5 was adapted with a tool that can measure the remaining width of the ligament region of each notched tissue strip from the image frames that were acquired at the end of each stepper motor displacement.

It can be seen in Figure 2.6 that, the adjacent dark blue marker spots were used in the same way as for the unnotched tissue strips to calculate the local tissue displacements, and therefore, the instantaneous stretch ratio, λ_i with Equation 2.1. A separate algorithm was also developed to compute the ligament widths of notched tissue strips in each consecutive image frame. The ligament width computation algorithm was set to use a red colour threshold to extract the top and bottom boundaries of the notched tissue strip from the RGB image. The ligament width was calculated as the closest distance between the extracted top and bottom tissue boundaries, which is depicted by the yellow line in Figure 2.6. The stretch ratio, λ_i and the ligament width, l_i were computed on all image frames of each notched tissue strip.

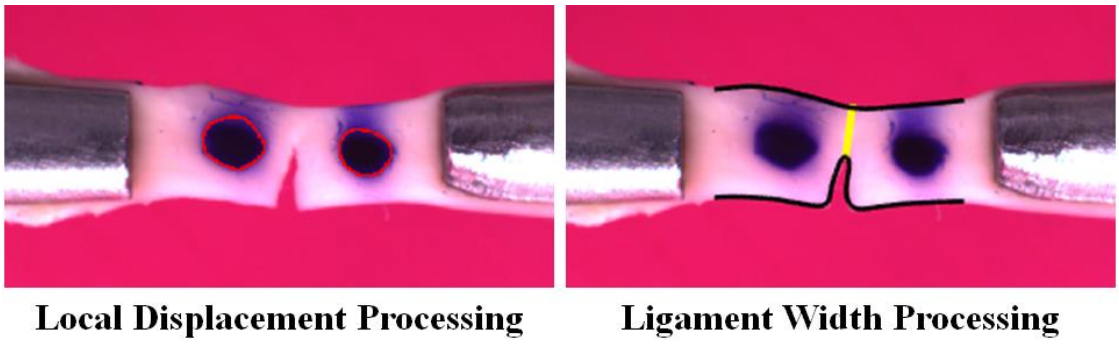

Figure 2.6. Local displacement and ligament width processing of a notched tissue strip.

The average stress across the ligament, σ_{L_i} was approximated as F_i/A_i^N, where F_i and A_i^N are the instantaneous force and the instantaneous notched tissue strip cross-sectional area, respectively. The value of A_i^N was determined as $w_i^N \times t_i^N$, where w_i^N and t_i^N are the instantaneous width and instantaneous thickness of each notched tissue strip, respectively. Since the instantaneous ligament width, l_i is equal to the actual load bearing width of each notched tissue strip, A_i^N can be calculated as $l_i \times t_i^N$. The incompressibility and isotropic material assumptions were then used to determine the instantaneous notched tissue strip thickness, t_i^N as $t_0/\sqrt{\lambda_i}$, where t_0 and λ_i are the initial tissue thickness that was measured from images acquired at rest and the instantaneous stretch ratio (Equation 2.1), respectively[15]. Final form of the equation that was used to approximate the average stress across the ligament, σ_{L_i} was then obtained by first substituting $t_i^N = t_0/\sqrt{\lambda_i}$ into $A_i^N = l_i \times t_i^N$ and then by substituting the resulting equation of A_i^N into $\sigma_{L_i} = F_i/A_i^N$, which yielded:

$$\sigma_{L_i} = \frac{F_i\sqrt{\lambda_i}}{l_i t_0} \tag{2.3}$$

2.3.3.2.2 J-integral

Toughness of the tested notched arterial tissue strips was quantified with the J-integral. This parameter is commonly used to quantify the strain energy release rate per unit fracture surface area of nonlinear elastic solids with cracks[15–17]. Under displacement control conditions, the magnitude of the instantaneous J-integral, J_i is given as $dU_i/(t_i^N \times da_i)$, where dU_i, t_i^N and da_i are the change in strain energy, instantaneous thickness and the change in crack length of a notched tissue strip[17]. The incompressibility and isotropic material assumptions were then used to express the instantaneous notched tissue strip thickness, t_i^N as $t_0/\sqrt{\lambda_i}$, where t_0 and λ_i are the initial tissue thickness that was measured from images acquired at rest and the instantaneous stretch ratio (Equation 2.1), respectively[15]. Therefore, the equation that was used to approximate the J-integral, J_i was obtained by substituting $t_i^N = t_0/\sqrt{\lambda_i}$ into $J_i = dU_i/(t_i^N \times da_i)$, which yielded:

$$J_i = \frac{\sqrt{\lambda_i}}{t_0}\frac{dU_i}{da_i} \tag{2.4}$$

The change in strain energy, dU_i was computed as the incremental change of the area under the stress-strain curves of notched tissue strips. In addition, the change in crack length, da_i was calculated as the incremental change of the ligament width, l_i values with strain.

2.3.3.2.3 Crack tip curvature

Bottom boundary of the notched tissue strips, which is depicted by the lower black line in the ligament width processing image of Figure 2.6, was also used to determine the crack tip curvature of the notched tissue strips in each image frame. A parabola was fitted to the lower tissue strip boundary coordinates lying within 400 μm neighbourhood of the crack tip. The crack tip curvature was then approximated as the curvature, c of the parabola at its vertex point. For a planar curve that is described by the equation $y = f(x)$, the curvature, c at any point is expressed in terms of its first and second derivatives as[18]:

$$c = \frac{|f''(x)|}{[1+(f'(x))^2]^{\frac{3}{2}}} \tag{2.5}$$

2.3.3.3 Rate of tissue strip failure

The rate of tissue strip failure was characterised as the slope, γ between the normalised intact tissue width and stretch ratio, λ_i for both unnotched and notched tissue strips. The relationship between the normalised intact tissue width and stretch ratio was formulated as:

$$\frac{d_i}{d_0} = \gamma(\lambda_i - 1) = \gamma\lambda_i - \gamma \tag{2.6}$$

where,

d_i = Intact tissue width at each stretch increment

d_0 = Intact tissue width prior to stretching

β = A constant

2.3.4 Statistical analysis

The Shapiro-Wilk normality test was performed on all sets of data, which revealed that the data sets were not normally distributed. Median and interquartile range of all mechanical and fracture properties were computed for different tissue types and provided in the form of: *median [25th percentile, 75th percentile]*, whenever necessary. Box-and-whisker plots were used to present the data, in which the central mark on the box indicates the median, and the bottom and top edges of the box indicate the 25th and 75th percentiles, respectively. Differences in mechanical and fracture properties between distinct tissue types were evaluated using the Wilcoxon signed rank test. Statistical analysis was performed in MATLAB. A significant difference was assumed if $p<0.05$.

2.4 Results

Mechanical data from 96 tissue strips of 8 aneurysm and dissection samples were prepared for analyses. This included 48 tissue strips from each of the unnotched and notched tensile testing groups. Each 48-tissue strip group consisted of two strips from each of the thickened intima, media and adventitia layers, where one of these strips was in the axial and the other one in the circumferential aorta direction of each sample.

2.4.1 Strength and extensibility of unnotched samples

In the case of unnotched samples, the Cauchy stress and stretch ratio values at the point of failure were taken as the ultimate material strength and extreme extensibility of each unnotched tissue strip, respectively. Tensile tests with unnotched tissue strips showed that the adventitia in the circumferential direction had the highest ultimate material strength, as it can be visualised in Figure 2.7A. The material strength of intima in the axial direction was similar to that of media in the same direction (395.9 [202.3, 567.2] vs 236.4 [213.3, 341.4], p=0.31; unit: kPa), and intima and media strengths were also similar in the circumferential direction (518.4 [249.5, 750.3] vs 606.5 [358.8, 708.2], p=0.84; unit: kPa). Within layers, the intima had similar material strengths in both directions (p=0.46), while the media and adventitia were stronger in the circumferential than the axial direction (both with p=0.02). In general, the extreme extensibilities of all layers in both directions were similar, except for the adventitia in the circumferential direction, which was more extendable than media in the same direction (1.33 [1.21, 1.54] vs 1.16 [1.14, 1.33], p=0.02), as it can be visualised in Figure 2.7B.

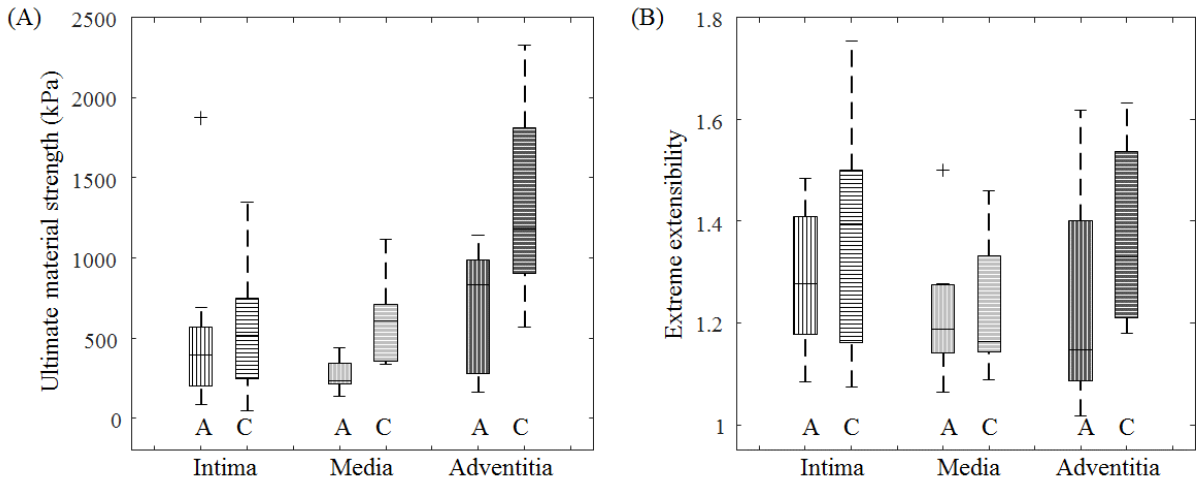

Figure 2.7. Ultimate material strength (A) and extreme extensibility (B) of unnotched tissue strips. Letters A and C at the bottom of the box-and-whisker plots indicate circumferential and axial aorta directions, respectively.

2.4.2 Nominal strength and extensibility of notched samples

In the case of notched samples, the average stress across the ligament and stretch ratio values at the point of failure were taken as the nominal ultimate material strength and extreme extensibility of each notched tissues strip, respectively. It can be visualised in Figure 2.8A that, as for the unnotched tissue strips, the nominal ultimate material strength of the adventitia in both directions was higher than the strength of intima or media in any direction ($p<0.05$). However, for each arterial layer, the strength difference between directions was not significant ($p>0.35$). The notched adventitia tissue strips in the axial direction were more extensible than intima or media in the same direction ($p<0.02$), with no significant difference in any other paired comparison of Figure 2.8B.

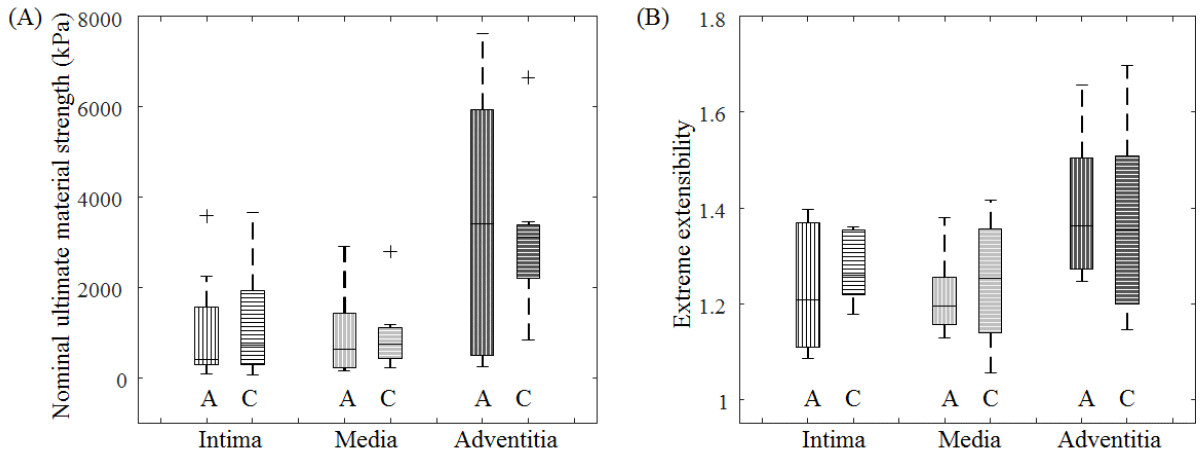

Figure 2.8. Nominal ultimate material strength (A) and extreme extensibility (B) of notched tissue strips. Letters A and C at the bottom of the box-and-whisker plots indicate circumferential and axial aorta directions, respectively.

2.4.3 Impact of notch on the failure rate of the tissue

The rate of tissue strip failure was characterised with the slope, γ between the normalised intact tissue width and stretch ratio, which was determined by Equation 2.6. The decrease in normalised intact tissue width with increasing stretch ratio is given for representative unnotched and notched tissue strips in Figure 2.9C. The absolute value of slope, γ of each tissue type is provided in Figure 2.9D, in which the left and right positioned box-and-whiskers in each arterial direction correspond to the unnotched and notched tissue strips, respectively. The absolute value of slope, γ of notched tissue strips from the intima and media layers was found to be significantly larger than their unnotched counterparts, nevertheless, the notched tissue strips did not fail at a low stretch level, which is also evident from the representative example in Figure 2.9B. Surprisingly, Figure 2.9D also illustrates that insignificant differences were obtained between the absolute slope values of notched and unnotched pairs from the adventitia layer in both of the axial and circumferential artery directions.

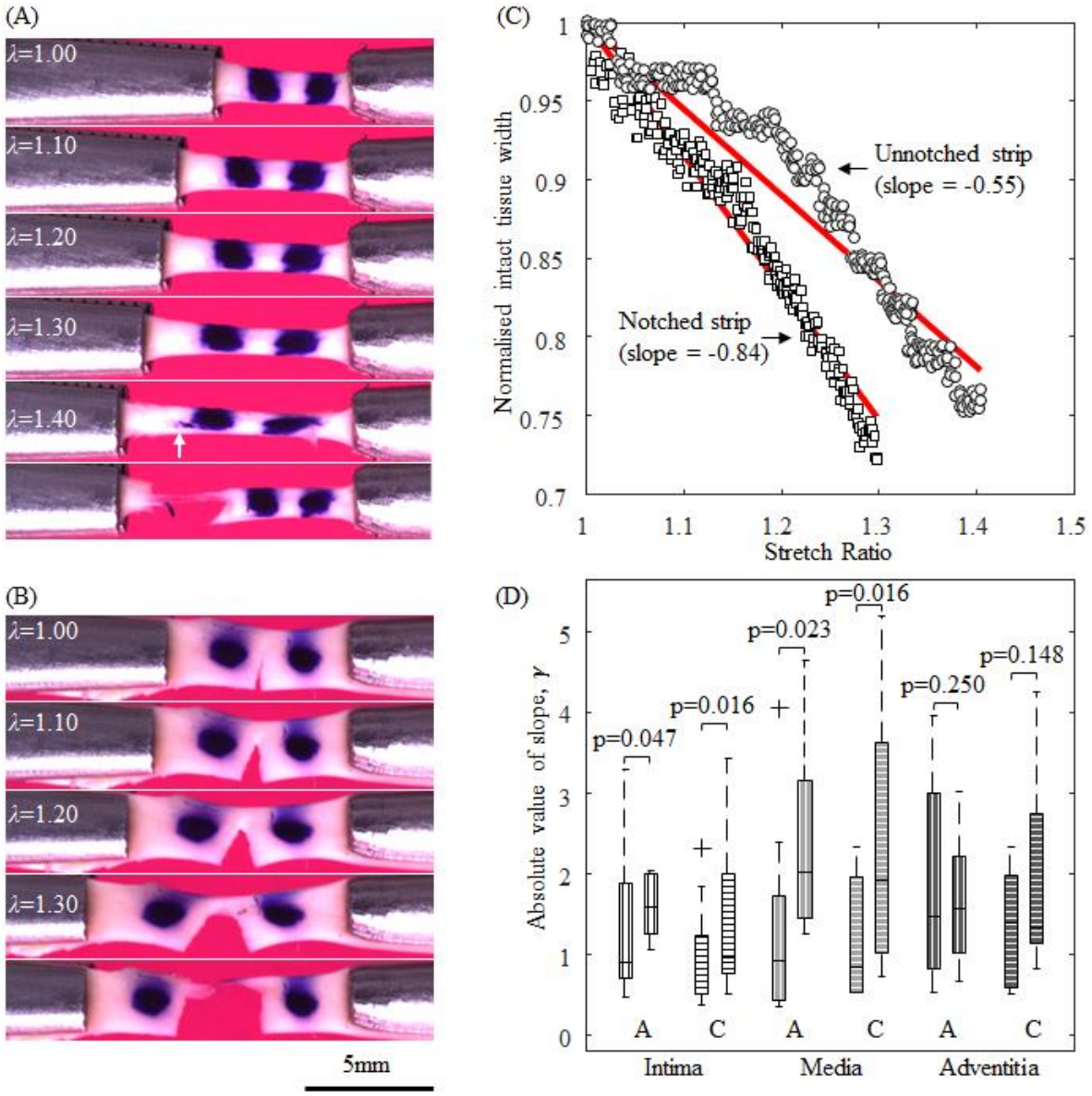

Figure 2.9. Representative unnotched (A) and notched (B) tissue strips under stretching. The linear regressions between normalised intact tissue width and stretch ratio (C) and the comparison of regression slopes between unnotched and notched tissue strips of different tissue types (D). Letters A and C at the bottom of the box-and-whisker plot indicate circumferential and axial aorta directions, respectively. In each pair in D, the left box-and-whisker is from unnotched and the right one is from notched tissue strips.

2.4.4 J-integral at failure of notched samples

J-integral values at the point of failure were recorded for notched tissues strips from all layers and directions, which are illustrated in Figure 2.10. The failure point J-integral value of adventitia samples was found to be significantly larger than that of intima samples in both the axial (2.7 [0.89, 3.8] vs 0.45 [0.32, 0.96], p=0.047; unit: $mJ.mm^{-2}$) and circumferential (1.9 [1.1, 3.9] vs 0.93 [0.74, 1.4], p=0.038; unit: $mJ.mm^{-2}$) artery directions. On the other hand, the failure point J-integral values of media samples in both axial (0.88 [0.25, 1.1]; unit: $mJ.mm^{-2}$) and circumferential (1.4 [0.77, 2.2]; unit: $mJ.mm^{-2}$) directions were found to be similar to their intima and adventitia counterparts.

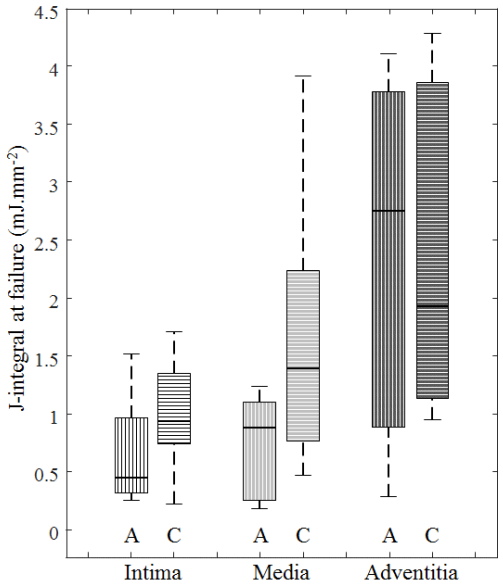

Figure 2.10. J-integral at failure of notched tissue strips. Letters A and C at the bottom of the box-and-whisker plot indicate circumferential and axial aorta directions, respectively.

2.4.5 Crack tip curvature at failure of notched samples

Crack tip curvature values were also recorded at the point of failure for notched tissue strips from all layers and directions, which are illustrated in Figure 2.11. The failure point crack tip curvature of media samples in the axial direction was found to be significantly larger than their axial adventitia counterparts (0.0029 [0.0021, 0.0068] vs 0.0016 [0.0012, 0.0021], p=0.021; unit: μm^{-1}) and this was the only significant difference that was obtained from all comparisons.

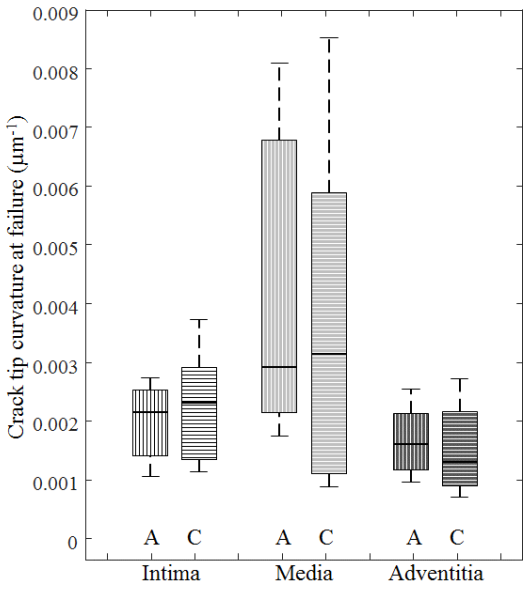

Figure 2.11. Crack tip curvature at failure of notched tissue strips. Letters A and C at the bottom of the box-and-whisker plot indicate circumferential and axial aorta directions, respectively.

2.5 Discussion

This study comprehensively characterised mechanical and fracture behaviour of arterial layers from aneurysm-affected aortas by tensile tests on their unnotched and notched tissue strips. In the case of unnotched tissue strips, the circumferential adventitia layer was found to have the highest ultimate material strength (Figure 2.7A), while the intima and media layers were found to have similar ultimate material strengths in both axial and circumferential directions. Moreover, within layers, the material strength of intima was found to be similar in the axial and circumferential directions, where both media and adventitia layers were stronger in the circumferential than the axial direction. These differences in material strength can be attributed to the fact that development of aortic aneurysms initiates from the intima layer and subsequently progresses into the media and the adventitia[19–21]. Since the pathophysiological process causes the highest level of detrimental microstructural changes within the intima, the healthy anisotropic material behaviour and consequently, the difference in the axial and circumferential direction material strengths of the intima is diminished.

On the other hand, since the media and adventitia layers are less affected by disease compared to the intima, they were able to preserve their healthy mechanical behaviours at a greater extent.

In the case of notched tissue strips, the nominal ultimate material strength of the adventitia in both directions was higher than the strength of intima or media in any direction (Figure 2.8A). Introduction of a structural defect has put the toughening mechanisms in each arterial layer to the test and revealed their capability of resisting propagation of a crack to maintain structural integrity. It is evident that the adventitia layer, which was least affected by disease, has preserved its natural toughening mechanisms, achieving much higher levels of nominal ultimate material strength compared to the intima and the media. As it can be seen in Figure 2.10, the relatively higher values of failure point J-integral that were obtained from the adventitia layer also supports the fact that the adventitia has preserved its natural toughening mechanisms to a greater extent, compared to the intima and the media.

The strength of materials is generally reduced in the presence of notches, especially for brittle materials. The notched tests in this study showed that the aneurysmal tissues tend to be notch-insensitive as they did not fail at a low stretch level. This might be because aneurysmal tissues are fibre-reinforced laminal materials with a distinct microstructure[22]. Nevertheless, it can be seen in Figure 2.9 that the presence of a notch has in general increased the rate at which the tissue strips reached failure.

It can be visualised in Figure 2.9B that, during stretching, the crack tip blunted to spread the damage in the ligament. Also, the fibres changed their network topology to bridge the crack tip to strengthen the material, in order to improve the load bearing capacity. The degree of crack tip blunting, measured by the crack tip curvature (Figure 2.11), showed little difference among different arterial layers. The notch-insensitive behaviour and weaker material strength between the lamellae (~150 kPa)[23,24] compared with the strength across the lamella[10] may explain the observation that the dissection entries are usually small and circumscribed and delamination propagates along the artery[20].

Some limitations also exist in this study: (1) the sample size is small (tissues from only 8 patients were collected and tested); (2) although uniaxial extension tests were performed in both circumferential and axial directions, biaxial tensile tests are required to obtain a complete understanding of the anisotropic tissue mechanics; (3) no controls were provided for comparison, e.g., the mechanical properties of healthy aortic tissues.

2.6 Conclusion

This study shows that, compared to the intima and the media layers, the pathophysiological changes that affect the arterial wall may have caused a lower degree of microstructural change to the adventitia, which has preserved the integrity of its fibrous network and therefore, retained its natural toughening mechanisms. Moreover, all aneurysm-affected arterial layers were largely able to blunt the tip of propagating cracks and hence show notch-insensitivity. Sufficiently accurate determination of aneurysm-affected aortic tissue mechanical and fracture behaviour is critical for the development of reliable mathematical models that can be used both for obtaining further understanding on diseased aortic tissue mechanics, and for optimisation of mechanical analysis systems that can assess the risk of aortic tissue rupture.

2.7 References

1. Stein, L. H. & Elefteriades, J. A. in *Thoraco-Abdominal Aorta: Surgical and Anesthetic Management* (eds. Chiesa, R., Melissano, G. & Zangrillo, A.) 25–32 (Springer Milan, 2011). doi:10.1007/978-88-470-1857-0_3

2. Davies, R. R. *et al.* Yearly rupture or dissection rates for thoracic aortic aneurysms: simple prediction based on size. *Ann. Thorac. Surg.* **73,** 17-27; discussion 27–8 (2002).

3. Elefteriades, J. A. & Farkas, E. A. Thoracic aortic aneurysm clinically pertinent controversies and uncertainties. *J. Am. Coll. Cardiol.* **55,** 841–57 (2010).

4. Vorp, D. A. & Vande Geest, J. P. Biomechanical determinants of abdominal aortic aneurysm rupture. *Arterioscler. Thromb. Vasc. Biol.* **25,** 1558–66 (2005).

5. Hall, A. J., Busse, E. F., McCarville, D. J. & Burgess, J. J. Aortic wall tension as a predictive factor for abdominal aortic aneurysm rupture: improving the selection of patients for abdominal aortic aneurysm repair. *Ann. Vasc. Surg.* **14,** 152–7 (2000).

6. Borghi, A., Wood, N. B., Mohiaddin, R. H. & Xu, X. Y. Fluid–solid interaction simulation of flow and stress pattern in thoracoabdominal aneurysms: A patient-specific study. *J. Fluids Struct.* **24,** 270–280 (2008).

7. Martufi, G. & Christian Gasser, T. Review: The Role of Biomechanical Modeling in the Rupture Risk Assessment for Abdominal Aortic Aneurysms. *J. Biomech. Eng.* **135,**

021010 (2013).

8. Mohan, D. & Melvin, J. W. Failure properties of passive human aortic tissue. II--Biaxial tension tests. *J. Biomech.* **16,** 31–44 (1983).

9. Mohan, D. & Melvin, J. W. Failure properties of passive human aortic tissue. I--uniaxial tension tests. *J. Biomech.* **15,** 887–902 (1982).

10. Teng, Z. *et al.* Layer- and Direction-Specific Material Properties, Extreme Extensibility and Ultimate Material Strength of Human Abdominal Aorta and Aneurysm: A Uniaxial Extension Study. *Ann. Biomed. Eng.* (2015). doi:10.1007/s10439-015-1323-6

11. Vorp, D. A. *et al.* Effect of aneurysm on the tensile strength and biomechanical behavior of the ascending thoracic aorta. *Ann. Thorac. Surg.* **75,** 1210–4 (2003).

12. Romo, A., Badel, P., Duprey, A., Favre, J.-P. & Avril, S. In vitro analysis of localized aneurysm rupture. *J. Biomech.* **47,** 607–16 (2014).

13. García-Herrera, C. M. *et al.* Mechanical behaviour and rupture of normal and pathological human ascending aortic wall. *Med. Biol. Eng. Comput.* **50,** 559–66 (2012).

14. Forsell, C., Björck, H. M., Eriksson, P., Franco-Cereceda, A. & Gasser, T. C. Biomechanical properties of the thoracic aneurysmal wall: differences between bicuspid aortic valve and tricuspid aortic valve patients. *Ann. Thorac. Surg.* **98,** 65–71 (2014).

15. Pruitt, L. A. & Chakravartula, A. M. *Mechanics of Biomaterials: Fundamental Principles for Implant Design*. *Cambridge Texts in Biomedical Engineering* (Cambridge University Press, 2011). doi:10.1017/CBO9780511977923

16. Rice, J. R. A Path Independent Integral and the Approximate Analysis of Strain Concentration by Notches and Cracks. *J. Appl. Mech.* **35,** 379 (1968).

17. Zhu, X.-K. & Joyce, J. a. Review of fracture toughness (G, K, J, CTOD, CTOA) testing and standardization. *Eng. Fract. Mech.* **85,** 1–46 (2012).

18. Finney, R. L. *Calculus: Graphical, Numerical, Algebraic*. (Prentice Hall, 2012). at <https://books.google.co.uk/books?id=-5dTewAACAAJ>

19. Baumann, F., Makaloski, V. & Diehm, N. Aortic aneurysms and aortic dissection:

epidemiology, pathophysiology and diagnostics. *Internist (Berl).* **54,** 535–42 (2013).

20. Isselbacher, E. M. in *Essential Cardiology: Principles and Practice* (ed. Rosendorff, C.) 681–690 (Humana Press, 2006). doi:10.1007/978-1-59259-918-9_37

21. Anand, A. & Xiu, P. *Pathology*. (Elsevier, 2012).

22. Schriefl, A. J., Zeindlinger, G., Pierce, D. M., Regitnig, P. & Holzapfel, G. A. Determination of the layer-specific distributed collagen fibre orientations in human thoracic and abdominal aortas and common iliac arteries. *J. R. Soc. Interface* **9,** 1275–86 (2012).

23. Tong, J., Sommer, G., Regitnig, P. & Holzapfel, G. A. Dissection properties and mechanical strength of tissue components in human carotid bifurcations. *Ann. Biomed. Eng.* **39,** 1703–19 (2011).

24. Sommer, G., Gasser, T. C., Regitnig, P., Auer, M. & Holzapfel, G. A. Dissection properties of the human aortic media: an experimental study. *J. Biomech. Eng.* **130,** 021007 (2008).

Chapter 3

Influence of microstructure on mechanical and fracture behaviours of diseased human aortic tissue

The author of this dissertation carried out all of the work and analysis in this chapter except as specified below. The histological image processing MATLAB platform was developed together with Shuo Wang from Department of Radiology, University of Cambridge. Diseased aortic tissue pieces were collected by Dr Priya Sastry from Department of Medicine, University of Cambridge. Optimisation of each immunohistochemistry protocol for paraffin embedded tissues and histological staining of the arterial tissue strips were performed by Nichola Figg from Department of Medicine, University of Cambridge. The work described in this chapter has been submitted for publication as described in the **Publications** *section at the beginning of this dissertation.*

3.1 Abstract

Fibre structure and pathological features, such as inflammatory burden and GAG deposition, are the primary determinants of aortic tissue mechanical properties which are associated with the development of aneurysm and dissection. Such structure-mechanics relationships have not yet been comprehensively studied. Histopathological examination was performed on the mechanically tested diseased human aortic tissues described in **Chapter 2**. Area ratios of collagen, elastin, macrophage and GAGs and collagen fibre dispersion were quantified. Associations between these parameters and mechanical properties were investigated. Collagen, elastin and GAGs were layer-dependent and the inflammatory burden in all layers was low. The local GAG ratio was negatively associated with the collagen ratio (r^2=0.173, $p<0.05$) but positively associated with elastin (r^2=0.037, $p<0.05$). Higher GAG deposition resulted in larger local collagen fibre dispersion in the media and adventitia, but not in the intima. The extreme extensibility of unnotched strips in both axial and circumferential directions was exclusively associated with elastin ratio. Collagen and GAG contents were both associated with ultimate strength in the circumferential direction, but not with the strength in the axial direction. Similar findings were found from tests with notched tissue strips, in that both collagen and GAGs but not elastin or macrophages were associated with tissue strength.

3.2 Introduction

TAAs are primarily associated with cystic medial degeneration, which may occur as part of the normal aging process, but may be accelerated by other conditions including hypertension, bicuspid aortic valve aortopathy and genetic alterations. The degeneration is typically characterised by deposition of proteoglycans in the aortic wall with fragmentation and loss of elastic laminae[1]. GAGs are long unbranched polysaccharides consisting of a repeating disaccharide, comprising an amino sugar, uronic acid sugar or galactose side chains, attached to proteins through O-glycosidic linkage. Although GAGs constitute a minor component of vascular tissue (2-5% by dry weight), they are important because of their diverse functionality and role in pathological processes. GAGs interact with lipoproteins, including low-density lipoprotein that might contribute to both extracellular and intracellular lipid accumulation in the arterial wall[2,3].

Under physiological conditions, the arterial wall is subject to mechanical loading due to dynamic blood pressure and flow. Such mechanical loading may modulate the biological functions of endothelium[4] and smooth muscle cells[5] within the arterial wall. Moreover, the degenerated aortic wall may be weak and prone to rupture or dissection driven by mechanical loading. There is therefore a need to understand the material strength of TAA and any association with its detailed compositional features. Elastin and collagen fibres are two well-known major load-bearing ECM components of the arterial wall. Studies on mechanical properties of arterial ECM generally focus on collagen and elastin, with GAGs often being neglected. Although GAGs are a minor ECM component, they may play an important role in the development of dissection[6] as high stress concentrations induced by the GAG aggregation may lead to arterial delamination[7]. In addition, removal of GAGs results in an earlier recruitment of elastin and collagen fibres in porcine thoracic aortas, leading to an earlier transition point of nonlinear stress-strain curves[8].

In this study, histopathological examination was performed on the TAA tissues, whose mechanical and fracture behaviours were characterised with the study described in **Chapter 2**. Collagen, elastin, macrophage and GAG contents, as well as the collagen fibre architectures of the mechanically tested arterial tissue strips were quantified. Statistical analyses were performed to explore the correlation between tissue mechanical and fracture properties and their detailed microstructural composition comprehensively for the first time.

3.3 Materials and methods

This section will explain the histological processing that was performed on the diseased human aortic tissues of **Chapter 2**, as well as the subsequent analysis that was aimed at identifying the influence of diseased tissue microstructural components on mechanical and fracture behaviours.

3.3.1 Immunohistochemical staining

As described in **Chapter 2**, during dissection of each aortic tissue piece into mechanical testing strips of the three arterial layers, multiple adjacent tissue strips were generated from intima, media and adventitia, along both axial and circumferential directions of the aorta.

Following mechanical testing of each arterial tissue strip, one adjacent and untested tissue strip was put into a storage vial and immersed with 10% neutral buffered formalin (NBF), refrigerated for about 24 hours and transferred to histological processing within the same laboratory. Since the microstructure of a tested tissue strip is expected to be highly disrupted and different from its untested state, an adjacent untested tissue strip was used in histological processing, to obtain the correct microstructural data.

After refrigeration in NBF, the arterial tissue strips were embedded in paraffin wax, cut into 4 μm thick slices and immunohistochemically stained to quantify collagen, elastin, GAGs and macrophages within their microstructures. The axial and circumferential intima, media and adventitia tissue strips were dissected into 4 μm thick slices parallel to the plane that lies along their lengths and through their elastic laminae. The dissection plane, which lies along the length and through elastic laminae of each tissue strip is illustrated in Figure 3.1.

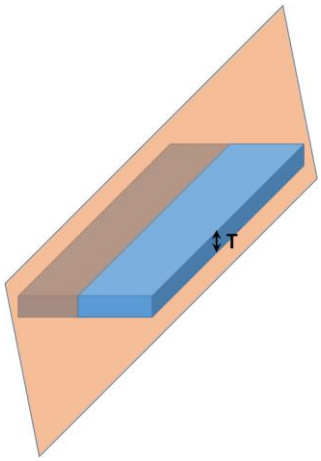

Figure 3.1. Orientation of the tissue strip dissection plane, where T refers to tissue thickness.

The obtained slices were immunohistochemically stained with Sirius Red, Elastin Van Gieson (EVG), Alcian Blue and Cluster of Differentiation 68 (CD68) stains to visualise collagen, elastin, GAGs and macrophages, respectively. Hematoxylin and Eosin (H&E) staining was also performed as part of the standard histological processing protocol. Stained arterial tissue microscope slides were then digitised at the magnification ratio of 40 into 904 nm resolution RGB images with the NanoZoomer Slide Imaging System (Hamamatsu, Hamamatsu City, Japan) at the Department of Physiology, University of Cambridge, Cambridge, UK. Digitised histological images of distinctly stained slices from an arterial tissue strip are provided as examples in Figure 3.2.

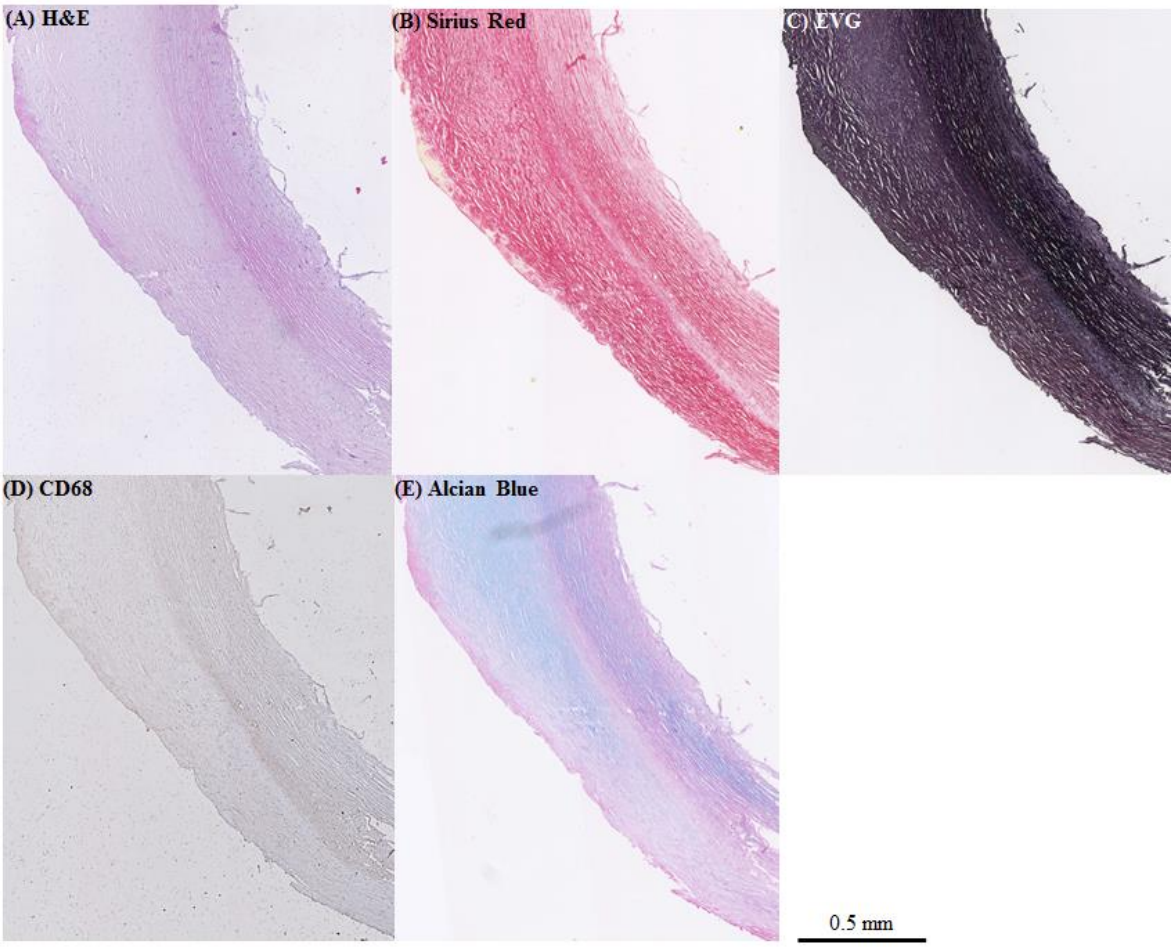

Figure 3.2. Digitised histological images of distinctly stained slices from an arterial tissue strip (A: H&E for an overall assessment; B: Sirius Red showing collagen fibres (Adapted with permission from[9]); C: EVG stain showing elastin; D: CD68 stain for macrophages; and E: Alcian blue stain for GAGs).

3.3.2 Computation of microstructural parameters

This section describes the tools that were developed to compute the densities of all targeted microstructural components, as well as the local directions and dispersions of collagen fibre orientations from the digitised histological images of arterial tissue strips.

3.3.2.1 Microstructural component densities

A semi-automatic MATLAB platform was developed to compute the densities of all microstructural components, where a screenshot of the developed platform is provided in Figure 3.3.

The example Sirius Red stained tissue histological image in Figure 3.2, which allows differentiation of collagen from the surrounding microstructural components, will be used to describe the algorithm that was developed to identify the targeted microstructural component pixels in images of all types of immunohistochemical stains. Upon initiation, the component pixel identification algorithm prompts the user to delineate the outer borders of all tissue pixels on the original RGB image. This is followed by removal of all pixels outside the delineated tissue pixel borders and subsequent transformation of the original RGB image into the LAB colour space.

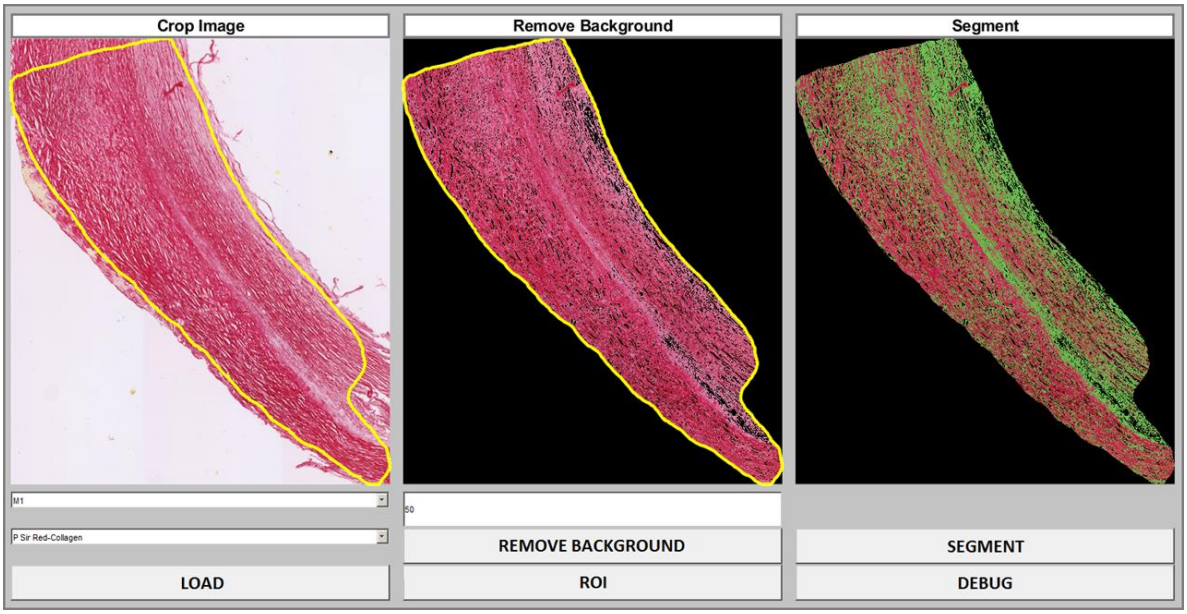

Figure 3.3. The semi-automatic MATLAB platform that was used to compute the densities of all microstructural components (Adapted with permission from[9]).

The outer pixels masked version of the example Sirius Red stained tissue image, as well as the L, A and B dimension images of the resulting LAB colour space transform can be visualised in Figure 3.4.

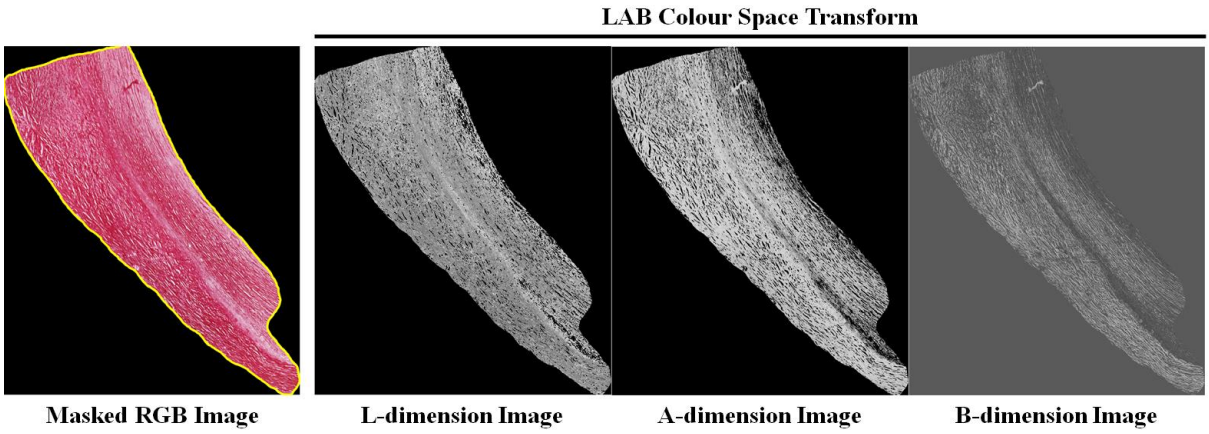

Figure 3.4. The outer pixels masked version of the example Sirius Red stained tissue image, as well as the L, A and B dimension images of the resulting LAB colour space transform (Adapted with permission from[9]).

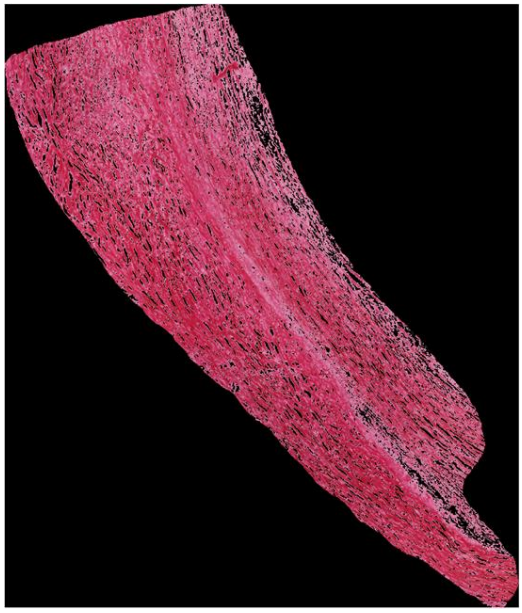

Figure 3.5. The example Sirius Red stained tissue image with the background removed (Adapted with permission from[9]).

The next algorithm step involves application of *Otsu's method* with the *multithresh* function of MATLAB on the L-dimension of the LAB colour space image, to obtain a single threshold that can separate the foreground pixels from those of the lightly coloured and mostly white background[10,11]. Since the L-dimension represents the lightness of a colour with darkest black at 0 and lightest white at 100, Otsu's method was able to find an adequate threshold to remove the background pixels in images of all immunohistochemical stain types. The background-removed version of the example Sirius Red stained tissue image, in which both the background pixels within the tissue region and the outer tissue-region pixels are coloured black can be visualised in Figure 3.5.

Otsu's method starts determination of the required threshold by computing the lightness level histogram and probabilities of the input L-dimension pixel values. The mean pixel lightness value of L-dimension is then used to separate the pixels into initial foreground and background groups. The obtained initial groups are then used to compute the initial means and inter-group variances of foreground and background pixels. Afterwards, the Otsu's method applies all of the remaining possible threshold values and compares the resulting intra-group variances of each pixel group with the corresponding values that were obtained by application of other thresholds. The threshold value that yields the minimum intra-group variance for both foreground and background pixel groups is selected to be the output threshold, which is used to remove the background pixels within the tissue strip region of each histological image[10,11].

Once all background pixels within the tissue strip region are removed, the resulting image is used to differentiate the targeted microstructural component pixels from the rest. In the case of the background removed Sirius Red image in Figure 3.5, the targeted microstructural component is collagen, which is coloured to the darker shades of red in a Sirius Red stained histological tissue. It is evident in the background removed image of Figure 3.5 that the Sirius Red stained tissue has entities that are coloured to both light and dark shades of the red colour.

To differentiate between the pixels with darker and lighter shades of red, another colour threshold was chosen by applying the Otsu's method on the A-dimension pixel values of the LAB colour space image, which represent the green-red colour components of each pixel.

The determined threshold was then used to separate the pixels with darker shades of red from the pixels that have a lighter red colour, effectively differentiating the darker red coloured collagen fibres from the other entities within the tissue strip region. The resulting Sirius Red stained tissue image, whose collagen fibre pixels have been differentiated from the rest is provided in Figure 3.6.

The thresholds for segmenting collagen from Sirius Red and GAGs from Alcian Blue stained tissue images were chosen by applying the Otsu's method on the A-dimension pixel values of the LAB colour space image. On the other hand, the thresholds for segmenting elastin from EVG and macrophages from CD68 stained tissue images were chosen by applying the Otsu's method on the red and green channels of their RGB images, respectively.

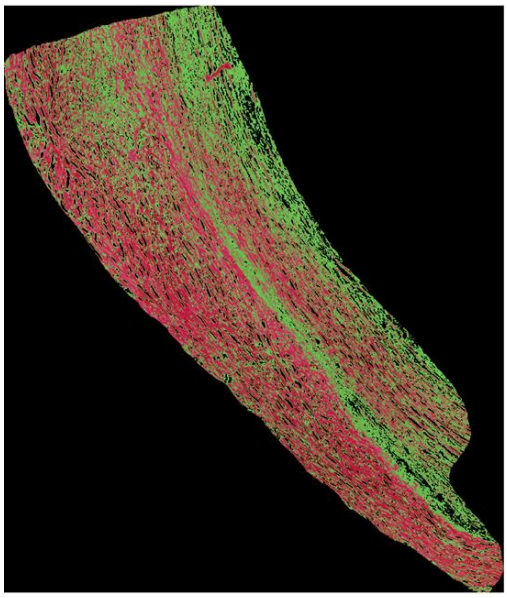

Figure 3.6. The collagen segmented version of the Sirius Red stained tissue image. The natural red colour of collagen fibre pixels is kept, while the background and foreground pixels that does not contain collagen fibres are coloured to black and green, respectively (Adapted with permission from[9]).

The component segmented images of all immunohistochemical stain types were continuously reviewed during development and optimisation of the image processing platform by Nichola Figg from the Department of Medicine, University of Cambridge, who is a senior histologist with over 15 years of experience in histological analysis of diseased arterial tissues.

Once the pixels of a targeted microstructural component were differentiated from the rest within the tissue strip region of a histological image, percentage area (area ratio) of the microstructural component was computed as:

$$Percentage\ Area = \frac{Number\ of\ Microstructural\ Component\ Pixels}{Total\ Number\ of\ Pixels\ in\ the\ Tissue\ Region} \times 100 \qquad (3.1)$$

3.3.2.2 Dispersions of collagen fibre orientations

Based on the segmentation results from Sirius Red stained images, local dispersions of collagen fibre orientations were computed. To accommodate the heterogeneous distribution of collagen fibres, 200 square patches with 0.18 mm (200 pixels) length were independently and randomly sampled in the tissue region. For each square patch, disconnected collagen fibres were recognized from the segmented mask and their orientation dispersion was computed as the *standard deviation* of all collagen fibre orientations within the patch.

3.3.3 Statistical analysis

Correlations between percentages of microstructural constituents (collagen, elastin, GAGs and macrophages) and the mechanical, as well as fracture properties were evaluated using a linear model with consideration of random effect using a least-squares fit. For each estimated coefficient, the coefficient of determination (r^2) and the corresponding p-value for t-statistic were reported. Differences in microstructural constituent percentages between different tissue types were evaluated using the Wilcoxon signed rank test. Statistical analysis was performed in MATLAB. A significant difference was assumed if $p<0.05$.

One of the microstructural aspects that was investigated in this study was the association between local GAG deposition and local collagen fibre architecture. Investigation of this aspect involved statistical analysis with multiple observations of local GAG area ratio and local collagen fibre dispersion from each tissue strip. Since multiple observations of each variable were obtained from each tissue strip, linear mixed-effects models were used to account for the data hierarchy. In addition, to better reflect the heterogeneity between strips, the models were set to assume both random intercepts and random slopes. The non-simultaneous marginal predictions and their 95% confidence intervals were then plotted to illustrate the population trend.

3.4 Results

Parameterised histological data from 96 tissue strips of 8 aneurysm and dissection samples were prepared for analyses, which included 48 tissue strips from each of the unnotched and notched tensile testing groups. Each 48-tissue strip group consisted of two strips from each of the thickened intima, media and adventitia layers, with one of these strips in the axial and the other in the circumferential aorta direction of each sample.

3.4.1 Layer-specific microstructural component contents and their correlations

As it can be visualised in Figure 3.7, collagen and elastin were the two main microstructural components in the diseased aortic wall, followed by GAGs and macrophages. Among the three layers, the thickened intima has the lowest collagen content and the adventitia has the highest collagen content.

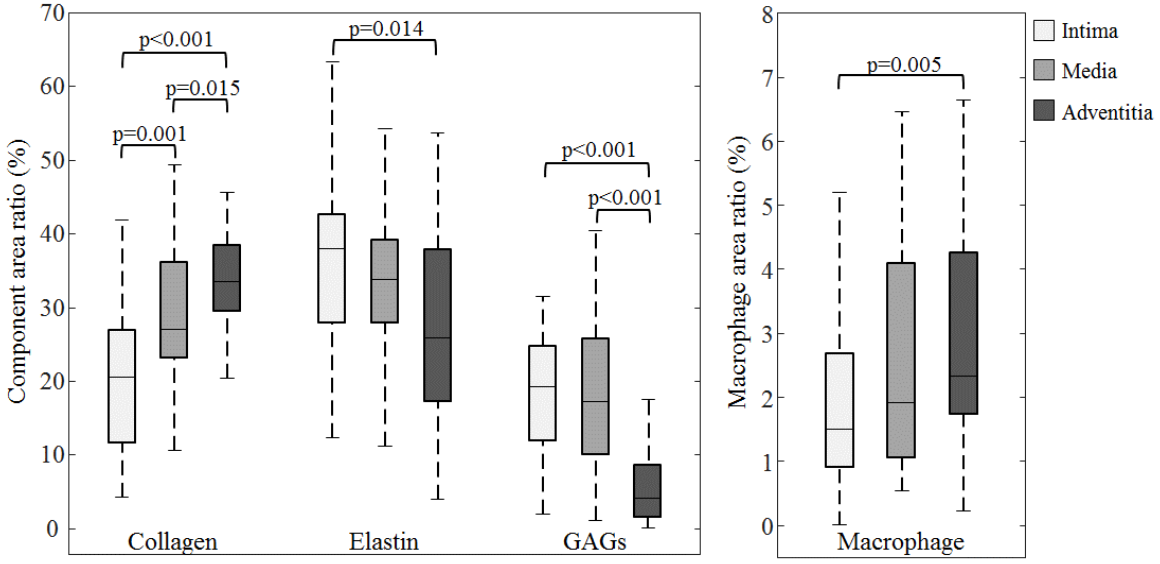

Figure 3.7. Area ratios of collagen, elastin, GAGs and macrophages in different arterial layers.

In contrast, the intima has more elastin than the adventitia and the elastin area ratio of intima and media is comparable. Both intima and media have higher GAG content than adventitia. Compared with collagen, elastin and GAGs, the macrophage area ratio in the arterial wall is significantly less ($p<0.001$). Correlation analysis showed that GAG area ratio negatively associates with the collagen ratio ($r^2=0.173$, $p<0.001$) but positively with elastin ($r^2=0.037$, $p=0.038$).

3.4.2 Relationship between microstructural component contents and tissue mechanical properties

In this section, the associations between mechanical parameters that were computed for all unnotched and notched tissue strips in **Chapter 2** and the corresponding area ratios of collagen, elastin, GAGs and macrophages are explored.

3.4.2.1 Unnotched tissue strips

Correlation analyses showed that the extreme extensibilities of unnotched tissue strips in both the axial and circumferential directions were associated only with elastin area ratio (Axial: $r^2=0.186$, $p=0.04$; Circumferential: $r^2=0.175$, $p=0.04$). However, collagen and GAG contents were both associated with ultimate material strength in the circumferential direction (Collagen: slope=32.7, $r^2=0.328$, $p=0.003$; GAGs: slope=-25.5, $r^2=0.227$, $p=0.019$), but not with strength in the axial direction.

Further multivariate analysis confirmed the association between the material strength in the circumferential direction with collagen and GAG contents (Collagen: slope=27.3, GAGs: slope=-18.4, $r^2=0.438$, $p=0.002$); and this association remained when data from both axial and circumferential directions were pooled (Collagen: slope=17.0, GAGs: slope=-12.6, $r^2=0.249$, $p=0.002$).

3.4.2.2 Notched tissue strips

Both collagen and GAG content were also associated with the tissue strength of notched tissue strips, but an association was not found with either elastin or macrophages. Univariate analyses showed that collagen and GAG contents were both associated with nominal ultimate material strength in the circumferential direction (Collagen: slope=127, r^2=0.428, p=0.001; GAGs: slope=-104, r^2=0.253, p=0.012), and in the axial direction (Collagen: slope=120, r^2=0.378, p=0.002; GAGs: slope=-187, r^2=0.373, p=0.007). Multivariate analyses further confirmed these associations for strength in the circumferential (Collagen: slope=104, GAGs: slope=-40.3, r^2=0.454, p=0.002) and the axial (Collagen: slope=83.9, GAGs: slope=-122, r^2=0.492, p=0.001) directions. This association remained when data from both axial and circumferential directions were pooled (Collagen: slope=91.3, GAGs: slope=-80.7, r^2=0.460, p<0.001).

3.4.3 Association of collagen fibre architecture with GAG deposition

Collagen fibre is the most important mechanical constituent of arterial tissue[12,13]. Since an increase in GAG content was found to reduce the strength of diseased aortic tissues, the association between collagen dispersion and GAG deposition was also explored. Fibre dispersion shows the spread of fibre orientations, and a smaller dispersion implies stronger alignment in a reference direction. Collagen fibre dispersion in the intima was 43.5° [40.8°, 44.4°] (median [interquartile range]) in the circumferential and 42.3° [40.2°, 44.6°] in the axial direction, with no significant difference between these two directions (p=0.677). Fibre dispersions in the media and adventitia were smaller in the circumferential than in the axial direction (39.4° [36.2°, 40.7°] vs 44.2° [42.5°, 46.2°], p<0.001 for media and 44.9° [42.1°, 49.2°] vs 48.2° [44.4°, 50.7°], p<0.001 for adventitia). Moreover, fibre dispersion of media in the circumferential direction was smaller than intima (p=0.003). Local GAG content was correlated positively with fibre dispersion in media and adventitia in the axial and circumferential directions, but not in either direction of intima, as shown in Figure 3.8.

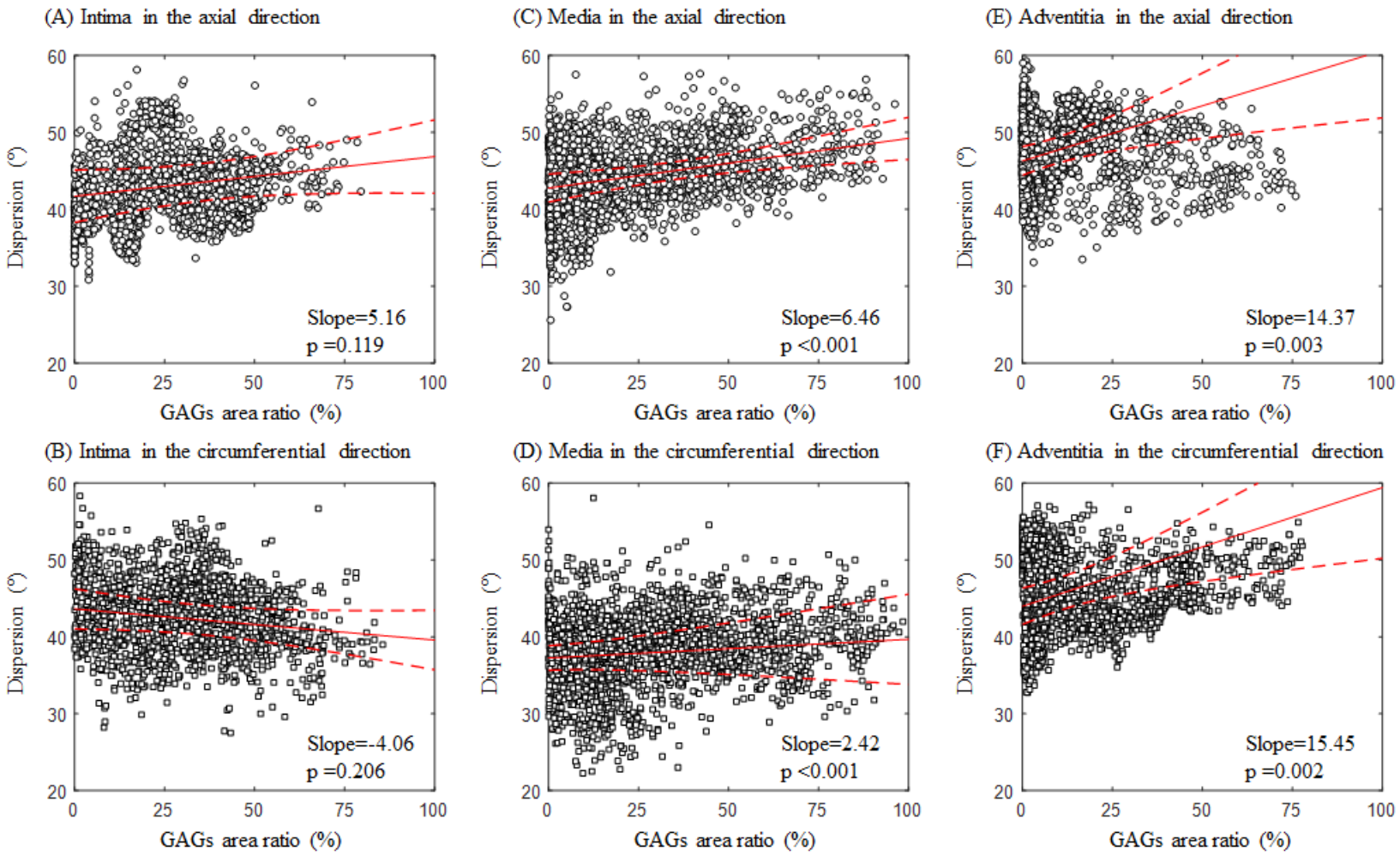

Figure 3.8. Correlation analysis using linear mixed-effects model showing the local correlation between dispersion of collagen fibre orientations and GAGs area ratio in different layers in both axial and circumferential directions. The non-simultaneous marginal predictions and their confidence intervals are plotted to illustrate population-wise association.

3.5 Discussion

This study showed that the distribution of collagen, elastin, GAGs and macrophages was layer-dependent and GAG deposition was associated with local collagen fibre dispersion. Collagen and GAG content of unnotched and notched tissue strips was also found to associate with their extreme extensibilities and material strengths.

The negative relationship between GAG content and material strength and the positive relationship between GAG content and extreme extensibility in the axial direction implies that GAGs are a weaker material than collagen. This is in agreement with their molecular structures that consist of linear chains of repeating disaccharide units[14]. GAGs are highly negatively charged and thus sequester water and contribute directly to the compressive, rather than tensile stiffness of the artery[6,14]. The negatively charged GAGs could alter the regional distribution of interstitial water causing a swelling pressure, which has been speculated to be similar in magnitude to blood pressure[6]. Such swelling might damage the arterial wall by separating the fibre lamellae[15,16], as evidenced by greater separation distances between elastic lamellae where accumulation of GAGs were found[17].

Apart from the inherent material characteristic of GAGs which will modify the local structure and strength, the deposition of GAG pools also alters the mechanical environment. Due to the lower tensile stiffness, pooled GAG deposition could elevate the local stress concentration by 3-5 times as compared with the far-field stresses, which are not affected by the local pooling of GAGs[7]. This GAG pooling-induced stress concentration and swelling pressure might cause local delamination in the aortic wall and therefore contribute to the development of aortic dissection.

GAG deposition has been thought to play an important role in atherosclerotic plaque erosion in the coronary arteries. Plaque erosion involves the formation of thrombus in an area of endothelial denudation adjacent to an atherosclerotic plaque without disruption of the fibrous cap[18,19] and is responsible for ~25% of deaths due to acute myocardial infarction[18]. Histopathological analyses have demonstrated the superficial accumulation of specific GAGs and hyaluronan at the sites of plaque erosion[19], as it can be visualised in Figure 3.9.

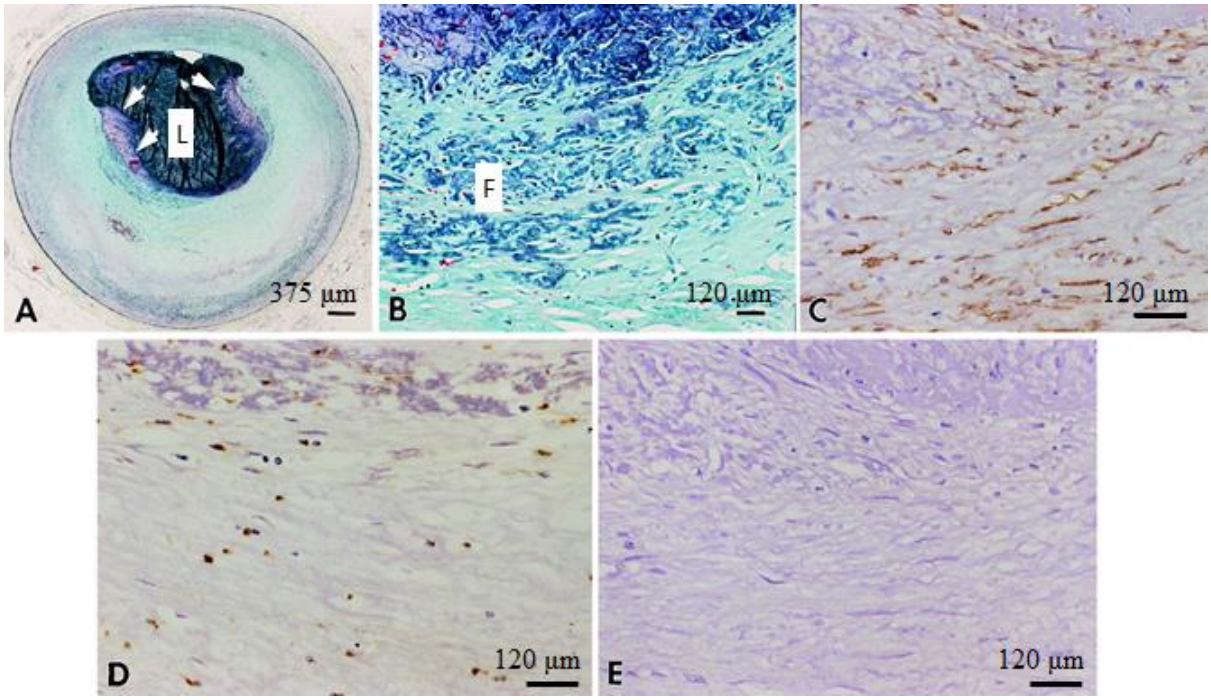

Figure 3.9. A typical case showing luminal thrombi (dark-gray barium gelatin shown at low power in A; L, lumen) developed over a stable coronary plaque whose luminal surface eroded and is rich in GAGs (green colour by Movat staining in A and B; F, fibrous tissues with GAG deposition and fibrin thrombus penetration). Immunohistochemical stains demonstrate numerous smooth muscle cells at the luminal plaque surface in contact with the thrombus (in C). Occasional macrophages (in D) are present with negative staining for Human Leukocyte Antigen – DR Isotype (HLA-DR) (in E), (Adapted with permission from[19]).

Glycans are extracellular matrix molecules that play an important role under physiopathological conditions[20,21]. These molecules influence fundamental cellular and extracellular events associated with the pathogenesis of vascular lesions, such as thrombosis[22], lipid metabolism[3,23], as well as vascular proliferation[24] and cell migration[25]. Such physiopathologic effect of glycans might contribute to the plaque erosion resulting in the local formation of fatal thrombosis. As shown in this study, the GAG accumulation weakens the local material, implying that the superficial accumulation of GAGs can elevate the local stretch.

Mechanical simulation results of the atherosclerotic plaque cross-section in Figure 3.9A are provided in Figure 3.10. The mechanical analysis shown in Figure 3.10 has followed a previously reported technique by Teng et al.[26], and mechanical properties of each plaque component were adopted from another study by Teng et al.[27]. The elevated stretch level (Figure 3.10A) might promote local endothelium cell apoptosis[4], leading to endothelial denudation. It also induces specific changes in the synthesis and organisation of GAGs by vascular smooth muscle cells[28], e.g., large stretch increases versican, biglycan and perlecan core proteins, and this generates a positive feedback loop further promoting the accumulation of GAGs.

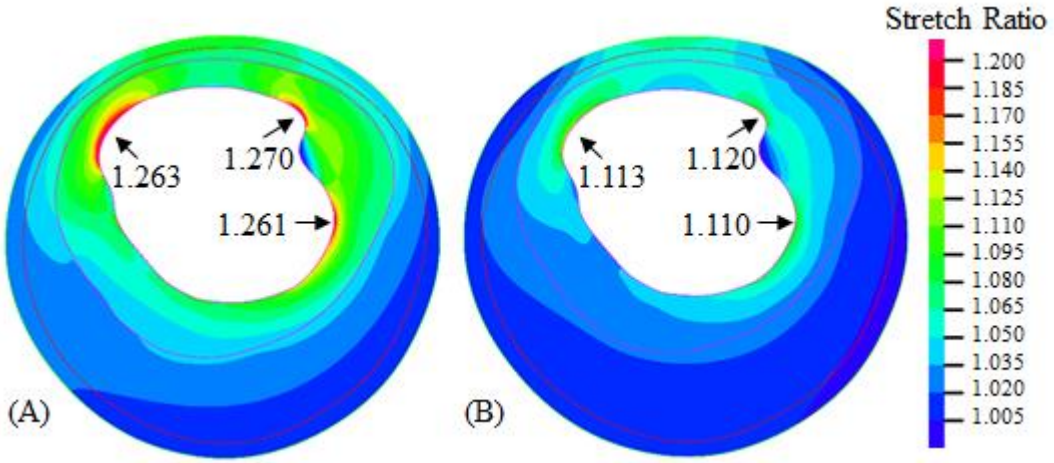

Figure 3.10. Mechanical simulation results of the atherosclerotic plaque cross-section in Figure 3.9A. These results demonstrated that the superficial GAG deposition induced increased local tissue stretch, in particular around the lumen region. In A, the material properties of tissue regions with GAG deposition were assumed to be the same as lipid; and B is the case assuming no GAG deposition in the fibrous tissue. If no GAG deposition was assumed, the stretch level reduced by over 10% (B).

Moreover, given the large stretch together with weaker material, the GAG accumulation might damage the local tissue integrity by forming micro-fissures. The endothelial denudation and micro-fissures alone or in combination might lead to the local development of thrombosis and fatal events[29,30].

This study also showed a heterogeneous transmural distribution of GAGs. Both intima and media had a significantly higher GAG content than adventitia, and similar distribution patterns have been reported in the healthy arterial wall[31]. Such heterogeneous transmural distribution may be a source of residual stress[31], which manifests as an opening angle when a radial cut is made on a healthy arterial ring[32] or a ring from atherosclerotic lesion[33].

The interaction between GAGs and other extracellular components also plays an important role in the mechanics of the arterial wall. Although removal of GAGs results in an earlier transition point of the nonlinear stress-strain curves during extension mechanical testing, the stiffness was not significantly different after GAG removal[8]. Microscopic examination showed that when GAGs were removed, the adventitial collagen fibres were straighter and both elastin and collagen fibres recruited at lower levels of strain, in agreement with the mechanical change[8].

Sodium magnetic resonance imaging (MRI), delayed gadolinium-enhanced MRI of cartilage (dGEMRIC) and T_1-rho mapping have been developed to permit the visualisation of the charged GAG distribution in cartilage[34]. These imaging techniques might be modified for the detection of GAGs accumulation in the aortic wall, in particular, in the thoracic aorta where most dissections are located. Successful development of this aspect would be beneficial for a prediction of dissection development.

Despite the interesting findings obtained, limitations exist in this study: (1) no controls were provided for comparison, e.g., the GAG contents in the healthy aortic tissues; (2) although tissues used for histopathological examination were from a narrow adjacent region, the heterogeneity of aneurysmal tissues means that measurements from adjacent tissue strips might not represent the inherent histopathological features; and (3) the fibre architecture might be distorted by the processing procedure for histopathological stains.

3.6 Conclusion

For the first time, this study has provided a unique comprehensive overview of the critical role of microstructural components, as well as the role of disease driven changes in their turnover and architecture on the mechanical properties of aortic aneurysms. It has also highlighted the important role of GAGs in arterial tissue mechanics, which has been largely neglected in the field. The obtained results indicate that, any investigation on structure-mechanics relationship of diseased aortic tissues should also be considering the potential influence of GAGs on the tissue mechanical and fracture behaviours. Improved understandings in the contribution of distinct microstructural components on diseased aortic tissue mechanical properties would assist development of clinical tools for accurate assessment of patient risk.

3.7 References

1. Sariola, H., Viljanen, T. & Luosto, R. Histological pattern and changes in extracellular matrix in aortic dissections. *J. Clin. Pathol.* **39,** 1074–81 (1986).
2. Karangelis, D. E. *et al.* Glycosaminoglycans as key molecules in atherosclerosis: the role of versican and hyaluronan. *Curr. Med. Chem.* **17,** 4018–26 (2010).
3. Camejo, G. The interaction of lipids and lipoproteins with the intercellular matrix of arterial tissue: its possible role in atherogenesis. *Adv. Lipid Res.* **19,** 1–53 (1982).
4. Jufri, N. F., Mohamedali, A., Avolio, A. & Baker, M. S. Mechanical stretch: physiological and pathological implications for human vascular endothelial cells. *Vasc. Cell* **7,** 8 (2015).
5. Sotoudeh, M. *et al.* Induction of apoptosis in vascular smooth muscle cells by mechanical stretch. *Am. J. Physiol. Heart Circ. Physiol.* **282,** H1709-16 (2002).
6. Humphrey, J. D. Possible mechanical roles of glycosaminoglycans in thoracic aortic dissection and associations with dysregulated transforming growth factor-β. *J. Vasc. Res.* **50,** 1–10 (2013).
7. Roccabianca, S., Ateshian, G. A. & Humphrey, J. D. Biomechanical roles of medial pooling of glycosaminoglycans in thoracic aortic dissection. *Biomech. Model. Mechanobiol.* **13,** 13–25 (2014).

8. Mattson, J. M., Turcotte, R. & Zhang, Y. Glycosaminoglycans contribute to extracellular matrix fiber recruitment and arterial wall mechanics. *Biomech. Model. Mechanobiol.* **16,** 213–225 (2017).

9. Wang, S. *et al.* Bayesian inference-based estimation of normal aortic, aneurysmal and atherosclerotic tissue mechanical properties: from material testing, modelling and histology. *IEEE Trans. Biomed. Eng.* 1–1 (2019). doi:10.1109/TBME.2018.2886681

10. Otsu, N. A Threshold Selection Method from Gray-Level Histograms. *IEEE Trans. Syst. Man. Cybern.* **9,** 62–66 (1979).

11. MathWorks. Matlab R2017b Documentation. (2017). at <https://uk.mathworks.com/help/images/ref/multithresh.html>

12. Fung, Y.-C. *Biomechanics: Mechanical Properties of Living Tissues*. (Springer New York, 1993). doi:10.1007/978-1-4757-2257-4

13. Humphrey, J. D. *Cardiovascular Solid Mechanics: Cells, Tissues, and Organs*. (Springer New York, 2002). doi:10.1007/978-0-387-21576-1

14. Alberts, B. *et al. Molecular Biology of the Cell*. (Garland, 2002).

15. Evanko, S. P. *et al.* Platelet-derived growth factor stimulates the formation of versican-hyaluronan aggregates and pericellular matrix expansion in arterial smooth muscle cells. *Arch. Biochem. Biophys.* **394,** 29–38 (2001).

16. Hosoda, Y. & Iri, H. Angiolathyrism. 1. A histological and histochemical study on successive changes of the lathyritic rat aorta. *Acta Pathol. Jpn.* **16,** 239–52 (1966).

17. Guo, D.-C. *et al.* Familial thoracic aortic aneurysms and dissections: identification of a novel locus for stable aneurysms with a low risk for progression to aortic dissection. *Circ. Cardiovasc. Genet.* **4,** 36–42 (2011).

18. Arbustini, E. *et al.* Plaque erosion is a major substrate for coronary thrombosis in acute myocardial infarction. *Heart* **82,** 269–72 (1999).

19. Farb, A. *et al.* Coronary plaque erosion without rupture into a lipid core. A frequent cause of coronary thrombosis in sudden coronary death. *Circulation* **93,** 1354–63 (1996).

20. Wight, T. N. Cell biology of arterial proteoglycans. *Arteriosclerosis* **9,** 1–20

21. Wight, T. N., Lara, S., Riessen, R., Le Baron, R. & Isner, J. Selective deposits of

versican in the extracellular matrix of restenotic lesions from human peripheral arteries. *Am. J. Pathol.* **151,** 963–73 (1997).

22. Bourin, M. C. & Lindahl, U. Glycosaminoglycans and the regulation of blood coagulation. *Biochem. J.* **289 (Pt 2,** 313–30 (1993).

23. Williams, K. J. & Tabas, I. The response-to-retention hypothesis of early atherogenesis. *Arterioscler. Thromb. Vasc. Biol.* **15,** 551–61 (1995).

24. Wight, T. N., Potter-Perigo, S. & Aulinskas, T. Proteoglycans and vascular cell proliferation. *Am. Rev. Respir. Dis.* **140,** 1132–5 (1989).

25. Wight, T. N., Kinsella, M. G. & Qwarnström, E. E. The role of proteoglycans in cell adhesion, migration and proliferation. *Curr. Opin. Cell Biol.* **4,** 793–801 (1992).

26. Teng, Z. *et al.* Coronary plaque structural stress is associated with plaque composition and subtype and higher in acute coronary syndrome: The BEACON i (Biomechanical Evaluation of Atheromatous Coronary Arteries) study. *Circ. Cardiovasc. Imaging* **7,** 461–470 (2014).

27. Teng, Z. *et al.* Material properties of components in human carotid atherosclerotic plaques : a uni-axial extension study. *ACTA Biomater.* **10,** 5055–5063 (2014).

28. Lee, R. T. *et al.* Mechanical strain induces specific changes in the synthesis and organization of proteoglycans by vascular smooth muscle cells. *J. Biol. Chem.* **276,** 13847–51 (2001).

29. Kolodgie, F. D. *et al.* Differential accumulation of proteoglycans and hyaluronan in culprit lesions: insights into plaque erosion. *Arterioscler. Thromb. Vasc. Biol.* **22,** 1642–8 (2002).

30. Partida, R. A., Libby, P., Crea, F. & Jang, I.-K. Plaque erosion: a new in vivo diagnosis and a potential major shift in the management of patients with acute coronary syndromes. *Eur. Heart J.* **39,** 2070–2076 (2018).

31. Azeloglu, E. U., Albro, M. B., Thimmappa, V. A., Ateshian, G. A. & Costa, K. D. Heterogeneous transmural proteoglycan distribution provides a mechanism for regulating residual stresses in the aorta. *Am. J. Physiol. Heart Circ. Physiol.* **294,** H1197-205 (2008).

32. Chuong, C. J. & Fung, Y. C. On residual stresses in arteries. *J. Biomech. Eng.* **108,**

189–92 (1986).

33. Teng, Z. *et al.* A uni-extension study on the ultimate material strength and extreme extensibility of atherosclerotic tissue in human carotid plaques. *J. Biomech.* **48,** 3859–67 (2015).

34. Gray, M. L., Burstein, D., Kim, Y.-J. & Maroudas, A. Magnetic resonance imaging of cartilage glycosaminoglycan: Basic principles, imaging technique, and clinical applications. *J. Orthop. Res.* **26,** 281–291 (2008).

Chapter 4

Constitutive modelling of healthy aortic, aneurysmal and atherosclerotic tissue mechanical properties

The author of this dissertation carried out all of the work and analysis in this chapter except as specified below. Shuo Wang from Department of Radiology, University of Cambridge optimised the Bayesian inference-based estimation algorithm for fitting of the arterial tissue strip stress-stretch curves and the data analysis was performed together with Shuo Wang. The work described in this chapter has been published[1] *as described in the* **Publications** *section at the beginning of this dissertation. Permission has been obtained to use the contents of the published paper in this dissertation.*

4.1 Abstract

Mechanical properties of healthy, aneurysmal and atherosclerotic arterial tissues are essential for assessing the risk of lesion development and rupture. Constitutive modelling with the strain energy density function (SEDF) has been widely used to describe these properties, where material constants of the SEDF are traditionally determined using the ordinary least square (OLS) method. However, the material constants derived using OLS are usually dependent on initial guesses. To avoid such dependencies, Bayesian inference-based estimation was used to fit experimental stress-stretch curves of 312 tissue strips from 8 normal aortas, 19 aortic aneurysms and 21 carotid atherosclerotic plaques to determine the constants, C_1, D_1 and D_2 of the modified Mooney-Rivlin SEDF. Compared with OLS, material constants varied much less with *prior* in the Bayesian inference-based estimation. Moreover, fitted material constants differed amongst distinct tissue types. Atherosclerotic tissues associated with the largest D_2, an indicator of the rate of increase in stress during stretching, followed by aneurysmal tissues and those from normal aortas. Histological analyses showed that C_1 and D_2 were particularly associated with details of the collagen configuration, specifically waviness and dispersion in the structure. Bayesian inference-based estimation robustly determines material constants in the modified Mooney-Rivlin SEDF and these constants can reflect the inherent physiological and pathological features of the tissue structure.

4.2 Introduction

In the current clinical practice, luminal stenosis and maximum wall diameter are the only validated risk assessment criteria for atherosclerotic disease and aneurysm, respectively. However, such size-based criteria showed only limited sensitivity and specificity[2–5]. Therefore, there is a clear need for novel risk-stratification biomarkers to estimate the risks of atherosclerosis and aneurysm in the hope of improving patient outcomes.

Under physiological conditions, both lesions are subject to mechanical loading due to dynamic blood pressure and flow. It has been shown that mechanical loading within the arterial tissue structure has an association with biological activities within the lesion[6–10], which can promote its development[11–13], leading to both progression and rupture. Accurate characterisation of mechanical properties of atherosclerotic and aneurysmal tissues is required for reliable prediction of mechanical loading in the lesion structure. A reliable prediction process should follow the steps of: (1) direct measurement of tissue stress-stretch curve[14]; (2) carefully selected SEDF[15]; and (3) determination of material constants in SEDF with an optimization method to minimise the objective function, which describes the difference between the predicted and measured stress-stretch curves. Several SEDFs have been used to characterize the tissue material[15]. It is challenging to obtain a robust estimation of material constants in an SEDF with traditional least squares methods, which often converge to a local minimum of the objective function in a narrow region around the initial guesses. This yields different sets of constants that can all fit the experimental data well. Although these distinct sets of material constants can lead to very similar stress predictions[15], it is inappropriate to characterise the tissue mechanical behaviour by using regressed material constants, whose values are highly dependent on their initial guesses. In other words, it is incorrect to assign a physical meaning to these regressed constants.

In this study, Bayesian inference was used to estimate the probability of each material constant across a wide range and the expectation was used to characterise the material constants for each tissue strip. This approach avoided non-uniqueness of parameter estimation associated with the commonly utilised least squares estimation method. With Bayesian inference, the fitted material constants gained uniqueness, which allowed identification of the physical meaning of each constant and enabled comparisons between the obtained parameters among distinct sample types. The correlation of those parameters with the corresponding microscopic structures was also investigated for the first time. The capability of the determined material constants to differentiate tissues from normal aorta, carotid atherosclerotic plaque and aortic aneurysm were assessed and the association between determined material constants and collagen fibre architecture in the tissue was explored.

4.3 Materials and methods

This section will describe the experimental methodology and the subsequent analysis that were used for constitutive modelling of healthy aortic, aneurysmal and atherosclerotic tissue pieces, as well as the parameters that were used to quantify the architecture of collagen fibres.

4.3.1 Collection of tissue samples and material testing

In this study, stress-stretch curves from direct material testing with 8 normal aortas[16], 19 aortic aneurysms[16] and 21 carotid atherosclerotic plaques[14] were collected from previous studies, except for 8 aneurysm samples. These 8 new aneurysmal samples are those utilised in the studies of **Chapter 2** and **Chapter 3**. Details of patient demographics, tissue preparation and material testing protocol have been described in the two previous studies[14,16], as well as in **Chapter 2** and **Chapter 3**. In brief, tissue strips from different arterial layers and distinct atherosclerotic plaque components were prepared for uniaxial tensile testing. Waterproof markers were placed on the tissue surface and each strip was mounted on an in-house designed micro tester. After pre-conditioning, the strip was pulled slowly until failure with the force and position of markers recorded. A displacement rate of 0.01 mm·s^{-1} was used in all tensile tests. The stress-stretch curve of each strip was then derived from the recorded signals, considering the initial dimensions and by assuming incompressibility. The initial width and thickness of the sample strips were measured from high-resolution images with ruler calibration in MATLAB.

4.3.2 Strain energy density function

In this study, the modified Mooney-Rivlin SEDF was used to characterise the mechanical behaviour of the tissue strips based on the consideration of material stability[15],

$$W = C_1(\bar{I}_1 - 3) + D_1\left[e^{D_2(\bar{I}_1-3)} - 1\right] + \xi(J-1) \qquad (4.1)$$

where, $\bar{I}_1 = J^{-2/3}I_1$; I_1 is the first invariant of the unimodular component of the left Cauchy-Green deformation tensor; J is the determinant of the deformation gradient; ξ is the Lagrangian multiplier for the assumption of incompressibility; C_1, D_1 and D_2 are the empirical material constants to be determined by experimental data.

In the case of a uniaxial tensile experiment, the Cauchy stress σ_{11} along the tensile direction is derived as,

$$\sigma_{11}(\lambda) = 2\left(\lambda^2 - \frac{1}{\lambda}\right)\left[C_1 + D_1 D_2 e^{D_2\left(\lambda^2 + \frac{2}{\lambda} - 3\right)}\right] \quad (4.2)$$

where,

λ = Stretch ratio

4.3.3 Ordinary least square fitting method

The OLS[17] fitting method was used to determine the material constants in Equation 4.1 by finding the local minimum of the objective function $\mathrm{S}(\mathrm{C}_1, \mathrm{D}_1, \mathrm{D}_2)$ around the initial guess of (C_{10}, D_{10}, D_{20}),

$$S(C_1, D_1, D_2) = \sum_{k=1}^{N} [\sigma_{11k}^P - \sigma_{11k}^M]^2 \quad (4.3)$$

where, N is the number of data points, σ_{11k}^P and σ_{11k}^M are the kth predicted and measured Cauchy stresses, respectively. All material constants were constrained to be positive to avoid any unphysical phenomenon. The relative error, γ was used to assess the fitting quality[18],

$$\gamma = \frac{\sum_{i=k}^{N} |\sigma_{11k}^P - \sigma_{11k}^M|}{\sum_{i=k}^{N} |\sigma_{11k}^M|} \times 100\% \quad (4.4)$$

4.3.4 Bayesian inference framework

In Bayesian inference, all unknown parameters are treated as random variables $\boldsymbol{\theta}$. Given the experimental data $\mathcal{D}$, its aim is to estimate the conditional distribution of unknown parameters $p(\boldsymbol{\theta}|\mathcal{D})$, which is referred to the posterior distribution (*"posterior"*). First a prior distribution (*"prior"*) $p(\boldsymbol{\theta})$ is assumed to represent the prior knowledge about unknown parameters. The prior distribution can be adapted from previous studies and/or from experts' opinions. If there is no established prior distribution for a problem, a non-informative *prior* can be applied using the Principle of Maximal Entropy[19–21].

An appropriate noise model and chosen constitutive equations are used to derive the likelihood function (*"likelihood"*) $p(\mathcal{D}|\boldsymbol{\theta})$. The *posterior* can be calculated by linking the *prior* and the *likelihood* using Bayes' theorem[19–21],

$$p(\boldsymbol{\theta}|\mathcal{D}) = \frac{p(\boldsymbol{\theta}) \times p(\mathcal{D}|\boldsymbol{\theta})}{p(\mathcal{D})} \tag{4.5}$$

The denominator of Equation 4.5 is a constant referred to as the probability of the evidence (*"evidence"*) and given by,

$$p(\mathcal{D}) = \int p(\boldsymbol{\theta}) \times p(\mathcal{D}|\boldsymbol{\theta}) d\boldsymbol{\theta} \tag{4.6}$$

The multi-dimensional integral in Equation 4.6 is generally difficult to evaluate. If the unknown parameters are the only ones of interest, Equation 4.6 can be rewritten as[19–21],

$$p(\boldsymbol{\theta}|\mathcal{D}) \propto p(\boldsymbol{\theta}) \times p(\mathcal{D}|\boldsymbol{\theta}) \tag{4.7}$$

Sampling methods, e.g., Markov Chain Monte Carlo (MCMC), can be applied to explore the *posterior* without explicitly computing the *evidence* (Equation 4.6). The strategy is to draw samples from a distribution similar to the *posterior* by using effective sampling methods. More details about Bayesian inference and different sampling methods can be found in references[19–21].

When Bayesian inference is used to estimate the material constants in Equation 4.1, a Gaussian noise model[19–21] is introduced for the uncertainty, hoping that $\sigma_{11k}^{P}(\lambda)$ equals $\sigma_{11k}^{M}(\lambda)$,

$$\sigma_{11}(\lambda) = 2\left(\lambda^2 - \frac{1}{\lambda}\right)\left[C_1 + D_1 D_2 e^{D_2\left(\lambda^2 + \frac{2}{\lambda} - 3\right)}\right] + \mathcal{N}(0, \varepsilon^2) \tag{4.8}$$

where, $\mathcal{N}(0, \varepsilon^2)$ is the additive Gaussian noise with zero mean and variance ε^2 (standard deviation ε). Therefore, the likelihood function can be written as,

$$p(\mathcal{D}|C_1, D_1, D_2, \varepsilon) = \prod_{k=1}^{N} \mathcal{N}(\sigma_{11k}^{P} - \sigma_{11k}^{M}|0, \varepsilon^2) \tag{4.9}$$

where, N is the number of experimental data points. In this study, the *prior* for C_1, D_1, D_2 and ε were assumed to be uniform distributions with ranges of [0, 5000] kPa, [0, 5000] kPa, [0, 5000] and [0, 5000] kPa, respectively.

The sensitivity to the *prior* was tested. The MCMC with Gibbs sampling method was implemented in the software WinBUGS (MRC Biostatistics Unit, University of Cambridge, Cambridge, UK) to estimate the posterior distribution of the parameters, i.e. $p(\boldsymbol{\theta}|\mathcal{D})$. The mean and standard deviation of the *posterior* was calculated for further analyses amongst tissues from different types of lesions and distinct morphological component.

4.3.5 Quantitative histological analysis

24 tissue strips adjacent to those used for mechanical testing from the 8 aneurysmal samples (1 strip from each of the intima, media and adventitia layers of each sample) were submitted to histological examination, where details of the histological processing protocol are described in **Chapter 3**. In brief, tissue slices in 4 μm thickness were stained with EVG and Sirius Red to visualise the elastin and collagen contents, respectively. Stained histological tissue slices were digitised with the NanoZoomer Slide Imaging System (Hamamatsu, Hamamatsu City, Japan) into 904 nm resolution RGB images. Elastin appears dark in EVG stain, and collagen appears red in Sirius Red stain. Elastin and collagen percentage of each tissue slice, as well as the collagen fibre dispersion (κ; a parameter describing the scatter of fibre orientations), and collagen fibre waviness, ω were quantified using the in-house designed MATLAB-based software as described in **Chapter 3**. The software was optimised with the help of Nichola Figg from the Department of Medicine, University of Cambridge, who is a senior histologist with over 15 years of experience in histological analysis of diseased arterial tissues.

Based on the segmented results from Sirius Red stained images, the waviness and dispersion were computed. Considering the heterogeneous distribution of collagen fibres, 16 square patches with 0.18 mm (200 pixels) in length were independently and randomly drawn in the tissue region. The final waviness, ω and dispersion, κ of the overall image was computed as the average of results from the 16 patches. For each square patch, each disconnected collagen fibre was recognized from the segmented mask.

In this study, the area percentages of elastin and collagen, as well as the collagen fibre orientation parameters κ, and ω were used to characterise the fibre architecture in the structure. Details of the collagen fibre dispersion, κ and waviness, ω parameters are provided in the following sections.

4.3.5.1 Dispersion of collagen fibres

Distribution of the collagen fibre orientations was characterised with the 2D planar form of the transversely isotropic and π-periodic von Misses distribution, similar to the methodology utilised in previous work on mathematical characterisation of arterial tissue[22–24].

The probability density function, $\rho(\theta)$ of the von Misses distribution was used to quantify the distribution of collagen fibre orientations within the 0° to 180° range:

$$\rho(\theta) = 4\sqrt{\frac{b}{2\pi}\frac{exp[b(cos(2\theta)+1)]}{erfi(\sqrt{2b})}} \tag{4.10}$$

where,

b = Concentration parameter

$\mathrm{erfi}(x)$ = Imaginary form of the error function

Imaginary form of the error function, $\mathrm{erfi}(x)$ was used in the equation above, so as to express the equation in the general form, which accounts for the imaginary values of x.The error function, $\mathrm{erf}(x)$ is a statistical tool that is used to predict the probability that a sample from a set of measurements has a difference less than x from the mean.

Concentration parameter, b in the equation above quantifies the degree of concentration of the angles that constitute the distribution around their mean. If $b = 0$, the distribution becomes uniform, which means that the angles of the distribution do not have a preferred orientation, where for larger values of b, the angles become more concentrated around their mean.

In contrast to the concentration parameter, a dispersion parameter, κ is commonly used to quantify the degree of dispersion of the distribution, which is defined in terms of the probability density function, $\rho(\theta)$ as:

$$\kappa = \frac{1}{4}\int_0^{180} \rho(\theta) sin^3\theta d\theta \tag{4.11}$$

The relationship between the concentration parameter, b and the dispersion parameter, κ is illustrated in Figure 4.1, where the relationship is defined only for values of κ between and including 0 and 1/3.

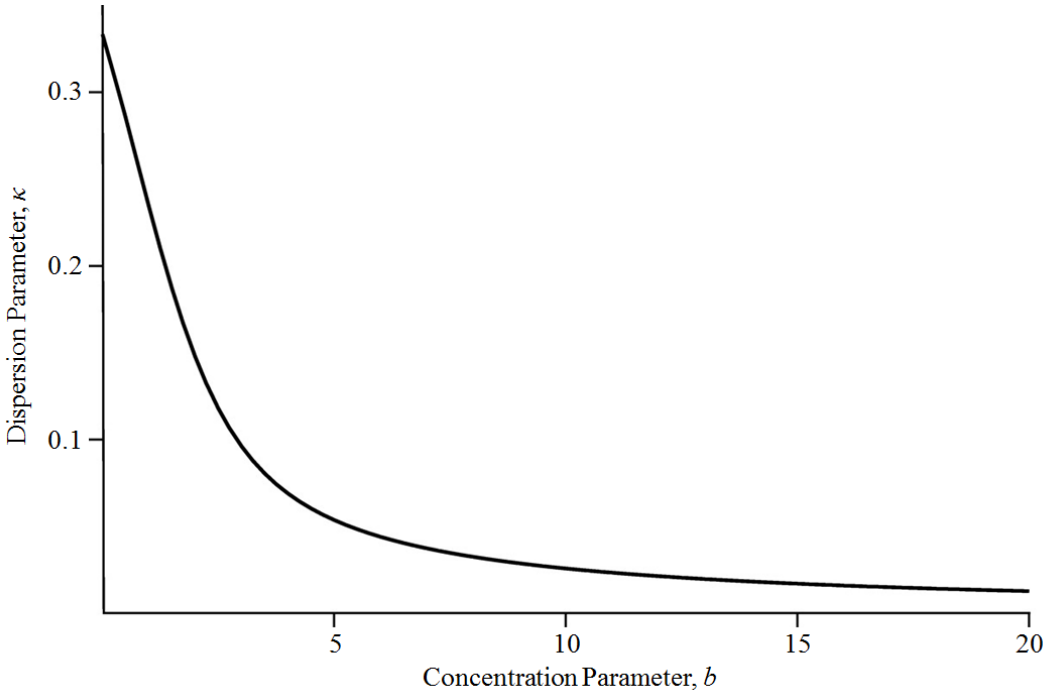

Figure 4.1. The relationship between the concentration parameter, b and the dispersion parameter, κ (Adapted with permission from[24]).

It can be visualised in Figure 4.1 that, when $\kappa = 0$, the value of b approaches infinity, which indicates that the angles that constitute the distribution are all concentrated at their mean orientation. On the other hand, when $\kappa = 1/3$, b approaches to zero and the angles attain an isotropic distribution.

A graph of the probability density function, $\rho(\theta)$ versus the preferred orientation misalignment angle curves, for different values of the dispersion parameter, κ is provided in Figure 4.2. The preferred orientation misalignment angles were determined by wrapping each distribution of angles with a mean of 0° within the -90° to +90° range.

The preferred orientation in Figure 4.2 is equivalent to the mean orientation of each group of collagen fibres.

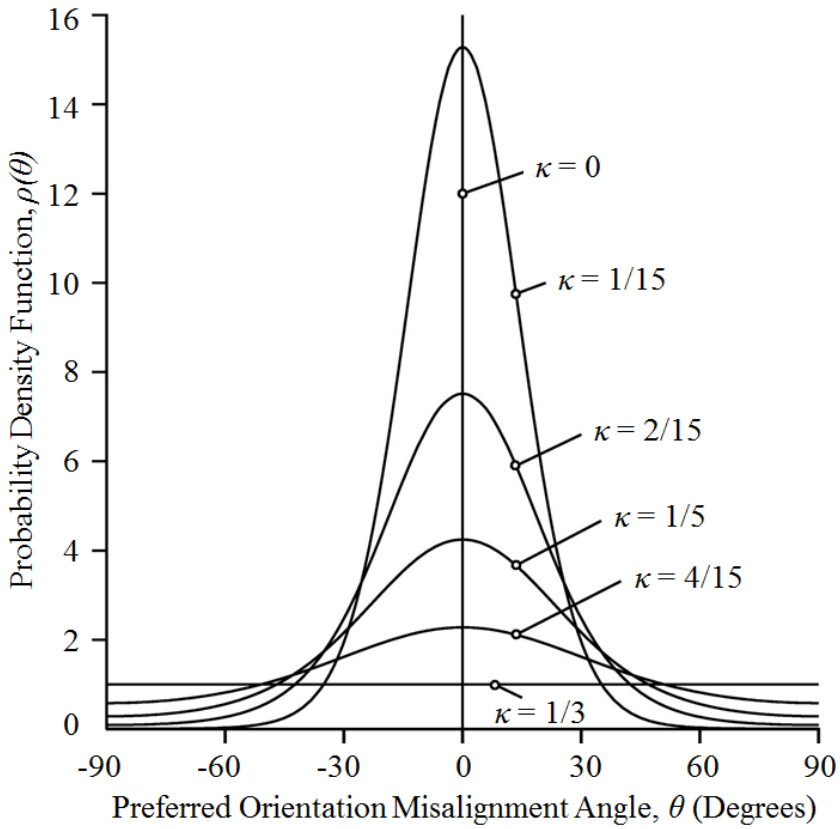

Figure 4.2. The probability density function, $\rho(\theta)$ versus the preferred orientation misalignment angle curves, for different values of the dispersion parameter, κ (Adapted with permission from[24]).

4.3.5.2 Waviness of collagen fibres

To compute the waviness, ω of collagen fibres, their major axis lengths and perimeters were determined by applying the *regionprops* function in MATLAB to their segmented masks. Smaller values of ω correspond to wavier fibres, and ω=1 indicates straight fibres. The waviness, ω of each fibre was calculated as:

$$\omega = \frac{Perimeter}{2 \times Major\ axis\ length} - 1 \tag{4.12}$$

4.3.6 Statistical analysis

The correlation between the percentage of collagens and the estimated material constants was assessed using Spearman correlation test. In this study, multiple samples were collected from each tissue piece and the linear mixed effect model was constructed to assess the difference of parameters from different tissue types, considering both random and fixed effects. Differences in microstructural constituent percentages between different tissue types were evaluated using the Wilcoxon signed rank test. The statistical analysis was performed in MATLAB. A significant difference was assumed if $p<0.05$.

4.4 Results

In this study, stress-stretch curves from 312 tissue strips in the circumferential artery direction were analysed using both OLS and Bayesian inference (Figure 4.3).

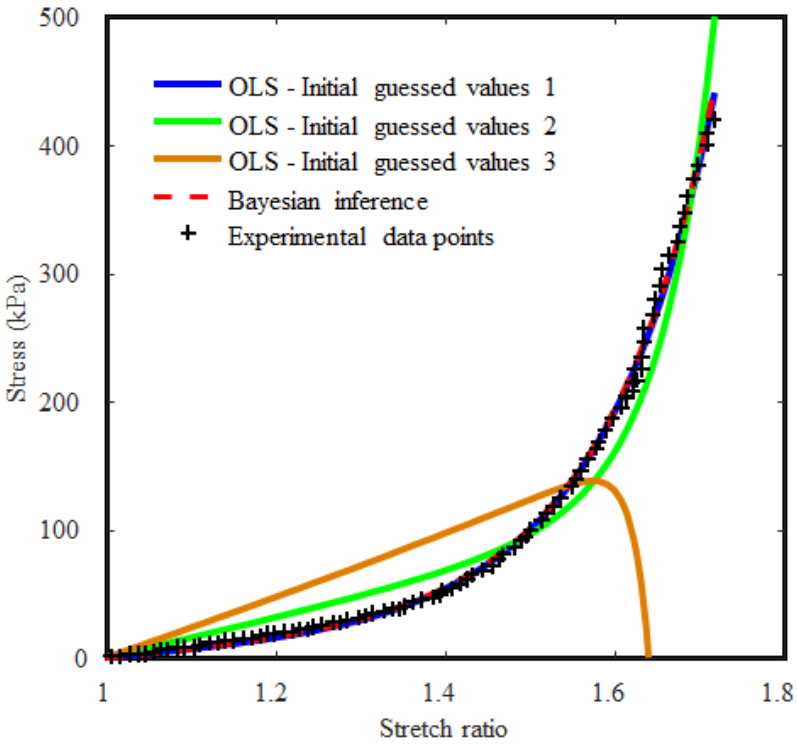

Figure 4.3. A representative example showing the fitted results using OLS method and Bayesian inference (initially guessed values 1 of (C_1, D_1, D_2) are (1, 1, 1), values 2 are (10, 10, 10), and values 3 are (100, 100, 100); the detailed fitted results are listed in Table 4.1; the experimental data were acquired from a media strip of a normal aorta).

In detail, the curves were from 15 media and 15 adventitial strips of 8 normal aortas; 28 adventitial, 36 media, 8 thickened intima and 27 thrombus strips of 19 aortic aneurysms; 65 media, 59 fibrous cap (FC), 38 lipid, and 21 intraplaque haemorrhage/thrombus (IPH/T) strips of 21 carotid atherosclerotic plaques. The difference in material constants determined by Bayesian inference of different tissue types was explored and the association between determined constants and tissue micro architectures was investigated.

4.4.1 Case study on material constants' uniformity

Figure 4.3 provides a representative example showing the fitted results using the OLS fitting method and Bayesian inference. The determined material constants were dependent on initial guesses when the OLS method was used. In the cases shown in Figure 4.3, when the initial guesses of (1, 1, 1) and (10, 10, 10) were used, the fitting results were very different (Table 4.1). A certain choice of initial guesses, e.g., (100, 100, 100), might lead to a poor regression (Figure 4.3). It is therefore inappropriate to use material constants determined by OLS to characterise the mechanical properties of arterial tissues. On the contrary, based on Bayesian inference, the determined material constants showed little changes (<5%) when the *prior* ranges of C_1, D_1 and D_2 all increased ten times from [0, 1000] to [0, 10000].

Table 4.1. Representative regressions using the OLS method with different initial values and Bayesian inference procedure with different prior ranges.

Fitting Method	$\boldsymbol{C_1}$ **(kPa)**	$\boldsymbol{D_1}$ **(kPa)**	$\boldsymbol{D_2}$	$\boldsymbol{\gamma}$
OLS - Initial values (1, 1, 1)	2.19	4.00	2.12	3.3%
OLS - Initial values (10, 10, 10)	25.56	0.04	5.27	15.1%
OLS - Initial values (100, 100, 100)	39.10	2.65×10^{-8}	19.92	444.5%
OLS - Initial values (0, 1, 0)	6.17	2.84	2.31	3.1%
Bayesian inference (*Prior* [0, 1000])	3.11	3.72	2.16	3.3%
Bayesian inference (*Prior* [0, 5000])	3.26	3.67	2.17	3.3%
Bayesian inference (*Prior* [0, 10000])	3.20	3.68	2.17	3.3%

In general, if the initially guessed value is properly chosen, OLS can fit the experimental data well. The fitting quality γ was 8.5% [6.0, 12.1] (Median [Interquartile range]), which is slightly better than that of the Bayesian inference-based estimation (8.8% [6.0, 12.3], p<0.0001).

4.4.2 Bayesian inference-based material constants of different tissue types

The values of C_1, D_1 and D_2 for each type of tissue are provided in Figure *4.4* (the outliers that are out of 1.75 quartile range were not shown) with actual values listed in Table 4.2.

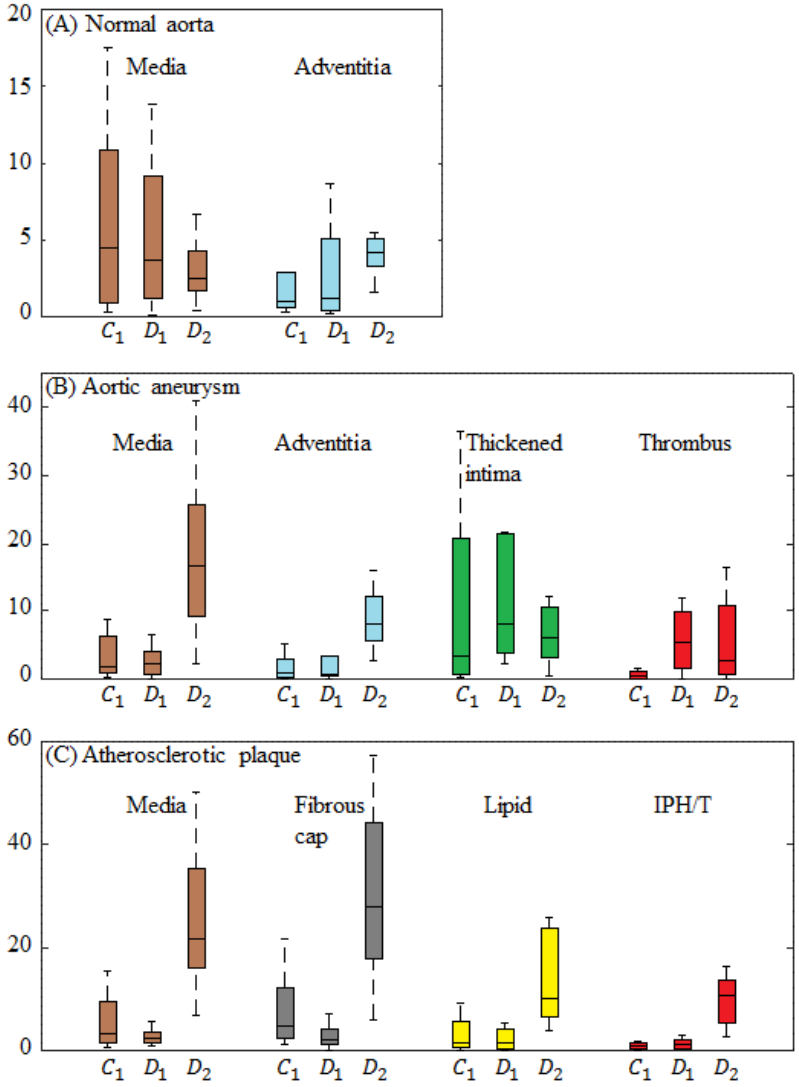

Figure 4.4. The visualisation of (C_1, D_1, D_2) of different tissue strips from different types of samples (A: tissue strips of media and adventitia from normal aortas; B: tissue strips of media, adventitia, thickened intima and thrombus from aortic aneurysms; C: tissues strips of media, fibrous cap, lipid and intraplaque haemorrhage/thrombus from carotid atherosclerotic plaques; Unit of C_1 and D_1 is kPa and D_2 is dimensionless).

Table 4.2. Bayesian inference-based estimations for different types of tissues (Median [Interquartile range]).

		C_1 (kPa)	D_1 (kPa)	D_2	γ (%)
Normal aorta	Media	4.53 [0.88, 10.84]	3.68 [1.19, 9.21]	2.53 [1.74, 4.29]	3.3 [2.3, 4.5]
	Adventitia	1.04 [0.60, 3.46]	1.46 [0.75, 6.51]	3.57 [3.12, 5.26]	9.8 [5.5, 13.6]
Aneurysm	Media	1.81 [0.83, 6.31]	2.33 [0.79, 4.02]	16.77 [9.12, 25.71]	11.8 [8.8, 14.7]
	Adventitia	0.96 [0.30, 2.88]	0.79 [0.56, 3.40]	8.04 [5.60, 12.13]	12.0 [7.2, 14.8]
	Intima	3.27 [0.74, 20.91]	7.98 [3.82, 21.42]	6.05 [3.04, 10.44]	7.9 [5.6, 11.5]
	Thrombus	0.46 [0.12, 1.17]	5.34 [1.66, 9.90]	2.80 [0.59, 10.77]	8.3 [7.2, 14.1]
Atherosclerosis	Media	3.34 [1.44, 9.60]	2.27 [1.45, 3.62]	21.78 [16.16, 35.24]	7.7 [6.6, 9.6]
	FC	4.87 [2.50, 12.33]	2.21 [1.26, 4.16]	28.06 [17.95, 44.17]	9.2 [7.0, 11.5]
	Lipid	1.48 [0.71, 5.62]	1.40 [0.28, 4.15]	10.07 [6.42, 23.66]	8.4 [5.9, 11.4]
	IPH/T	0.79 [0.18, 1.47]	1.17 [0.44, 2.20]	10.58 [5.45, 13.63]	10.8 [8.2, 18.4]

In normal aorta, the media and adventitia have comparable C_1 , D_1 and D_2 (p=0.18, 0.33, and 0.14, respectively). Samples from the aortic aneurysm, media and thickened intima showed a comparable C_1 (p=0.50), which is significantly higher than that in either adventitia or thrombus (p<0.05). Adventitia has the lowest value of D_1 (p<0.005); intima has the highest value of D_1 (p<0.01) but is comparable with the value for thrombus (p=0.21). Media has the highest D_2 value compared with adventitia, thickened intima and thrombus (p<0.05); and thrombus has the lowest value of D_2 (p<0.05) but is comparable with that of intima (p=0.29).

In carotid atherosclerosis, media and FC have a comparable C_1 (p=0.33), significantly higher than those of lipid and IPH/T (p<0.05). Compared with IPH/T, the C_1 value of lipid is significantly higher (p=0.03). The value of D_1 for media, FC and lipid is comparable (p>0.05), and IPH/T has the lowest value of D_1 compared with media and FC (p<0.01) but is comparable with that of lipid (p=0.87). Both media and FC have a comparable D_2 (p=0.33), as do lipid and IPH/T (p=0.39); both media and FC have a significantly higher D_2 than either lipid or IPH/T (p<0.005).

Media is the only common tissue type in normal aorta, aortic aneurysm and atherosclerotic plaque. Only material constants of media of these three types of tissue were therefore compared. The C_1 value of media from normal aorta, aortic aneurysm and carotid atherosclerotic plaque is comparable (p>0.05), as is D_1 (p>0.05). However, D_2 has the capacity to differentiate all three types of tissues. In general, smaller values of D_2 correspond to more extensible tissues (Figure 4.5D). The value of D_2 for the media from both aneurysm and plaque is significantly larger than that from normal aorta (p<0.0001), and the D_2 value of media from plaque is much larger than that from aneurysm (p=0.022).

4.4.3 Material constants and microstructural architecture of the tissue

24 tissue strips adjacent to those used for mechanical testing from the 8 aneurysmal samples were submitted for histological examination to study the collagen (Figure 4.5) and elastin in the tissue microstructure.

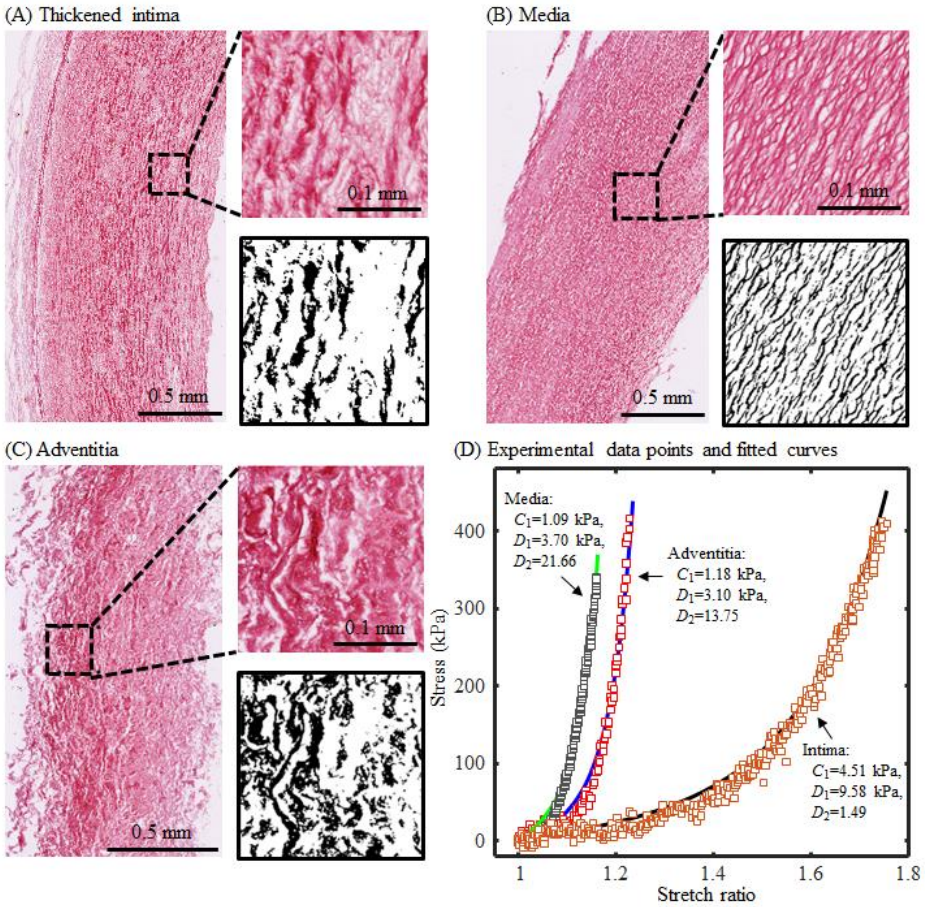

Figure 4.5. Representative Sirius Red stained images showing the collagen fibres in red in the thickened intima (A), media (B) and adventitia (C) of an aortic aneurysm. D: stress-stretch curves of the tissue strips that are shown in A-C. (More extensible tissues have smaller D_2).

As shown in Figure 4.6A, the area percentage of elastin in both thickened intima and media is higher than the adventitia, and thickened intima has the lowest area percentage of collagen (Figure 4.6B), followed by media, where the adventitia has the highest area percentage of collagen. The difference in elastin content in these three layers (Figure 4.6A) is consistent with the difference in C_1 value as listed in Table 4.2.

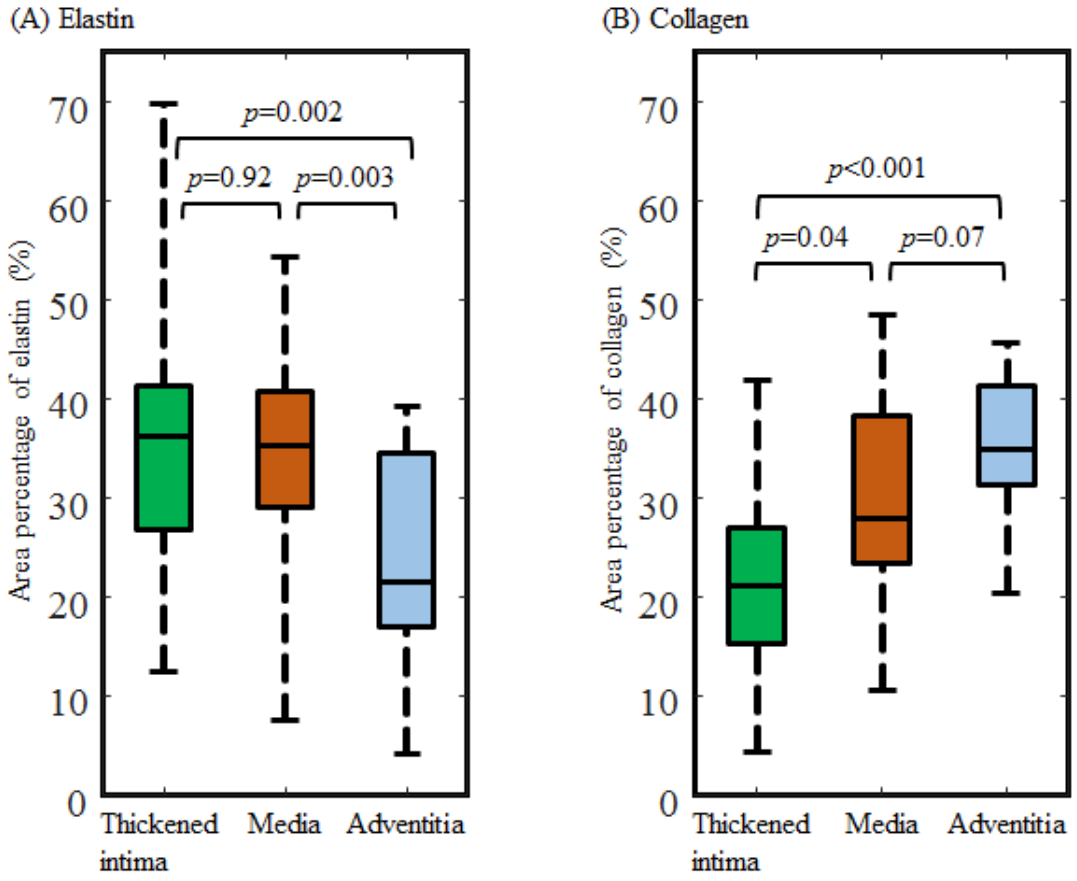

Figure 4.6. Comparison of area percentage of elastin (A) and collagen (B) contents in the thickened intima, media and adventitia from the 8 aortic aneurysms.

Compared with the media, the collagen fibre dispersion, κ is much bigger (0.14 [0.13, 0.15] vs 0.23 [0.19, 0.25], p=0.008), and the waviness, ω is higher in the adventitia (0.07 [0.09, 0.12] vs 0.16 [0.15, 0.18], p=0.008). When κ, ω, D_1 and D_2 of media and adventitia were pooled, κ was inversely associated with D_2 (ρ=-0.61, p=0.014) and ω was inversely associated with D_2 (ρ=-0.73, p=0.002) (Figure 4.7); but no association was found between D_1 and κ or ω.

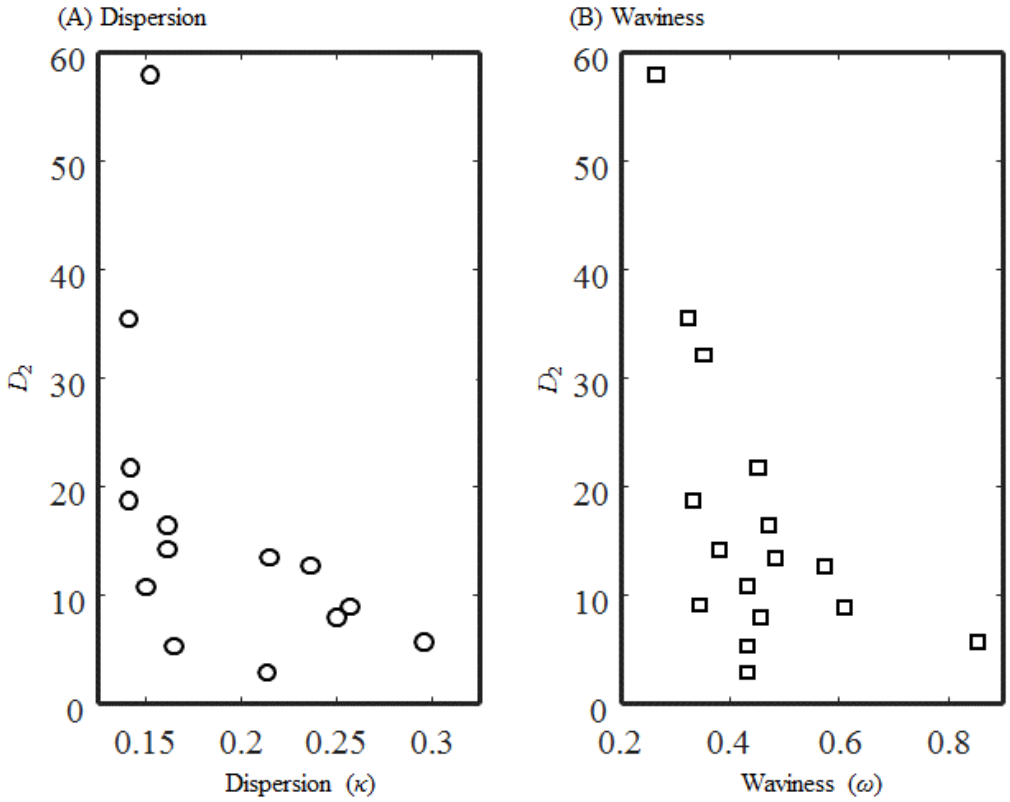

Figure 4.7. The association between D_2 and (A) collagen fibre dispersion, κ and (B) waviness, ω.

4.5 Discussion

Bayesian inference estimates the distribution of material parameters in the constitutive model rather than finding their point-based estimations. It is used in this study to avoid the sensitivity to initial guesses when OLS method is used, allowing characterisation of the tissue through comparison of material constants. Obtained results indicated that C_1 , D_1 and D_2 were tissue type dependent. In particular, D_2 is the most sensitive parameter in differentiating tissues of distinct arterial layers from a single type of sample, or of the same layer between different type of samples; and D_2 is also associated with tissue architectures, e.g., fibre dispersion and waviness. In general, atherosclerotic tissues have the biggest D_2 values, followed by those from aneurysms and then normal aortas.

A proper choice of both SEDF and material constants is important for material stability and numerical convergence in computational studies that aim to predict stress distribution within the lesion[15].

The robustness of the SEDF is reflected by its ability to reproduce several modes of deformation, including, but not limited to uniaxial, biaxial and pure shear deformations[15]. Considering its stability and broad capacity in characterizing distinct material properties, the modified Mooney-Rivlin SEDF appears as a practical choice for mechanical analyses to predict the critical mechanical conditions within vascular lesions, such as carotid atherosclerotic plaques[15]. In this study, stress-stretch data from uniaxial testing was used, since it is nearly impossible to perform biaxial and pure shear testing with atherosclerotic tissues, because of their non-homogeneity and irregularity.

Regarding material constants of the SEDF, using constraints on their values can make the SEDF convex to achieve material stability to a particular extent[25]. Although a wide search with multiple initial guesses might alleviate the sensitivity of material constants to the initial guess, an exhaustive search is not possible and moreover, different sets of material constants may all have a satisfactory regression, e.g., with a small γ value. However, this does not imply that the OLS provides uniqueness to the material constants as Bayesian approach does in a large space. For example, the initial guesses of (1, 1, 1) and (0, 1, 0) can both fit the experimental data points shown in Figure 4.3 well, but with very different material constants, in particular, C_1 and D_1 (Table 4.1). The employment of Bayesian inference-based approach can eliminate such dependencies. It provides an estimation of the distribution of the parameters instead of a point estimation. The expectation of the distribution is used as the determined material constant which provides the uniqueness, in particular for noisy data (please refer to Figure *4.8* and Table 4.3 and the associated discussion below for details).

The non-uniqueness of parameter estimation associated with OLS might be avoided with a hybrid approach by searching different initial guesses aiming at a global minimisation within a large space. MultiStart Algorithm[26] implemented in Global Optimization Toolbox of MATLAB was used to follow this principle. A parameter study was performed to compare the difference between this and Bayesian inference-based approaches. A standard stretch-stress curve was generated using C_1 =3.26 kPa, D_1 =3.67 kPa, D_2 =2.16 that fit the experimental data shown in Figure 4.3, which is illustrated as the *No noise* curve in Figure *4.8*.

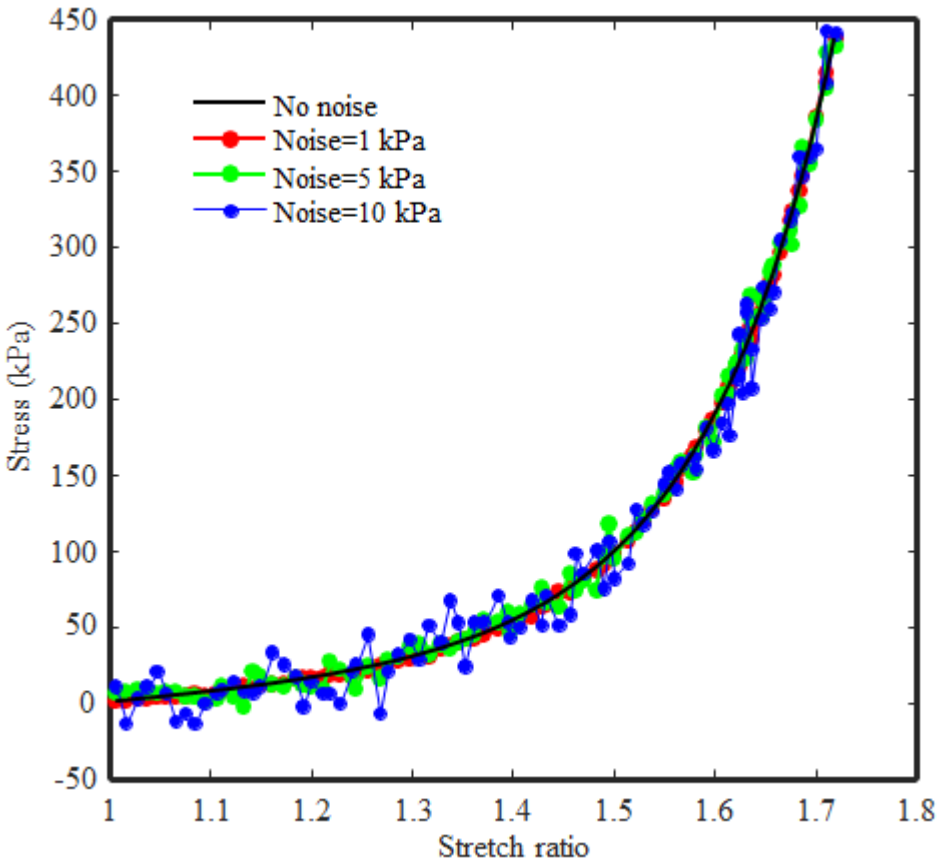

Figure 4.8. Representative curves with Gaussian noise and with different standard deviations (The template curve was generated with C_1 = 3.26 kPa, D_1 = 3.67 kPa, and D_2 = 2.16).

Gaussian noise with three different standard deviations (ε =1, 5 and 10 kPa) was added to the curve (Figure *4.8*) and the noising process was repeated independently for 1000 times for each σ to generate 1000 artificial curves. OLS with initial guesses of (0, 1, 0) and (1, 1, 1), OLS with MultiStart Algorithm and Bayesian inference-based approach were used to identify the constants as listed in Table 4.3.

In the case of no noise, the OLS method with initial guess (0, 1, 0) found a local minimum, where the fitted results did not match the gold standard well. The OLS method with (1, 1, 1) achieved equally good fitting results compared to OLS method with global minimisation algorithm, indicating (1, 1, 1) is a good initial guess. The Bayesian method found approximately the same parameters, with a gamma value of 0.1%. For all approaches, the shifting mean value of constants and increased γ at higher noise levels were found.

Table 4.3. Comparison of material constant determination methods (results are presented in Mean±SD).

Noise (kPa)	**Methods for the determination of material constants**	C_1 **(kPa)**	D_1 **(kPa)**	D_2	**γ (%)**
0	OLS - Initial values (0, 1, 0)	1.19	4.36	2.06	0.60
	OLS - Initial values (1, 1, 1)	3.26	3.67	2.16	0.00
	OLS with MultiStart Algorithm	3.26	3.67	2.16	0.00
	Bayesian inference	3.25	3.67	2.16	0.10
1	OLS - Initial values (0, 1, 0)	1.64±0.86	4.22±0.30	2.08±0.04	1.0±0.1
	OLS - Initial values (1, 1, 1)	3.35±0.48	3.65±0.16	2.16±0.02	0.9±0.1
	OLS with MultiStart Algorithm	3.36±0.47	3.65±0.15	2.16±0.02	0.9±0.1
	Bayesian inference	3.32±0.48	3.67±0.16	2.16±0.03	0.9±0.1
5	OLS - Initial values (0, 1, 0)	1.57±1.75	4.30±0.60	2.08±0.10	4.6±0.5
	OLS - Initial values (1, 1, 1)	3.71±2.28	3.62±0.73	2.18±0.12	4.5±0.5
	OLS with MultiStart Algorithm	3.71±2.28	3.62±0.74	2.18±0.12	4.5±0.5
	Bayesian inference	3.56±1.65	3.66±0.54	2.18±0.10	4.9±0.7
10	OLS - Initial values (0, 1, 0)	1.71±2.70	4.37±1.00	2.08±0.18	9.0±1.0
	OLS - Initial values (1, 1, 1)	4.41±3.90	3.54±1.23	2.22±0.23	9.0±1.1
	OLS with MultiStart Algorithm	4.41±3.90	3.54±1.23	2.22±0.23	9.0±1.1
	Bayesian inference	4.20±2.32	3.59± 0.73	2.20±0.15	9.8±1.5

Bayesian method obtained similar mean values and standard deviations to the OLS method with global minimization, although when the noise level increased to 5 kPa and higher, Bayesian inference-based approach performed slightly better with a closer mean value to the gold standard and smaller standard deviation. It can be expected that its performance could be further improved with an appropriate *prior*. Other sophisticated minimization algorithms, e.g., genetic algorithms[27], are also available to achieve a global optimum within a large space to avoid non-uniqueness in material parameters identification.

The material constants, C_1 , D_1 and D_2 contribute differently to the stress when the tissue strip is subject to stretching as shown in Equation 4.2. Taking the results in Figure 4.3 as an example, when λ=1.2 the term with C_1 contributes 21.2% to the total stress and the term with D_1 and D_2 contributes the rest; when λ=1.6, the proportion from the term with C_1 decreases to 6.3%, and that from D_1 and D_2 increases to 93.7%. In general, the change in curve is insensitive to the change of C_1, more prominent with changes in D_1, and very profound with changes in D_2.

The quantitative relationship between the stress change and the change of constants can be found through individual partial derivatives,

$$\frac{\partial \sigma_{11}(\lambda)}{\partial C_1} = 2\left(\lambda^2 - \frac{1}{\lambda}\right) \tag{4.13}$$

$$\frac{\partial \sigma_{11}(\lambda)}{\partial D_1} = 2\left(\lambda^2 - \frac{1}{\lambda}\right) D_2 e^{D_2\left(\lambda^2+\frac{2}{\lambda}-3\right)} \tag{4.14}$$

$$\frac{\partial \sigma_{11}(\lambda)}{\partial D_2} = 2D_1\left(\lambda^2 - \frac{1}{\lambda}\right)\left[1 + D_2\left(\lambda^2 + \frac{2}{\lambda} - 3\right)\right] e^{D_2\left(\lambda^2+\frac{2}{\lambda}-3\right)} \tag{4.15}$$

Therefore, the change in each constant has a distinct effect on the calculated stress. Figure 4.9 shows the stress-stretch curves when C_1(=3.26 kPa), D_1(=3.67 kPa) and D_2(=2.17) decrease by 50% and increase by 50% in intervals of 10%.

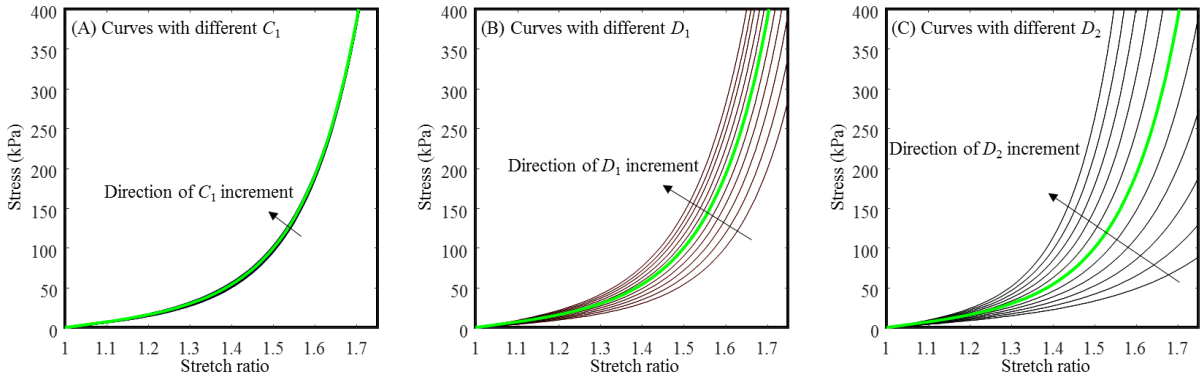

Figure 4.9. The change of stress-stretch curves with the change of C_1, D_1 and D_2 (all constants decrease and increase 50% from the baseline values of C_1= 3.26 kPa, D_1= 3.67 kPa and D_2= 2.17, which are from the case shown in Figure 4.3).

The extracellular matrix components, specifically the mix of elastin and collagen in the vessel wall, determine the passive mechanical properties of large arteries. C_1, D_1 and D_2 might be used to characterise their mechanical behaviour under physiological and pathological conditions. In an unloaded healthy artery, both elastin and collagen appear undulated and wavy, where they straighten as the artery begins to bear load[28]. The elastin is mostly straight at physiological pressures[28]. Upon involvement of C_1, the term in Equation 4.1 and Equation 4.2 may reflect this procedure. In contrast to the elastin, less than 10% of the collagen fibres are straight and load-bearing at physiological pressures[29]. As the pressure increases, more collagen fibres become load-bearing and their stiffness limits arterial distension, providing the classical nonlinear behaviour observed in arterial mechanics[30]. This is characterised by the term in Equation 4.1 and Equation 4.2 with D_1 and D_2 involvement, particularly, D_2 dominates the rate of increase in stress. Elastin and collagen fibres can be degraded by several members of the MMP family. Increased expression of MMP-1 and MMP-9, for example, have been reported in aneurysms, which are characterized by fragmentation of both elastin and collagen fibres[31], where the increased expression of MMP-2 is localized to sites of fragmentation in the elastic lamellae[32]. These pathological changes lead to a stiffer artery, that is, stress increases quicker during stretching. The bigger D_2 value of aneurysmal and atherosclerotic tissues can be the consequence of these pathological changes.

It is worth noting that the modified Mooney-Rivlin SEDF is a phenomenological approximation of the material behaviour. Information from microstructure was not used, and therefore material parameters C_1 , D_1 and D_2 can only loosely link to the fibre architecture. Moreover, the exponential term describing the toe region in the stress-stretch curve is oversimplified and unbounded, allowing the tangential stiffness to rise infinitely with increasing stretch. Such limitations can be overcome by employing a more microstructurally informed model, which takes gradual recruitment of collagen fibres into consideration[33–35]. In their stress-free state, the collagen fibres rest in a crimped configuration with waviness following a right-skewed distribution[36,37]. As a result, the likelihood of collagen fibres becoming newly recruited follows a Gamma distribution,

$$\Gamma(\bar{I}_1;\alpha,\beta) = \frac{\beta^{\alpha}(\bar{I}_1-3)^{\alpha-1}e^{-\beta(\bar{I}_1-3)}}{\Gamma(\alpha)} \tag{4.16}$$

where, Γ_α is a complete Gamma function, and α and β are the shape and rate parameters.

Both parameters relate to the microstructure of the tissue, with $\alpha\beta^{-1}$ and $\alpha\beta^{-2}$ being the expectation and variance of $\bar{I}_1 - 3$ at which the collagen fibres become recruited. Integrating this probability density function gives the cumulative likelihood of collagen fibres contributing to stiffness. Thus, SEDF at a given stretch level can be obtained as follows,

$$W = C_1(\bar{I}_1 - 3) + D_1 \int_0^{\bar{I}_1} \Gamma(x;\, \alpha, \beta) dx \qquad (4.17)$$

where, C_1 and D_1 reflect the contribution (incorporating fibre stiffness, alignment and relative volume fraction) of elastin and collagen fibres, respectively. Such a formulation offers more flexibility in fitting and better insights in the mechanical response[34,35], however the whole fitting procedure is much more complicated than either OLS or Bayesian inference-based estimation. Given that phenomenological models already lead to comparable goodness of fit[34], we conducted the present study using modified Mooney-Rivlin models for conciseness.

It is important to reiterate that the experimental data used in this study were mostly from two previous reports[14,16]. The non-uniqueness in the material constants identification using OLS was mentioned in one of them[14]. To obtain a determined set of material constants for each type of tissue, an energy-based average algorithm was employed. It is certain that the findings and conclusions obtained in this study do not relate to any of these two previous reports.

The obtained estimations listed in Table 4.2 can serve as *priors* for future studies to improve the accuracy of the estimation. Despite the interesting findings, limitations exist in this study: (1) the stress-stretch curve used in this study was from uniaxial tensile tests and modified Mooney-Rivlin SEDF is an isotropic model, so that the anisotropy was not considered. The anisotropic SEDF considering microstructures can be found in studies by Gasser et al.[24]; (2) modified Mooney-Rivlin SEDF usually can fit the whole stress-stretch curve of the normal aorta well, but not for all tissue strips of aneurysm and atherosclerotic plaque, in particular, in the region with a low stretch level (Figure 4.5D).

4.6 Conclusion

This study demonstrated for the first time that material constants of SEDFs show variations both between distinct arterial layers from a single type of lesion, and between samples of the same arterial layer that are obtained from different lesion types. Moreover, the material constants were also found to associate with the microstructural architecture of diseased arterial tissues. Nevertheless, in contrast to the traditionally used OLS method, utilisation of relatively robust curve fitting methodologies (such as the Bayesian inference-based estimation) is essential for accurate determination of material constant values. The obtained constants reflect the physiological and pathophysiological state of healthy and diseased arterial tissues. Furthermore, the material constants can also be used with their SEDFs to perform mechanical simulations for studying the critical mechanical conditions of diseased arteries.

4.7 References

1. Wang, S. *et al.* Bayesian inference-based estimation of normal aortic, aneurysmal and atherosclerotic tissue mechanical properties: from material testing, modelling and histology. *IEEE Trans. Biomed. Eng.* 1–1 (2019). doi:10.1109/TBME.2018.2886681
2. North American Symptomatic Carotid Endarterectomy Trial Collaborators *et al.* Beneficial effect of carotid endarterectomy in symptomatic patients with high-grade carotid stenosis. *N. Engl. J. Med.* **325,** 445–53 (1991).
3. Lederle, F. A. *et al.* Immediate repair compared with surveillance of small abdominal aortic aneurysms. *N. Engl. J. Med.* **346,** 1437–44 (2002).
4. Nicholls, S. C., Gardner, J. B., Meissner, M. H. & Johansen, H. K. Rupture in small abdominal aortic aneurysms. *J. Vasc. Surg.* **28,** 884–8 (1998).
5. Powell, J. T., Brown, L. C., Greenhalgh, R. M. & Thompson, S. G. The rupture rate of large abdominal aortic aneurysms: is this modified by anatomical suitability for endovascular repair? *Ann. Surg.* **247,** 173–9 (2008).
6. Asanuma, K., Magid, R., Johnson, C., Nerem, R. M. & Galis, Z. S. Uniaxial strain upregulates matrix-degrading enzymes produced by human vascular smooth muscle cells. *Am. J. Physiol. Heart Circ. Physiol.* **284,** H1778-84 (2003).

7. Vallabhaneni, S. R. *et al.* Heterogeneity of tensile strength and matrix metalloproteinase activity in the wall of abdominal aortic aneurysms. *J. Endovasc. Ther.* **11,** 494–502 (2004).

8. von Offenberg Sweeney, N. *et al.* Cyclic strain-mediated regulation of endothelial matrix metalloproteinase-2 expression and activity. *Cardiovasc. Res.* **63,** 625–34 (2004).

9. Maier, A. *et al.* Correlation of biomechanics to tissue reaction in aortic aneurysms assessed by finite elements and [18F]-fluorodeoxyglucose-PET/CT. *Int. j. numer. method. biomed. eng.* **28,** 456–71 (2012).

10. Huang, Y. *et al.* High Structural Stress and Presence of Intraluminal Thrombus Predict Abdominal Aortic Aneurysm 18F-FDG Uptake: Insights From Biomechanics. *Circ. Cardiovasc. Imaging* **9,** (2016).

11. Stevens, R. R. F. *et al.* Biomechanical changes during abdominal aortic aneurysm growth. *PLoS One* **12,** e0187421 (2017).

12. Thondapu, V. *et al.* Biomechanical stress in coronary atherosclerosis: emerging insights from computational modelling. *Eur. Heart J.* **38,** 81–92 (2017).

13. Tuenter, A. *et al.* High shear stress relates to intraplaque haemorrhage in asymptomatic carotid plaques. *Atherosclerosis* **251,** 348–354 (2016).

14. Teng, Z. *et al.* Material properties of components in human carotid atherosclerotic plaques : a uni-axial extension study. *ACTA Biomater.* **10,** 5055–5063 (2014).

15. Teng, Z. *et al.* The influence of constitutive law choice used to characterise atherosclerotic tissue material properties on computing stress values in human carotid plaques. *J. Biomech.* **48,** 3912–21 (2015).

16. Teng, Z. *et al.* Layer- and Direction-Specific Material Properties, Extreme Extensibility and Ultimate Material Strength of Human Abdominal Aorta and Aneurysm: A Uniaxial Extension Study. *Ann. Biomed. Eng.* (2015). doi:10.1007/s10439-015-1323-6

17. Galton, F. Regression Towards Mediocrity in Hereditary Stature. *J. Anthropol. Inst. Gt. Britain Irel.* **15,** 246 (1886).

18. Farnum, N. R. Improving the Relative Error of Estimation. *Am. Stat.* **44,** 288–289

(1990).

19. Madireddy, S., Sista, B. & Vemaganti, K. A Bayesian approach to selecting hyperelastic constitutive models of soft tissue. *Comput. Methods Appl. Mech. Eng.* **291,** 102–122 (2015).

20. Madireddy, S., Sista, B. & Vemaganti, K. Bayesian calibration of hyperelastic constitutive models of soft tissue. *J. Mech. Behav. Biomed. Mater.* **59,** 108–127 (2016).

21. Doraiswamy, S., Criscione, J. C. & Srinivasa, A. R. A technique for the classification of tissues by combining mechanics based models with Bayesian inference. *Int. J. Eng. Sci.* **106,** 95–109 (2016).

22. Holzapfel, G. A., Gasser, T. C. & Ogden, R. W. A New Constitutive Framework for Arterial Wall Mechanics and a Comparative Study of Material Models. *J. Elast.* **61,** 1–48 (2000).

23. Holzapfel, G. A. & Ogden, R. W. Constitutive modelling of arteries. *Proc. R. Soc. A Math. Phys. Eng. Sci.* **466,** 1551–1597 (2010).

24. Gasser, T. C., Ogden, R. W. & Holzapfel, G. A. Hyperelastic modelling of arterial layers with distributed collagen fibre orientations. *J. R. Soc. Interface* **3,** 15–35 (2006).

25. Ogden, R. W. in *Biomechanics of Soft Tissue in Cardiovascular Systems* (eds. Holzapfel, G. A. & Ogden, R. W.) 65–108 (Springer Vienna, 2003). doi:10.1007/978-3-7091-2736-0_3

26. Ugray, Z. *et al.* Scatter Search and Local NLP Solvers: A Multistart Framework for Global Optimization. *INFORMS J. Comput.* **19,** 328–340 (2007).

27. Chaparro, B. M., Thuillier, S., Menezes, L. F., Manach, P. Y. & Fernandes, J. V. Material parameters identification: Gradient-based, genetic and hybrid optimization algorithms. *Comput. Mater. Sci.* **44,** 339–346 (2008).

28. Clark, J. M. & Glagov, S. Transmural organization of the arterial media. The lamellar unit revisited. *Arteriosclerosis* **5,** 19–34 (1985).

29. Armentano, R. L. *et al.* Assessment of elastin and collagen contribution to aortic elasticity in conscious dogs. *Am. J. Physiol. Circ. Physiol.* **260,** H1870–H1877 (1991).

30. Wolinsky, H. & Glagov, S. Structural Basis for the Static Mechanical Properties of the

Aortic Media. *Circ. Res.* **14,** 400–13 (1964).

31. Tamarina, N. A., McMillan, W. D., Shively, V. P. & Pearce, W. H. Expression of matrix metalloproteinases and their inhibitors in aneurysms and normal aorta. *Surgery* **122,** 264-71; discussion 271–2 (1997).

32. Li, Z., Froehlich, J., Galis, Z. S. & Lakatta, E. G. Increased expression of matrix metalloproteinase-2 in the thickened intima of aged rats. *Hypertens. (Dallas, Tex. 1979)* **33,** 116–23 (1999).

33. Bank, A. J. *et al.* Contribution of collagen, elastin, and smooth muscle to in vivo human brachial artery wall stress and elastic modulus. *Circulation* **94,** 3263–70 (1996).

34. Hill, M. R., Duan, X., Gibson, G. A., Watkins, S. & Robertson, A. M. A theoretical and non-destructive experimental approach for direct inclusion of measured collagen orientation and recruitment into mechanical models of the artery wall. *J. Biomech.* **45,** 762–71 (2012).

35. Sacks, M. S. Incorporation of experimentally-derived fiber orientation into a structural constitutive model for planar collagenous tissues. *J. Biomech. Eng.* **125,** 280–7 (2003).

36. Chen, H. *et al.* Biaxial deformation of collagen and elastin fibers in coronary adventitia. *J. Appl. Physiol.* **115,** 1683–93 (2013).

37. Rezakhaniha, R. *et al.* Experimental investigation of collagen waviness and orientation in the arterial adventitia using confocal laser scanning microscopy. *Biomech. Model. Mechanobiol.* **11,** 461–73 (2012).

Chapter 5

Stretch driven microstructural reorganisations in notched and unnotched tissue samples of porcine carotid arteries

The author of this dissertation carried out all of the work and analysis in this chapter except as specified below. The uniaxial stretching and simultaneous multiphoton microscope imaging experiments were carried out by Dr Graeham R. Douglas, Department of Engineering, University of Cambridge, who collected the raw data and transferred it to the author of this dissertation for the subsequent analysis.

5.1 Abstract

Artery is a fibrous material with collagen and elastin being key constituents. Uniaxial tensile tests with unnotched and notched tissue strips from four porcine carotid arteries loaded in the circumferential and axial (blood flow) directions were performed while imaging with multiphoton microscopy. Three dimensional images of the microstructure were acquired and processed to derive fibre structure at a series of stretch levels. At rest, fibres in the intima tended towards the axial direction and in the media the primary fibre orientation was about 45° relative to the circumferential direction. After stretching, fibres rotated towards the direction of stretch. In the circumferential strips, as the stretch increased from 1.00 to 1.75, the circular mean fibre orientation relative to the direction of stretching changed from 78° to 36° in the intima and from -40° to -24° in the media. The median fibre dispersion decreased from 0.29 to 0.27 in the intima and from 0.28 to 0.20 in the media. For notched samples, fibres rearranged themselves to redistribute loads away from the notch tip and to bridge the crack. Fibre structure changed as a consequence of stretching, which may provide an explanation of strain stiffening and fracture toughness material properties of arterial tissues.

5.2 Introduction

Rupture of the atherosclerotic plaque is the direct outcome of fibrous tissue fracture. Plaque fracture mechanisms are poorly understood, which limits the development of improved bioengineering-based techniques and parameters for risk assessment[1]. Collagen and elastin are the primary mechanical components of arterial tissue[2,3]. Therefore the collagen and elastin microstructure will contribute to the artery mechanical behaviour, including anisotropy, strain stiffening, and modes of failure[3]. This dependency of mechanical properties on fibre microstructure has been demonstrated for gelatin scaffold material[4], where notched samples were fixed under an applied stretch and then imaged using a scanning electron microscope. Failure mechanisms and fracture toughness were found to be highly dependent on the fibrous microstructure. Variance in microstructure between individuals and between specific locations in an artery may explain the wide range of results that are reported in experimental material studies. The highly localised nature of tissue microstructure could explain the poor performance of current risk metrics in predicting clinical events[5].

To better understand the mechanics of arteries, computational modelling has attracted considerable research focus. Material models have included the fibrous nature of the tissue[6], or even local fibre structures[7]. Phenomenological parameters for these models were fitted from material test data. Where fibre structure is included in a material model, properties are typically derived from an assumed fibre structure or from microscopy of unstretched tissue. However, significant changes to the fibre microstructure during stretching could dramatically affect the mechanical response of the tissue. Understanding these interactions requires imaging the stretched tissue microstructure.

Collagen fibre structure was characterised in healthy human thoracic aorta, abdominal aorta, and common iliac arteries by polarised light microscopy[8,9]. Most arterial layers had two families of fibres, each wound helically about the longitudinal axis of the vessel in opposing primary orientations. Fibres within each family were dispersed around the primary orientation[8,9]. The exception was the medial layer of common iliac arteries, which had a single fibre family that was oriented in the circumferential plane. The two-family helical systems in other samples had angles of approximately 45° to the axial direction, and were more axial in the adventitia, but more circumferential in the media. The fibres were mostly aligned with one another in the adventitia, and most dispersed in the intima. In all layers, the fibres were essentially tangential to the luminal surface, and their orientation had little or no radial component[8,9].

Multiphoton microscopy allows imaging of three dimensional (3D) microstructures without stains, preservatives, or coatings, which might alter the mechanical properties of the sample[10–13]. Therefore, multiphoton microscopy can be used *in situ* with materials testing to compare fibre structure at varying stretches[12]. Schriefl et al. has compared 3D fibre structures for the three artery layers in optically cleared human aorta[14]. Multiphoton microscopy has also been used with mechanical testing to study the relationship between fibre structure and mechanics under uniaxial loading[15], pressurisation[16], biaxial tension[17], bulge inflation[18], and pressurisation with axial tension[19].

In this study, unnotched and notched tissue strips of healthy porcine carotid arteries were stretched uniaxially, while 3D image stacks were acquired with a multiphoton microscope. The fibre microstructure was characterised by the orientation and fibre dispersion. The aims were to identify the degree to which the fibre structure change with increasing stretch and the details of fibre microstructural changes around defects. These experiments can be used to understand how fibre re-organisation affects artery stiffness and rupture.

5.3 Materials and methods

The uniaxial stretching and multiphoton microscope imaging of unnotched and notched porcine carotid artery tissue strips, and the analysis on their microstructural reorganisations are described in this section. The work in sections **5.3.1**, **5.3.2** and **5.3.3** were carried out by Dr Graeham R. Douglas, as described in his thesis[20]. Brief descriptions of the utilised protocols are given below. The collected raw data was transferred to the author of this dissertation, who carried out the image processing described in section **5.3.4** and data analysis.

5.3.1 Sample selection and preparation

Four porcine carotid arteries were harvested by an abattoir (Leech and Sons, Melbourn, Cambridgeshire, UK) from healthy animals that were slaughtered for butchering. The arteries were refrigerated at 4°C and used in experiments between 24 and 72 hours after harvesting. The arteries had connective tissues, adventitia and minor branches removed. From each artery, two axial and two circumferential strips were prepared for mechanical testing with approximate dimensions of 1.5 mm × 0.7 mm × 15 mm (width × thickness × gauge length). One of each paired sample was notched through the thickness of the strip, with a notch depth of about a third of the strip's width, to mimic tissue damage and investigate the fibre structure around cracks. The coordinate system for artery and tissue strips are shown in Figure 5.1.

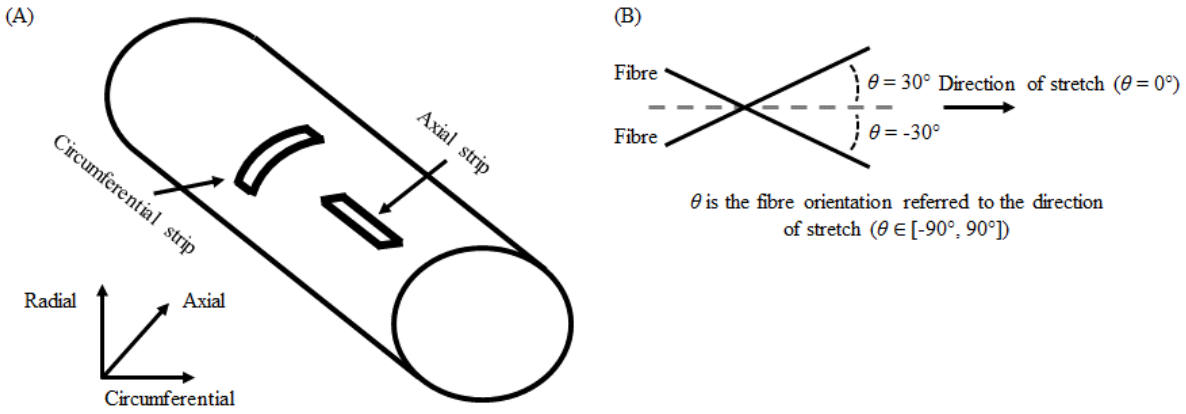

Figure 5.1. Schematic drawing for (A) the direction of tissue strips, and (B) fibre orientation related to the direction of stretch.

5.3.2 Uniaxial tensile testing

A custom uniaxial tensile testing system was used comprising a motorised linear stage (Miniature Steel Motorised Linear Stage, Newport Corporation, USA), a motor controller (SMC100-PP, Newport Corporation, USA), a custom-made linear load cell, and a data acquisition module (USB-6002, National Instruments, USA). LabVIEW software (National Instruments, USA) was used to operate the uniaxial tensile testing apparatus.

Tissue strips were immersed in distilled water and clamped at each end with their luminal surfaces towards the microscope lens. The clamp at one end of the strip was attached to the linear stage and the clamp at the other end was attached to the force sensor. Remaining pretension or sag in the samples was removed and each sample was preconditioned with a stretch ratio of ~1.25, repeated 5 times.

During each test, the linear stage was moved in 50 μm steps with a displacement rate of approximately 7 μm per second. Therefore, the loading can be considered quasi-static. Loading was paused every 500 μm for about 90 seconds to scan the fibre structure of the sample. The pauses caused stress relaxation, which decreased incremental tension by about 10% at each displacement. Stretch of the sample (λ) was calculated from the slack length of the sample (l_0) and displacement (x) as:

$$\lambda = \frac{x + l_0}{l_0} \tag{5.1}$$

5.3.3 Multiphoton microscope imaging

In multiphoton microscopy, excitation photons from the light source undergo non-linear molecule-dependent interaction with the sample, which produces emission photons through two mechanisms: second harmonic generation (SHG) and two-photon fluorescence (TPF)[12,13]. SHG photons are produced by collagen (but not elastin) at a wavelength which is half of that of the excitation photons. The SHG signal has a high intensity for a small bandwidth around this emission wavelength[13], while the TPF has emission for both collagen and elastin with a wide bandwidth of emission wavelengths (elastin peak at about 495 nm, combined material peak at about 510 nm)[12].

In this study, a multiphoton microscope (LaVision BioTec TriM Scope II, Germany, with an Insight Deepsee light source, Spectra-Physics, USA) was used to image the microstructure of each tissue strip during stretching. The microscope's laser wavelength was set to 830 nm. A 400-700 nm band-pass filter was used to remove any reflected excitation photons or low-wavelength photons, which are not produced by either SHG or TPF. The microscope and signal acquisition were controlled by the microscope's provided software, with the following parameters: gain of 70, line average of 2, scanning region of 400×400 μm^2, and an image size of 505×505 pixels. At every 500 μm increment of linear stage displacement, the tests were paused and the multiphoton microscope was manually focussed on the sample.

Image stacks were acquired starting from the luminal surface, then at 5.0 μm increments of depth until the emission signal had attenuated to such a degree that it was indistinguishable from noise. Typically, this would be at a stack depth of 200-300 μm.

Since the IEL appeared in the form of densely packed sheets of elastin with elliptic fenestrations (Figure 5.2), they did not provide useful data for fibre orientation analysis.

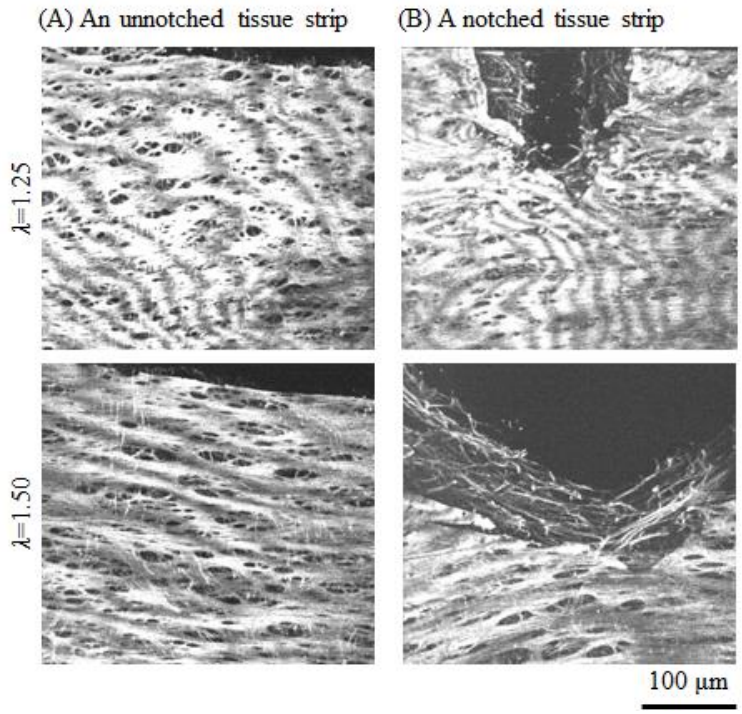

Figure 5.2. The IEL appeared in the form of wavy, densely packed sheets of elastin, which had elliptic fenestrations. As the dense sheet does not have a sparse fibrous structure like the intima and media layers, fibre structures for the IEL are not reported (Adapted with permission from[20]).

5.3.4 Image processing

Image processing was performed in MATLAB. Each multiphoton stack was first resampled to have isotropic voxels with 0.8 μm edges. The resulting smaller voxel size allowed separation of distinct arterial layers more accurately from one another, while increasing the number of slices that correspond to each arterial layer within a stack. Fibres were detected and fibre properties (fibre orientations (θ) and dispersion of fibre orientations (κ)) were calculated using a previously-reported algorithm[7,20]. Since θ is 180°-periodic, the circular mean, $\bar{\theta}$, was calculated where appropriate in this study,

$$\bar{\theta} = \frac{1}{2} atan2\left[\frac{\sum sin(2\theta)}{\sum cos(2\theta)}\right], \bar{\theta} \in [-90°, 90°] \quad (5.2)$$

Fibre properties were calculated for each slice of the multiphoton image stack, parallel to the axial-circumferential plane. Mean and median values of each fibre property was obtained by identifying the slices that correspond to each arterial layer, followed by separate averaging of fibre parameters that were computed from intima, media and adventitia slices of all samples. In this study, fibre orientation (θ) used the direction of stretching as the reference defining θ=0° (Figure 5.1B). Distribution of the collagen fibre orientations was characterised with the 2D planar form of the transversely isotropic and π-periodic von Mises distribution[6], which is detailed in **Chapter 4**. In brief, the von Mises distribution with a probability density function (PDF) of orientation, $P(\varphi)$ was assumed:

$$P(\varphi) = 4\sqrt{\frac{b}{2\pi}\frac{exp[b(cos(2\varphi)+1)]}{erfi(\sqrt{2b})}}, \varphi \in [0°, 180°] \quad (5.3)$$

where b is the concentration parameter, φ is the fibre orientation (θ) referenced to $\bar{\theta}$, and erfi(x) is the imaginary form of the error function. The dispersion parameter κ was computed as:

$$\kappa = \frac{1}{4}\int_0^{180} P(\varphi) sin^3\varphi d\varphi \quad (5.4)$$

where κ=0 corresponds to parallel fibres and κ=1/3 is a uniform (isotropic) distribution.

5.4 Results

Three layers of four healthy porcine carotid arteries were observed in the multiphoton microscopy-based uniaxial stretching experiments. Intact and notched tissue strips were tested in both the circumferential and axial directions. The intima was ~40 μm thick, the IEL was thinner (~10 μm), and the media was typically visible over a depth of 200-300 μm before the signal was too attenuated to image the tissue.

5.4.1 Fibre architecture in unnotched samples

Maximum intensity projection (MIP) images are used to visualise the 3D volume of each multiphoton stack as a 2D image (Figure 5.3). These MIP images are in the axial-circumferential plane, taking the maximum intensity from each radial column of voxels and from selected stack slices. The MIP images combine about 15 slices with a total thickness of 12 μm into a single image with the same length and width as the image stack slices.

Results from all four arteries showed that, in general, reorganisation during stretch made fibres more aligned towards the stretching direction. In the unstretched circumferential tissue strips (λ=1.00) the mean fibre orientation $\bar{\theta}$ was 78° in the intima and -40° in the media, relative to the circumferential loading direction. During stretch, fibres reorganised and tended towards the direction of stretch (the circumferential direction). When λ increased to 1.75, $\bar{\theta}$ decreased to 36° in the intima, and to -24° in the media. A similar result was observed in the axial tissue strips. For the unstretched sample, $\bar{\theta}$ was -19° in the intima and 33° in the media, relative to the axial loading direction. During stretching the fibres reorganised and tended towards the direction of stretch (the axial direction). When λ increased to 1.75, $\bar{\theta}$ decreased to -6.6°in the intima and to 6.9° in the media. Figure 5.4A and Figure 5.4B illustrate these changes in mean fibre orientation for the different samples as a function of stretch.

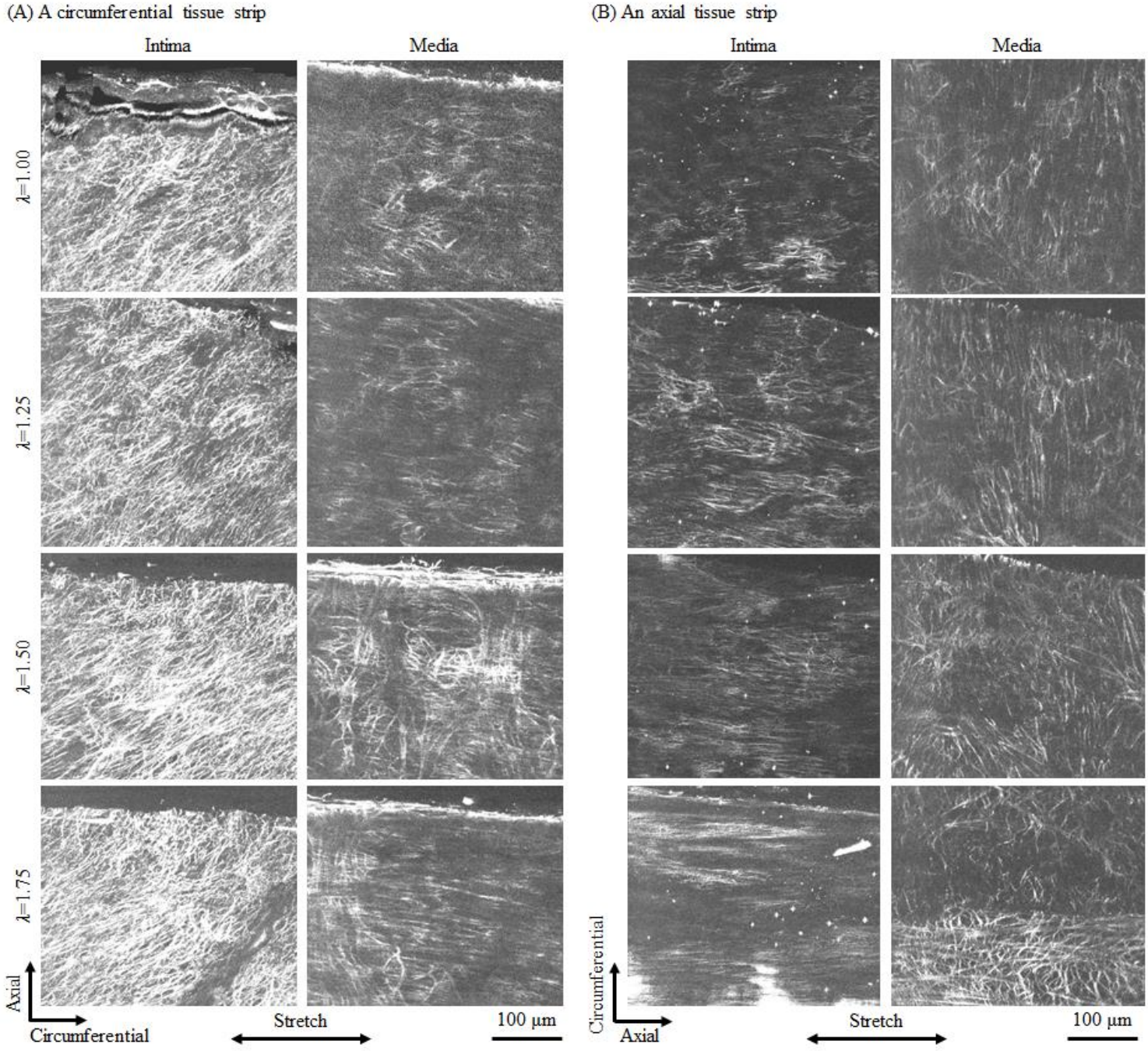

Figure 5.3. Multiphoton MIP images showing the fibre architecture in intima and media under different stretch levels (A: circumferential tissue strip; and B: axial tissue strip) (Adapted with permission from[20]).

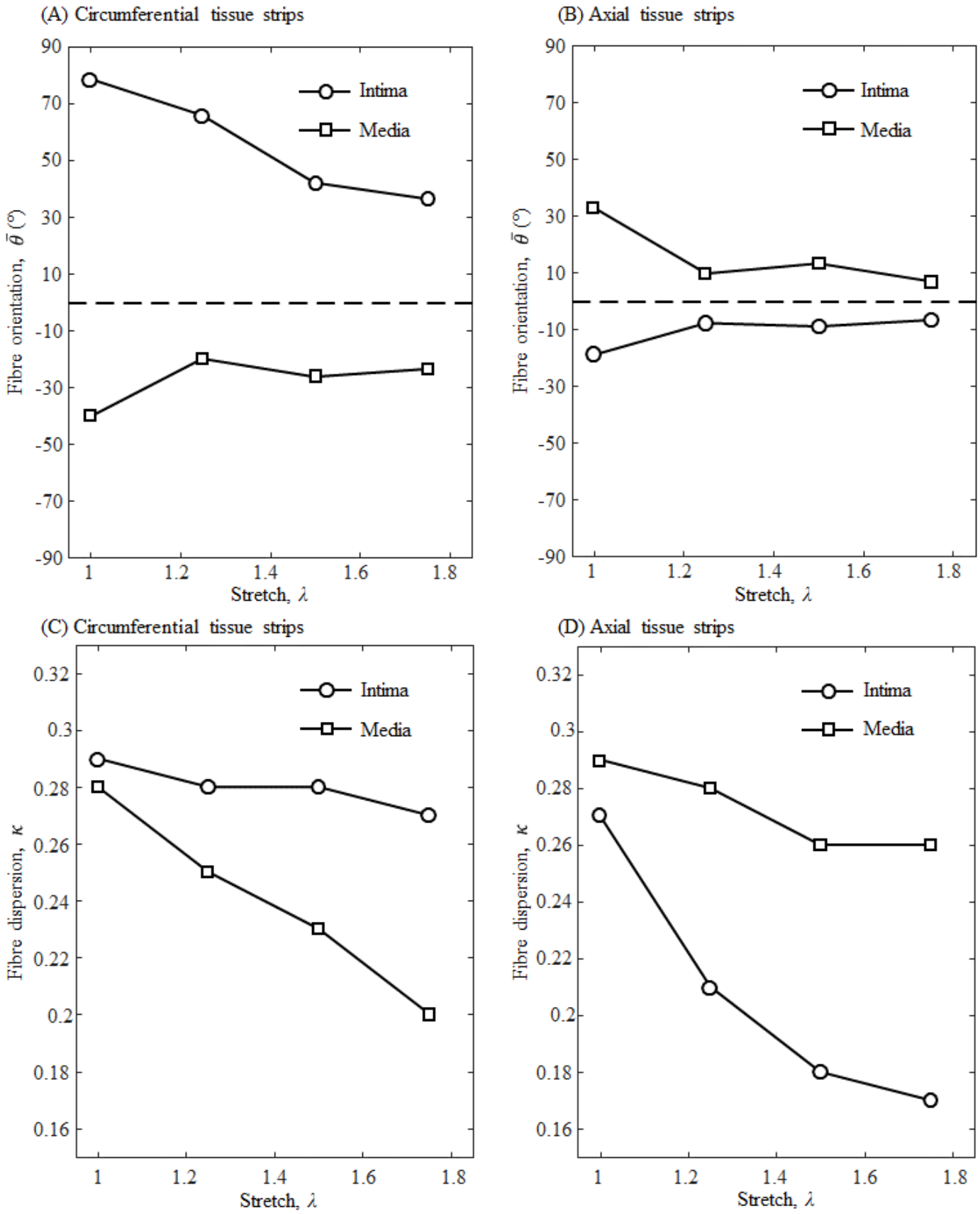

Figure 5.4. The change of fibre orientation (circular mean) (A and B) and dispersion (C and D) with increasing stretch of both circumferential (A and C) and axial (B and D) unnotched tissue strips.

Increasing stretch also led to a decreased dispersion (Figure 5.4C and Figure 5.4D). For example, κ decreased from 0.29 to 0.27 in the intima and from 0.28 to 0.20 in the media of circumferential strips stretched from λ=1.00 to λ =1.75. For axial strips, κ decreased from 0.27 to 0.17 in the intima and from 0.29 to 0.26 in the media when λ increased from 1.00 to 1.75. The changes to fibre structures corresponded to the layer's initial fibre orientation relative to the stretch direction ($\bar{\theta}$). For example, fibres in the media of circumferential strips were closer to the stretch direction than those in the intima. With increasing stretch, a greater change in $\bar{\theta}$ was observed for the intima and a greater change in κ was observed for the media. The opposite changes were observed for respective layers of strips stretched in the axial direction. Representative circumferential and axial tissue strips showing these fibre behaviours are discussed in detail in the following sub-sections.

5.4.1.1 A circumferential sample

Figure 5.3A shows MIP images of the intima and media at uniaxial stretch ratios (λ) of 1.00, 1.25, 1.50, and 1.75 for an unnotched circumferential tissue strip. The circumferential and stretch directions are horizontal on the figure. Fibres in the intima (left column of Figure 5.3A) had a single family of fibres that was oriented nearer to the axial than the circumferential direction. With increasing circumferential strain, the intimal fibres rotated to be more aligned with the circumferential direction. Deeper in the tissue, the media had dispersed fibres at low stretches (right column of Figure 5.3A), which were mainly oriented circumferentially. At increasing strain, the fibres aligned and sometimes showed a fibre family in both the circumferential and axial directions.

Figure 5.5A is a series of heat maps showing the fibre orientation distribution for the unnotched circumferential sample (Figure 5.3A) during stretching. The horizontal axis of each heat map plots the orientation, the vertical axis the depth into the sample and the colour gives the probability of the fibre orientation (the value of orientation probability density function, Equation 5.3).

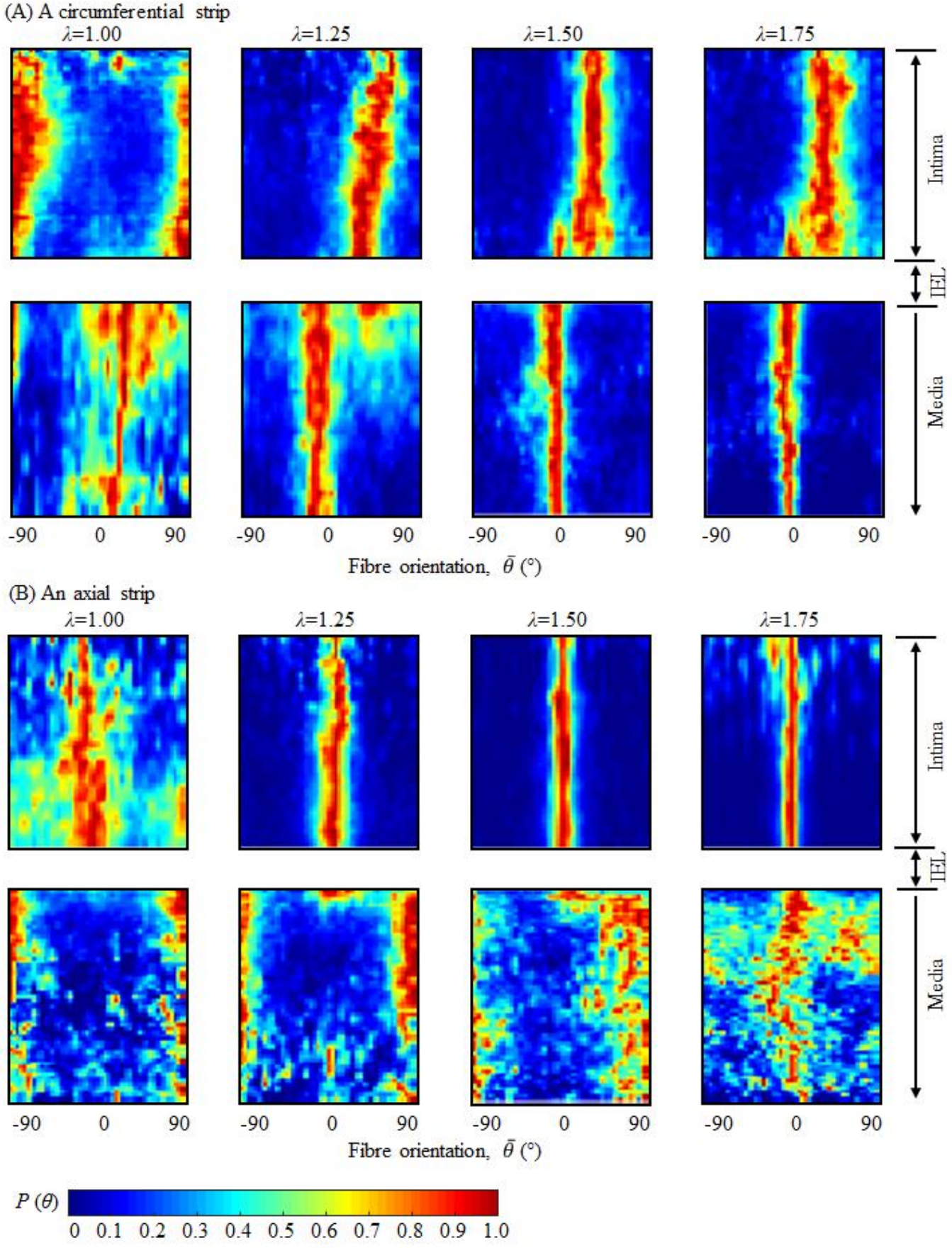

Figure 5.5. The density map of fibre orientation, θ, at different tissue depth from the intima to the media at different stretch levels for the same strips as shown in Figure 5.3. The thickness of each layer was normalised to be identical.

Each row of pixels in the heat map is equivalent to the orientation probability density function for one slice of the multiphoton stack. Each subplot corresponds to a different value of the stretch ratio (λ). The orientation angles are relative to the stretch direction, so that 0° corresponds to the direction of stretch (please refer to Figure 5.1B for the schematic drawing of the fibre orientation).

Initially (λ=1.00), fibres in the intima were more aligned with the axial direction (corresponding to a ±90° direction), whereas fibres in the media were more aligned with the circumferential direction (the 0° orientation). Fibres in the media had wider orientation distributions than the intima region.

With increasing stretch, the orientation of fibres in all layers tended towards the direction of stretch. Moreover, the fibre distributions narrowed in all tissue layers with increasing stretch, corresponding to decreasing fibre dispersion, as indicated by the narrowing of the band of reddish orientations with increasing λ.

5.4.1.2 An axial sample

An equivalent set of MIP images are shown for an unnotched axial tissue strip under uniaxial tension in Figure 5.3B. The axial and stretch directions are horizontal on the figure. For the axial test strip, fibres in the intima (left column of Figure 5.3B) had a preferred orientation towards the axial direction of the strip.

With increasing strain, intimal fibres rotated to be even more in the axial direction, while dispersion of the fibres decreased. The media of the axial test strips (right column of Figure 5.3B) had fibres that were initially oriented mainly in the circumferential direction but highly dispersed. Increasing stretch caused fibres in the media to become more oriented in the axial direction.

Figure 5.5B shows corresponding fibre orientation distributions for the unnotched axial sample shown in Figure 5.3. The 0° reference direction is set to be along the stretch direction (here, the axial direction).

At a low stretch (λ=1.00), the fibre distribution is similar to that of the circumferential sample with λ=1.00 (recall the loading direction used as reference has shifted by 90°). Fibres in the intima tended to be along the axial direction, while media fibres tended towards the circumferential direction. Fibres in both layers had relatively high dispersion. With increasing stretch, fibres in the intima remained in the axial direction and fibre dispersion decreased, with the reddish band in Figure 5.5B concentrating towards θ=0°. In the media, fibre dispersion initially increased with stretch, giving the broad distribution of orientations seen for λ=1.75. Upon further stretch, fibres in the media oriented towards the axial direction and fibre dispersion decreased as the reddish band became more concentrated towards θ=0°.

5.4.2 Changes in fibre organisation at crack tips

Notched samples were imaged by focusing the microscope lens to the crack (Figure 5.6). A 150×150 μm^2 region of interest (ROI) (e.g., the red dash box in Figure 5.6) was used for analysis to quantify the change of fibre structure during crack propagation. The ROI was manually placed such that the mid-point of the upper edge of the ROI was at the crack tip. Considerable reorganisation aligning the fibres towards the direction of stretch was observed at the crack tips, contributing to blunting of the notch at all depths in the artery. For the circumferential strips (Figure 5.6A), when stretch increased from 1.05 to 1.75, $\bar{\theta}$ in the RIO of intima decreased from 26° to 11°; and in the media it changed from -41° to -2.1°. For the axial strips (Figure 5.6B), when stretch increased from 1.05 to 1.75, $\bar{\theta}$ in the RIO of the intima decreased from -21° to -2.7°; and in the media it changed from 25° to 1.7°. The change of $\bar{\theta}$ during stretch in both layers of both circumferential and axial tissues strips is visualised in Figure 5.7A and Figure 5.7B. As with the unnotched strips, the fibre dispersion reduced with stretch (Figure 5.7C and Figure 5.7D). For example, κ decreased from 0.28 to 0.24 in the intima and from 0.28 to 0.23 in the media of circumferential strips stretched from λ=1.00 to λ=1.75. Axial strips had κ decrease from 0.27 to 0.18 in the intima and from 0.31 to 0.25 in the media, for the same change in stretch.

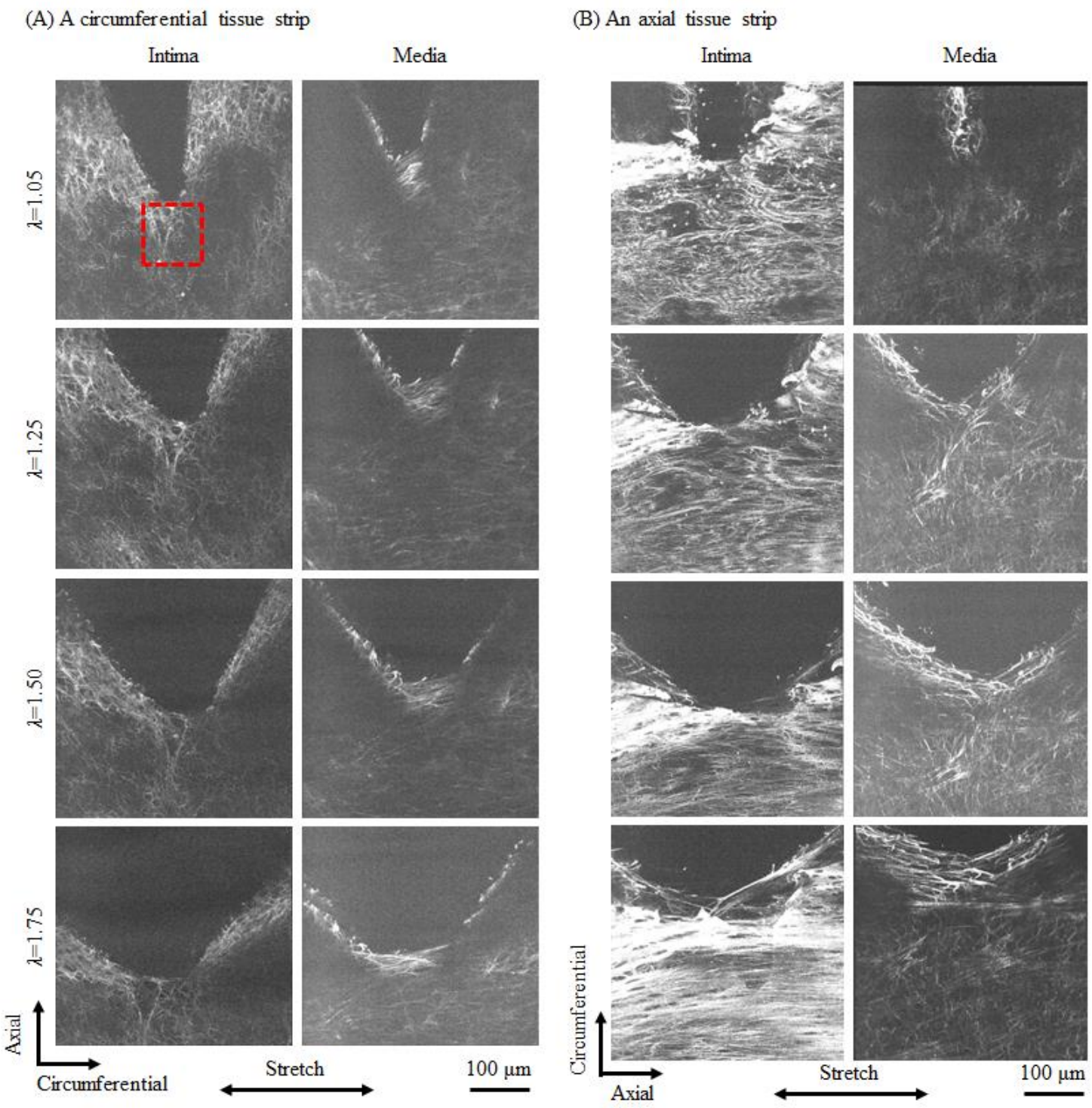

Figure 5.6. The multiphoton images showing the fibre at the crack tip of a circumferential (A) and an axial (B) tissue strip (The red dashed box shows a representative region of interest for analyses) (Adapted with permission from[20]).

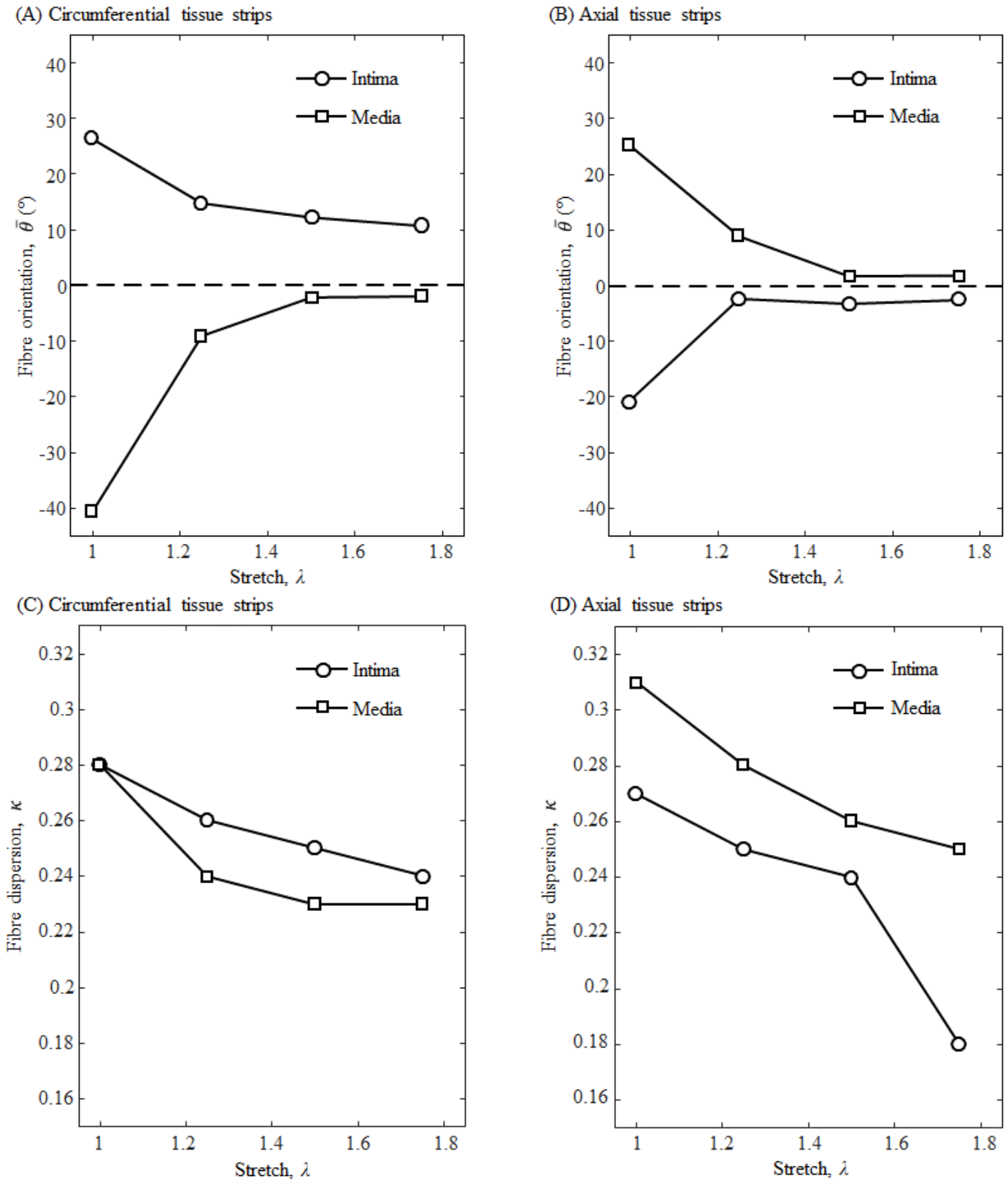

Figure 5.7. The change of fibre orientation (circular mean) (A and B) and dispersion (C and D) with increasing stretch of both circumferential (A and C) and axial (B and D) notched tissue strips.

5.5 Discussion

Fibres in the intima were primarily in the axial direction and those in the visible part of the media were primarily in the circumferential direction. With increasing stretch, including at physiological levels (~1.25), fibres in all layers rotated towards the direction of stretch (Figure 5.4A and Figure 5.4B) and tended to become less dispersed in orientation (Figure 5.4C and Figure 5.4D). For fibres initially aligned with the stretch direction, the effect was greater on fibre dispersion than orientation. For fibres initially less aligned with the stretch direction, the effect was greater on rotating fibres toward the stretch direction. Fibre bridging at the crack tip was always observed in the notched samples (Figure 5.6). Although there is variability among different samples (Figure 5.8), close observation of their individual trends reveals that, with an increase in the level of stretch, the orientation of fibres approaches 0° indicating that fibres in general rotate towards the direction of stretch.

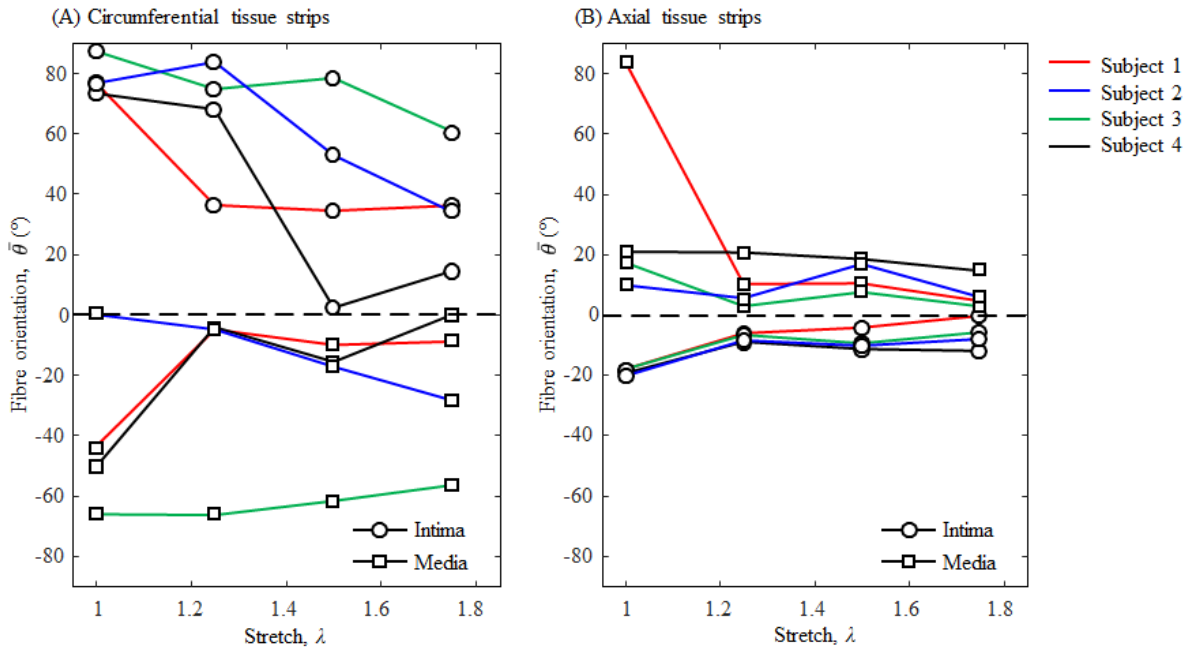

Figure 5.8. The change of fibre orientation (circular mean) with increasing stretch of unnotched circumferential (A) and axial (B) tissue strips.

Material tests under the multiphoton microscope provided a powerful way to link mechanics to fibre structure at different tissue depths and stretches. Constitutive material laws motivated by these observations could be developed with fibre reorganisation used to account for the non-linear strain stiffening behaviour of the material.

The alignment of fibres in the direction of stretch and decrease in fibre dispersion with increasing stretch has previously been demonstrated by experimental and computational studies of nonwoven fabrics[21,22].

Previous models of arterial tissue have largely ignored the effect of stretch-dependent fibre structure. For example, the constitutive model developed by Gasser et al. used a constant value for κ and an exponential function to account for strain-stiffening of the material[6]. Results suggest that a constitutive model which uses a strain-dependent κ would better represent the fibre architecture and may better account for strain-stiffening.

Significant fibre reorganisation and crack bridging were observed in the notched samples, which could be pertinent to understanding fibrous cap rupture. It has been reported that fissures were observed in 58% of carotid plaques and 20% of plaques had multiple fissures[23]. Thus, it appears that the mechanical conditions for initial tearing or fracture are common, but that initial fracture does not always lead to a critical rupture leading to clinical events. Fibre reorganisation and bridging might prevent crack propagation. Fibre bridging appeared to be more developed in the intima of axial strips compared to circumferential strips (Figure 5.6). Conversely, fibres in the media seemed to have more bridging in the circumferential strips. As the intima fibres were initially more in the axial direction and media fibres were more in the circumferential direction, the relative alignment between the crack and fibres may affect the mechanisms of fibre reorganisation near the crack. Ridruejo et al. have performed uniaxial tensile tests on notched nonwoven fabrics, whose fibrous microstructure resemble that of an arterial layer. They also observed significant amounts of fibre bridging across the crack tip, which spread the damage away from the crack and improved the load bearing capacity of the material. The initial notch size was also found to have an effect on the degree of fibre bridging and consequently on material strength[24].

Despite these interesting findings, there is still room for improvements that could be addressed in follow-up studies. Multiphoton techniques can distinguish between the type of fibre (collagen or elastin), which should be considered in the future[12]. Samples could be scanned with higher depth-resolution, to allow assessment of fibre structure in the radial planes of the tissue.

The light source power can be set to a depth-dependent profile, allowing for a stronger signal from deeper fibres with lower risk of photo damage to the tissue surface. Although efforts were made to reduce misalignments between the artery coordinate system (axial and circumferential), as-cut strips, clamps in test rig, and microscope coordinate system, this experiment was designed to understand changes to fibre structure with stretch. Other approaches may be more suited to study absolute fibre orientations.

5.6 Conclusion

In summary, uniaxial tensile tests with *ex vivo* multiphoton imaging found distinct fibre structures for the intima and media of porcine carotid arteries. With increasing stretch, fibres in both intima and media rotated towards the direction of applied stretch and the fibre orientations tended to become less dispersed. Fibre bridging at the crack tip was observed in all notched samples. Results of this study can be used to guide development and optimisation of experimental methodologies and microstructural component based mathematical models to further investigate the micromechanical behaviour of arterial tissues.

5.7 References

1. Sadat, U., Teng, Z. & Gillard, J. H. Biomechanical structural stresses of atherosclerotic plaques. *Expert Rev. Cardiovasc. Ther.* **8,** 1469–81 (2010).
2. Fung, Y.-C. *Biomechanics: Mechanical Properties of Living Tissues*. (Springer New York, 1993). doi:10.1007/978-1-4757-2257-4
3. Humphrey, J. D. *Cardiovascular Solid Mechanics: Cells, Tissues, and Organs*. (Springer New York, 2002). doi:10.1007/978-0-387-21576-1
4. Koh, C. T., Strange, D. G. T., Tonsomboon, K. & Oyen, M. L. Failure mechanisms in fibrous scaffolds. *Acta Biomater.* **9,** 7326–7334 (2013).
5. North American Symptomatic Carotid Endarterectomy Trial Collaborators *et al.* Beneficial effect of carotid endarterectomy in symptomatic patients with high-grade carotid stenosis. *N. Engl. J. Med.* **325,** 445–53 (1991).
6. Gasser, T. C., Ogden, R. W. & Holzapfel, G. A. Hyperelastic modelling of arterial layers with distributed collagen fibre orientations. *J. R. Soc. Interface* **3,** 15–35 (2006).

7. Douglas, G. R. *et al.* Impact of Fiber Structure on the Material Stability and Rupture Mechanisms of Coronary Atherosclerotic Plaques. *Ann. Biomed. Eng.* **45,** 1462–1474 (2017).

8. Schriefl, A. J., Reinisch, A. J., Sankaran, S., Pierce, D. M. & Holzapfel, G. A. Quantitative assessment of collagen fibre orientations from two-dimensional images of soft biological tissues. *J. R. Soc. Interface* **9,** 3081–93 (2012).

9. Schriefl, A. J., Zeindlinger, G., Pierce, D. M., Regitnig, P. & Holzapfel, G. A. Determination of the layer-specific distributed collagen fibre orientations in human thoracic and abdominal aortas and common iliac arteries. *J. R. Soc. Interface* **9,** 1275–86 (2012).

10. Chow, M., Turcotte, R., Lin, C. P. & Zhang, Y. Arterial Extracellular Matrix: A Mechanobiological Study of the Contributions and Interactions of Elastin and Collagen. *Biophys. J.* **106,** 2684–2692 (2014).

11. Tsamis, A. *et al.* Fiber micro-architecture in the longitudinal-radial and circumferential-radial planes of ascending thoracic aortic aneurysm media. *J. Biomech.* **46,** 2787–94 (2013).

12. Zoumi, A., Lu, X., Kassab, G. S. & Tromberg, B. J. Imaging coronary artery microstructure using second-harmonic and two-photon fluorescence microscopy. *Biophys. J.* **87,** 2778–86 (2004).

13. Zoumi, A., Yeh, A. & Tromberg, B. J. Imaging cells and extracellular matrix in vivo by using second-harmonic generation and two-photon excited fluorescence. *Proc. Natl. Acad. Sci. U. S. A.* **99,** 11014–9 (2002).

14. Schriefl, A. J. Quantification of Collagen Fiber Morphologies in Human Arterial Walls. (Graz University of Technology, 2013). doi:10.3217/978-3-85125-238-5

15. Krasny, W., Morin, C., Magoariec, H. & Avril, S. A comprehensive study of layer-specific morphological changes in the microstructure of carotid arteries under uniaxial load. *Acta Biomater.* **57,** 342–351 (2017).

16. Sugita, S. & Matsumoto, T. Multiphoton microscopy observations of 3D elastin and collagen fiber microstructure changes during pressurization in aortic media. *Biomech. Model. Mechanobiol.* **16,** 763–773 (2017).

17. Yu, X., Wang, Y. & Zhang, Y. Transmural variation in elastin fiber orientation

distribution in the arterial wall. *J. Mech. Behav. Biomed. Mater.* **77,** 745–753 (2018).

18. Cavinato, C. *et al.* Biaxial loading of arterial tissues with 3D in situ observations of adventitia fibrous microstructure: A method coupling multi-photon confocal microscopy and bulge inflation test. *J. Mech. Behav. Biomed. Mater.* **74,** 488–498 (2017).

19. Krasny, W., Magoariec, H., Morin, C. & Avril, S. Kinematics of collagen fibers in carotid arteries under tension-inflation loading. *J. Mech. Behav. Biomed. Mater.* **77,** 718–726 (2018).

20. Douglas, G. R. Fibre Microstructure and Mechanics of Atherosclerotic Plaques. (PhD Thesis, University of Cambridge, 2018). doi:10.17863/CAM.18503

21. Martínez-Hergueta, F., Ridruejo, A., González, C. & LLorca, J. Deformation and energy dissipation mechanisms of needle-punched nonwoven fabrics: A multiscale experimental analysis. *Int. J. Solids Struct.* **64–65,** 120–131 (2015).

22. Martínez-Hergueta, F., Ridruejo, A., González, C. & LLorca, J. A multiscale micromechanical model of needlepunched nonwoven fabrics. *Int. J. Solids Struct.* **96,** 81–91 (2016).

23. Daemen, M. J. *et al.* Carotid plaque fissure: An underestimated source of intraplaque hemorrhage. *Atherosclerosis* **254,** 102–108 (2016).

24. Ridruejo, A., Jubera, R., González, C. & LLorca, J. Inverse notch sensitivity: Cracks can make nonwoven fabrics stronger. *J. Mech. Phys. Solids* **77,** 61–69 (2015).

Chapter 6

Microstructural component based finite element modelling of arterial tissue

The author of this dissertation carried out all of the work and analysis in this chapter.

6.1 Abstract

The majority of the fatal clinical events occur as a result of failure of the artery wall that has experienced disease-driven alterations in its microstructure. The main structural changes that are seen by an artery during disease affect the tissue at the microscale. It is these microscale changes that dictate the micromechanical behaviour and therefore the structural integrity of diseased arterial tissue. Despite this, little is known about the microscale behaviour of distinct structural components during macroscale deformations of the arterial tissue, in both healthy and diseased tissue. This study is aimed at development of a micromechanical model that can help bridge this gap in the knowledge. A number of studies utilised constitutive modelling to try and understand the micromechanical behaviour of arterial tissues, while others have utilised models that consisted only of individual collagen fibres. Nevertheless, a comprehensive study that utilises a complete microstructural component-based model of the arterial tissue, which incorporates both the collagen fibres and the other structural entities (such as elastin and GAGs) does not yet exist. This study involved development, optimisation and use of such a model to study the influence of distinct microstructural parameters on the mechanical behaviour of arterial tissues. The collagen fibre length was found to be a critical determinant of the micromechanical behaviour, whose influence almost completely outweighed the influence of the change in fibre cross-link stiffness on the model behaviour.

6.2 Introduction

Arterial wall rupture can lead to a fatal clinical condition commonly involving failure of the media and the adventitia in the case of AAs and ADs. In the case of atherosclerosis, the rupture of the arterial wall involves failure of the developed vulnerable fibrous cap[1,2]. A structure will fail when the applied loading generates structural stresses that exceed its material strength. The main load bearing constituents of the composite arterial tissue microstructure are the elastin and collagen fibres at low and high levels of stretch, respectively. Moreover, the primary contributor of material strength are the collagen fibres due to their superior strength compared to the other microstructural components and the interconnected network that they form. Consequently, distribution of the induced structural stresses within the arterial tissue is highly dependent on the density and fibrous network integrity of collagen fibres, as well as on the distribution of their orientations[3–6].

In their critical review of existing problems in vascular biomechanics, Taylor and Humphrey suggested that failure of the arterial wall is the key link between the fatal clinical events and the disease-driven alterations undergone by the arterial microstructure[7]. Although the fundamental mechanical changes experienced with development of arterial diseases occur at the microscale level, currently existing medical imaging modalities used in everyday diagnosis cannot provide sufficient microstructural information to allow accurate prediction of fatal clinical events. Nevertheless, identification of parameters that serve as micromechanical damage indicators can guide development of new tools for medical diagnosis and therapy.

FEA of arterial tissue has attracted significant research focus for both constitutive and microstructural component-based modelling to study and understand how distinct microstructural components and parameters contribute to the structural integrity and mechanical behaviour of the arterial tissue[7–9]. Constitutive material models have been successful in demonstrating the nonlinearity and the collagen fibre orientation dependent anisotropy of the arterial tissue. A comprehensive review of the common methodologies in constitutive modelling has been done by Holzapfel and Ogden[8].

Bottom-up built finite element models that are based directly on the distinct microstructural components can provide an improved alternative to constitutive material models, as they allow extraction of microstructural information directly from the individual microscale constituents. The collagen fibre based model by Koh et al. is an example of microstructural constituent-based modelling of fibrous materials and tissues[10–14]. Since the model by Koh et al. did not incorporate a ground matrix, it does not provide valuable information about the interactions between distinct microstructural components and the associated micromechanical phenomena.

This study presents a complete microstructural component-based model of the arterial tissue, containing collagen fibres and ground matrix as two separate structural entities to allow comprehensive assessment of tissue micromechanics. This will enable studying the influence of distinct microstructural parameters on the micromechanical behaviour. The transfer of stress between the modelled microstructural components will be investigated. The effect of changes in microstructural component features, such as collagen fibre length and cross-link stiffness on the model mechanical behaviour will also be studied.

6.3 Development of the model

This section describes the methodology that was followed for development of a microstructural component based finite element unit cell model. The architecture, finite element formulations, geometrical definitions and boundary conditions of the unit cell model are described.

Architecture of the unit cell model was based on the organisation and interconnections between the microstructural components that constitute the real arterial tissue. Collagen fibres and the ground matrix were assumed to be the two main classes of arterial ECM components, similar to the previous work on microstructural modelling of arteries[5,8,15]. Collagen fibres and the ground matrix were modelled with distinct finite element formulations, which are readily available in the commercial FEA software ABAQUS (ABAQUS 6.14, Dassault Systèmes, France). The process that led to identification of the utilised formulations involved testing different types of readily available finite elements of ABAQUS with distinct parameters, applied strain fields and boundary conditions. Collagen fibre cross-links, as well as the fibre to ground matrix links (FGMLs) that were specifically incorporated to bond the collagen fibres to the ground matrix were both modelled with the connector elements of ABAQUS.

The model generation was automated in MATLAB with programmatic interface to PYTHON and ABAQUS. The automatic model generator is programmed to provide control on respective geometric and structural features such as the statistical distribution of the collagen fibre orientation and the cross-linking density.

6.3.1 Finite element architecture of the model

The developed model does not explicitly contain all of the microstructural components that would exist in an actual unit cell of the arterial tissue, as it can be seen in Figure 6.1. While the collagen fibres were modelled with the beam type finite elements, the collective contribution of the remaining ECM constituents, such as the randomly distributed elastin fibres, elastic laminae and GAGs to the mechanical behaviour of the actual arterial tissue were modelled with a single set of solid continuum type finite elements.

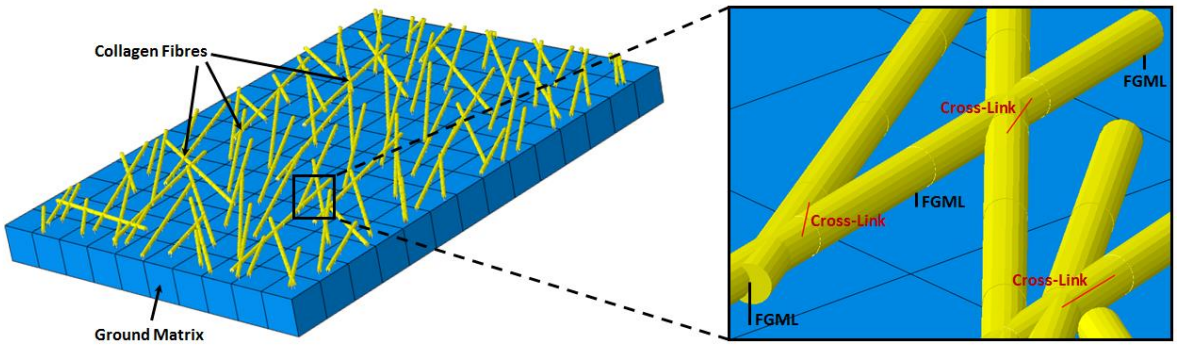

Figure 6.1. The developed finite element unit cell model of arterial tissue microstructure.

The model consisted of collagen fibres and a ground matrix, which were discretised into circular profile cross-section beam and hexahedral solid continuum elements of ABAQUS, respectively. All collagen fibres and their beam elements were assumed to be straight in their unloaded state. The natural crimping and the resulting axial bilinear mechanical behaviour of the collagen fibres were incorporated into the finite element formulation and material controls. Each collagen fibre was discretised into at least 9 elements, more refined meshes used 18 and 36 elements per collagen fibre. Following discretisation, 10 equally spaced nodes along the length of each collagen fibre were cloned and the generated new set of nodes were translated and tied onto the surface of the 3D solid continuum ground matrix elements. The FGMLs were then generated by connecting each of the original collagen fibre beam element nodes to their corresponding clones using connector elements of ABAQUS. The connector elements were also utilised to generate the cross-links between intersecting fibres. The cross-links were created by linking the closest pair of nodes on the intersecting collagen fibres with a connector element. FGML and the cross-link connector elements can be seen in Figure 6.1. The details of the interconnections between distinct element types of the model are described below in section **6.3.2**.

6.3.2 Finite element formulations of the microstructural components

A schematic illustrating the interconnections between distinct element types of the model is provided in Figure 6.2. Collagen fibres were modelled with B31H type elements, which are hybrid 3D beam elements with linear nodal variable interpolation. To have complete control over the mechanical behaviour of each beam element, the generalised cross-sectional behaviour definition was used.

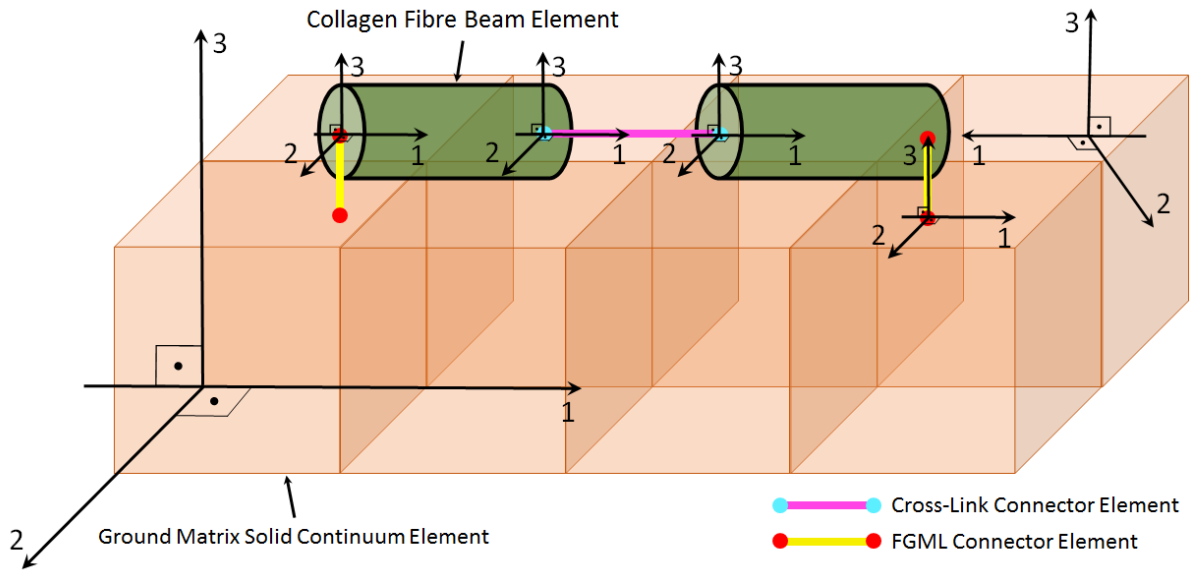

Figure 6.2. Schematic of the interconnections between distinct element types of the model. The local nodal coordinate system orientations of the cross-link and FGML connector elements, with respect to those of the collagen fibre beam and ground matrix solid continuum elements are illustrated.

To mimic the actual mechanical behaviour of the individual collagen fibres, the generalised beam section behaviour was set to be nonlinear in the axial direction and linear perpendicular to the longitudinal beam axis, respectively. The ground matrix was modelled with C3D8H type elements, which stands for the hybrid hexahedral solid continuum elements with linear nodal variable interpolation. Following the common methodology utilised in previous work on microstructural component based modelling of arterial tissue[5,8,15], the material property of the ground matrix elements was set to be isotropic, incompressible and linearly elastic.

The cross-links and the FGMLs were both modelled with CONN3D2 type elements, which stands for the 3D connector elements. The cross-link and the FGML connector elements were both set to be formulated by the projection cartesian type connections. The selected projection cartesian formulation does not constrain any component of relative motion between the two nodes, where it measures and allows description of connector mechanical behaviour separately in and about each one of the three local nodal coordinate system directions. The cross-link and the FGML connector elements were assumed to be linear and therefore, single constant spring stiffness values were used to define their mechanical behaviours. The detailed mathematical formulations of the distinct element types can be found in the theory manual of ABAQUS[16].

6.3.3 Geometrical definitions of the model

This section describes the geometrical definitions of the model, which include descriptions of the preferred orientation and directional distribution of collagen fibres, along with the length, density, as well as cross-linking density of the collagen fibres in each unit cell.

6.3.3.1 Preferred direction and distribution of collagen fibre orientations

Preferred orientation of the collagen fibres was defined between 0° and 180°. Modelling of the collagen fibres was initiated by creation of a set of evenly distributed 2D coordinates that served as their central seeds, from which the collagen fibres were later extended as straight fibres. The fibre cross-link density was controlled based on the angle of intersection of the extended collagen fibres. A cross-link between two intersecting fibres was created only when the angle of intersection of the fibres was less than the input angular threshold.

The planar distribution of the fibre longitudinal axis orientations on the ground matrix surface was characterised with the 2D planar form of the transversely isotropic and π-periodic von Mises distribution, similar to the methodology utilised in previous work on microstructural component-based modelling of arterial tissue[5,6,8], as detailed in **Chapter 4**. In brief, the von Mises distribution with a PDF of orientation, $P(\theta)$ was assumed:

$$P(\theta) = 4\sqrt{\frac{b}{2\pi}\frac{exp[b(cos(2\theta)+1)]}{erfi(\sqrt{2b})}}\,,\theta \in [0°, 180°] \qquad (6.1)$$

where b is the concentration parameter, θ is the fibre orientation (θ) referenced to $\bar{\theta}$, and $\mathrm{erfi}(x)$ is the imaginary form of the error function. The dispersion parameter κ was computed as:

$$\kappa = \frac{1}{4}\int_0^{180} P(\theta)sin^3\theta d\theta \qquad (6.2)$$

where κ=0 corresponds to parallel fibres and κ=1/3 is a uniform (isotropic) distribution.

6.3.3.2 Outer geometry and composition of the model

A unit cell model, whose predefined regions are assigned with distinct colours, is provided in Figure 6.3. The ground matrix and collagen fibre element nodes that are above the load bearing region are displaced upwards, while the nodes that are below the load bearing region are displaced downwards, so as to apply a longitudinal stretch on the model.

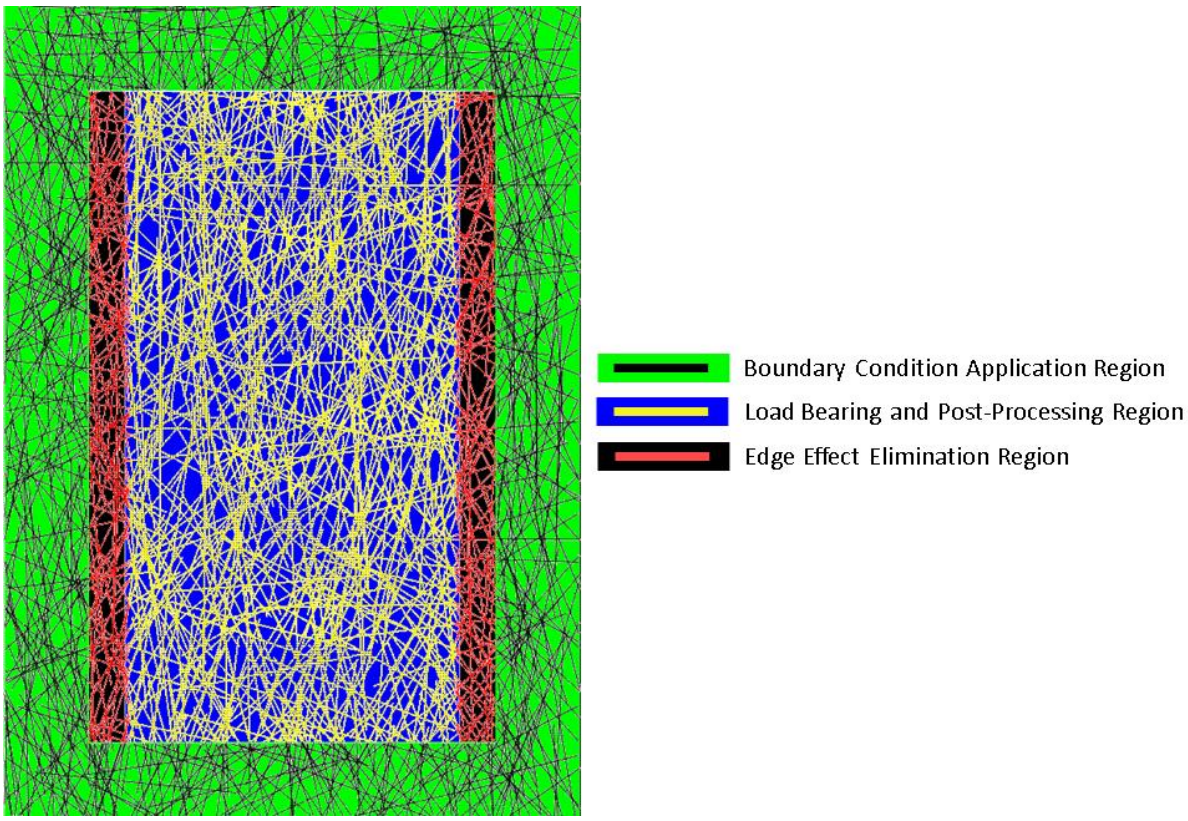

Figure 6.3. The unit cell model, with different regions identified with different colours.

To ensure that the model maintains a Poisson's ratio, ν, of 0.5 during stretching, the boundary condition application region nodes that fall on the left and right sides of the load bearing region are displaced to compress the model, with a strain whose magnitude is half of the longitudinal stretch (Figure 6.3). Since the elements inside the edge effect elimination region always developed stress concentrations at their borders with the boundary condition application region, they were excluded from the subsequent analysis. Only the elements within the load bearing and post-processing region were used to study the resulting unit cell model behaviour.

The actual physical density of collagen fibres was computed in the form of percentage area occupied by the collagen fibres on each model surface as:

$$Fibre\ Area\ Percent = \frac{Total\ Area\ of\ All\ Collagen\ Fibres}{Surface\ Area\ of\ the\ Model\ Ground\ Matrix} \times 100\% \qquad (6.3)$$

6.3.4 Mechanical behaviour of collagen fibres

Individual collagen fibres exhibit bilinear stress versus stretch ratio behaviour in the axial direction. This arises from the fact that, in the unloaded state, each collagen fibre is crimped and, upon loading, they start to elongate with approximately zero stress up to about 3% strain. Once the collagen fibre is fully uncrimped, it follows a linear-elastic behaviour and starts to elongate with a constant stiffness. The collagen fibres are also extremely slender, so that the axial stiffness is much larger than the bending stiffness[17].

For beam elements, ABAQUS allows direction-dependent nonlinear and linear material behaviours to be defined only in terms of a force versus strain curve and a single stiffness value, respectively. Therefore, in order to approximate the axial direction bilinear stress versus stretch behaviour of the collagen fibres, a bilinear force versus strain curve was used as the axial behaviour of the beam elements.

Type I collagen fibres are the main microstructural component of the load bearing fibrous tissue network of the intima, media and the adventitia artery layers. Material properties of the fibres were determined from the available literature on the mechanical behaviour of Type I collagen[17–24]. The uncrimped fibre force versus strain curve gradient was determined by converting the mean uncrimped collagen fibre modulus values from the literature into their corresponding force versus strain gradients[18–24]. The average force versus strain relationship gradient was found to be 6.57×10^7 pN[18–24].

The bilinear force versus strain curve that was used to define the axial behaviour of collagen fibre beam elements can be visualised in Figure 6.4. The gradient of the uncrimped collagen fibre region was set to 6.57×10^7 pN. The crimped fibre region stiffness was set to a value that is at least $1/10^3$ of the uncrimped region stiffness. In addition, the crimped to uncrimped region transition of the bilinear force versus strain curve was smoothed, so as to reduce the possibility of experiencing numerical solution problems. The low stiffness bending behaviour was approximated by assigning linear bending stiffness values which were approximately $1/10^6$ of the uncrimped region gradient.

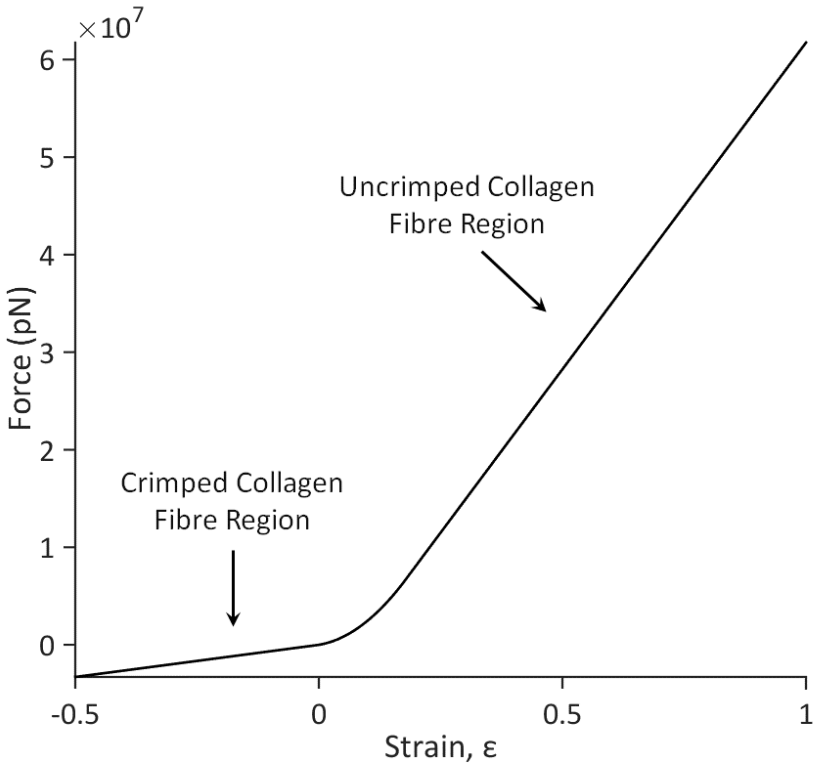

Figure 6.4. The bilinear force versus strain curve that was used to define the axial behaviour of collagen fibre beam elements.

6.3.5 2D simulation setup and the boundary conditions

Although the unit cell model was built from 3D beam and 3D solid continuum elements, the nodes of all elements were constrained and allowed to move only in 2D, within the plane that is parallel to the ground matrix surface. The uniaxial stretching boundary conditions were created by displacing the top region nodes of the model in Figure 6.3 upwards and its bottom region nodes downwards. All nodes outside the boundary condition region were allowed to move in the plane parallel to the ground matrix surface.

6.4 Influence of fibre alignment on model mechanical behaviour

This section describes the analysis in which the unit cell model was treated as unidirectional and bidirectional fibre reinforced composites and used to study the effect of variations in fibre alignment orientation on its mechanical behaviour. Mesh refinement was performed, and it was found that the unit cell model behaviour is similar for an element size of 0.0014 mm or less. Consequently, an element size of 0.0014 mm was chosen for use in all of the unit cell model simulations that are described in the remainder of this chapter.

6.4.1 Fibre alignment study simulations

A unit cell model, whose ground matrix is 0.8 mm long and 0.4 mm wide was used in this study. The model was incorporated with discontinuous 0.4 mm long collagen fibres. Since elastin is the second largest contributor of arterial tissue stiffness after collagen, in the absence of collagen, stiffness of the ground matrix was assumed to be equal to that of elastin, therefore, the stiffness of the ground matrix was set to $1/10^3$ of the uncrimped region stiffness of the curve in Figure 6.4. Moreover, the area percent of the collagen fibres was kept at 10% and the cross-linking connector elements were set to be rigid, while the stiffness of each FGML connector element was set equal to that of the ground matrix.

Three categories of unit cell models were simulated. The three model categories were referred to as *basic*, *unidirectional* and *bidirectional* fibre alignment models. There were 4 basic fibre alignment models, whose collagen fibres were aligned at 0°, 45°, ±45° and 90° to the longitudinal stretching direction of the model, which can be visualised in Figure 6.5.

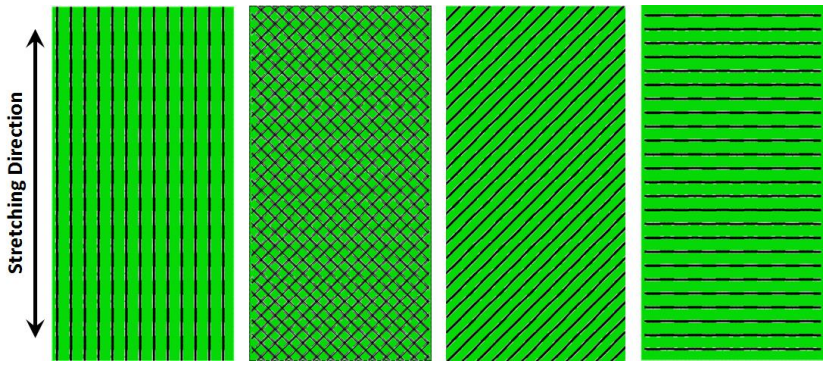

Figure 6.5. Basic fibre alignment models with 0°, ±45°, 45° and 90° fibres, from left to right.

The unidirectional fibre alignment models contained fibres that were aligned at a single orientation with respect to the stretching direction of the model. Fibre orientations of the unidirectional models were 0°, 15°, 30°, 45°, 60°, 75° and 90° to the direction of stretching. The bidirectional fibre alignment models had fibres aligned at 0°, ±15°, ±30°, ±45°, ±60°, ±75° and ±90° to the direction of stretching. Since the unit cell model was set to generate cross-links only at the intersection points of neighbouring fibres, all of the discontinuous collagen fibres in each fibre alignment study model were shifted by 1°, towards the direction that would yield an intersection with adjacent fibres. All intersecting discontinuous fibres were also cross-linked so that fibres can pull on one another, therefore recruiting new fibres to bear the stress that is transmitted across the model.

6.4.2 Results

The normalised Cauchy stress versus stretch ratio curve of each model was computed and plotted separately for each category of fibre alignment study models. The Cauchy stress values were normalised with the average uncrimped modulus of the modelled collagen fibres, E_f, which was calculated to be 1.42 GPa from literature[17–24].

6.4.2.1 Influence of basic fibre alignments

The normalised Cauchy stress versus stretch ratio plot of basic fibre alignment models can be visualised in Figure 6.6. The stiffest response was exhibited by the model whose fibres were aligned in the direction of stretching. This stiffest response was also accompanied with a curve shape, which resembled the input bilinear axial behaviour of individual collagen fibres. It is also evident in Figure 6.6 that the unit cell model decreases in stiffness with increasing fibre misalignment to the direction of stretching. Since the axial stiffness of collagen fibre is much greater than the stiffness of the ground matrix, the overall decrease in stiffness is a result of reduced axial fibre recruitment, due to the increasing misalignment of fibres to the direction of stretching.

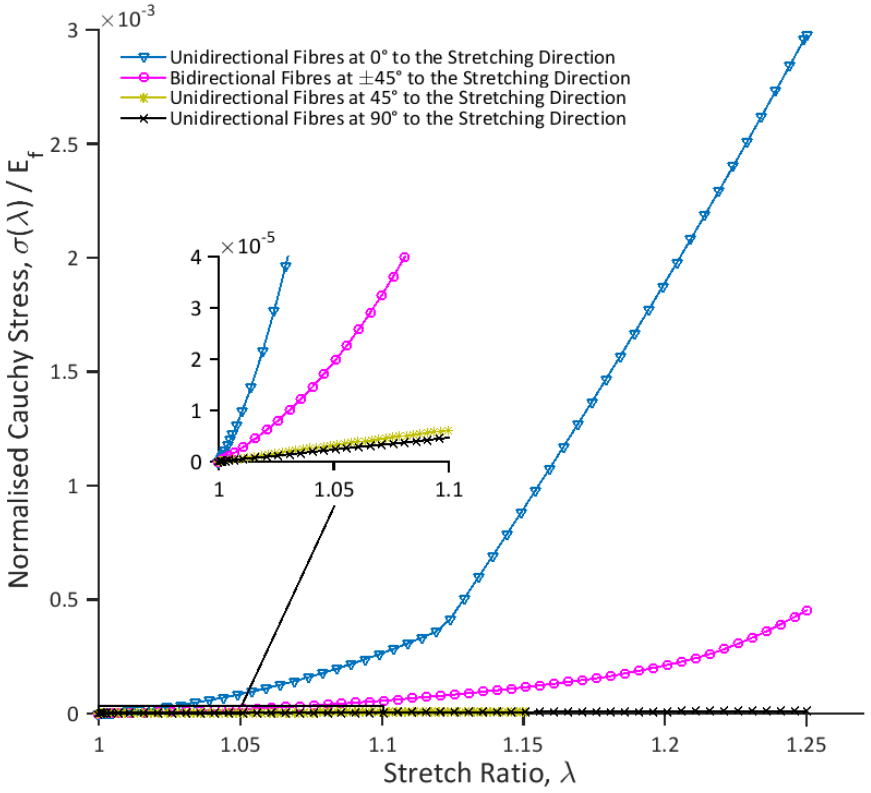

Figure 6.6. The normalised Cauchy stress versus stretch ratio plot of basic models.

It can be seen in Figure 6.6 that, while the unidirectional 0° and bidirectional ±45° basic fibre alignment models exhibited a nonlinear mechanical behaviour, the unidirectional 45° and 90° models behaved linearly. This change in mechanical behaviour is a result of the sudden shift in the main direction of stress that is transmitted across the model. The band plots in Figure 6.7 illustrate the phenomenon that changed the mechanical behaviour of unit cell model from nonlinear to linear. The maximum principal stress in the bidirectional ±45° model was found to be distributed much more homogeneously throughout the ground matrix and at relatively lower values than those of the stress concentrations, which were determined at the ground matrix edges of the unidirectional 45° model. It is also evident in Figure 6.7 that, the collagen fibre axial reaction force is relatively higher and much more homogeneously distributed within the bidirectional ±45° model. Moreover, in the unidirectional 45° model, the axial reaction force is zero in majority of the collagen fibres, with insignificant force levels that are mainly concentrated towards the centre of the model.

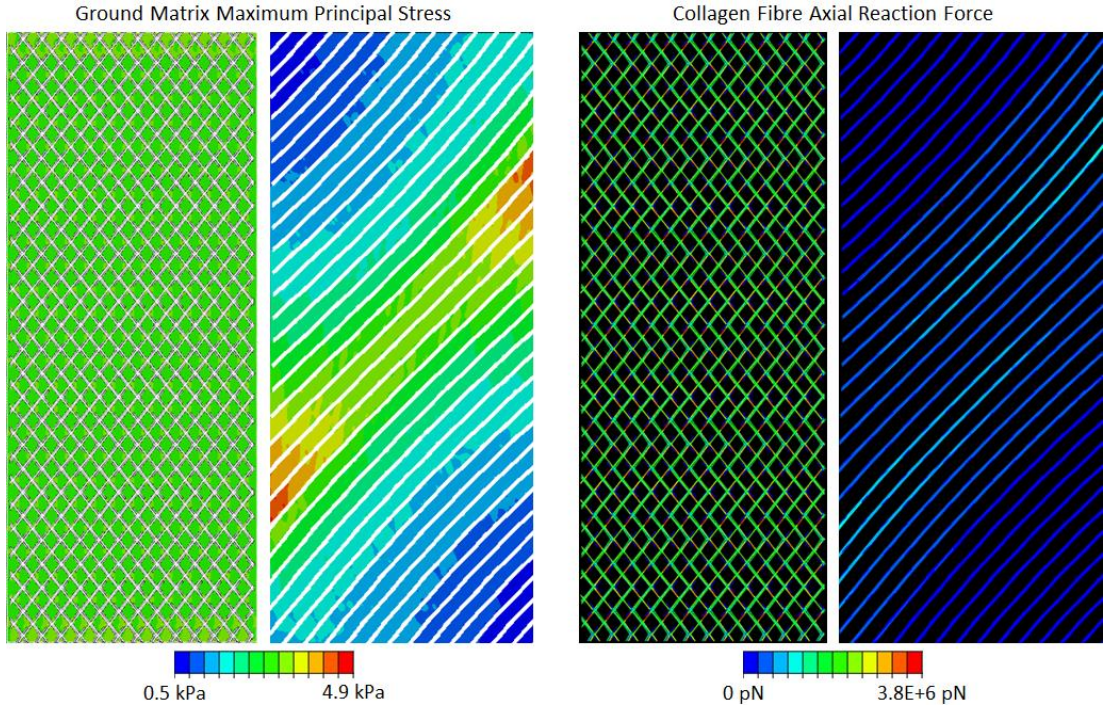

Figure 6.7. The ground matrix maximum principal stress and collagen fibre axial reaction force band plots of bidirectional ±45° and unidirectional 45° fibre alignment study models.

Since the collagen fibres that cross one another at 90° are always cross-linked in the bidirectional ±45° model, they are able to carry the majority of the stress within their network. Consequently, the mechanical behaviour of bidirectional ±45° model is dictated by the axially bilinear collagen fibres, giving the model an overall nonlinear response.

On the contrary, once all collagen fibres are aligned at 45° to the direction of stretching, they immediately lose their stress bearing ability, leaving almost all of the stress to the ground matrix. Once majority of the stress within the model is transferred to the ground matrix, the contribution of collagen fibres to the unit cell model behaviour becomes insignificant, therefore making the model linear elastic.

6.4.2.2 Influence of unidirectional fibre alignments

It can be seen in the normalised Cauchy stress versus stretch ratio plot of unidirectional fibre alignment models in Figure 6.8 that, the simulated unit cell models were not always stretched to the same extent. This is because, except for the 0° fibre alignment model, all unit cell models experienced excessive ground matrix continuum element distortions. The unidirectional collagen fibres quickly lost their stress bearing ability with increasing misalignment to the direction of stretching and transferred the load to the ground matrix. The rapid decrease in overall unit cell model stiffness and the resulting linear model behaviours are additional facts, which support the loss of contribution of collagen fibres to the mechanical behaviour of the unit cell model.

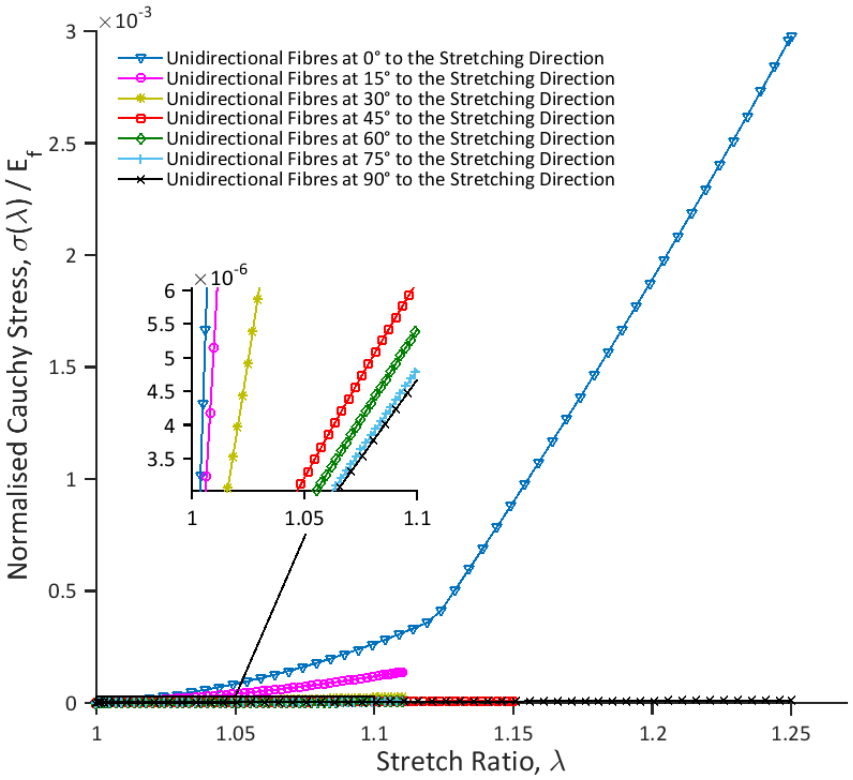

Figure 6.8. The normalised Cauchy stress versus stretch ratio plot of unidirectional models.

6.4.2.3 Influence of bidirectional fibre alignments

The normalised Cauchy stress versus stretch ratio plot of bidirectional fibre alignment models is provided in Figure 6.9. Similar to the bidirectional ±45° fibre alignment model in Figure 6.7, all bidirectional fibre alignment models consisted of fully cross-linked collagen fibres, which were aligned in two separate orientations to the direction of stretching. This enabled efficient transmission of the stress across the fibre network, therefore shadowing the ground matrix from excessive elemental distortions.

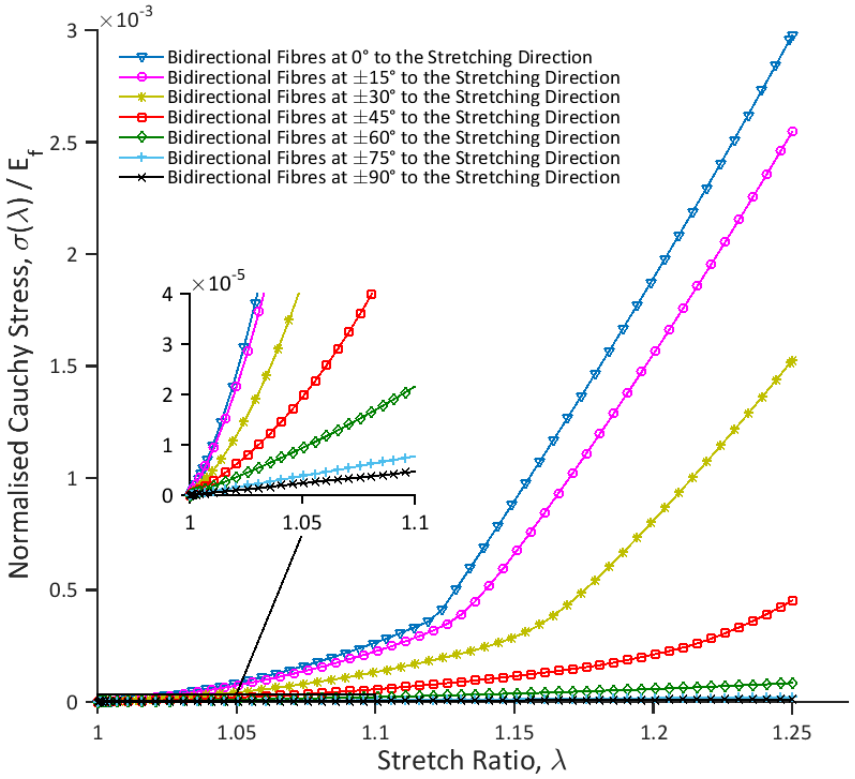

Figure 6.9. The normalised Cauchy stress versus stretch ratio plot of bidirectional models.

The plot in Figure 6.10 allows comparison between linearised modulus change of unidirectional and bidirectional fibre alignment models with increasing fibre misalignment to the direction of stretching. The linearised modulus values in Figure 6.10 were computed by fitting a linear model to the Cauchy stress values of each unit cell model from 0 to 1.1 stretch level. Since some of the unidirectional fibre alignment models diverged beyond 1.1 stretch level, only the values between 0 and 1.1 stretch levels were used in linear fitting.

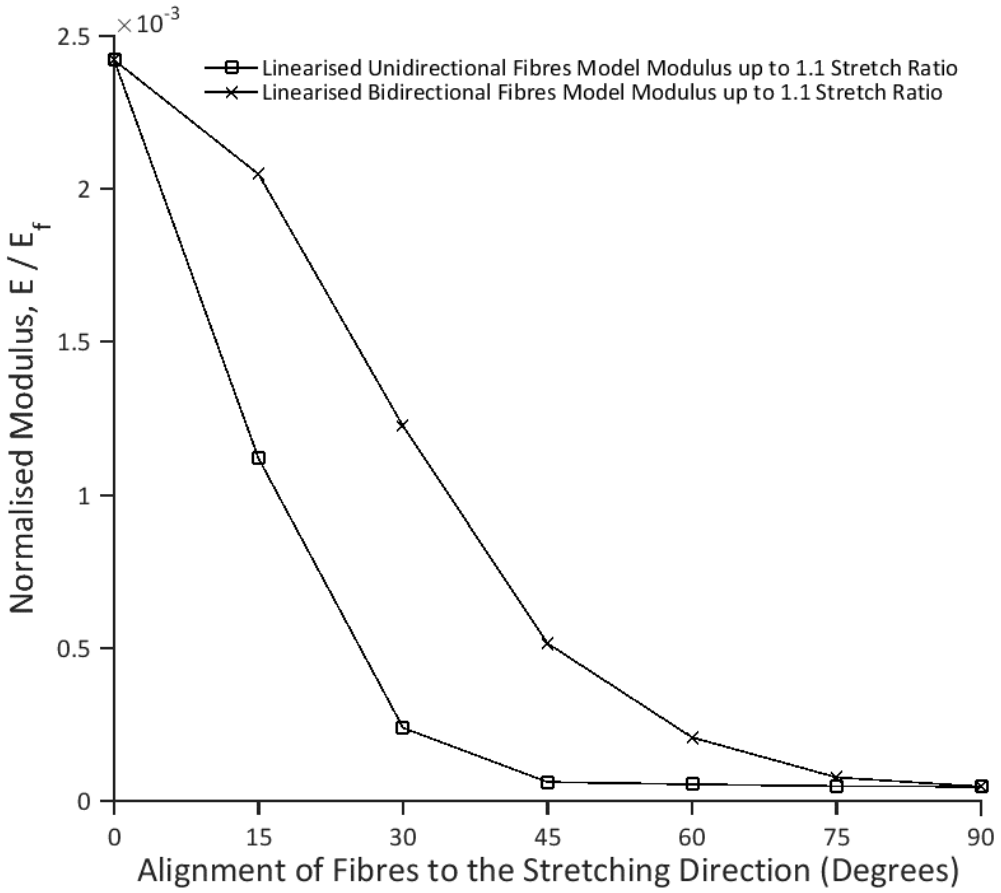

Figure 6.10. The normalised modulus versus alignment of fibres to stretching direction plot for unidirectional and bidirectional fibre alignment models.

Gradients of the resulting linear fits were then divided by the average uncrimped modulus of the modelled collagen fibres, E_f to obtain the normalised values of modulus. The obtained normalised modulus change plot revealed that the stiffness of the bidirectional fibre alignment models decreased at a slower rate compared to that of the unidirectional models, with increasing fibre misalignment to the direction of stretching.

6.5 Influence of microstructural factors on behaviour of models with distributed fibre orientations

This section describes the study that was aimed at understanding the influence of changes in the structure and material properties of microstructural constituents on the model mechanical behaviour. In this study, planar distribution of fibre longitudinal axis orientations on the ground matrix surface was characterised with the dispersion parameter, κ of the von Misses distribution, so as to mimic the organisation of collagen fibres in an actual arterial tissue.

6.5.1 Microstructural factors study simulations

Similar to the fibre alignment study, the ground matrix of all unit cell models in the microstructural factors study was set to be 0.8 mm long and 0.4 mm wide, as illustrated in Figure 6.11. All of the elemental material properties of each model was also set identical to those of the fibre alignment study models (section **6.4**). On the other hand, fibre length and cross-link stiffness were selected as the microstructural factors of interest, where the study was designed to investigate their influence on the model mechanical behaviour.

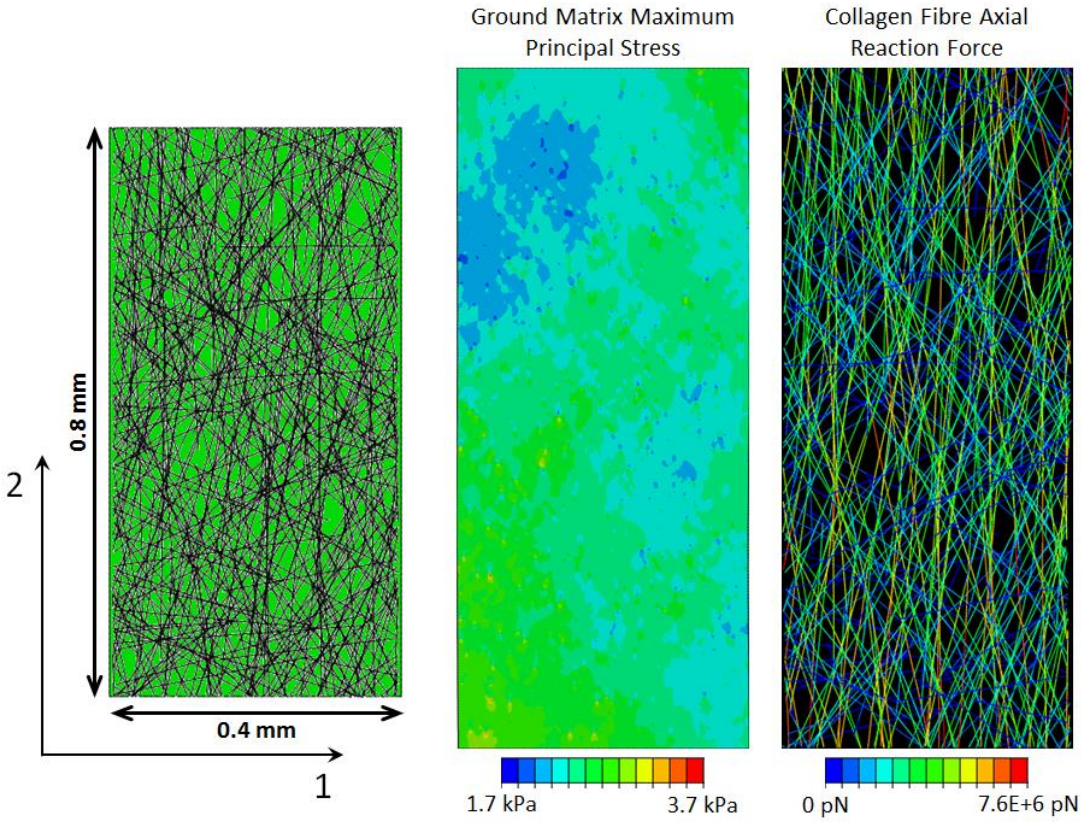

Figure 6.11. A microstructural factors study model with distributed fibre orientations, together with its corresponding ground matrix maximum principal stress and collagen fibre axial reaction force band plots, from left to right.

Five separate distributed fibre orientation unit cell models with 0.05 mm, 0.1 mm, 0.2 mm, 0.4 mm and 0.8 mm fibre lengths were simulated to study the influence of fibre length, L_f on model mechanical behaviour. The cross-link stiffness, k_{cl} of all fibre length influence study models was set to a constant median value of 100×10^6 pN.mm^{-1}.

The maximum cross-link stiffness value was set to be $1600x10^6$ pN.mm^{-1}, therefore, the 8 subsequently doubling cross-link stiffness values were set as $6.25x10^6$ pN.mm^{-1}, $12.5x10^6$ pN.mm^{-1}, $50x10^6$ pN.mm^{-1}, $100x10^6$ pN.mm^{-1}, $200x10^6$ pN.mm^{-1}, $400x10^6$ pN.mm^{-1} and $800x10^6$ pN.mm^{-1}, resulting in a median value of $100x10^6$ pN.mm^{-1}.

The area percent of the collagen fibres was set to 10% and the dispersion parameter, κ of fibre orientations was set to 0.25 for all microstructural factors study models. Moreover, the intersecting fibres in both fibre length and cross-link stiffness influence study models were only cross-linked when their angle of intersection was less than 45°. Since there is no evidence that all intersecting fibres in an actual arterial tissue are cross-linked, an angular cross-linking threshold of 45° was used.

6.5.2 Results

The Cauchy stress values were normalised with the average uncrimped modulus of the modelled collagen fibres, E_f, which was calculated to be 1.42 GPa from literature[17–24]. The relationship between overall model modulus and fibre length, as well as that between overall model modulus and cross-link stiffness were established. Moreover, the decrease in dispersion parameter, κ upon stretching of each unit cell model was computed and compared between models with distinct fibre lengths and cross-link stiffnesses.

6.5.2.1 Influence of fibre length

It can be visualised in the normalised Cauchy stress versus stretch ratio plot of Figure 6.12 that, the increase in fibre length causes an increase in the unit cell model modulus. In addition, overall behaviour of the model became increasingly nonlinear with increase in fibre length. Considering that the collagen fibres in the model are axially bilinear and 1000 times stiffer than the linear ground matrix at the higher stiffness region of their prescribed axial response curve, increases in overall model nonlinearity and stiffness can be attributed to the subsequent increase in contribution of collagen fibres to model mechanical behaviour.

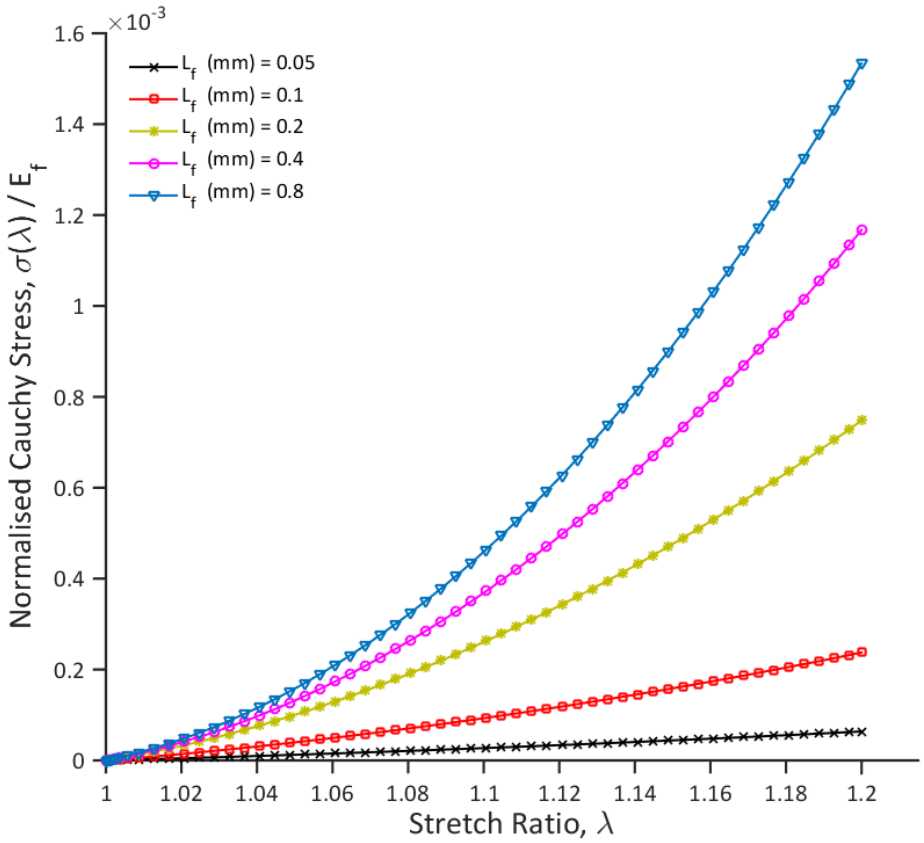

Figure 6.12. The normalised Cauchy stress versus stretch ratio plot of distributed fibre orientation models with distinct fibre lengths.

Figure 6.13 shows the relationship between the normalised modulus of distributed fibre orientation models and their corresponding fibre lengths. There is a very strong linear relationship between the normalised model modulus and the natural logarithm of normalised fibre length ($r^2 = 0.98$, $p < 0.001$).

The normalised modulus values in Figure 6.13 were computed by fitting a linear model to the Cauchy stress versus stretch ratio curve of each unit cell model, where the gradients of the resulting linear fits were then divided by the average uncrimped modulus of the modelled collagen fibres, E_f to obtain the normalised values of modulus. On the other hand, the fibre length, L_f values were normalised by dividing them with the minimum fibre length, L_f^{min} value, before obtaining their natural logarithms.

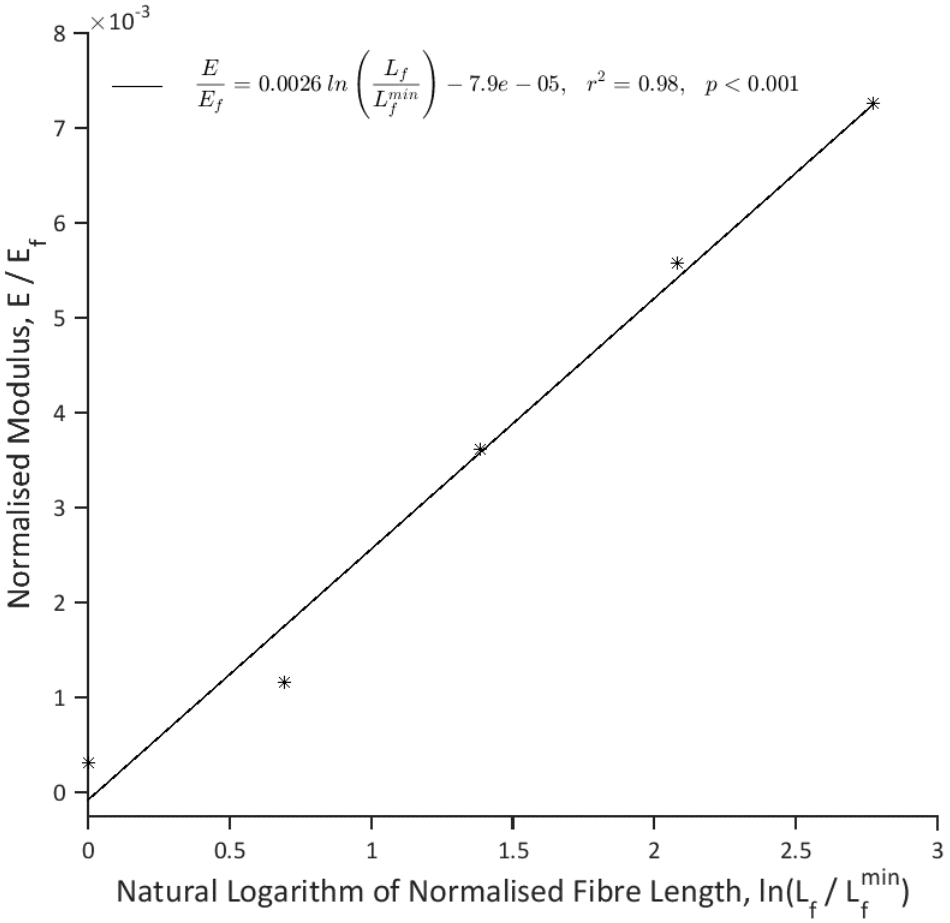

Figure 6.13. The normalised modulus versus natural logarithm of normalised fibre length plot.

The change in dispersion parameter, κ upon straining of each unit cell model to a stretch ratio of 1.2 was also computed for the models with distinct fibre lengths. The plot in Figure 6.14 illustrates the decrease in dispersion parameter, κ with increasing fibre length, in which the natural logarithm of the normalised fibre length was used as the independent variable. It is evident in Figure 6.14 that increasing the fibre length causes the decrease in dispersion parameter, κ to fluctuate, while resulting in a corresponding overall increase in its value.

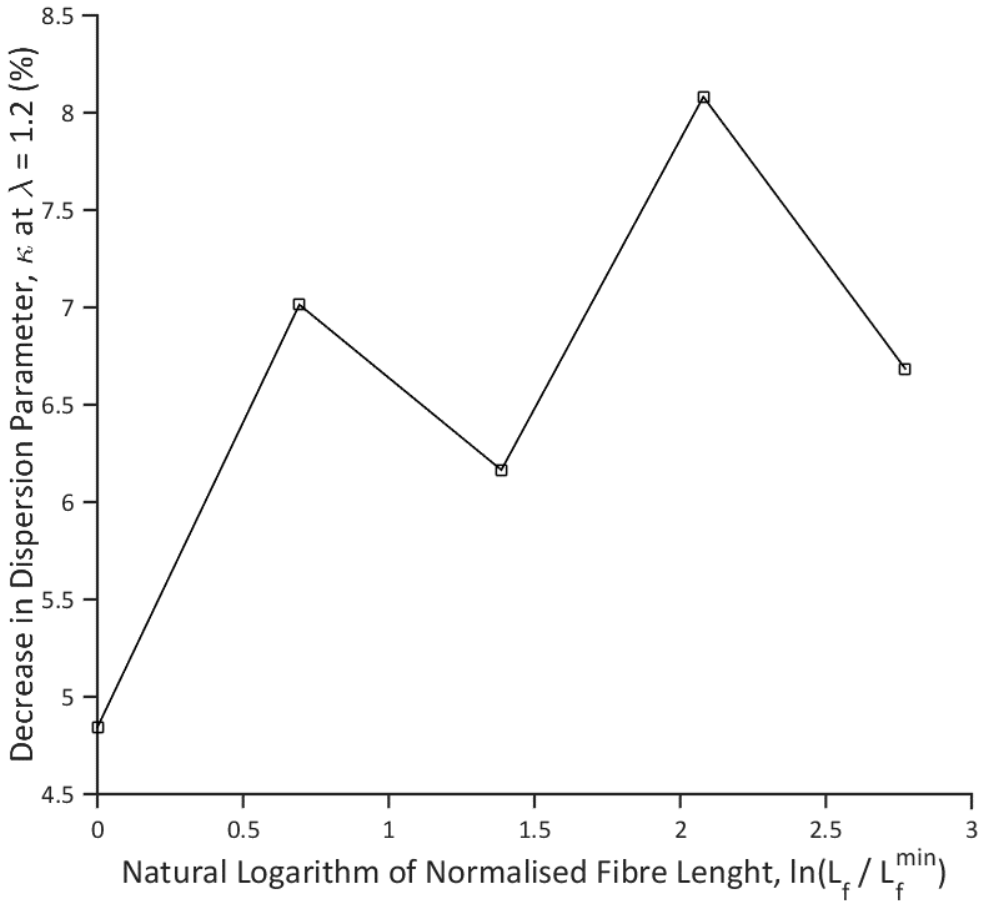

Figure 6.14. The decrease in dispersion parameter, κ at λ = 1.2 versus natural logarithm of normalised fibre length plot.

6.5.2.2 Influence of cross-link stiffness

Modulus of the model increased, and its overall behaviour became gradually more nonlinear with subsequently doubled cross-link stiffness, as it can be seen in Figure 6.15. The increases in modulus and overall nonlinearity are direct results of increased levels of force transmission across the fibrous network. As the cross-link stiffness is increased, the fibres pull more strongly on one another, therefore leading to recruitment and axial loading of more fibres at subsequently greater extents. This increase in the number and extent of axially bilinear fibre loading leads to increases in both the modulus and nonlinearity of the unit cell model.

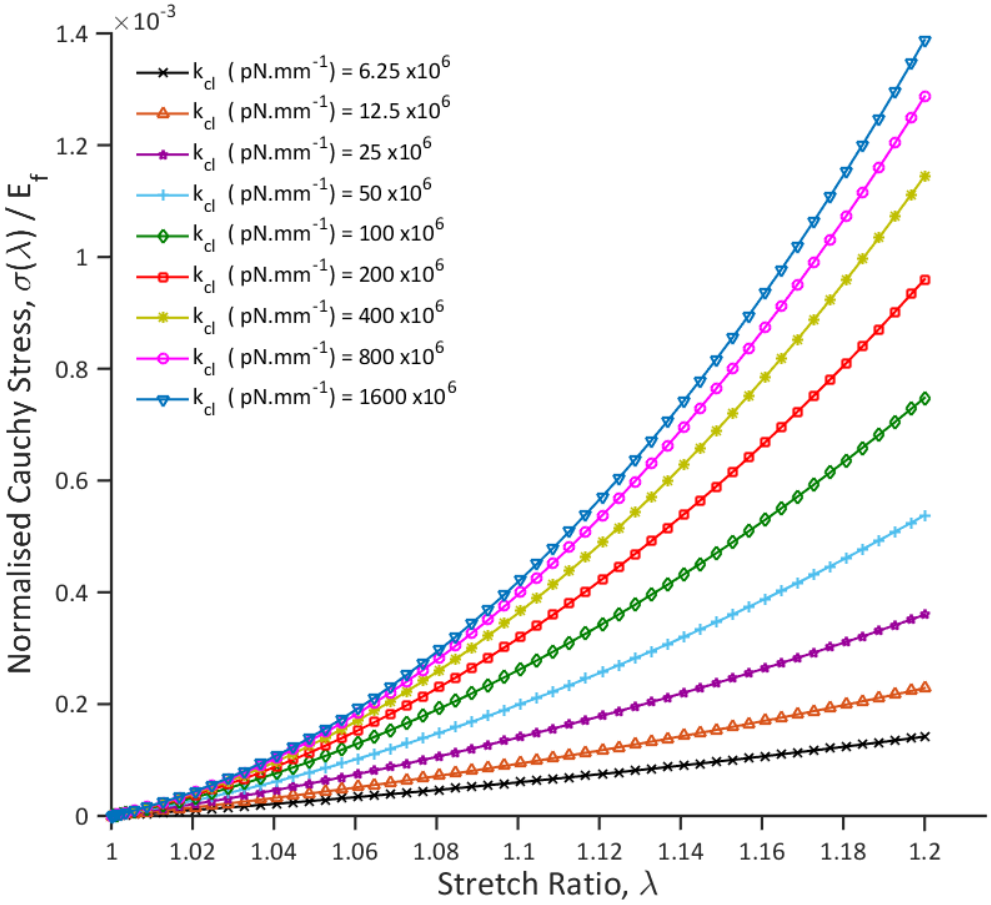

Figure 6.15. The normalised Cauchy stress versus stretch ratio plot of distributed fibre orientation models with distinct cross-link stiffnesses.

A relationship between the linearised modulus of distributed fibre orientation models and their corresponding cross-link stiffnesses was established in the plot of Figure 6.16. Similar to the plot in Figure 6.13, the normalised modulus values in Figure 6.16 were computed by fitting a linear model to the Cauchy stress versus stretch ratio curve of each unit cell model and then dividing the obtained gradients with the average uncrimped modulus of the modelled collagen fibres, E_f. The cross-link stiffness, k_{cl} values were also normalised by dividing them with the minimum cross-link stiffness, k_{cl}^{min} value. The normalised model modulus was plotted against the natural logarithm of normalised fibre length, which yielded a very strong linear relationship ($r^2 = 0.99$, $p < 0.0001$) between the two parameters (Figure 6.16). Comparison of the linear model gradients in Figure 6.13 and Figure 6.16 revealed that the increase in linearised model modulus per unit increase in natural logarithm of fibre length is more than two times larger ($0.0026 < 0.0012$) than the increase experienced with a unit increase in natural logarithm of cross-link stiffness.

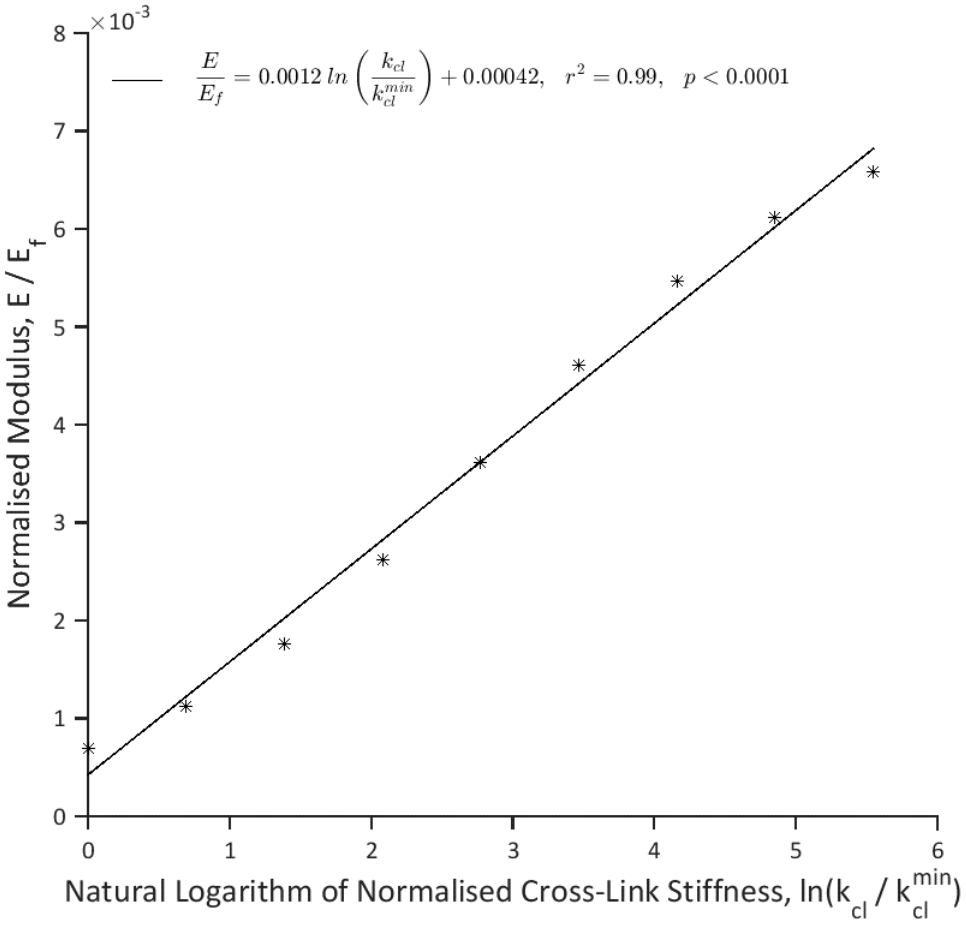

Figure 6.16. The normalised modulus versus natural logarithm of normalised cross-link stiffness plot.

The plot in Figure 6.17 illustrates the decrease in dispersion parameter, κ with increasing cross-link stiffness, upon straining of each unit cell model to a stretch ratio of 1.2. The natural logarithm of the normalised cross-link stiffness is used as the independent variable. Comparison of the plots in Figure 6.14 and Figure 6.17 revealed that the increase in cross-link stiffness resulted in an opposite effect relative to that of the increase in fibre length and slightly reduced the magnitude of decrease in dispersion parameter, κ. On the other hand, the magnitude of the obtained reduction was insignificant compared to the magnitudes of change that was caused by increase in fibre length.

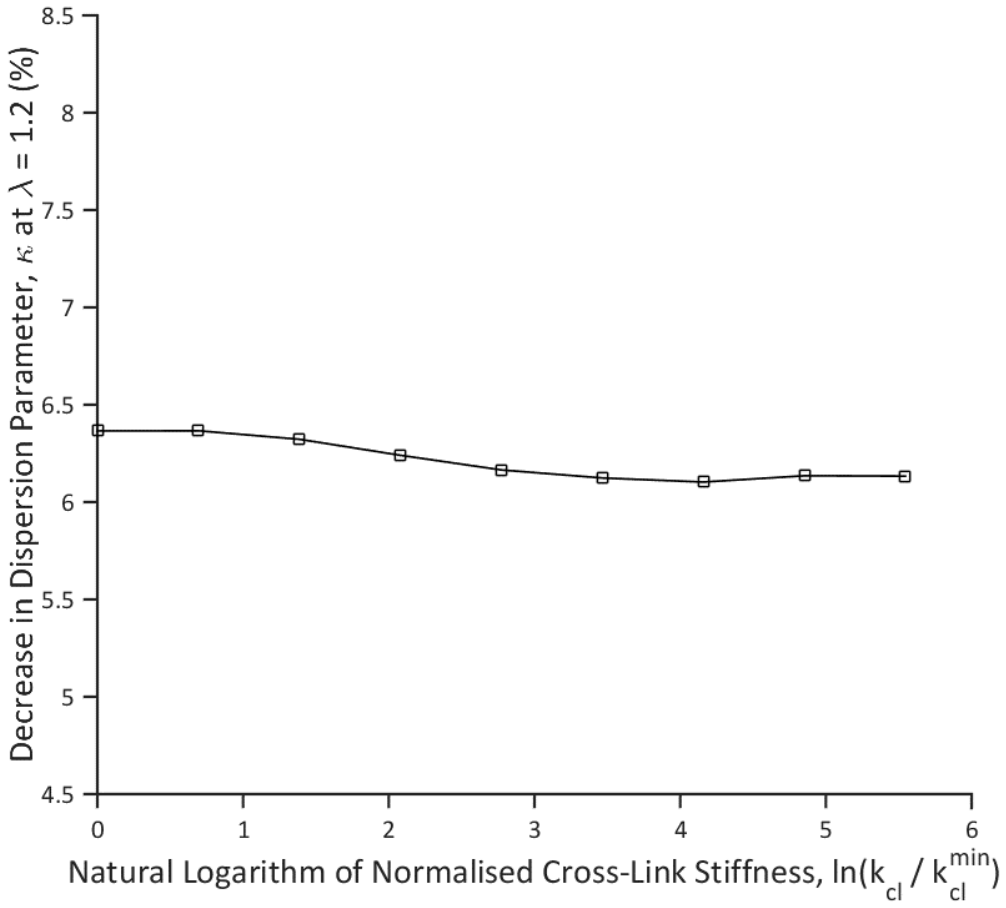

Figure 6.17. The decrease in dispersion parameter, κ at λ = 1.2 versus natural logarithm of normalised cross-link stiffness plot.

6.6 Discussion

In this study, a finite element model, which consists of the cross-linked collagen fibres and a ground matrix was developed and optimised to study the micromechanical behaviour of arterial tissue. The model provides complete control of both the geometry and material behaviour of the collagen fibres and the ground matrix, where the ground matrix represents the contribution of the remaining microstructural components, such as those of the elastin fibres and GAGs to the arterial tissue mechanics. In the cases of both unidirectional and bidirectional fibre alignment models, the change in unit cell modulus versus change in fibre alignment behaviour (Figure 6.10) followed a pattern similar to the theoretical behaviour of fibre reinforced composite materials[25].

In both the unidirectional and the bidirectional fibre models, the stiffest response was exhibited by the model whose fibres were aligned in the direction of stretching, for which the shape of the resulting stress-strain curve was similar to that of the nonlinear collagen fibres. When the collagen fibres are aligned at 0° to the direction of stretching, the cross-links between the fibres transmit the load directly from one fibre to the next, across the length of the unit cell, keeping the load that is transferred to the ground matrix at a minimum level. Consequently, the stress-stretch behaviour of the model is dominated almost entirely by that of the collagen fibres.

It is also evident in Figure 6.10 that, in both types of fibre alignment models, with increasing fibre misalignment to the direction of stretching, the models experienced a decrease in stiffness. Moreover, the unidirectional fibre models were found to undergo a relatively sharper decrease in stiffness compared to the bidirectional fibre models, as the angle of fibre misalignment is increased. This phenomenon may be the main reason behind the fact that collagen fibres in the artery wall are often found in the form of two families of fibres that cross over one another[6,8,26,27]. The main advantage of having two families of crossing collagen fibres is that the cross-linking families will transfer the load between themselves to minimise the effect of variations in local fibre alignment on the overall artery modulus and structural integrity. The two band plots in Figure 6.7 provide a visual description of such a phenomenon. The bidirectional fibre model, which resembles the two-family collagen fibre architecture of arterial tissue, was able to distribute the load much more evenly across the collagen fibre network, while in the unidirectional model, the load in the collagen fibres was transferred almost entirely to the ground matrix. Consequently, the unidirectional fibre model becomes highly susceptible to local stress concentrations, which could lead to material failure in the case of real arterial tissue.

The unit cell models with distributed collagen fibre orientations (**Section 6.5**) were aimed at modelling real arterial tissues, whose collagen fibres also have distributed orientations[8,26–30]. The distribution of collagen fibre orientations was set to be the same in all models (with dispersion parameter κ set to 0.25). The influences of the changes in collagen fibre length and fibre cross-link stiffness were investigated. A linear relationship between the modulus of the unit cell model and the natural logarithms of both the fibre length and the cross-link stiffness were obtained.

On the other hand, it is evident from Figure 6.14 and Figure 6.17 that, in the case of dispersion parameter κ, an increase in cross-link stiffness caused an opposite effect compared to that of the increase in fibre length and slightly reduced the magnitude of the decrease in κ. However, the magnitude of the obtained reduction was insignificant compared to the magnitudes of change caused by increases in fibre length. This indicates that, during stretching, the length of individual collagen fibres can dictate their microstructural reorganisation, regardless of the stiffness of the links that connect them to one another.

The finite element model was hampered by excessive ground matrix continuum element distortions, as well as by stress singularities in both the ground matrix continuum and the collagen fibre beam elements. These factors have caused a large number of simulations to diverge and terminate prematurely, without giving any useful results. The simulations with distributed collagen fibre orientation unit cell models were particularly difficult as identification of a converging model with distributed collagen fibres took relatively large number of attempts with different models that had the same dispersion parameter κ. The unit cell model also experienced severe singularities and elemental distortions when the cross-linking density was changed. Moreover, the finite element method proved to be incapable of allowing simulations with local deformations that are large enough to mimic the microstructural reorganisation in real arteries. Utilisation of different types of mechanical modelling both in conjunction with or as a replacement for the finite element method can overcome these limitations. For instance, the discrete element modelling method is regarded as especially suitable for modelling of large strains, which can be either used on its own or in a hybrid model together with the finite element method[16].

6.7 Conclusion

This study presents a unique example of microstructural component-based modelling of the arterial tissue, with the collagen fibres and the ground matrix modelled as two separate structural entities. The stretch-driven stress transfer between the modelled microstructural entities were observed and influence of collagen fibre length and cross-link stiffness on the mechanical behaviour were investigated. The length of individual collagen fibres was found to be a critical determinant of the micromechanical behaviour. Development of similar models that permit larger local deformations would enable further investigation of micromechanical behaviour of arterial tissue.

6.8 References

1. Erbel, R. *et al.* 2014 ESC Guidelines on the diagnosis and treatment of aortic diseases. *Kardiol. Pol.* **72,** 1169–252 (2014).

2. Virmani, R., Burke, A. P., Farb, A. & Kolodgie, F. D. Pathology of the Vulnerable Plaque. *J. Am. Coll. Cardiol.* **47,** C13–C18 (2006).

3. Humphrey, J. D. *Cardiovascular Solid Mechanics: Cells, Tissues, and Organs*. (Springer New York, 2002). doi:10.1007/978-0-387-21576-1

4. Fung, Y.-C. *Biomechanics: Mechanical Properties of Living Tissues*. (Springer New York, 1993). doi:10.1007/978-1-4757-2257-4

5. Holzapfel, G. A., Gasser, T. C. & Ogden, R. W. A New Constitutive Framework for Arterial Wall Mechanics and a Comparative Study of Material Models. *J. Elast.* **61,** 1–48 (2000).

6. Gasser, T. C., Ogden, R. W. & Holzapfel, G. A. Hyperelastic modelling of arterial layers with distributed collagen fibre orientations. *J. R. Soc. Interface* **3,** 15–35 (2006).

7. Taylor, C. A. & Humphrey, J. D. Open problems in computational vascular biomechanics: Hemodynamics and arterial wall mechanics. *Comput. Methods Appl. Mech. Eng.* **198,** 3514–3523 (2009).

8. Holzapfel, G. A. & Ogden, R. W. Constitutive modelling of arteries. *Proc. R. Soc. A Math. Phys. Eng. Sci.* **466,** 1551–1597 (2010).

9. Sadat, U., Teng, Z. & Gillard, J. H. Biomechanical structural stresses of atherosclerotic plaques. *Expert Rev. Cardiovasc. Ther.* **8,** 1469–1481 (2010).

10. Koh, C. T. & Oyen, M. L. Branching toughens fibrous networks. *J. Mech. Behav. Biomed. Mater.* **12,** 74–82 (2012).

11. Koh, C. T., Strange, D. G. T., Tonsomboon, K. & Oyen, M. L. Failure mechanisms in fibrous scaffolds. *Acta Biomater.* **9,** 7326–7334 (2013).

12. Koh, C. T. & Oyen, M. L. Toughening in electrospun fibrous scaffolds. *APL Mater.* **3,** 014908 (2015).

13. Koh, C. T. & Oyen, M. L. Fracture toughness of fibrous membranes. *Tech. Mech.* **32,** 333–341 (2012).

14. Koh, C. T., Low, C. Y. & Yusof, Y. Bin. Structure-property Relationship of Bio-Inspired Fibrous Materials. *Procedia Comput. Sci.* **76,** 411–416 (2015).

15. Cacho, F., Elbischger, P. J., Rodríguez, J. F., Doblaré, M. & Holzapfel, G. A. A constitutive model for fibrous tissues considering collagen fiber crimp. *Int. J. Non. Linear. Mech.* **42,** 391–402 (2007).

16. Dassault Systèmes, F. Abaqus 6.14 Documentation. (2014). at <http://abaqus.software.polimi.it/v6.14/index.html>

17. Fratzl, P. *Collagen: Structure and Mechanics*. (Springer US, 2008). doi:10.1007/978-0-387-73906-9

18. Eppell, S. J., Smith, B. N., Kahn, H. & Ballarini, R. Nano measurements with micro-devices: mechanical properties of hydrated collagen fibrils. *J. R. Soc. Interface* **3,** 117–121 (2006).

19. Shen, Z. L., Dodge, M. R., Kahn, H., Ballarini, R. & Eppell, S. J. Stress-Strain Experiments on Individual Collagen Fibrils. *Biophys. J.* **95,** 3956–3963 (2008).

20. Shen, Z. L., Dodge, M. R., Kahn, H., Ballarini, R. & Eppell, S. J. In Vitro Fracture Testing of Submicron Diameter Collagen Fibril Specimens. *Biophys. J.* **99,** 1986–1995 (2010).

21. Liu, Y., Ballarini, R. & Eppell, S. J. Tension tests on mammalian collagen fibrils. *Interface Focus* **6,** 20150080 (2016).

22. van der Rijt, J. A. J., van der Werf, K. O., Bennink, M. L., Dijkstra, P. J. & Feijen, J. Micromechanical Testing of Individual Collagen Fibrils. *Macromol. Biosci.* **6,** 697–702 (2006).

23. Yang, L., van der Werf, K. O., Dijkstra, P. J., Feijen, J. & Bennink, M. L. Micromechanical analysis of native and cross-linked collagen type I fibrils supports the existence of microfibrils. *J. Mech. Behav. Biomed. Mater.* **6,** 148–158 (2012).

24. Poissant, J. & Barthelat, F. In Situ Mechanical Testing of Hydrated Biological Nanofibers Using a Nanoindenter Transducer. *Exp. Mech.* **52,** 1287–1295 (2012).

25. Hull, D. & Clyne, T. W. *An Introduction to Composite Materials*. *Cambridge Solid State Science Series* (Cambridge University Press, 1996). doi:10.1017/CBO9781139170130

26. Schriefl, A. J. Quantification of Collagen Fiber Morphologies in Human Arterial Walls. (Graz University of Technology, 2013). doi:10.3217/978-3-85125-238-5

27. Schriefl, A. J., Zeindlinger, G., Pierce, D. M., Regitnig, P. & Holzapfel, G. A. Determination of the layer-specific distributed collagen fibre orientations in human thoracic and abdominal aortas and common iliac arteries. *J. R. Soc. Interface* **9,** 1275–86 (2012).

28. Schriefl, A. J., Reinisch, A. J., Sankaran, S., Pierce, D. M. & Holzapfel, G. A. Quantitative assessment of collagen fibre orientations from two-dimensional images of soft biological tissues. *J. R. Soc. Interface* **9,** 3081–93 (2012).

29. Douglas, G. R. *et al.* Impact of Fiber Structure on the Material Stability and Rupture Mechanisms of Coronary Atherosclerotic Plaques. *Ann. Biomed. Eng.* **45,** 1462–1474 (2017).

30. Sugita, S. & Matsumoto, T. Multiphoton microscopy observations of 3D elastin and collagen fiber microstructure changes during pressurization in aortic media. *Biomech. Model. Mechanobiol.* **16,** 763–773 (2017).

Chapter 7

Conclusion and future work

7.1 Conclusion

The main goals of this study were to investigate the mechanical behaviour of arterial tissues both in the absence and presence of a structural defect and to identify the associations between its microstructure and mechanics.

First, a uniaxial tensile testing study was performed for comprehensive characterisation of mechanical and fracture behaviours of arterial layers from aneurysm-affected aortas. Unnotched and notched uniaxial tensile tests were performed on diseased aortic tissues and mechanical, as well as fracture parameters were calculated. These parameters were compared amongst tissues from the intima, media and adventitia layers, which were sampled along both the axial and circumferential directions of the aorta. The unnotched circumferential adventitia samples were found to have the highest material strength amongst all other unnotched tissue types, while the intima and media layers were found to have similar ultimate material strengths along both directions of the aorta. On the other hand, the unnotched media and adventitia layers were found to be stronger in the circumferential than the axial direction. In this study, the structural defect was mimicked with a single edge notch. In the presence of this defect, the material strength of the adventitia in both directions was higher than the strength of intima or media in any direction. The notched adventitia samples were also found to exhibit higher fracture toughnesses compared to the other arterial layers, which was confirmed by their failure point J-integral values. Aneurysmal tissues also exhibited a notch-insensitive behaviour as the tissue strips with notches did not fail at a low level of stretch. This study is the first comprehensive experimental investigation that is aimed at simultaneous characterisation of both mechanical and fracture behaviours of diseased aortic tissues.

The mechanical and fracture behaviour investigation was followed by a study that aimed at exploration of the association between the microstructural components and the mechanical properties of aortic aneurysms. This study highlighted the role of microstructural components, as well as the role of disease-driven changes in their turnover and architecture on the mechanical properties. Histological processing was performed on the mechanically tested diseased human aortic tissues. The obtained histological tissue slides were digitised into RGB images and area percentages of collagen, elastin, macrophage and GAGs, as well as collagen fibre dispersion were quantified. Collagen, elastin and GAGs were layer-dependent and the inflammatory burden in all layers was found to be low.

The GAG area percentage was found to be negatively correlated with the collagen area percentage, but positively with that of elastin. Higher GAG deposition resulted in larger local collagen fibre dispersion in the media and adventitia, but not in the intima. On the other hand, the extreme extensibility of unnotched tissue strips in both axial and circumferential aorta directions was exclusively associated with elastin ratio. Collagen and GAG contents were both associated with material strength in the circumferential direction, but not in the axial. Similar findings were also obtained from tests with notched tissue strips, in which both collagen and GAGs but not elastin or macrophages were associated with material strength. Studies of arterial micromechanics have often focused on collagen and elastin, with GAGs being neglected. This study showed that, despite being a minor ECM component, GAGs can play an important role in the micromechanical architecture and mechanical behaviour of arterial tissues and therefore, their contribution should not be neglected.

Following investigation of the mechanical properties and the relationship between mechanics and microstructural components of diseased aortic tissues, curve fitting was used to determine constitutive material model constants of uniaxially tested specimens from health aortic, aneurysmal and atherosclerotic tissues. The modified Mooney-Rivlin material model was fitted to each stress-stretch curve with the Bayesian inference-based estimation method, which was found to be relatively robust compared to the other curve fitting methodologies (such as the ordinary least square). Curve fitting allowed determination of C_1 , D_1 and D_2 constants of the modified Mooney-Rivlin model, where the correlation of the determined material constants with the corresponding microstructural entities were investigated. Fitted material constants were found to differ amongst distinct tissue types. Atherosclerotic tissues associated with the biggest D_2, which is an indicator of the rate of increase in stress during stretching, followed by aneurysmal tissues and those from healthy aortas.

Obtained results indicated that C_1 , D_1 and D_2 constants of the modified Mooney-Rivlin model were tissue type dependent. In particular, D_2 was found to be the most sensitive parameter in differentiating tissues of distinct arterial layers from a single type of sample, or of the same layer between different type of samples. D_2 was also associated with tissue architectures, namely the fibre dispersion and fibre waviness. This study has proved that, through utilisation of a robust curve fitting methodology, constitutive material model constants can indicate the pathophysiological state of the arterial tissue.

After establishing a better understanding of the relationship between the microstructural state and mechanical, as well as fracture behaviour of arterial tissue, the focus was shifted towards investigating the microstructural reorganisations of the fibrous network during stretching. Unnotched and notched healthy porcine carotid artery tissue strips were stretched uniaxially, while 3D images of their microstructure were acquired with a multiphoton microscope. The orientation and dispersion of the imaged fibres were quantified at increasing levels of stretch. Fibres in the intima and media layers rotated towards the direction of applied stretch as the level of the applied stretch was increased, which was accompanied with a corresponding decrease in the dispersion of fibre orientations. In the case of notched tissue strips, fibres rearranged themselves to redistribute loads away from the crack tip, essentially bridging the crack. The results of this study clearly indicate that the fibrous network undergo extensive reorganisations to accommodate the load that is transferred across the arterial tissue microstructure. Moreover, in the presence of structural defects, the fibres play a critical role in preventing propagation of cracks as they toughen the arterial tissue by bridging the crack.

Finally, a further study on the microstructure-mechanics relationship of arterial tissue was performed with the use of finite element modelling. A microstructural component based and bottom-up built arterial tissue finite element model was developed and optimised for use in simulations that are aimed at understanding the influence of microstructural component parameters on the macroscale mechanical behaviour of arterial tissues. In the model, the collagen fibres and the arterial tissue ground matrix (the ground matrix represents the mechanical contribution of all other microstructural entities, such as elastin and GAGs) were modelled as two separate entities with beam and solid continuum elements[1], respectively. The collagen fibres were cross-linked to one another and linked to the ground matrix as well. The finite element model allowed visualisation of the stress transfer between the modelled microstructural entities, providing a clearer view of the microscale interactions during stretching.

The collagen fibre length was found to be a critical determinant of the micromechanical behaviour and outweighed the influence of the change in fibre cross-link stiffness on the macroscale behaviour. The finite element model was greatly hampered by excessive elemental distortions and singularities during stretching, which limited its capability in allowing simulations with local deformations that are large enough to closely mimic the microstructural reorganisation in real arteries. Consequently, future studies should prioritise utilisation of modelling methodologies that allow large enough local deformations that are similar to those in real arterial tissue.

7.2 Future work

Although the mechanical and fracture properties of diseased human aortic tissues were comprehensively explored, reference properties from healthy human aortic tissue are missing. Therefore, a future experimental study on characterisation of mechanical and fracture behaviours of the healthy aortic tissue would allow comparison between the healthy and diseased tissue properties, to provide better understanding of the changes experienced with disease. On the other hand, the arterial tissue is naturally anisotropic, therefore, it has distinct mechanical properties in different directions. In the current experimental investigation, axial and circumferential tissue strips were tested separately, and the mechanical properties of the artery were characterised separately along its two main directions. However, the loading that is applied on the artery wall in the body by blood also has a multidirectional configuration. Therefore, the utilised uniaxial tensile testing methodology can be replaced with either biaxial loading or pressurisation of the artery wall to better mimic the loading that is applied on the artery by blood.

The fracture behaviour of arterial tissues was studied by uniaxial tensile testing of single edge notched axial and circumferential tissue strips. The single edge notch was made either along the axial or the circumferential artery direction, however, the tear that is experienced by the diseased arterial tissue during initiation of an aortic dissection, or during rupture of an aortic aneurysm is more likely to be oriented along the radial artery direction. Therefore, in a future study, an experimental methodology can be developed to allow fracture mechanics tests on both healthy and diseased aortic tissues with radial notches. The developed methodology should also enable control of the notch width, as well as its depth into the tested arterial layer.

Moreover, enabling simultaneous multiphoton microscopy imaging of the tested tissue microstructure would provide information on the stretch-driven microstructural reorganisations around the radial notch.

In the case of histopathological examinations on aortic tissues, similar to the case of mechanical investigations, data from healthy tissues were not available for comparison with the microstructural component parameters that were obtained from diseased aortic tissues. Consequently, a future histopathological examination on healthy aortic tissues can provide valuable data that can be compared with the existing data of diseased aortic tissues.

On the other hand, a different methodology can be utilised to obtain more accurate information on the microstructural organisation of distinct components. This can involve use of a 3D imaging technique, such as confocal microscopy, to provide detailed 3D data on the microstructural architecture of arterial tissues. Each microstructural component can be stained with a specific dye, which would colour the distinct components with different colours so that sufficient contrast is obtained when the tissue is imaged with the confocal microscope. Collagen, elastin, GAGs and macrophage cells can all be dyed to distinct colours and appear all together in the same 3D image volume, allowing a detailed study of their microstructural organisation.

In the constitutive modelling study, the fitted stress-stretch curves were from uniaxial tensile tests and the utilised constitutive modified Mooney-Rivlin model was an isotropic model, consequently, the anisotropy of the aortic tissue was not considered. This study can be repeated in the future with biaxial tensile tests and by using an anisotropic constitutive model such as the one reported by Gasser et al.[2].

A significant amount of future work can also be pursued by utilising the preliminary findings from the multiphoton microscope investigations on the stretch driven microstructural reorganisations of arterial tissue. These investigations only scratched the surface of what is happening in the microstructure during stretching. This is mainly because only four carotid arteries were utilised in the current study, which were from healthy pigs. Therefore, the immediate improvements should involve increasing the sample number and using human arterial tissue samples. Biaxial tensile testing experiments can also be utilised to observe the anisotropic micromechanical behaviour of the fibrous network.

Multiphoton microscopy has the ability to allow differentiation between collagen and elastin fibres, which should be utilised in the future to study the microstructural reorganisations of collagen and elastin separately[3].

Finally, the developed microstructural component based finite element model should serve as a starting point for more capable models that can converge much easier with distinct microstructural component organisations, while allowing larger local strains that are more similar to those of the real arterial tissue. It is important to note that finite element modelling should not be considered as the only possible way of mechanical modelling and other types of modelling, such as discrete element modelling[1] should also be considered to allow achieving the required model performance.

One major aspect of arterial micromechanics that was not studied by the current model was reorganisation of collagen fibres around structural defects. A future model should allow introduction of distinctly shaped structural defects, so that the microstructural reorganisation of fibres, as well as the stress transfer between the fibres around the structural defect can be studied. In the current model, the collagen fibres are simply laid on top of the ground matrix and connected to it through elemental nodes. Nevertheless, a more realistic model can include a ground matrix that completely surrounds each collagen fibre. Such a model would yield simulations, which have more realistic stress transfers between the fibres and the ground matrix.

7.3 References

1. Dassault Systèmes, F. Abaqus 6.14 Documentation. (2014). at <http://abaqus.software.polimi.it/v6.14/index.html>

2. Gasser, T. C., Ogden, R. W. & Holzapfel, G. A. Hyperelastic modelling of arterial layers with distributed collagen fibre orientations. *J. R. Soc. Interface* **3,** 15–35 (2006).

3. Zoumi, A., Lu, X., Kassab, G. S. & Tromberg, B. J. Imaging coronary artery microstructure using second-harmonic and two-photon fluorescence microscopy. *Biophys. J.* **87,** 2778–86 (2004).